

**Numerical stability studies of one-phase and
immiscible two-phase jets and wakes**

by

Outi Tammissola

June 2011
Technical Reports from
Royal Institute of Technology
KTH Mechanics
SE-100 44 Stockholm, Sweden

Akademisk avhandling som med tillstånd av Kungliga Tekniska Högskolan i Stockholm framlägges till offentlig granskning för avläggande av teknologie doktorsexamen måndagen den 13 juni 2011 kl 10.15 i sal F3, Kungliga Tekniska Högskolan, Lindstedtsvägen 26, Stockholm.

©Outi Tammissola 2011

Universitetsservice US-AB, Stockholm 2011

Outi Tammissola 2011, **Numerical stability studies of one-phase and immiscible two-phase jets and wakes**

KTH Mechanics, SE-100 44 Stockholm, Sweden

Abstract

The initial linear instability growth of two-dimensional plane wakes and jets is investigated, by temporal two-dimensional global modes, and local spatial stability analysis. Comparisons are also made to experiments, direct numerical simulations, and methods designed for weakly-non-parallel flows. The studies proceed through three different flow setups with increasing complexity.

The first flow analysed is a convectively unstable liquid sheet surrounded by a stagnant or co-flowing gas. The experimentally measured growth rates are found to be in excellent agreement with spatial stability calculations, if the air boundary layer is taken into account, and not otherwise. The stabilizing effect of moderate air co-flow is quantified in the numerical study, and the governing parameters found to be the speed difference between water and air, and the shear from air at the water surface (inversely proportional to the air boundary layer thickness).

The second flow case is a one-phase confined wake, *i.e.* a wake in a channel. The effect of confinement (wall distance) on the global stability of wakes is analysed by linear global modes, and compared to the results from DNS and weakly-non-parallel theory. At $Re = 100$, confinement is globally stabilizing, mostly due to a faster development towards a parabolic profile for confined flows. The stabilizing effect of confinement almost disappears at $Re \approx 400$. However, when the structural sensitivity of the wakes is analysed by an adjoint-based approach, fundamental differences are seen in the global wavemakers of confined and unconfined wakes at $Re \approx 400$.

The third and most complex flow case is immiscible two-fluid wakes and jets. A parallel multi-domain spectral code is developed, where the kinematic and dynamic conditions on the interface are imposed as coupling conditions. It is shown that intermediate values of surface tension can destabilize stable wakes and jets. In addition, surface tension has a considerable influence on the global oscillation frequency and spatial shape of the global mode for unstable wakes. The character of the mode is gradually changed from a wake instability to a global shear layer instability. Both symmetric and antisymmetric modes are encountered for both wakes and jets, depending on the strength of the surface tension (value of the Weber number) and the flow case.

Preface

This thesis considers numerical studies of global and local hydrodynamic instabilities in wake and jet flows. The first part, Overview, contains an introduction to the field, and sets the present work into a broader context. The second part, Papers, consists of six papers. The papers are adjusted to comply with the present thesis format, but their contents have not been altered compared to published or submitted versions, except for minor corrections. The included papers are:

Paper 1 Outi Tammisola, Atsushi Sasaki, Fredrik Lundell, Masaharu Matsubara & L. Daniel Söderberg:

Stabilizing effect of surrounding gas flow on a plane liquid sheet. *Journal of Fluid Mech.* 672 (2011), 5–31.

Paper 2 Outi Tammisola, Fredrik Lundell, Armin Wehrfritz, Philipp Schlatter & L. Daniel Söderberg:

Global linear and nonlinear stability of viscous confined plane wakes with co-flow. *Journal of Fluid Mech.* 675 (2011), 397–434.

Paper 3 Outi Tammisola, Fredrik Lundell & L. Daniel Söderberg:

Effect of surface tension on global modes of confined wake flows. *Phys. Fluids* 23 (2011), 014108.

Paper 4 Matthew Juniper, Outi Tammisola & Fredrik Lundell:

Comparison of local and global stability properties of confined wake flows. *To appear in Journal of Fluid Mech.*

Paper 5 Outi Tammisola:

Oscillatory sensitivity patterns for global modes in wakes. *Submitted.*

Paper 6 Outi Tammisola, Fredrik Lundell & L. Daniel Söderberg:

Surface tension induced global destabilisation of plane jets and wakes. *To be submitted.*

May 2011, Stockholm

Outi Tammisola

Contents

Abstract	iii
Preface	iv
Chapter 1. Introduction	1
1.1. Jets and wakes in paper manufacturing	3
1.2. Scope and structure of the thesis	5
Chapter 2. Basic stability concepts	6
2.1. Linear global stability	6
2.2. Local spatiotemporal analysis	9
2.3. Transient growth of global modes and convective instability	12
2.4. Sensitivity	13
2.5. Local nonlinear theory	14
2.6. Concluding remarks	15
Chapter 3. Global stability of one-phase wakes	16
3.1. Cylinder wake	16
3.2. Co-flow wakes	21
3.3. Linearisation around the nonlinear mean flow	22
3.4. Linear global modes in complex geometries	23
Chapter 4. Stability of two-fluid immiscible shear flows	25
4.1. Coaxial wakes and jets with surface tension	25
4.2. Plane wakes, jets and shear layers with surface tension	28
Chapter 5. Flow cases in the present work	36
5.1. Single-phase co-flow wakes	36
5.2. Wakes and jets with surface tension	38

5.3. Liquid sheet	40
Chapter 6. Governing equations and numerical solution	43
6.1. Base flows	43
6.2. Numerical algorithms for solving eigenvalue problems	46
6.3. Global stability of wakes	50
6.4. Structural sensitivity of wakes	55
6.5. Global stability of wakes and jets with surface tension	57
6.6. Local stability of the liquid sheet surrounded by gas	60
Chapter 7. Summary of the results of the present work	63
7.1. Stabilizing effect of air co-flow on a plane liquid sheet	63
7.2. The influence of confinement on wake instability	65
7.3. The effect of surface tension on wakes and jets	72
Chapter 8. Conclusions and outlook	77
8.1. Conclusions	77
8.2. Outlook	80
Chapter 9. Papers and authors contributions	82
Acknowledgements	86
References	88
Paper 1. Stabilizing effect of surrounding gas flow on a plane liquid sheet	99
Paper 2. Global linear and nonlinear stability of viscous confined plane wakes with co-flow	141
Paper 3. Effect of surface tension on global modes of confined wake flows	195
Paper 4. The local and global stability of confined planar wakes at intermediate Reynolds number	227
Paper 5. Oscillatory sensitivity patterns for global modes in wakes	257

**Paper 6. Surface tension induced global destabilisation of
plane jets and wakes**

291

Part I

Overview and summary

CHAPTER 1

Introduction

Gases and liquids are also called *fluids*¹. The motion of a fluid around a solid body generates friction and lift forces on the body (*e.g.* drag and lift on an airplane). Fluids and particles are transported in pipelines and channels, where the consistency of the outgoing flow and the required pressure drop are important. Many industrial processes involve mixing of two fluids, *e.g.* the liquid and the air in sprays, the fuel and the oxidizer in a combustion engine, different pulp streams in papermaking or flows in food and agriculture industry.

The mixing efficiency is inherently related to the time-dependent flow patterns, *i.e.* the unsteadiness of the flow. Imagine that you have just poured milk into a cup of coffee. If the flow just rotates slowly around with almost constant velocity, there is practically no mixing. However, you take the spoon and make small and fast rotations, thereby creating vortices of many different sizes that mix up the two liquids very efficiently.

Strictly speaking, the liquid and air in sprays never mix but remain always as separate phases due to the *surface tension* between them. They are therefore called *immiscible* to each other. The apparent "mixing" in this case is due to the breakup of the liquid into drops. Coffee and milk on the other hand are *miscible*, and build a homogeneous mixture at the end.

The motion of a fluid can be represented by its velocity distribution in time and space. Most often, a fluid can be treated as a continuous medium², and the laws of Newton governing its motion are formulated in the Navier-Stokes equations, knowing its viscosity³ and initial state⁴.

¹Sometimes, a flow of solid particles can also be described as a "fluid".

²The exception is rarified gases.

³In fact, many real fluids involving small particles are *non-Newtonian*, so that their viscosity is related to the velocity field, often in a way that is unknown. The attempt to find this relation for suspensions is a vital field of research today.

⁴in terms of the initial velocity, pressure, density and temperature.

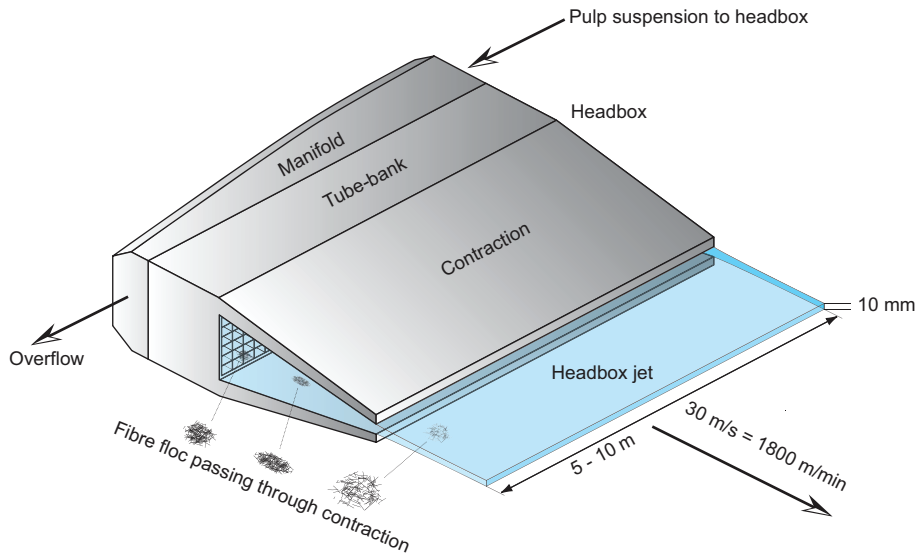


FIGURE 1.1. The flow of a fibre suspension through a paper machine nozzle, from where it enters air as a thin liquid sheet. One aim of the sharp contraction is to drag apart fibre flocs. Figure from Lundell *et al.* (2011).

However, the complication comes in that the most known flows are unstable, drifting away from steady solutions to periodic or chaotic ones, with many different time and spatial scales to resolve. Chaotic flows with a continuous range of scales are called *turbulent*, and only a few of those can be accurately computed today (even in a statistical sense), despite the huge increase of computational power the last decades.

The pattern of the transition from a steady to an unsteady state depends on the nature of the *instability* of the flow. For example, the breakup of a liquid jet into small drops in a spray is initiated by the growth of small waves on its surface⁵. By influencing the wave growth, the breakup can be either delayed or promoted. This thesis deals with the initial growth of surface waves and other hydrodynamic instabilities. The type of flows under study are *wakes* and *jets*, inspired by the paper manufacturing process.

⁵The details of the final breakup and the resulting drop distribution are complicated, and out of scope of this thesis.

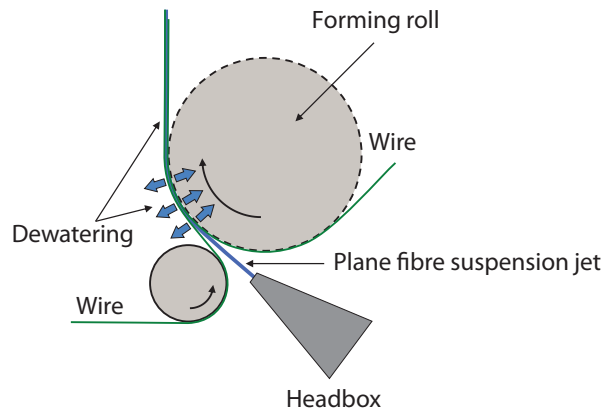


FIGURE 1.2. The jet from the paper machine nozzle finally hits two permeable wires. As the water flows through, the fibres remain and build a "fibre mat". The structure of this fibre network is important for the properties of the final paper sheet. Figure from SPCI Summer Meeting 2007.

1.1. Jets and wakes in paper manufacturing

This paper you are holding in your hand right now is made of cellulose fibres. However, its flat surface is not created by just pressing fibres together — in that case it would hardly be possible to print anything on it. To be able to get a homogeneous structure, we start with a suspension of approximately 99 % water and 1% fibres. In a paper machine, this suspension flows through structures that either generate mixing for homogeneous fibre distribution, or accelerate the flow to drag apart the dense structures the elongated fibres tend to form together, called *fibre flocs*.

The suspension finally flows through a converging nozzle, the *head-box* (figure 1.1), from which it enters air as a thin liquid sheet. The sheet is typically 1 cm thick and 10 m wide. After a short distance this sheet hits one or enters between two permeable screens, *wires*, where water flows through and fibres remain (figure 1.2). Here the "paper is made" — the fibre network on the wires resembles the structure of the final paper. The structure is also influenced by subsequent stages, where

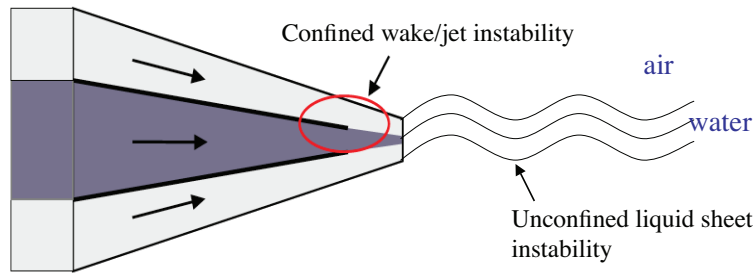


FIGURE 1.3. The hydrodynamic instabilities occurring near the papermachine nozzle — 1) vortex shedding behind the vanes (or a possible jet instability in the case of water filled AQ-vanes) and 2) waves in the surface of the liquid sheet surrounded by stagnant air. Confinement means near-lying walls.

the paper is pressed and dried. The pressing and drying section is more than ten times longer than the wire section — so much energy is spent on taking out the water that we put the fibres into in the first place! The water is necessary in order to distribute the fibres homogeneously. A more detailed description about the different stages of the papermaking process can be found in Lundell, Söderberg & Alfredsson (2011); Norman, Engström & co-authors (2005).

Imagine now that we wish to make a paper with different layers — *e.g.* put some fine fibres on the surfaces, but less costly and unbleached rough fibres in the middle to save both money and environment. Inside the headbox, different pulp streams could in principle be separated by solid plates, *vanes* (figure 1.3). However, after the vanes we get *wakes*, regions with locally lower velocity. Wakes are known to be susceptible for oscillations (for a flow behind a cylinder, these oscillations are the famous *von Kármán vortex street*, see Sec. 3.1). Furthermore, when the liquid sheet moves through the air, waves appear on its surface. Both flow instabilities, in the wakes and in the sheet (figure 1.3), cause the pulp streams to mix with each other, and distort the layers in the final paper.

The wake alone might be stabilised by *base bleed* — building a small channel inside the vane from which water flows out at the vane end turning the wake into a more stable *jet*, a region with a locally higher velocity. The concept is called an *AQ-vane*. But even so, we have the surface waves on the liquid sheet interface. It is not known how the different kinds of instabilities will interact and how to achieve the most stable flow conditions for the liquid sheet.

1.2. Scope and structure of the thesis

This thesis aims to contribute to the understanding and control of instabilities in plane wake and jet flows. This includes both one-fluid flows, and those where two immiscible fluids with different velocities meet and "mix". The focus is on the occurrence of *self-sustained oscillations* through so-called *global instabilities*. The precise meaning of the concept will be clarified in the following chapters.

The instability in two-phase wakes and jets is governed by many parameters: velocities, densities and viscosities of the two fluids, and the strength of the surface tension, to name a few. We expect the present work to solve a piece of this puzzle, by increasing the fundamental understanding in the field. The method of linear global modes has been implemented for immiscible two-phase flows and carefully evaluated for one-phase flows. At present, the parameters occurring in the papermachine are not reachable, but at sight the findings might help to understand whether or not global modes can occur in papermaking.

The thesis is organized as follows: The first part (Overview and summary) with nine chapters contains an introduction to the subject, methods, results and conclusions. Chapter 2 gives a basic introduction to global and local stability. The next two chapters present relevant results from the literature, for one-phase (Ch. 3) and immiscible two-fluid wakes and jets (Ch. 4). The rest of the overview deals with the present work. The flow cases under study are presented in Ch. 5, and the numerical methods used in Ch. 6. The main results are summarized in Ch. 7, and the conclusions and an outlook are found in Ch. 8. The last chapter (Ch. 9) quantifies the work division between authors in the manuscripts in the second part.

The second part (Papers) consists of six papers. Paper 1 deals with the local stability of a plane liquid jet in air, papers 2, 4 and 5 with the global stability of confined wakes, and paper 3 and 6 with the global stability of immiscible wakes and jets with surface tension.

CHAPTER 2

Basic stability concepts

Global self-sustained oscillations of flows are an area of interest for experimental as well as theoretical work. The ultimate goal is to characterise whether a flow behaves as a *noise amplifier* returning towards the basic state when the disturbance level is lowered, or if the flow is an *oscillator* and continues to amplify the noise even if the source is removed. Below the main theoretical framework around the self-sustained oscillators, *i.e.* globally unstable flows, that will be used in other parts of this thesis is summarised. Methods and theory behind studies of noise amplifier flows are also touched on, since the liquid sheet in Paper 1 of this thesis belongs to this category.

2.1. Linear global stability

When a flow problem has only time-independent boundary conditions, it would seem natural to always observe a steady flow field. If the flow is incompressible, the candidate for a steady flow field should then satisfy the steady incompressible variant of the Navier-Stokes equations, *i.e.* the law of motion for a Newtonian fluid:

$$U_j \frac{\partial U_i}{\partial x_j} = -\frac{\partial P}{\partial x_i} + \frac{1}{Re} \frac{\partial U_i}{\partial x_j \partial x_j} \quad (2.1)$$

$$\frac{\partial U_j}{\partial x_j} = 0, \quad (2.2)$$

in tensor notation, where $i = 1, 2, 3$ denotes the spatial coordinate (x , y or z), and $Re = \rho^* U^* L^* / \mu^*$ is the *Reynolds number*. The equations here are brought into the *nondimensional* form, where the velocities are scaled with an appropriate reference velocity scale U^* , the spatial coordinates with a length scale L^* , and ρ^* denotes the density and μ^* the dynamic viscosity of the fluid.

However, this solution is not necessarily observed in reality, unless all initial flow states go towards the steady solution. In reality, the flow starts from a different state (*e.g.* when the flow fills a pipe for

the first time), and more importantly, there are always disturbances, such as sound waves, vibrations or surface imperfections, that are not accounted for in the equations above¹. Depending on the *stability* of the steady solution above, the flow might develop towards this solution (if the steady state is asymptotically stable), or migrate away from it (if the steady state is unstable) until it reaches a different, time-dependent state.

Linear stability investigates the stability of the steady state (\bar{U}, P) , against small amplitude deviations (\bar{u}, p) . The overbars denote vectors, and are related to the tensor notation as $\bar{U} = (U_i, i = 1, 2, 3)$. The total flow field (the steady flow and deviation) can then be written as:

$$U_{tot,i}(x, y, z, t) = U_i(x, y, z) + u_i(x, y, z, t), \quad (2.3)$$

$$P_{tot}(x, y, z, t) = P(x, y, z) + p(x, y, z, t). \quad (2.4)$$

In the following, the steady part denoted by capital letters will be called the *base flow* and the deviation with lowercase letters a *disturbance*. This disturbance is introduced directly into the flow field and should be distinguished from the disturbance sources mentioned above; we do not address the *receptivity* process by which for example the sound waves or surface imperfections are transformed into small deviations (\bar{u}, p) . We rather assume that small noise with all shapes and frequencies is always available, and investigate what kind of noise a particular steady state is unstable to.

The division of terms (2.3–2.4) is introduced into Navier-Stokes equations:

$$\begin{aligned} \frac{\partial u_i}{\partial t} + U_j \frac{\partial U_i}{\partial x_j} = \\ - \frac{\partial P}{\partial x_i} - \frac{\partial p}{\partial x_i} + \frac{1}{Re} \frac{\partial U_i}{\partial x_j \partial x_j} + \frac{1}{Re} \frac{\partial u_i}{\partial x_j \partial x_j} \end{aligned} \quad (2.5)$$

$$\frac{\partial U_j}{\partial x_j} + \frac{\partial u_j}{\partial x_j} = 0. \quad (2.6)$$

Since the base flow satisfies Eq. (2.1–2.2), all terms with only capital letters cancel each other. Further, the *linear* stability assumes that the disturbance is so small that the nonlinear term in the disturbance $(u_j \frac{\partial u_i}{\partial x_j})$ can be neglected. We are left with the *linearized* Navier–Stokes

¹or in the case of surface roughness, in the boundary conditions

equations (LNSE):

$$\frac{\partial u_i}{\partial t} + U_j \frac{\partial u_i}{\partial x_j} + u_j \frac{\partial U_i}{\partial x_j} = -\frac{\partial p}{\partial x_i} + \frac{1}{Re} \frac{\partial u_i}{\partial x_j \partial x_j} \quad (2.7)$$

$$\frac{\partial u_j}{\partial x_j} = 0. \quad (2.8)$$

Now, we have an equation for the disturbance (lowercase letters) as a variable, and the base flow (uppercase letters) as known coefficients, and we would like to know which disturbances are amplified in time by extracting energy from the steady flow, and which ones just decay. The coefficients (steady flow) are independent of time, so we can Fourier-transform in time:

$$u_i = \hat{u}_i(x, y, z)e^{-i\omega t}, \quad (2.9)$$

and similarly for pressure and possible other disturbance quantities (such as the unsteady interface displacement in interfacial flows). Here, $i = \sqrt{-1}$ and $\omega = \omega_r + i\omega_i$ is thus a complex number. The Fourier-transformed LNSE will now take the form:

$$-i\omega \hat{u}_i + U_j \frac{\partial \hat{u}_i}{\partial x_j} + \hat{u}_j \frac{\partial U_i}{\partial x_j} = -\frac{\partial \hat{p}}{\partial x_i} + \frac{1}{Re} \frac{\partial \hat{u}_i}{\partial x_j \partial x_j} \quad (2.10)$$

$$\frac{\partial \hat{u}_j}{\partial x_j} = 0. \quad (2.11)$$

These can be seen as the kinematic equations for a small sinusoidal oscillation around the steady state, with an oscillation frequency ω_r and an exponential growth or decay in time with exponent ω_i . A disturbance with an arbitrary ω and an arbitrary spatial shape does not satisfy these equations. Mathematically, this becomes as an eigenvalue problem, where ω is an eigenvalue, and each possible ω comes together with its corresponding eigenfunction $q = (\hat{u}, \hat{p})$, giving the spatial shape of the disturbance oscillating with this particular ω . The equations can be written formally as:

$$\Lambda q = -i\omega Bq, \quad (2.12)$$

where Λ is a linear operator acting on q to produce all the spatial terms in Eq. (2.10–2.11), and $Bq = \hat{u}$. After spatial discretisation, Λ and B become matrices, q a vector, and the problem can be solved with standard methods for eigenvalue computations (Sec. 6.2).

The collection of ω for which a solution exists is called the *spectrum*. A spectrum can have both a discrete part, where eigenvalues are separated from each other by a certain finite distance, and a continuous part,

where the possible solutions form a curve or a surface. Strictly speaking, one should invert a Fourier integral (or an infinite sum) over all ω , weighted depending on the initial condition, to obtain the predicted dynamical behaviour of the flow. However, one can often gain enough information by looking at a discrete subset of the spectrum. How this set should be chosen, depends on the physical character of the disturbances, and will be clarified further in sections 2.2 and 2.3.

Equations (2.9–2.11) above are general and yield the stability for base flows of any space dimension. When the base flow is plane two-dimensional, we can Fourier-transform also in the cross-stream (z -) direction :

$$u_i = \hat{u}_i(x, y)e^{\beta z - i\omega t}, \quad (2.13)$$

where β is a *real* number; it is inappropriate to assume spatial growth in a coordinate direction where the base flow vanishes. In this thesis, we further assume that $\beta = 0$, *i.e.* that the disturbances at the onset of the instability are two-dimensional:

$$u_i = \hat{u}_i(x, y)e^{-i\omega t}. \quad (2.14)$$

In the latter case, the governing equation then simplifies to two space dimensions, *i.e.* $i = 1, 2$ in Eq. (2.10–2.11).

If Ansatz (2.9) is applied on a three-dimensional base flow, one obtains *three-dimensional global modes*. Correspondingly, if Ansatz (2.13) or (2.14) is applied, one obtains *two-dimensional global modes*, which is the case in this thesis.

For flows where the disturbance structure is wave-like in the streamwise direction, and the length scale of the base flow variations in the streamwise direction is much longer than the disturbance wavelength, it is possible to do a further simplification using the local spatio-temporal theory and one-dimensional eigenfunctions, described in the next section. We shall also see that for disturbances that take the form of wave packets convected downstream, the local theory provides a more straightforward physical description of the disturbance.

2.2. Local spatiotemporal analysis

For base flows with one dominating velocity component, approximations of the flow behaviour can be found based on one-dimensional eigenfunctions of the local velocity profile in each streamwise position. This *locally parallel flow assumption* means that all streamwise base flow gradients

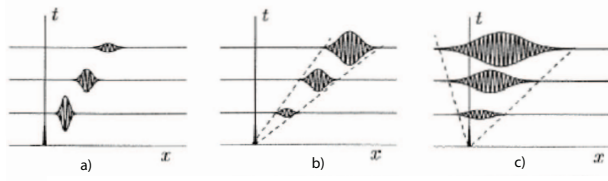


FIGURE 2.1. Classification of the local stability of a flow in terms of an impulse response: (a) stable, (b) convectively unstable, (c) absolutely unstable. Figure and classification from Huerre & Monkewitz (1990).

are neglected in the equations:

$$\bar{U} = (U(y), 0, 0), \quad (2.15)$$

and then the disturbance can be Fourier-transformed also in x -direction, resulting in the ansatz:

$$u_i = \hat{u}_i(y) e^{i\alpha x - i\omega t + \beta z}. \quad (2.16)$$

This leads to the local linear stability equations:

$$-i\omega \hat{u} + i\alpha U \hat{u} + \frac{\partial U}{\partial y} \hat{v} = -i\alpha \hat{p} + \frac{1}{Re} (-\alpha^2 \hat{u} + D^2 \hat{u}), \quad (2.17)$$

$$-i\omega \hat{v} + i\alpha U \hat{v} = -D \hat{p} + \frac{1}{Re} (-\alpha^2 \hat{v} + D^2 \hat{v}), \quad (2.18)$$

$$i\alpha \hat{u} + D \hat{v} = 0, \quad (2.19)$$

where $D = \frac{\partial}{\partial y}$, $D^2 = \frac{\partial^2}{\partial y^2}$, \hat{u} is the streamwise and \hat{v} the vertical disturbance velocity.

Here we will only address two-dimensional base flows, but the theory can be extended to three-dimensional flows as well. For two-dimensional base flows, β is again a real wavenumber. However, to allow for spatial growth of the disturbance in the streamwise direction, α needs to be a complex number. Its real part (α_r) is inversely proportional to the streamwise wavelength of the disturbance, and the imaginary part α_i is the spatial growth rate (in the streamwise direction). The appropriate method for analysis of the flow depends on the character of the instability, as explained below.

To classify different kinds of oscillations in the local setting, (Briggs 1964; Huerre & Monkewitz 1990) introduced the concept of *absolute* and

convective instability related to the linear impulse response of flows (Fig. 2.1). Here, a flow field is disturbed locally at one streamwise point at one instant in time, and the development of the generated wave packet is investigated. If the amplitude of the linear impulse response grows without a limit, but at the same time is convected downstream from the source, the flow is locally convectively unstable (figure 2.1 b). If the impulse response grows without a limit and is not convected away as $t \rightarrow \infty$, the flow is locally absolutely unstable (figure 2.1 c). For flows with weak streamwise gradients of the base flow, *i.e.* weakly non-parallel flows, a large enough region of local absolute instability shall give rise to the same unstable two-dimensional linear global mode as obtained from Ansatz 2.14 (Huerre & Monkewitz 1990), and the frequency and shape of the global mode can be approximated through a local theory. The theory is originally formulated for the Ginzburg-Landau equation, a one-dimensional model equation for Navier-Stokes equations, but gives reasonably good results for many real flows.

The global mode can be determined from local analysis by the following procedure. Equations (2.17–2.19) relate ω and α to each other, which is called a *dispersion relation*. The *local absolute frequency* ω_0 is given by a saddle point of the dispersion relation in the complex ω - α -plane (remember that both are complex-valued), such that $\partial\omega/\partial k = 0$, and the so-called Briggs criterion is satisfied (Briggs 1964). The predicted frequency of the linear global mode is then obtained by an analytic continuation of the dispersion relation into the complex plane in the streamwise coordinate x and finding a point such that $\partial\omega_0/\partial X = 0$, where X is complex. If the growth rate ω_i in this saddle point is positive, then the flow is predicted to have an unstable linear global mode. The frequency and growth rate of the global mode are predicted by this saddle point, and the spatial shape can also be extracted by some further elaboration (as is done in Paper 4 in this thesis). Details of this analysis are out of the scope of the present work. The procedure might sound very abstract. Fortunately, points of local absolute instability are relatively easy to find in practice by standard methods (for basic principles, see *e.g.* Huerre & Monkewitz (1990)).

The connection to local analysis shows also that if a flow supports waves with zero group velocity, this can lead to an unstable linear global mode². If the flow is once locally disturbed, the wavepacket issuing

²Other mechanisms can also create global instabilities, such as recirculation and pressure feedback in cavity flows.

from this location never leaves the flow domain, but continues to grow exponentially even when the original source is removed, until nonlinear effects come into play and saturate its amplitude to a certain finite level. It is important to notice that many unsteady flows do not support zero group velocity waves. The boundary layer on a flat plate and one-phase mixing layer are known examples, but there are numerous other such flows.

So, how does the local analysis treat the instability in flows that are not absolutely unstable, but convectively unstable? The noise in the environment is most often not restricted to an impulse, but is continuously present, at many different frequencies. How the flow responds to small-amplitude forcing at a certain frequency is decided by the *spatial* stability analysis. In this analysis, one decides a priori the value of a real frequency ω , while a complex wavenumber α is sought, allowing for spatial exponential growth in the streamwise direction (depending on the sign of α_i). Then the equations constitute a nonlinear eigenvalue problem for α , which can also be solved by standard methods (Schmid & Henningson 2001). Then, the mode with most negative α_i can be followed as a function of ω , to decide for which frequencies the spatial growth is maximum. Those frequencies (and corresponding wavelengths α_r) are then assumed to dominate the flow.

Note that spatial stability has no significance for flows with an unstable global mode (a large enough region of absolute instability). The maximal amplitude reached by the spatial growth depends on the streamwise length of the flow domain. If one frequency is amplified exponentially in time, it will finally overcome the maximal spatial growth for any domain of finite extent.

2.3. Transient growth of global modes and convective instability

A peculiarity of the global modes obtained by solving the full linear problem is that they become increasingly nonorthogonal for more parallel base flows (*e.g.* high Reynolds numbers). This means that there might be *transient growth* — during a long time, the sum of the modes can grow faster in amplitude than any individual modes, before the exponential growth of the least stable mode takes over. The transient growth makes it possible, although cumbersome, to study convectively unstable flows by looking at a sum of many stable global eigenmodes. This was done for the Blasius boundary layer by Ehrenstein & Gallaire (2005), who by animating a sum of modes in the global spectrum got

structures that propagated downstream and increased in amplitude at the same time, resembling in shape the Tollmien-Schlichting waves found in their local spatial analysis. Closely related to the transient growth is the notion of an optimal initial condition — the initial sum of modes that will result to the largest amplification of energy after a certain time. This can be calculated at the same time with the transient growth — for details, see Schmid & Henningson (2001). For the Blasius boundary layer, the optimal initial condition was seen to consist of a combination of Tollmien-Schlichting waves and streamwise tilted structures experiencing transient growth through the so-called Orr mechanism (Åkervik, Ehrenstein, Gallaire & Henningson 2008). In general, a large number of global eigenmodes are needed to correctly determine the dynamics of convectively unstable flows, and without a priori knowledge of the flow, their streamwise boundary conditions are ambiguous. For these reasons, other methods are often preferred.

2.4. Sensitivity

Non-normality of the global modes is also connected to the sensitivity of the eigenvalue to structural perturbations of the system matrix. The region where the spectrum is most sensitive to small local perturbations can be identified by invoking the concept of structural sensitivity (Giannetti & Luchini 2007), based on the eigenfunctions of the linear global stability problem and its *adjoint problem*³. One can show that if a local perturbation with a fixed amplitude is introduced into the linearized momentum equations, the largest movement of the eigenvalue occurs when the perturbation is placed inside the region where direct and adjoint eigenmodes overlap, *i.e.* the *wavemaker region*⁴ (Giannetti & Luchini 2007). A consequence regarding the numerical solution is that the linear problem must be well resolved inside the wavemaker region, and naturally, that the wavemaker region must be inside the computational domain.

Physically, a sensitivity of the eigenvalues for changes in the flow field can be exploited to control the flow. The arbitrary structural perturbations have been further developed by Marquet, Sipp & Jacquin (2008) to yield specifically the sensitivity to base flow modifications. Furthermore, the presence of a small control cylinder in the flow field

³The adjoint equations are presented in Sec. 6.4.

⁴The term wavemaker is also used in the context of the local weakly non-parallel method (Sec. 2.2), for the streamwise location of the complex saddle point determining the global mode frequency. This is not what is meant here.

has been modelled as a steady volume force by Marquet, Sipp & Jacquin (2008), and both steady and unsteady force by Pralits, Brandt & Giannetti (2010). Other means of passive flow control could potentially be modelled in similar ways. The formulations are linear in terms of the base flow modification, which has two immediate consequences: the forcing needs to be of a small amplitude, and only local forcing can be investigated. Any mechanism requiring a certain spatial extent or structure of the forcing cannot be treated, nor interactions between several mechanisms.

It should be noted that an adjoint-based sensitivity approach was introduced earlier by Hill (1992), to model specifically the effect of a small control cylinder inserted in a cylinder flow, and the derivation seems to be equivalent to the ones of Marquet *et al.* (2008) and Pralits *et al.* (2010). However, the expressions given by Giannetti & Luchini (2007) and Marquet *et al.* (2008) are also applicable for other flow cases.

2.5. Local nonlinear theory

In parallel to the linear global modes always taking into account the whole domain, another idea has developed during the recent years from the *front concept*, where the oscillating flow field is divided into two parts — an upstream part which can be considered as linear, and a downstream part which is in the *bifurcated state*, experiencing a nonlinear oscillation. If this division can be done, could it be possible to predict the nonlinear frequency by looking at the linear stability properties in the "last linear point"? This attempt resulted in the concept of *nonlinear absolute instability*, defined in terms of the nonlinear impulse response: if the trailing edge of a saturated nonlinear wave train induced by any finite amplitude perturbation at $t = 0$ is moving downstream, the instability is nonlinearly convective. If the trailing edge is moving upstream, it is nonlinearly absolute.

In the local nonlinear theory for the Ginzburg-Landau equation with variable coefficients, the frequency of the nonlinear oscillation is selected by the frequency of the point separating the locally linearly convectively unstable and locally linearly absolutely unstable point, ω_{ca} (Pier & Huerre 2001). So in this sense, this theory returns to the early concepts in Huerre & Monkewitz (1990), previously introduced to simplify the linear global mode problem. The nonlinear *elephant mode* rises steeply with the same shape as the spatial downstream propagating k^- -wave towards the onset point of local absolute instability, where it saturates. It has been demonstrated recently that slowly spatially developing flows

might support this kind of nonlinear global mode. The results are further described in Ch. 3.

2.6. Concluding remarks

In this chapter, different complementary (and sometimes competing!) approaches on the stability analysis of flows have been presented. Some useful methods are left out since they are not referred to in this thesis. In particular, the parabolized stability equations (PSE) for studies of convective instability and the weakly nonlinear theory around linear global modes for studies of global instability should be included to make the list complete.

The relation between local and global methods presented in this section can be summarized as follows. Obviously, some base flows develop too fast in any direction to be characterised by local methods only taking into account one velocity component. Then either linear global modes or fully nonlinear simulations must be used. This also applies to flows where a three-dimensional disturbance is more amplified than any two-dimensional disturbance — these cases are often not accounted in the local analysis (where Squire’s theorem is valid, see *e.g.* Schmid & Henningson (2001)). But on the other hand, in the cases where the streamwise direction of a 2D flow is more homogeneous, the global modes might be too non-orthogonal to give a good picture of the flow. In particular, convective instabilities, and global oscillations in almost parallel but strongly nonlinear flows, are hard to represent using linear global modes. In these cases, there is hope that local methods might be both cheap and useful.

All the methods in this section deal with predicting stability behaviour of the flow based on the steady solution only. This should be distinguished from structure identification of the final nonlinear flow field; for that purpose, a time-dependent flow field can be projected into a set of POD modes (Berkooz, Holmes & Lumley 1993), Fourier modes (Rowley, Colonius & Basu (2002) or Paper 1 in this thesis) or Koopman modes (Rowley, Mezic, Bagheri, Schlatter & Henningson 2009)⁵. The purpose of the methods of stability analysis presented in the current section is partly to predict the stability of the flow when the whole time-dependent flow field is unknown, and partly to understand the physical mechanisms behind the initial growth of instabilities in different flows.

⁵An approximate linear method to do structure identification and sometimes gain insight into linear dynamics in nonlinear flows will be mentioned in Sec. 3.3.

CHAPTER 3

Global stability of one-phase wakes

In this chapter, some classical results and newer developments on global instability of one-phase wakes are presented. One-phase jets are not described, since they are most often globally stable at moderate Reynolds numbers. For confined jets at high Reynolds numbers, separation bubbles at the wall can create instabilities that could potentially have a global origin (Villermaux & Hopfinger (1994); Malm, Schlatter & Henningson (2011)). Results for other shear flows are touched upon in Sec. 3.4 about global modes in complex geometries.

3.1. Cylinder wake

A plane wake behind a circular cylinder is known to become unsteady at a critical Reynolds number $Re \approx 47 - 49$, and start to shed two-dimensional, alternating vortices in the wake region. The unsteady flow oscillates periodically in time around its mean, and the resulting vortex pattern is called the *von Kármán vortex street*. The nondimensional oscillation frequency or Strouhal number is defined as $St = Ud/\nu$, where d is the cylinder diameter and U the (uniform) inflow velocity. The Strouhal number lies in the range $St = 0.1 - 0.2$ for a two-dimensional vortex street. Transition to three-dimensional vortex shedding is observed around $Re \approx 180$ (Williamson 1996).

The transition from a steady flow to vortex shedding is theoretically classified as a Hopf bifurcation (*e.g.* Noack & Eckelmann (1994)), the onset of which can be tracked from the destabilization of a linear global mode. Due to the importance of the wake behind a cylinder in engineering applications and its computational simplicity at low Reynolds numbers, this flow has been a test case for many conceptual studies of wake instabilities and global modes in general. In this section, a few works on cylinder wakes that will be referred to in Part II of this thesis are presented.

3.1.1. *Passive control of cylinder wakes*

In the experiments of Strykowski & Sreenivasan (1990), the dynamics of a cylinder wake was modified by inserting a much smaller control cylinder in the near-wake region. They showed that placing the control cylinder in certain spatial regions could suppress the vortex shedding, and determined the limits of the stabilizing region for different Reynolds numbers up to $Re = 70$ ¹. The effect was always observed in the near-wake region. The oscillations were never suppressed if the control cylinder was placed further downstream from the large cylinder than four (large cylinder) diameters, neither further upstream than one diameter.

The effect was first modelled theoretically in the often overlooked work of Hill (1992)². He modelled the small cylinder as a force, with a steady component acting on the base flow, and an unsteady component acting on the disturbance. Then he considered changes in the eigenvalue due to small changes in base flow and disturbance due to both the steady and unsteady part of the force, by linearizing the equations with respect to these changes and projecting to the adjoint global modes (equations presented in Sec. 6.4 of this thesis). He obtained regions where the control cylinder should be placed in order to stabilize the flow, for different Reynolds numbers. The regions and their development with Reynolds number were qualitatively similar to Strykowski & Sreenivasan (1990), although a quantitative agreement was not reached.

The adjoint-based sensitivity approach has been rediscovered in different forms by several authors in the recent years, as described in Sec. 2.4. Here, we look into results for a circular cylinder. The structural sensitivity of a cylinder wake to small perturbations in the momentum equations was examined in the work of Giannetti & Luchini (2007), who also compared this with the stabilizing region of Strykowski & Sreenivasan (1990). A qualitative similarity was found for $Re \approx 50$. They also gave an expression for the sensitivity to an arbitrary volume forcing. If the force model for the small cylinder of Hill (1992) is inserted into this expression, one gets an expression identical to Hill (1992) for the unsteady part of the cylinder effect, which indicates that the two approaches are equivalent.

¹The largest value of Re for which the vortex shedding could be suppressed depended on the diameter of the control cylinder. In the same paper, an example of suppressed vortex shedding is shown for $Re = 90$, with diameter ratio 7 between the original and control cylinders.

²I would like to thank Vassilis Theofilis for pointing out the significance of this reference for me.

The sensitivity to a steady volume force (*i.e.* a volume force acting on the base flow) was rediscovered by Marquet *et al.* (2008) for a stationary cylinder. Pralits *et al.* (2010) included both the steady and unsteady forces for a rotating cylinder. Beside presenting sensitivity maps for the change in growth rate and frequency as functions of forcing position, Marquet *et al.* (2008) also modelled a small control cylinder as a steady force. Their approach seems to be equivalent to the one of Hill (1992) regarding the steady part, apart from a different choice of constants in the drag model. The stabilizing regions given by Marquet *et al.* (2008) without a model for the unsteady force give better agreement with experimental results than Hill (1992) for some parameter values, and worse for others. This could indicate that the model for the unsteady force in Hill (1992) should be developed further, although the reason could also be that the linear theory based on small modifications (Sec. 2.4) is only approximately valid.

A different experiment on cylinder wake control was made by Unal & Rockwell (1987). They inserted a long splitter plate along the centerline of a cylinder wake, and measured the vortex formation length depending on the position of the leading edge of this plate. The vortex formation length gives the distance from the cylinder to the first vortex, and was shown to be inversely proportional to the amplitude of the near-wake velocity oscillations. According to Williamson (1996), the vortex formation length has generally been found to be inversely proportional to the maximum of velocity fluctuations.

For $Re = 142$ in Unal & Rockwell (1987), the oscillations were suppressed in when the (nondimensional) distance L between the wake and the cylinder was shorter than $L = 3$. For larger distances ($L > 3$), the plate did not alter the wake structure. For higher Reynolds numbers however ($Re = 785$ and $Re = 3645$), the vortex formation length oscillated as a function of the splitter plate position, *i.e.* it had several successive local maxima and minima with changing plate position, also quite far downstream (the last minimum shown in the paper occurs at $x = 13.5$). This shows that the fluctuations of the velocity field are affected by the presence of the plate, which the authors suggest is due to a weaker absolute instability for this higher Reynolds number. This result indicates that wakes at higher Reynolds numbers can to some extent be controlled by interference in the assumably convectively unstable flow region downstream. Also, the effect of this interference has successive minima and maxima in space. The amplitude of the pressure signal in

the splitter plate position does not seem to have any successive minima and maxima, however.

3.1.2. *Confined cylinder wakes*

The mixing and heat transfer in a channel flow can be increased by inserting small cylinders in the channel. Therefore, wakes behind a cylinder confined between two walls parallel to the direction of the incoming flow, have also been studied extensively.

Experiments on wake instability behind cylindrical rods confined in a channel were performed by Shaw (1971), Davis, Moore & Purtell (1984) for a rectangular cross-section of the rods, and by Richter & Naudascher (1976) for a circular cross-section. The inflow velocity to the channel was kept fixed, while the cylinder-to-channel diameter ratio was varied from 0.05 to 0.35 (Shaw 1971) and 0.167 to 0.5 (Richter & Naudascher 1976). All studies report a substantial increase in the non-dimensional frequency for confined flows compared to unconfined ones, up to 12 %. The Reynolds numbers in these studies cover a broad range, from $Re = 100$ (Davis *et al.* 1984) to $Re = 10^6$ (Richter & Naudascher 1976), so the increase of frequency with confinement can be assumed to be universal.

When it comes to stability, Richter & Naudascher (1976) report an increased amplitude of the lift-force oscillations with confinement, which could be coupled to destabilisation. Furthermore, a DNS study of cylinders with a quadratic cross-section by Suzuki, Inoue, Nishimura, Fukutani & Suzuki (1994) reported that the critical Reynolds number (based on the cylinder height) increased with confinement; if, instead, Re was based on total channel height, the trend was the opposite. The same was found by Davis *et al.* (1984) at low cylinder Reynolds numbers, but for $Re \approx 750$ and higher, confinement increased the amplitude of the lift oscillations regardless the definition of the Reynolds number.

It should be noted that both the geometrical constraints, definition of the Reynolds number on the incoming flow, and the absence of co-flow, lead to that the results for cylinder wakes are not directly applicable to co-flow wakes, the flow case investigated in Papers 2, 4 and 5 of this thesis. One would however intuitively expect a similar behaviour for co-flow wakes at high enough Reynolds numbers.

3.1.3. *Nonlinear absolute instability of cylinder wakes*

The review of Chomaz (2005) reports results for a parallel wake that is globally linearly stable, but in DNS produces a vortex shedding with a frequency in agreement with the local nonlinear theory (Sec. 2.5). Such departures in well converged global *stability limits* of real nonparallel flows³ are not yet known to the author of this thesis, but the final nonlinear oscillation often differs in shape and frequency from the linear global mode.

To see which one of the theories for weakly non-parallel flows is more relevant for characterising the saturated nonlinear oscillation, Pier & Huerre (2001) compared two different frequency predictions for the wake behind a cylinder: the saddle point frequency ω_s (local linear weakly-nonparallel theory) and ω_{ca} (local nonlinear theory).

In a marginally unstable case, the oscillation frequency practically coincided with ω_s and departed from ω_{ca} by more than 20 %, thus validating a linear approach. When the Reynolds number was increased beyond onset, the local linear frequency ω_s gradually departed from the nonlinear frequency observed in DNS. However, ω_{ca} approached the observed frequency and coincided with it around $Re = 180$, just beyond the onset of three-dimensional oscillations. At that point the deviation from ω_s was 50 %. This demonstrates the possibility of local linear analysis to predict frequencies in the globally nonlinear regime.

A similar analysis was made for a low-density jet numerically by Lesshaft, Huerre, Sagaut & Terracol (2006) and experimentally by Hallberg & Strykowski (2006). This flow admits an absolutely unstable inlet profile, so a transition point from locally convective to locally absolute instability is not present. The local nonlinear theory conjectures instead that if the absolutely unstable region is large enough, a nonlinear global oscillation will be observed with the absolute frequency at the inlet. Both studies found a reasonable agreement with that frequency.

Both theories are based on the local framework. However, the flow becomes more parallel with increasing Re , so according to the weakly nonparallel theory, ω_s should gradually approach the frequency of a linear global mode. Therefore, if a linear global mode (ansatz 2.13) would be computed, it would probably also depart from the DNS frequency for high Re , as ω_s above does.

³Here, the term "real flows" refers to spatially developing base flows obtained by solving the steady Navier-Stokes equations (Eq. 2.1–2.2), as opposed to artificial parallel base flows.

3.2. Co-flow wakes

Already Huerre & Monkewitz (1990) addressed the appearance of absolute instability in co-flow (or counterflow) wakes and jets. The jets and wake base flows were symmetric with respect to the centerline, and both the inner and the outer stream had plug flow (*i.e.* uniform) velocity profiles. Furthermore, the analysis was fully inviscid. It was shown that uniform density wakes and jets can have absolute instability, and that this absolute instability is enhanced by a high velocity difference between the two streams (or equivalently, a high absolute value of the shear ratio, presented in Sec. 3.2.1).

A way to control the wake behind a flat plate is based on this idea. By blowing air/liquid out of the plate so that the velocity ratio between the wake and the free stream decreases, the oscillations can be suppressed. In agreement with the basic theory presented in Huerre & Monkewitz (1990), base bleed is known to be mostly stabilizing (*e.g.* Wood (1967); Wong (1985); Schumm, Berger & Monkewitz (1994)).

Hammond & Redekopp (1997) made direct numerical simulations for asymmetric and symmetric wakes behind a flat plate, with and without suction at the trailing edge. They showed that a high enough suction speed stabilized the global mode. With suction, the velocity difference at the inlet increases, but the wake region shortens, and can at the end no longer sustain a global mode.

3.2.1. Confined co-flow wakes

The effect of confinement on the absolute instability of wakes and jets, represented by the same type of symmetric model profiles as in the previous studies, was conducted by Juniper (2006). The stability analysis was still inviscid, and the base flow profile step-like, with zero shear layer thickness and without wall boundary layers.

Juniper (2006) parameterized the flow in terms of two nondimensional numbers, termed h and Λ , characterizing wall distance and velocity ratio of inner and outer streams, respectively. For a more precise definition and an illustrative figure, the reader is directed to Sec. 5.1, where nondimensional parameters of the present work are introduced.

It was shown that in the inviscid limit, uniform density wakes are most absolutely unstable when $h = 1$, a case where the wall distance is twice the wake thickness. In a recent paper (Rees & Juniper 2010), the analysis was extended to viscous stability of velocity profiles with a finite shear layer thickness, although the slip condition on the wall

was retained for both the base flow and the (linear) disturbance in the stability analysis. The destabilising effect of confinement observed in the inviscid case was still present, but somewhat weaker for viscous wakes, and the most absolutely unstable case occurred at a larger wall distance than for inviscid wakes.

The analyses above are made on model velocity profiles, but they can be extended to spatially developing flows in the weakly nonparallel flow theory described in Sec. 2.2, as is done in Paper 4 of this thesis.

3.3. Linearisation around the nonlinear mean flow

In some works (*e.g.* Hammond & Redekopp (1997) and Camarri & Giannetti (2007)), the nonlinear mean flow is used as a base flow for a linear stability analysis, rather than the steady solution to Navier-Stokes equations. There might be two reasons to use such an approach. First, in some cases it can be easier to obtain the mean flow than to solve the steady Navier-Stokes equations, *e.g.* from already performed direct numerical simulations (as in Hammond & Redekopp (1997)), Reynolds-averaged Navier-Stokes (RANS), or even from measurements. Second, one might try to involve some nonlinearities in the linear computations, to obtain information on structures and frequencies occurring in the final nonlinear flow field, instead of the initially growing disturbances. Camarri & Giannetti (2007) did the latter, searching for the inversion point of vortices observed in the nonlinear DNS of confined wakes by performing a global linear analysis around the nonlinear mean flow. They explained the observed structures based on the changes in the mean flow due to nonlinear diffusion.

Naturally, this approach can only be expected to work when there is a clear separation of scales, and the global mode does not actively interact with its harmonics. It might also be necessary to include the effect of the nonlinear diffusion on the mode itself, by introducing an appropriate eddy viscosity model, which has been done in the local linear stability around a mean flow in a turbulent boundary layer (Hoyas & Jimenez (2006), and later refined by Pujals, Garcia-Villalba, Cossu & Depardon (2009)).

For the mean flow approach to be really consistent, one should also get a neutrally stable global mode as a result. If the global mode around a mean flow still has a positive growth rate, it obviously does not represent a saturated oscillation. It was shown by Sipp & Lebedev (2007) that the mean flow approach for a cavity yields only global modes with

strongly positive growth rates and frequencies far from the observed nonlinear frequencies, while for the wake behind a cylinder it yields a neutrally stable mode with a frequency close to the nonlinear one. Both cases were made without an eddy viscosity model.

Obviously, more work is required before any definite conclusions are drawn on the usefulness and applicability of stability methods based on the mean flow. It might be argued that the physical information potentially gained is not worth the effort, and that it is more reliable to extract the nonlinear frequencies and structures directly from a nonlinear simulation. There is, however, a great need for methods for predicting the behaviour of flows without exact knowledge of the actual time-dependent flow fields, not the least in industry.

3.4. Linear global modes in complex geometries

With increasing computational power, we have seen global modes in more and more complicated flows. Development of numerical methods to handle large eigenvalue problems has also stimulated this field. With iterative Krylov subspace methods it is possible to recover a large number of the least stable modes of large systems. Memory requirement during the computation is still a problem, which might be helped either by solving the system in parallel, like in the present work, or by using a time-stepping method based on a linear Direct Numerical Simulation code. The former numerical approaches is further described in Ch. 6.

The practical requirements on the code can have large differences depending of the Reynolds number, geometry and dimensionality of the ansatz (2.14 respective 2.13 or 2.9). The typical size of the global mode problem increases from Gb to Tb when going from two to three dimensions. For complex geometries, the boundary conditions and varying resolutions needed in different regions can be considerably more difficult to implement than for simple, almost rectangular geometries. For this reason, existing direct numerical simulation codes are often the tool of choice to compute linear global modes in complex geometries or three-dimensional flows.

Three-dimensional global modes (using ansatz 2.9) have recently been computed by a time-stepping method for a few flow cases, for example the jet in cross-flow (Bagheri, Schlatter, Schmid & Henningson (2009), Ilak, Schlatter, Bagheri & Henningson (2011)). This is the only possible approach for three-dimensional base flows. Two-dimensional global modes with an inclusion of a spanwise periodicity (Eq. 2.14) are

also sometimes called "three-dimensional global stability", although the computational requirements are similar to those of (Eq. 2.13), and many works using the latter approach can be found. Some of the more recent ones are the compressible global modes of a cold supersonic jet (Nichols & Lele 2011), and the same ones of swept Hiemenz flow (Mack & Schmid 2011).

The inclusion of a spanwise wavenumber (2.14) can be very relevant in cases where the first bifurcation is not a priori known to be two-dimensional. Laminar two-dimensional separation bubbles behind sharp (*e.g.* Barkley, Gomes & Henderson (2002)) and smooth (*e.g.* Marquet, Lombardi, Chomaz, Sipp & Jacquin (2009)) backward-facing steps, and in a boundary layer (*e.g.* Theofilis, Hein & Dahmann (2000)) are known examples of flows, where spanwise periodic global modes always seem to be more amplified than purely two-dimensional global modes. The spanwise periodic modes were also destabilized for lower values of recirculation (Barkley *et al.* (2002) and Theofilis *et al.* (2000)) than the purely two-dimensional ones, due to a lift-up mechanism.

CHAPTER 4

Stability of two-fluid immiscible shear flows

When streams of two different fluids with different velocities meet, a two-phase shear layer, a wake or a jet is formed. Section 4.1 deals with axisymmetric wakes and jets. This background is necessary to highlight the similarities and differences to plane wakes and jets, which are the main topic of this thesis. Section 4.2 presents more thoroughly the basics of instability of plane shear layers, wakes and jets. Only immiscible fluids are studied in this thesis, and the review below reflects this basic assumption. Miscibility effects have been investigated by *e.g.* Govindarajan (2004) regarding the local stability of two-fluid plane Poiseuille flow, Selvam, Merk, Govindarajan & Meiburg (2007) for core-annular flow, and d’Olce, Martin, Rakotomalala, Salin & Talon (2009), Selvam, Talon, Lesshafft & Meiburg (2009) for absolute instability of miscible coaxial flows.

4.1. Coaxial wakes and jets with surface tension

The stability of a cylindrical liquid jet injected into gas or another liquid is one of the fundamental problems in fluid mechanics, and is of importance in a large number of applications including ink jet printing, spray atomization, and emulsification in microchannels. The reason is that the instability directly controls the breakup to droplets and the following droplet size distribution. The section is divided into two parts. First, we look at the classical case of a high-speed liquid jet surrounded by gas. Second, we see how absolute instability occurring in certain low-speed liquid jets surrounded by another liquid can be related to flow patterns of the jet.

4.1.1. *Liquid jets surrounded by gas at high Reynolds numbers*

The first theoretical stability study of liquid jets was made already by Rayleigh (1878). He showed analytically that a cylindrical liquid jet in the absence of ambient fluid is unstable to all wavelengths longer than its circumference. The assumption of a liquid jet in vacuum was made

to imitate the situation where the liquid jet is surrounded by a medium with a much lower density, *i.e.* a gas. Since the growth rate of this *Rayleigh instability* was maximum for a wavelength slightly longer than the circumference, the liquid jet would according to Rayleigh (1878) break into droplets with a diameter comparable to the jet diameter¹. Later, Weber (1931) extended the study to take into account the liquid viscosity, and the density of the ambient fluid. He postulated that while Rayleigh instability dominates for high surface tension and low velocity difference between liquid and ambient fluid (low *Weber numbers*), in other flow regimes the aerodynamic shear from the ambient fluid is more important for the stability. It was shown by Taylor (1962) that when the inertia of the surrounding gas is dominant (high *Weber numbers*), a liquid jet will break up into droplets substantially smaller than its diameter. This flow regime is utilized in air-blasted atomization, where a high speed gas is blown in parallel with the liquid jet, to obtain a rapid breakup of the jet into small drops.

The problem of the original theory of Weber (1931) was that it seemed to greatly underpredict the growth rates and overpredict the break-up lengths seen in experiments. Sterling & Sleicher (1975) improved the theory with partial success. They proved indirectly that relaxation destabilized the flow — by deriving a parameter to account for the relaxational effect, and by comparing the fit to experiments for various lengths of the inlet pipe. Another new feature that Sterling & Sleicher (1975) considered was the viscosity of the ambient gas. This was done by a semi-empirical correction of the normal stress at the jet surface, considering the pressure in a shearing flow over a wavy cylinder. The conclusion was that the viscosity of the ambient gas had a stabilising effect.

The effects described above form the basic ingredients of all further research on liquid jets surrounded by gas at moderate to high Reynolds numbers, and are introduced for comparison with planar liquid sheets later on. The literature on cylindrical liquid jets is rich. The theoretical studies have been extended towards nonlinear stability (*e.g.* Yuen (1968), Chaudhary & Redekopp (1980)), absolute instability (*e.g.* Leib & Goldstein (1986)), and various other physics such as electrohydrodynamic instability (Mestel 1994).

¹It should be noted that the drop formed from a liquid cylinder of length $2\pi r$ has the radius $1.67r$. Also, the most unstable wavelength is slightly larger than the jet circumference.

4.1.2. *Absolute instability of liquid-liquid jets*

Coaxial jets formed when two different liquids meet and mix inside a channel appear in chemical processing, microemulsification and polymer extrusion (Guillot, Colin, Utada & Ajdari 2007). Liquids often have higher viscosities than gases, and more equal densities than one gas and one liquid, and the assumption of one phase being inviscid and/or dynamically less important might not apply. In such cases, both phases need to be modelled (Meister & Scheele 1967). Visualisations of different flow patterns for a confined oil-in-water jet, including both axisymmetric and sinusoidal oscillations, rapid atomisation and steady straight jets, can be seen in Charalampous, Hardalupas & Taylor (2010).

Opposite to the inviscid flow regime, many of the liquid-liquid jets (and some of the liquid-gas jets such as ink jets) occur in the low Reynolds number (or Stokes flow) regime; the cases connected to micromixing of several liquids and production of small droplets have grasped much attention lately (*e.g.* Barrero & Loscertales (2007); Joanicot & Ajdari (2005); Cubaud & Mason (2006); Guillot *et al.* (2007)). Two distinct flow regimes can be observed for liquid-liquid jets at low Reynolds numbers: *dripping*, where the jet breaks up to droplets directly at or close to the nozzle, and *jetting*, where the jet remains steady for a few diameters or even does not break up at all (Meister & Scheele 1968). In the case of jetting, depending of the density and viscosity ratio between inner and outer flows, the jet either expands or contracts before breakup. Since the droplets produced are of similar size as the *local* jet circumference, the droplet size is controlled by the inner and outer flow rates in jetting, but not in dripping.

It should be mentioned that the physics of instability in micromixing flows is very different from the conventional shear flow instability (Ch.3). Close to the zero Reynolds number limit, the advective terms can be neglected, and all production mechanisms where fluctuations extract energy from the mean flow shear are simply absent. In particular, the growth of unstable global modes in shear flows tend to depend on a competition between energy production (from the base flow gradients) and advection with the base flow velocity, but for low Reynolds numbers both these terms are very small.

Despite the differences compared to conventional shear flows, in the study of Guillot *et al.* (2007), dripping was seen to be connected to the appearance of local absolute instability in the flow. The limit between dripping and jetting in their experiments was accurately predicted

by the appearance of absolute instability of the inlet flow profile in a very simplified model, neglecting inertia and radial gradients of both flows (and naturally, using the locally parallel flow assumption). The inlet profile became absolutely unstable for $We < 1$. Later, Utada, Fernandez-Nieves, Gordillo & Weitz (2008) showed experimentally and computationally that a liquid jet surrounded by a more viscous liquid could be convectively unstable at the inlet but become absolutely unstable downstream and start to produce drops. This was attributed to the expansion of the liquid jet into the more viscous liquid, and the consequent deceleration and decrease of Weber number to $We < 1$.

Absolute instability to lateral disturbances, *i.e.* waves with a nonzero azimuthal wavenumber, was considered by Herrada, Ferrera, Montanero & Gañán-Calvo (2010), who also relaxed the assumption of zero Reynolds number. This led to a different form of absolute instability, the sinuous oscillations called *whipping*. The whipping prevented the jetting regime to be reached for some of the high-viscosity jets.

Similar transitions between different flow patterns have been observed in numerical simulations of related, but more complicated flow configurations, such as the flow in a micro-fluidic T-junction (Gupta & Kumar 2010), and diverging microchannels (Cubaud & Mason 2006).

Since regions of absolute instability exist for the microjets, the transition from jetting to dripping could be controlled by a destabilization of a linear global mode. The approach presented in this thesis for plane two-dimensional two-phase jets would apply to axisymmetric flows as well, but require the derivation of a new set of interfacial boundary conditions. The concept of absolute instability does not apply in any straight-forward manner to three-dimensional flows, which necessitates either the computation of three-dimensional linear eigenmodes or the use of structure identification methods such as POD modes (Berkoöz *et al.* 1993).

4.2. Plane wakes, jets and shear layers with surface tension

Plane wakes and jets are in one way fundamentally different from the cylindrical ones: a plane liquid interface increases its surface area when perturbed, so surface tension acting alone will try to return the interface to its unperturbed position. Hence, there is no counterpart to Rayleigh instability (Sec. 4.1.1) for planar jets and wakes, *i.e.* no convective instability caused purely by surface tension. Basics of the convective shear layer instability of two fluids, starting from effects in

Kelvin-Helmholtz setup, will be presented in section 4.2.1. Absolute instability of plane wakes, jets and mixing layers is introduced in the following section (4.2.2), and section 4.2.3 concentrates on the plane liquid sheet surrounded by gas at moderate Reynolds numbers.

4.2.1. Convective instability of two-fluid shear layers

A shear flow where one upper and one lower fluid stream move with different (free stream) velocities is called a *shear layer*. The shear layers usually support a convective instability. If both layers are assumed to have uniform mean velocities, and an inviscid stability analysis is made, one obtains the *Kelvin-Helmholtz* instability. The growth rate of the Kelvin-Helmholtz instability is linearly proportional to the wavenumber, so the growth rate goes to infinity when the wavenumber increases (*i.e.* when the wavelength decreases). For real shear layers, the growth rate curve follows the Kelvin-Helmholtz line at low wave numbers α , but departs from it at high wavenumbers, at a value dependent on the shear layer thickness (Rayleigh 1984). The point of departure (or alternatively, the point where the flow becomes stable) is then called the *cut-off wavenumber*.

Density ratio can easily be included in the Kelvin-Helmholtz setup, with the intuitively apparent conclusion that having the heavier fluid on top (unstable stratification) enhances the instability, while a lighter fluid on top (stable stratification) reduces the tendency of the flows to mix and is therefore stabilizing (Drazin & Reid 1981).

If surface tension alone is included in the local Kelvin-Helmholtz problem, it will act as a stabilizing mechanism and damp the Kelvin-Helmholtz instability for short wavelengths, thus introducing a cut-off wavelength similarly to a finite shear layer thickness. This is the dominating effect for viscous shear layers as well.

Viscosity alone, without any density gradients or surface tension, can create shear layer instabilities. Yih (1967) noticed that plane Couette and Poiseuille flows became linearly unstable at any Reynolds number with an appropriately chosen viscosity stratification. One explanation Yih (1967) provided was that the mean flow profile with viscosity stratification had an inflection point. This shows that a viscosity jump at an interface not only can promote, but can sometimes be the main source of a shear layer instability.

Kelvin-Helmholtz stability is inviscid, but a viscosity ratio can be included implicitly by choosing the slopes of the velocity profiles in each

layer so that the continuity of shear stress is satisfied. This piecewise-linear setup was investigated by *e.g.* Boeck & Zaleski (2005), for a stably stratified configuration of two fluids of moderate to high density ratios ("liquid" vs. "gas"). They showed that in addition to the usual Kelvin-Helmholtz instability, the shear layer in the more dense fluid ("liquid") was inviscidly unstable, and that this instability could exceed the one of the Kelvin-Helmholtz mode if not damped by surface tension. The effect occurred for high Weber numbers at high density ratios, such as water-to-air. This result also shows that the effects of density and viscosity ratio and surface tension can be coupled.

The most natural way to study the effect of viscosity gradients is still by including the viscosities of both fluids in the model. This was also made by Yecko, Zaleski & Fullana (2002) and Boeck & Zaleski (2005) for the same setup, and both identified three modes. The first one was called the H -mode, with an inviscid origin of either type mentioned above. The others were the liquid TS² mode and the gas TS mode. As the name says, the origins of the two latter modes were in the boundary layers of the liquid and the gas, respectively. If the gas-to-liquid viscosity ratio was small enough, the growth rate of the liquid TS mode could exceed that of the inviscid mode. This effect was suggested to partly explain the higher growth rates and most unstable wavenumbers observed in round jet atomisation experiments, than what would be obtained with the inviscid piecewise-linear profile. On the other hand, the fully viscous stability computations of a liquid sheet in the atomization regime by Lozano, Barreras, Hauke & Dopazo (2001) and later spatial computations by Altimira, Rivas, Ramos & Anton (2010) do not reveal several unstable modes.

In conclusion, the stability of shear layers of two different fluids is far more complicated than the stability of one-phase shear layers: it involves several parameters that can have coupled or independent effects on the stability, depending on the flow regime.

4.2.2. *Absolute instability of two-fluid shear layers, jets and wakes*

Absolute instability of wakes and jets with uniform velocities and densities in each layer (*i.e.* plug flow) was considered first by Yu & Monkewitz (1990). They concluded that absolute instability of a jet is promoted if the jet has a lower density than the surrounding flow, and the opposite applies for a wake. This behaviour was also observed in jet experiments

²TS=Tollmien-Schlichting

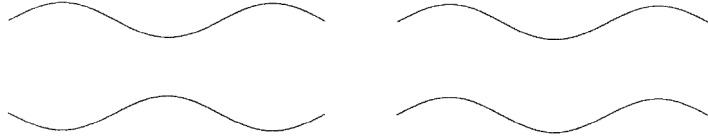


FIGURE 4.1. Definition of a varicose *i.e.* symmetric (left) and a sinuous *i.e.* antisymmetric (right) mode in terms of the displacements of the two interfaces of a jet or a wake.

of *e.g.* Sreenivasan, Raghu & Kyle (1989) and Yu & Monkewitz (1993), and is today considered to be general knowledge.

One-phase inviscid mixing layers are convectively unstable. However, surface tension can induce absolute instability in the Kelvin-Helmholtz setup as shown by Rees & Juniper (2009). Furthermore, for inviscid wakes and jets with plug flow profiles, a certain degree of surface tension considerably lowers the critical shear ratio for the onset of absolute instability, for both wakes and jets. This is especially clear for the symmetric (varicose) modes (see Fig. 3 for the definition of symmetry/antisymmetry). The increase in absolute instability is by Rees & Juniper (2009) attributed to the interface acting like an elastic sheet between the fluids, creating a way for information to be transported upstream. Rees & Juniper (2009) also mention that high enough surface tension stabilizes both varicose and sinuous modes.

The mechanism is strongest when densities of the two liquids are comparable, and cannot create absolute instability for *e.g.* high density jets, such as a water sheet in air. It was shown by Turner, Healey, Sazhin & Piazzesi (2011) that finite shear layer thickness, modelled with a broken-line profile, increases absolute instability and can move the absolute stability limit to somewhat lower density ratios, of the order $1/2$. Söderberg (2003) has shown that a viscous relaxational water sheet in air can also be absolutely unstable. The special case of a liquid sheet (convective and absolute instability) will be investigated further in the next section.

4.2.3. *Liquid sheets surrounded by gas at moderate Reynolds numbers*

A thin planar liquid jet is called a liquid sheet. As was already mentioned, liquid sheets do not possess Rayleigh instability. This was shown by Squire (1953), using the same assumptions as Rayleigh (1878) for the liquid cylinder. However, when there is a velocity difference between the

liquid sheet and the gas (cmp. aerodynamic shear by Weber (1931) for the cylindrical jet), a complex interplay of inertia, capillary and viscous forces will decide the stability or form of the instability.

Hagerty & Shea (1955) studied the local temporal stability of an inviscid liquid sheet surrounded by an inviscid stationary gas. They concluded that:

1. the only modes possible were symmetric (varicose) or antisymmetric (sinuous) (Fig. 3),
2. the instability was of aerodynamic nature, *i.e.* caused by a velocity difference between water and air, and
3. surface tension always acted as a stabilising force.

These main conclusions are mostly valid for viscous liquid sheets as well. Li & Tankin (1991) added the viscosity of the liquid, and found two instability modes — firstly, the aerodynamic instability of an inviscid nature which was not affected by Reynolds number, and secondly a *viscosity-enhanced* instability mode for low Reynolds and Weber numbers ($We \approx 0.1$). The latter mode was not found in a later spatial analysis (Li 1993). For high Weber numbers ($We \gg 1$), the more common case where the aerodynamic instability dominates, they found that the liquid viscosity stabilised the flow and shifted the instability to longer wavelengths.

The first spatio-temporal analysis, searching for absolute instability for a viscous liquid sheet surrounded by inviscid gas, was made by Lin, Lian & Creighton (1990)³. They found a curious phenomenon - a *pseudo-absolute instability* for the sinuous mode for Weber numbers below unity, which means that the linear impulse-response does not vanish in any streamwise point in time, but always remains bounded. This instability had zero frequency and infinite wavelength. Later the analysis was refined by Li (1993). The conclusions are summarised below:

1. for $We < 1$ the sheet is pseudo-absolutely unstable, otherwise convectively unstable,
2. for $We \gg 1$, and $\tilde{\rho}We \ll 1$, where $\tilde{\rho}$ is the gas-to-liquid density ratio, the convective instability is sinuous, and the liquid viscosity reduces the spatial growth rate and wavenumber,

³Before this, there had been other similar analyses disregarding the ambient fluid.

3. for $We \gg 1$ and $\tilde{\rho}We \gg 1$ sinuous and varicose instability are of the same magnitude,
4. for varicose instabilities the liquid viscosity always reduces the spatial growth rate and wavenumber.

Some authors believe that the pseudo-absolute instability indicates algebraic absolute instability that could explain an explosive rupture of the liquid sheet for low We (de Luca 1999). However, a physical interpretation of absolute instability with a vanishing wavenumber and frequency is somewhat unclear, and the mathematical background has also been questioned (Luchini 2004).

Liquid viscosity does not only affect the disturbances, but also the mean flow development. An important consequence is the relaxation of the velocity profile, for both a liquid sheet and a cylindrical jet (Sterling & Sleicher 1975). When the sheet emerges from a nearly straight channel, the velocity profile at the channel outlet is not uniform, but closer to parabolic. When the sheet enters into gas or vacuum, due to the free surface, the velocity relaxes towards a uniform profile. Due to conservation of mass and momentum, the jet also contracts in this process (cmp. cylindrical liquid-liquid-jets in Sec. 4.1.2). First, we investigate the temporal instability of relaxational liquid jets.

Hashimoto & Suzuki (1991) studied a relaxational liquid jet, and found fine interfacial waves with a wavelength smaller than the sheet thickness near the nozzle, as opposed to the inviscid instabilities that would occur for long wavelengths for their parameter values. They tried to explain the waves by a temporal stability analysis disregarding the ambient gas, and found two sinuous and two varicose modes in the calculations. Söderberg & Alfredsson (1998) extended the study to viscous ambient gas experimentally and numerically, with local temporal and spatial approaches. They found a fifth unstable mode, which was sinuous. The most unstable mode found in the experiments could be explained by looking at a linear combination of two of the sinuous modes.

Regions of genuine absolute instability (not pseudo-absolute) close to the nozzle of a relaxational liquid sheet were found by Söderberg (2003). His water sheet emerged from a straight channel, and in the stability analysis he assumed a parabolic profile at the channel outlet, *i.e.* the inlet of the stability computation. The sheet thickness at the inlet was held constant (0.55 mm) and he varied the inlet velocity. This means that the Reynolds and Weber number changed simultaneously.

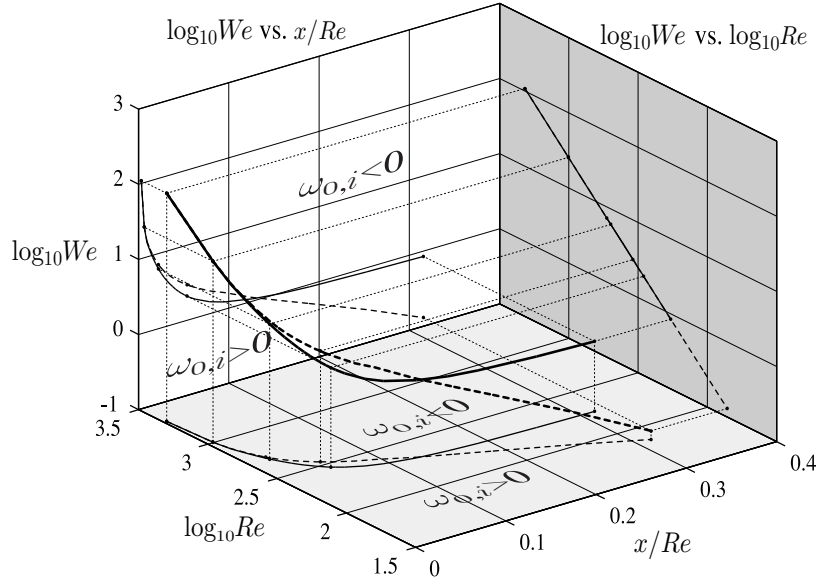


FIGURE 4.2. Region of absolute instability for an 0.55 mm thick water jet in air, as a function of Re and We (note that these are coupled). Figure from Söderberg (2003).

The resulting boundary of absolute instability as a function of x/Re and Re can be seen in figure 4.2 by projection of the three-dimensional curve to that plane. The absolutely unstable region then extends from the inlet to the projection of the line. For low Reynolds numbers $Re \lesssim 200$ the whole sheet is absolutely unstable, as is expected since then $We < 1$. For higher Reynolds (and Weber) numbers there is a finite region of absolute instability, that moves closer to the inlet with Reynolds number. For $Re = 1000$ the region only extends to approximately 5 sheet thicknesses from the inlet.

Lozano *et al.* (2001) made experiments where a co-flowing air stream was blown with different velocities in parallel to a liquid sheet, aimed at understanding the atomization process. The air velocity was consequently at least 10 times larger than the sheet velocity. They found that the air boundary layer thickness damped the disturbances, and reduced the wavelength and growth rate. They also compared their temporal stability calculations to experiments, but the agreement was only modest.

In addition, many flow visualisations have been made during the years, in order to shed some light on the breakup process (*e.g.* Mansour & Chigier (1991); Park, Huh, Li & Renksizbulut (2004)), which is more complicated for the sheet than for a cylindrical jet — first the sheet breaks up into ligaments and then drops, with unpredictable sizes. The details of this process are of great interest for spray applications. The most unstable mode is generally sinuous, and it is not intuitively clear why this would lead into break-up, since the water surfaces oscillate in phase, preserving their distance to each other. Some recent theories and future challenges in this field are summarized in the last section of Eggers (2011).

CHAPTER 5

Flow cases in the present work

Here, the flow cases studied in the papers of the thesis are briefly introduced, to make it possible to understand Ch. 6 and 7. The parameter values differ in different manuscripts, but a basic division can be made as follows: the single-phase co-flow wakes (Sec. 5.1) are the topic of Papers 2, 4 and 5, the wakes and/or jets with surface tension (Sec. 5.2) of Paper 3 and 6, and the liquid sheets (Sec. 5.3) of Paper 1.

5.1. Single-phase co-flow wakes

The first flow case is a two-dimensional plane wake with one single fluid. The base flow is assumed to be invariant in the spanwise (z)-direction, and the streamwise and vertical coordinates are denoted by x and y , respectively.

The base flows for single-phase wakes have a symmetric inlet profile consisting of one inner stream of lower velocity and two outer streams of higher velocity (Fig. 5.1). Both flow streams have uniform velocity profiles¹. This inlet profile was chosen since it generates a strong instability, and has been used in a previous inviscid wake study (Juniper 2006).

In the following, dimensional quantities are denoted by stars. The dimensional parameters are given in Fig. 5.1. The inner flow quantities are marked with subscript 1, and the outer flow quantities with subscript 2.

The inlet profile is fixed, but the base flow develops in the streamwise direction due to viscous diffusion. The flow is assumed to be surrounded by walls in the vertical direction, located at $y^* = \pm(h_1^* + h_2^*)$. In most of the cases under study, a no slip condition is set at the walls, and the flow approaches a parabolic profile downstream. An example of such a flow field is seen in Fig. 5.2. Note that the viscous development gives

¹The corners are slightly smoothed when spectral element method is used to compute the base flow, to prevent numerical oscillations.

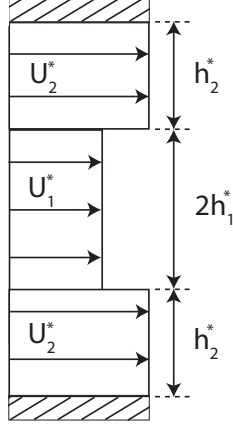


FIGURE 5.1. The inlet profile of a co-flow wake with dimensional parameters.

rise to a recirculation region at $x \approx 1 - 3$, even though both streams have a positive streamwise velocity at the inlet. Such a backflow region appears for some of the wakes, but not for all.

The flow can be conveniently parameterized in terms of the inlet profile. Following Juniper (2006), we have the *shear ratio* Λ characterizing the ratio between shear and momentum:

$$\Lambda = \frac{(U_1^* - U_2^*)}{(U_1^* + U_2^*)} , \quad (5.1)$$

and the confinement parameter:

$$h = \frac{h_2^*}{h_1^*} . \quad (5.2)$$

In addition, the viscous problem involves the Reynolds number:

$$Re = \frac{U_2^* h_1^*}{\nu^*} , \quad (5.3)$$

where ν^* is the kinematic viscosity of the fluid.

Our Reynolds number characterizes a wake surrounded by a free stream with velocity U_2^* , being confined with vertical plates, so that the free stream velocity is not altered by confinement. The average of inner and outer velocities $(U_1^* + U_2^*)/2$ is commonly used as the velocity scale in other works. Both definitions focus on the wake properties. Depending

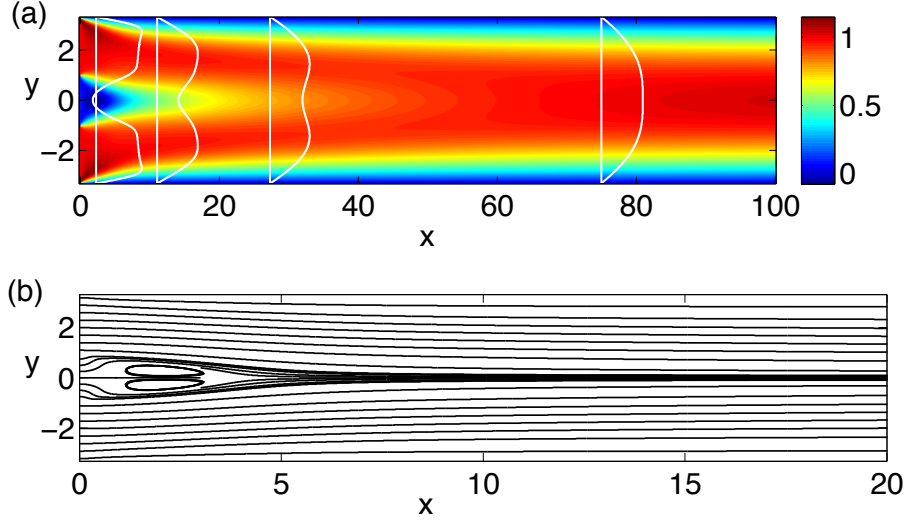


FIGURE 5.2. A co-flow wake baseflow: (a) The streamwise velocity field in colorscale. A few local velocity profiles are drawn in white on top of the picture. (b) Streamlines in the region $x = 0 - 20$. $Re = 100$, $\Lambda^{-1} = -1.2$, $h = 2.33$.

on the type of confinement, a Reynolds number based on the channel width and channel mean velocity could also be relevant.

5.2. Wakes and jets with surface tension

The second flow case has the same type of inlet profile as the wakes in the previous section (Fig. 5.1). Now, the inner and outer streams represent two different fluids that meet at $x = 0$. In Paper 6 we also extend the studies to configurations where $U_2^* < U_1^*$, *i.e.* jets.

The reference velocity is always the *faster moving* fluid: $U_{ref}^* = U_2^*$ for wakes, and $U_{ref}^* = U_1^*$ for jets. The Reynolds number is now defined as:

$$Re = \frac{U_{ref}^* h_1^*}{\nu^*}, \quad (5.4)$$

In addition, surface tension appears on the interfaces between the fluids, characterized by the *Weber number* We :

$$We = \frac{\rho^* U_{ref}^* h_1^*}{\gamma^*}, \quad (5.5)$$

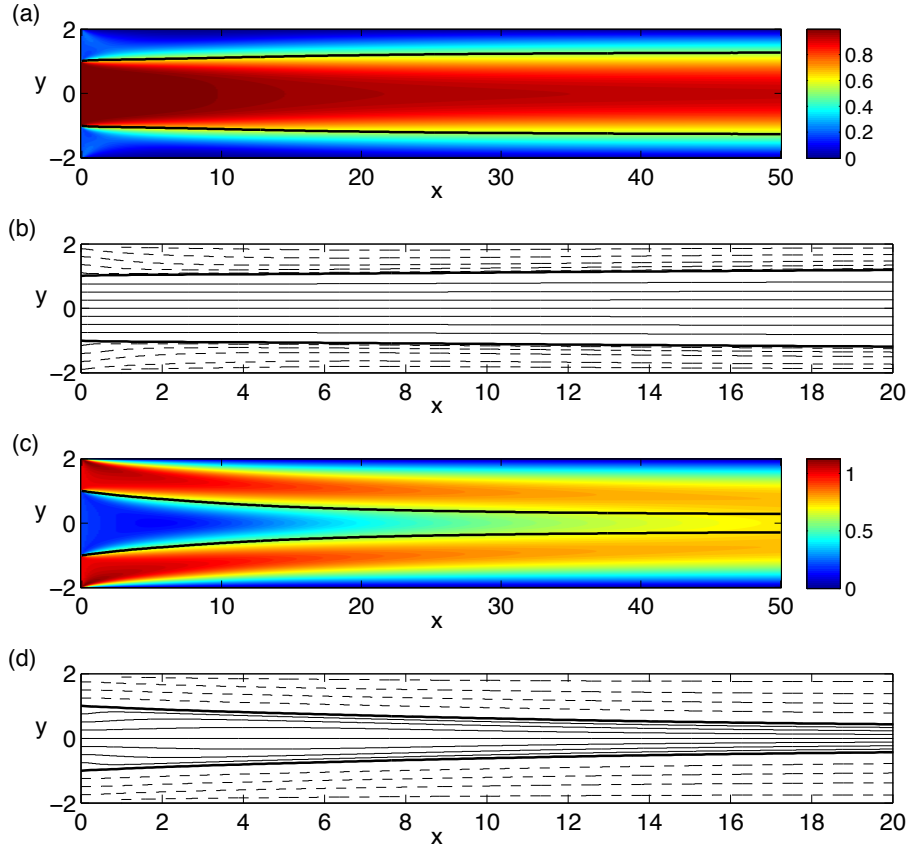


FIGURE 5.3. Example base flows for wakes and jets with surface tension: (a) Jet ($Re = 316$, $\Lambda^{-1} = 1.5$, $h = 1$): The streamwise velocity field in colorscale. (b) Jet: streamlines in the region $x = 0$ – 20 . The streamlines for the inner flow are solid, for the outer flow dashed. (c) The same as (a), but for a wake ($Re = 316$, $\Lambda^{-1} = -1.4$, $h = 1$). (d) The same as (b) but for the wake.

where ρ^* is the density and γ^* the surface tension coefficient between the fluids.

Both fluids are assumed to have the same density (and viscosity), to make surface tension the only new parameter compared to the single-phase wakes (Sec. 5.1). This configuration is not as physically strange as it might seem at first sight. Surface tension is a chemical property, and does not require a density or viscosity difference between the fluids; *e.g.*

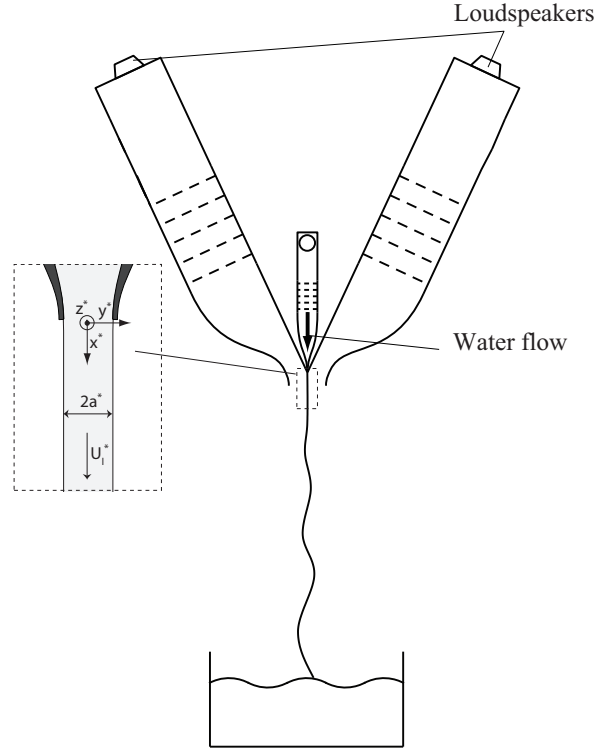


FIGURE 5.4. The facility used for experiments in Paper 1. The computations are also based on the experimental flow conditions.

the configuration of mineral oil on water is immiscible and has surface tension, despite the fluids having similar densities.

A representative jet base flow is shown in Fig. 5.3 (a)–(b) and a wake base flow in Fig. 5.3 (c)–(d). None of the base flows shown has recirculation bubbles (cmp. Fig. 5.2 b). Recirculation occurs for some of the flows under study, but is not important for the stability of wakes and jets with surface tension.

5.3. Liquid sheet

A liquid sheet is a plane two-dimensional liquid jet (invariant in the z -direction). However, its physics is quite different from the other two flow cases (previous subsections), since the density of the liquid sheet is much

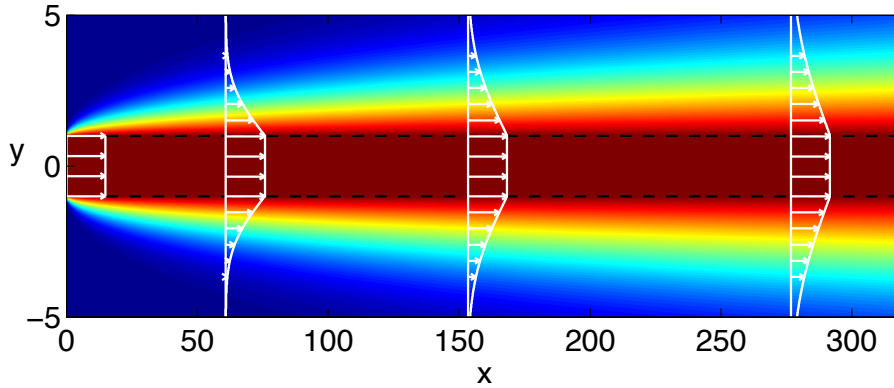


FIGURE 5.5. The streamwise velocity of a base flow field used for computations. The interface between water and air is flat, and given by the black dashed line. Local velocity profiles in a few streamwise position are drawn in white.

higher than the density of the surrounding gas. The liquid sheet in this thesis is a water sheet surrounded by either stagnant or co-flowing air. The flow velocity is of the order 1–10 m/s, which makes the Reynolds number for the sheet much higher than in the other two flow cases.

In Paper 1, the liquid sheet is studied through both experiments and computations, so even if this thesis focuses on the numerical part, the experimental setup is introduced in Fig. 5.4. It has one inner nozzle for water, and two symmetrically placed outer nozzles for air. Both the water and the air streams have a sharp contraction before the exits, which aims at creating uniform velocity profiles at the nozzle exit. Pitot tube measurements have confirmed that the boundary layers of the water profile just outside the nozzle are fairly thin. Since the density of water is much higher than the density of air, the water profile is even more uniform downstream.

In the computations, a uniform profile is assumed in water, while the growing boundary layers in air need to be modelled. The computations are local, so only knowledge of the local velocity profile(s) in the measurement area is required. The local air boundary layer shape can be obtained from a similarity solution of the boundary layer equations, with the free stream velocities of air and water as the vertical boundary conditions. The boundary layer thickness is then determined using the nozzle exit as the virtual leading edge. An alternative method to determine the air boundary layer profile is also used in Paper 1, and it

is shown that for the same boundary layer thickness both models give very similar results. The streamwise base flow velocity field from the latter model is shown in colorscale in Fig. 5.5, with a few velocity profiles drawn with white lines on top.

The Reynolds and Weber number for the sheet are based on the liquid quantities:

$$Re = \frac{U_l^* a^*}{\nu_l^*}, \quad (5.6)$$

$$We = \frac{\rho_l^* U_l^{*2} a^*}{\gamma^*}, \quad (5.7)$$

where the subscript l denotes liquid, a^* is the half thickness of the liquid sheet and γ^* the surface tension coefficient between water and air. They are of the order $Re \approx 3000$ and $We \approx 300$ for the current experiments. These are the common nondimensional numbers for a liquid sheet in stagnant gas, and are adopted for the present work where the gas co-flow speed is moderate².

²In atomisation studies the gas has at least one order of magnitude higher velocity than the liquid. Thus, in atomisation it is more common to concentrate on the gas quantities, or at least use the velocity difference between liquid and gas as the velocity scale.

Governing equations and numerical solution

All papers in this thesis are concerned with linear stability, with the division into a steady base flow (capital letters) and disturbance (lowercase letters) (Eq. 2.3–2.4). All flows in the present work are two-dimensional. The disturbance is computed from the global ansatz (Eq. 2.13), except in Paper 6. Hereafter, we name the variables for the streamwise and vertical velocities as $U_1 = U$ and $U_2 = V$, and similarly for \hat{u}_i .

6.1. Base flows

Here, the methods to obtain base flows are presented, except from the base flows for the liquid sheet study (Paper 1), which are obtained directly from similarity solutions¹.

The wake and jet base flows are solutions to the two-dimensional variant of the time-independent Navier-Stokes equations (Eq. 2.1–2.2). The flow configuration (Sec. 5.1) is symmetric in the vertical direction, and the base flow is computed in the region $y > 0$. The computational domain with boundary conditions is illustrated in Fig. 6.1.

The inlet profile (Fig. 5.1) becomes in the dimensional form:

1. for wakes:

$$U(y) = \frac{(\Lambda^{-1} + 1)}{(\Lambda^{-1} - 1)} \quad \text{for } y < 1, \quad U(y) = 1 \quad \text{for } y > 1. \quad (6.1)$$

2. for jets:

$$U(y) = 1 \quad \text{for } y < 1, \quad U(y) = \frac{(\Lambda^{-1} - 1)}{(\Lambda^{-1} + 1)} \quad \text{for } y > 1. \quad (6.2)$$

In the spectral element code Nek5000, the infinite gradients of the inlet profile are replaced by sharp but continuous gradients, to avoid numerical oscillations (see Paper 1).

¹The similarity solution of the so-called Stokes' model is obtained analytically, and the equation for the Sakiadis model is solved by a shooting method.

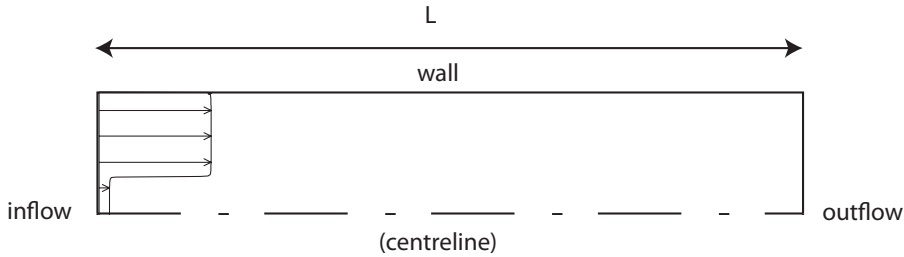


FIGURE 6.1. Illustration of the computational domain for wake and jet base flows. The inlet profile shown is shown for a wake.

At the walls, a no slip boundary condition is set (except in some cases in Paper 4, where a slip condition is tested for comparison). The length of the base flow domain L_b is always chosen longer than the stability domain L_s , to eliminate effects from the outlet boundary condition (typically, if $L_s = 200$, then $L_b = 250$). Thus, any standard outflow condition will suffice. A Neumann condition for velocities (and zero pressure) is set in Nek5000, and a vanishing normal stress in COMSOL Multiphysics.

Two codes are used to compute base flows in this work, presented in the two coming subsections. The spectral element code Nek5000 is used in most studies, in combination with the FLUPACK spectral stability code. COMSOL Multiphysics is used for both the base flows and the structural sensitivities in Paper 5 (with a validation against Nek5000 and FLUPACK), and in a few verifications of the results in the other studies.

6.1.0a. *Nek5000*. The code Nek5000 is based on a spectral-element method (SEM). Spectral element methods combine some properties of finite element methods (FEM) and spectral methods.

Each spectral element is rectangular, or a suitable coordinate mapping of a rectangle, as in spectral methods. The basis functions inside each element consist of Legendre polynomials in two space dimensions, of the order N for velocity, and $N - 2$ for pressure, where typically $N \geq 6$; they are the Lagrangian interpolants based on the Gauss-Lobatto-Legendre (GLL) quadrature points (compare to Gauss-Lobatto-Chebyshev points in the Chebyshev spectral method). Continuity of the velocity field over element boundaries is obtained by matching the velocities there. Thus, the derivatives of the velocity field are not continuous.

As for FEM, the equations are cast into a weak form, and the integrated residual is minimized. It can be shown that the method has a spectral convergence in N (so-called p -refinement), and the convergence of a high order FEM method with respect to the number of elements (h -refinement).

The wake base flows are obtained simply by starting from a zero initial condition, and integrating the equations forward in time until a steady state is reached. The only instabilities in these flows are anti-symmetric, and are eliminated by imposing a symmetry condition at the centerline (Fig. 6.1). The steadiness of the flow can be verified by checking the difference of successive iterates in a suitable norm. In this work, the time $t_{end} = 500$ was seen to be sufficient.

6.1.0b. *COMSOL Multiphysics*. COMSOL Multiphysics software provides several different *modes*, where the dynamical equations are already programmed, and the physical model can be built by only creating a geometry and specifying the relevant physical parameters (such as density and viscosity in fluid dynamics) and boundary conditions. Also, general PDE modes are provided, where the governing equations and boundary conditions can be specified by the user. Several different options and settings are available regarding both the mesh, elements and solvers, and the choices below are not further optimized than what was necessary.

For the base flow computations with COMSOL Multiphysics, the Fluid Dynamics mode is used, in a steady incompressible formulation. The mesh consists of triangular elements with node points in corners and in the middle of each edge, and the shape functions are the corresponding Lagrangian second-order interpolants for velocities, but the first order for pressure. The integration is performed with a quadrature rule of the order double of the element (shape function) order, and the boundary conditions are discretized using pointwise constraints with the same point order as the element order.

A damped Newton method is chosen to find the stationary solution. The Newton Method is a general method to find zeros of nonlinear equation systems $f(U) = 0$, based on a linearized problem: $U_{i+1} = \delta U$, where $J(U_i)\delta U = -f(U_i)$, and J is the local Jacobian of f . The Newton method converges quadratically if the initial guess U_0 is close enough to the solution (see any standard textbook in applied numerical methods). The damping factor λ is used to adjust the convergence rate, and thereby the sensitivity to the initial guess ($\lambda = 1$ gives the ordinary Newton method). Error estimates from successive iterations are used

(modified Newton correction). If the error increases between two iterations, the value of λ is decreased. The method stops when the relative error of the solution vector in a weighted euclidean norm falls below the given convergence criterion. Note that this means that the local error is typically much smaller than the constraint. In the present work, the value 10^{-6} is typically used, leading to convergence in less than 10 iterations.

6.1.1. Base flows for wakes and jets with surface tension

For wakes and jets with surface tension, the position of the interface between the two fluids in the base flow needs to follow a streamline. The curvature of the streamlines for our jet and wake flows is so small that the pressure gradient caused by surface tension are typically two orders of magnitude smaller than the other pressure gradients occurring in the flow field. This assumption can be verified a posteriori.

Therefore, base flows computed without surface tension provide a good approximation for the actual wake and jet base flows. For simplicity, all base flows in the present work are computed without surface tension. The model might be less appropriate for very large values of surface tension $We^{-1} > 1$, and in the immediate vicinity of the contact line at $x = 0, y = 1$. However, a precise modeling of the inlet conditions (including splitter plates) and the contact line are out of scope of the present work.

Note that despite the assumption of a small curvature for the base flow, surface tension is very important for the global modes. The curvature of the wavy interface depends on the wavelength, and the gradients of the capillary forces caused by the waviness have the same length scale as the global mode.

6.2. Numerical algorithms for solving eigenvalue problems

In the computation of global modes, we need to solve eigenvalue problems of the form:

$$\mathbf{A}\mathbf{q} = \lambda\mathbf{B}\mathbf{q}, \quad (6.3)$$

where $\mathbf{B}\mathbf{q} = (\mathbf{u}, \mathbf{v}, 0)$ and $\lambda = -i\omega$. Due to the appearance of the matrix B , this is a *generalized eigenvalue problem*, but can be solved with slight modifications of the methods originally developed for *standard eigenvalue problems* of the form:

$$\mathbf{A}'\mathbf{x} = \lambda\mathbf{x}, \quad (6.4)$$

which will be discussed here. The primes will be dropped for convenience.

Most of the eigenvalue algorithms available today are based on the *power iteration*. It can be shown that if any vector² x_0 is repeatedly multiplied by the matrix A , it will converge to the eigenvector \mathbf{x}_{\max} corresponding to the eigenvalue of largest magnitude λ_{\max} . So, the basic algorithm of power iteration becomes:

\mathbf{q}_0 =starting vector, ε chosen, $\mathbf{x}_1 = \mathbf{x}_0 + 2\varepsilon$, $k = 1$,
while ($\|\mathbf{x}_k - \mathbf{x}_{k-1}\| > \varepsilon$): $\mathbf{x}_{k+1} = \mathbf{A}\mathbf{x}_k$, $\mathbf{x}_{k+1} = \mathbf{x}_{k+1}/\|\mathbf{x}_{k+1}\|$, $k = k + 1$,

where the norm $\|\cdot\|$ is chosen appropriately. When the eigenvector has converged, the eigenvalue can be extracted from the *Rayleigh quotient*:

$$\lambda_{\max} = \frac{\mathbf{x}_{\max}^H \mathbf{A} \mathbf{x}_{\max}}{\mathbf{x}_{\max}^H \mathbf{x}_{\max}}.$$

Unfortunately, the largest magnitude eigenvalue is of a very small interest in stability computations. It is the most unstable eigenvalues that are our target. It is easily shown that the eigenvalue closest to a certain complex number $\sigma = \sigma_r + i\sigma_i$ (a shift) can be obtained by power iteration with the matrix $(\mathbf{A} - \sigma\mathbf{I})^{-1}$, where \mathbf{I} is the identity matrix. The shift can then be chosen to have a large imaginary part, to hopefully catch the most unstable eigenvalue. In this *inverse power iteration with shifts*, the matrix inverse is not actually formed, but the multiplication $\mathbf{x}^{j+1} = (\mathbf{A} - \sigma\mathbf{I})^{-1}\mathbf{x}^j$ is obtained by solving the equation system: $(\mathbf{A} - \sigma\mathbf{I})\mathbf{x}^{j+1} = \mathbf{x}^j$. The shift can also be updated during the iterations if desired, to give a faster convergence.

Power iteration (inverse or direct) gives only one eigenvector at a time, which becomes very expensive if a whole spectrum is desired. Methods for computing several eigenvectors at once are discussed next.

Similarly to power iteration, if a starting matrix \mathbf{X} with p independent columns is multiplied by \mathbf{A} repeatedly, its columns will converge to the subspace spanned by the p eigenvectors of \mathbf{A} , from which the p largest magnitude eigenvalues of \mathbf{A} can be reconstructed. However, in the process \mathbf{X} becomes very ill-conditioned, since all its columns converge to the first eigenvector at different rates, and are therefore highly non-orthogonal. A smart way to avoid this is to perform a so-called QR-factorization of the matrix \mathbf{X} at each iteration: $\mathbf{X}\mathbf{Q} = \mathbf{Q}\mathbf{R}$, where

²The starting vector expanded in the eigenvector basis needs to have a component along the largest eigenvector, but usually the numerical errors are enough to introduce such a component. There are also other ways to ensure this.

\mathbf{Q} is a unitary matrix (*i.e.* a matrix with orthonormal columns) and \mathbf{R} is upper triangular. As a bonus, upon convergence, the eigenvalues of \mathbf{A} appear on the diagonal of \mathbf{R} . If \mathbf{X} and \mathbf{A} are of the same size (all eigenvalues and eigenvectors of A computed), then the process is called QR-iteration. Usually, the matrix A is first brought into *upper Hessenberg form* with zeros below the first subdiagonal, before starting the actual QR-iterations. The first step requires $O(n^3)$ operations for a matrix of size $n \times n$, but is non-iterative, and the cost of the subsequent QR-iterations is then $O(n^2)$.

The QR-algorithm converges very fast, but it has two drawbacks: it does not preserve a possibly sparse structure of the original matrix (which could enable the use of sparse arithmetics), and is difficult to parallelize efficiently. A method that both preserves the structure of the original matrix and is parallelizable is the Arnoldi algorithm (Arnoldi 1951).

The Arnoldi algorithm creates an approximate upper Hessenberg form of the first m columns of \mathbf{A} iteratively, with only matrix-vector products with \mathbf{A} (and vector-vector products). This approximation is called the Arnoldi-factorization. An Arnoldi factorization of size m is defined as:

$$\mathbf{A}\mathbf{V}_m = \mathbf{V}_m\mathbf{H}_m + \mathbf{f}_m\mathbf{e}_m^T,$$

such that \mathbf{V}_m is a unitary matrix (*i.e.* a matrix with orthonormal columns) of size $n \times m$, \mathbf{H}_m is an upper Hessenberg matrix of size $m \times m$, and $\mathbf{V}_m^H\mathbf{f}_m = 0$, and $\mathbf{e}_{m,j} = \delta_{mj}$ (Sorensen 1996). The columns of \mathbf{V}_m are called *Arnoldi vectors*. They are computed one at a time, by the procedure in table 1, explained below.

In step (1) a new vector is obtained by multiplying the previous vector with \mathbf{A} (cmp. power iteration). In step (2), the new vector is orthogonally projected to each of the previous eigenvectors, and the components along the previous vectors are subtracted from the new vector in step (3). In step (4), the new vector is normalized to 1. Steps (2–4) are the classical Gram-Schmidt orthogonalization, maintaining the matrix \mathbf{V} unitary. The step (5) updates the subdiagonal entry of \mathbf{H} .

The eigenvalues of the upper Hessenberg matrix \mathbf{H} can be easily obtained by *e.g.* Givens rotations (as in the QR-method), and are called *Ritz values*, and the corresponding eigenvectors are *Ritz vectors*. It can be shown that the Ritz values θ are actually Rayleigh quotients of the Ritz vectors \mathbf{y} , with respect to the matrix \mathbf{A} : $\theta = \mathbf{y}^H\mathbf{A}\mathbf{y}/\mathbf{y}^H\mathbf{y}$.

```

v0=starting vector with unit norm
V = v0, H = empty.
for k=1,m
  w = Avk-1 (1)
  vk = w
  for j=1,k
    hk(j)=v(j-1)Hw (2)
    vk = vk - hk(j)v(j-1) (3)
  end for
  fk=vk
  vk=vk/||vk|| (4)
  if (k < m) then
    hk(k+1)=||vk|| (5)
    V=(V, vk)
  end if
H=(H, hk)
end for

```

TABLE 1. Principle of the k-step Arnoldi factorization

The number of Arnoldi vectors needed to approximate well a particular eigenvalue might be very large, and is impossible to know a priori. An observation is that if the starting vector used to build the Arnoldi factorization has components only along m eigenvectors, then the columns of \mathbf{V}_m will span the subspace corresponding to these vectors, and the Ritz values are then exactly the corresponding eigenvalues of A (compare to the matrix \mathbf{R} in the QR-factorization). By successively restarting the Arnoldi factorization with a better starting vector, based on *e.g.* residual information from a previous step, one can thus obtain a better factorization. In these restarting steps, spurious eigenvalues resulting from that the columns of \mathbf{V}_m are slightly nonorthogonal can also be filtered out by *e.g.* *DGKS correction* (Sorensen 1996).

Now, we return to the generalized eigenvalue problem (Eq. 6.3). If a shift σ is desired, the governing equation becomes:

$$(\mathbf{A} - \sigma\mathbf{B})\mathbf{q} = (-i\omega - \sigma)\mathbf{B}\mathbf{q}.$$

This leads to the following changes in the algorithm:

$$(\mathbf{A} - \sigma\mathbf{B})\mathbf{w} = \mathbf{B}_i\mathbf{v}^{k-1} \quad (1)$$

$$\mathbf{h}^k(j) = \mathbf{v}^{(j-1)H}\mathbf{B}\mathbf{w} \quad (2)$$

With a singular matrix \mathbf{B} (Sorensen 1996), as is the case in the discretized Eq. 6.5–6.7 here, infinite eigenvalues appear, and a *purification* needs to be performed to purge these. This purification is built in naturally in the implicitly restarted Arnoldi algorithm with shifts (Sorensen 1996), available in the open-source software package ARPACK.

In this work, two different codes are used to solve the stability problem, FLUPACK and COMSOL Multiphysics, presented in the next section. Both codes take advantage of parallel respective serial versions of ARPACK³ when computing the eigenvalues.

6.3. Global stability of wakes

The equations (2.10–2.11) with Ansatz (2.13) can be written out as:

$$-U \frac{\partial \hat{u}}{\partial x} - V \frac{\partial \hat{u}}{\partial y} - \hat{u} \frac{\partial U}{\partial x} - \hat{v} \frac{\partial U}{\partial y} - \frac{\partial \hat{p}}{\partial x} + \frac{1}{Re} \left(\frac{\partial^2 \hat{u}}{\partial x^2} + \frac{\partial^2 \hat{u}}{\partial y^2} \right) = -i\omega \hat{u}, \quad (6.5)$$

$$-U \frac{\partial \hat{v}}{\partial x} - V \frac{\partial \hat{v}}{\partial y} - \hat{u} \frac{\partial V}{\partial x} - \hat{v} \frac{\partial V}{\partial y} - \frac{\partial \hat{p}}{\partial y} + \frac{1}{Re} \left(\frac{\partial^2 \hat{v}}{\partial x^2} + \frac{\partial^2 \hat{v}}{\partial y^2} \right) = -i\omega \hat{v}, \quad (6.6)$$

$$\frac{\partial \hat{u}}{\partial x} + \frac{\partial \hat{v}}{\partial y} = 0. \quad (6.7)$$

The next step is the choice of discretization. For the present work, the FLUPACK⁴ code with a spectral discretization has been developed (Sec. 6.3.1), but also COMSOL Multiphysics FEM code (Sec. 6.3.2) is used to some extent.

The system also needs boundary conditions to be complete. Since the base flow is symmetric, it can be easily shown that symmetric and antisymmetric modes can be computed separately in the linear problem. Therefore, only the upper half of the domain is used, and on the centerline we set for antisymmetric modes:

$$\hat{u}(x, 0) = \frac{\partial \hat{v}}{\partial y}(x, 0) = \hat{p}(x, 0) = 0. \quad (6.8)$$

³The parallel version is called PARPACK.

⁴The name of FLUPACK refers to fluid-dynamical eigenvalue computations.

and for symmetric modes:

$$\frac{\partial \hat{u}}{\partial y}(x, 0) = \hat{v}(x, 0) = 0. \quad (6.9)$$

The p -condition is needed for antisymmetric modes, since the v -condition in this case already follows from the u -condition through incompressibility on the boundary.

At the wall we set a no slip condition:

$$\hat{u} = \hat{v} = 0. \quad (6.10)$$

The streamwise boundary conditions are not as straight-forward. The natural boundary condition for a global mode is to decay when $x \rightarrow \pm\infty$. The amplitude of the global mode thus vanishes at some point, but its extent is not known a priori. Further, inappropriate boundary conditions can alter the dynamics of the flow, by causing a false destabilization (see *e.g.* Appendix A of Paper 2). Thus, it should be assured that at least all the unstable eigenvalues remain unchanged with change of locations of the outer boundaries.

At the inlet, we set a homogeneous Dirichlet condition (no slip):

$$\hat{u} = \hat{v} = 0. \quad (6.11)$$

Since the inlet condition might also affect the global modes, an extensional region is tested in some cases, described in Appendix A of Paper 1 and Paper 5. The purpose is to allow the global mode to decay more smoothly, but without generating new instabilities, so an artificial splitter plate needs to be inserted between the flow streams. An implementation of this "damping region" exist for both FLUPACK and Comsol. When the effect of the inlet condition is small, it is safe to skip the extensional region, and set the Dirichlet condition above at $x = 0$.

Different outlet boundary conditions are used in different parts of this thesis. For the wakes in Paper 2 and 4, we use the Neumann condition:

$$\frac{\partial \hat{u}}{\partial x} = \frac{\partial \hat{v}}{\partial x} = 0. \quad (6.12)$$

The more physical "stress-free" boundary condition (*e.g.* Giannetti & Luchini (2007)) is used in Paper 5:

$$-\hat{p} + \frac{1}{Re} \frac{\partial \hat{u}}{\partial x} = \frac{\partial \hat{v}}{\partial x} = 0. \quad (6.13)$$

With the stress-free condition, shorter domains are required for convergence than with the Neumann condition.

Additional conditions are required in FLUPACK to eliminate the up to eight spurious pressure modes (the exact number depending on the boundary conditions) inherent in the spectral discretization.

6.3.1. Stability in FLUPACK

In FLUPACK, equations (6.5–6.7) are discretized in space by a spectral method, using Chebyshev-polynomials in both streamwise and vertical directions:

$$\hat{u}(x, y) \approx \sum_{i=1}^{N_x} \sum_{j=1}^{N_y} c_{ij} \phi^i(x) \phi^j(y) \quad (6.14)$$

where ϕ^k is the k^{th} Chebyshev polynomial. The values of the unknown coefficients c_{ij} are obtained by requiring the discretized equations to be satisfied exactly at the $N_x \times N_y$ collocation points, which are selected as the Gauss-Lobatto points to assure an exponential convergence rate (Weideman & Reddy 2000). A linear transformation of the domain from $[-1, 1] \times [-1, 1]$ to $[0, L_x] \times [0, h_1 + h_2]$ is applied in the wake problem. Finally, the global differentiation matrices become Kronecker products of differentiation matrices in one spatial direction and identity matrices in the other spatial direction (see Weideman & Reddy (2000)).

In global eigenvalue computations, a main issue is the storage of the system matrix \mathbf{A} , of size $(3 \times N_x \times N_y)^2$. The steps (1) and (2) in the Arnoldi algorithm require that we can solve equation systems, and perform matrix multiplications, with \mathbf{A} . There are ways to circumvent the building and storage of the matrix, by performing these operations by means of a linear DNS (*e.g.* Barkley, Gomes & Henderson (2002)). This was not appropriate here, since the goal of the development of FLUPACK has been to solve global stability problems in interfacial flows, described in the next section, and a good linear (also in terms of the interface displacement) DNS code for interfacial flows was not available.

In FLUPACK, the matrix is instead built and stored in pieces on different processors, and parallel matrix routines based on MPI are utilized. The distribution of the matrix between processors is made following the so-called *square block-cyclic distribution*, based on BLACS processor grids, which is required by the library ScaLAPACK, since it has proven to be the most efficient way for equation system solution. To illustrate this way of distributing the matrix, let us take as the following

matrix as an example:

$$M = \begin{bmatrix} 1 & 2 & 3 & 4 & 5 & 6 & 7 & 8 & 9 & 10 \\ 11 & 12 & 13 & 14 & 15 & 16 & 17 & 18 & 19 & 20 \\ 21 & 22 & 23 & 24 & 25 & 26 & 27 & 28 & 29 & 30 \\ 31 & 32 & 33 & 34 & 35 & 36 & 37 & 38 & 39 & 40 \\ 41 & 42 & 43 & 44 & 45 & 46 & 47 & 48 & 49 & 50 \\ 51 & 52 & 53 & 54 & 55 & 56 & 57 & 58 & 59 & 60 \end{bmatrix}$$

Assume now that we have a BLACS grid of 3×2 processors,:

$$\begin{array}{l} p_{00} \ p_{01} \ p_{02} \\ p_{10} \ p_{11} \ p_{12} \end{array}$$

and want to create a block-cyclic representation with a (square) block size 2. First, we divide the matrix M into submatrices of size 2×2 . Then, we distribute the first three blocks of the uppermost "row of blocks" to processors p_{00} , p_{01} and p_{02} . The second three blocks of the first block row are again distributed to the same processors in the same order. Note that this means that each processor gets blocks that are separated from each other in the original matrix (by distance $2 \times nr$ of rows in the BLACS grid in this case). The next "row of blocks" is distributed to processors p_{10} , p_{11} and p_{12} in the same way, and the third "row of blocks" again to p_{00} , p_{01} and p_{02} .

When the process is completed, each processor obtains the following matrices:

$$\begin{array}{l} M_{00} = \begin{bmatrix} 1 & 2 & 7 & 8 \\ 11 & 12 & 17 & 18 \\ 41 & 42 & 47 & 48 \\ 51 & 52 & 57 & 58 \end{bmatrix} \quad M_{01} = \begin{bmatrix} 3 & 4 & 9 & 10 \\ 13 & 14 & 19 & 20 \\ 43 & 44 & 49 & 50 \\ 53 & 54 & 59 & 60 \end{bmatrix} \quad M_{02} = \begin{bmatrix} 5 & 6 \\ 15 & 16 \\ 45 & 46 \\ 55 & 56 \end{bmatrix} \\ \\ M_{10} = \begin{bmatrix} 21 & 22 & 27 & 28 \\ 31 & 32 & 37 & 38 \end{bmatrix} \quad M_{11} = \begin{bmatrix} 23 & 24 & 29 & 30 \\ 33 & 34 & 39 & 40 \end{bmatrix} \quad M_{12} = \begin{bmatrix} 25 & 26 \\ 35 & 36 \end{bmatrix} \end{array}$$

It is this matrix that each processor will pass to the parallel equation system solver in ScaLAPACK, together with the BLACS grid.

If the matrix M can be built serially (like in the above example), it is easy to extract the necessary blocks and distribute to the processors. However, when a wholly parallel solution is desired, the matrices M_{ij} need to be built on the processors without knowledge of the total matrix M . To be able to do this automatically for arbitrary numbers of grid

points requires some care, especially in the implementation of boundary conditions.

In FLUPACK, the block size is taken equal to N_x , the number of grid points in the x -direction. The blocks are numbered per row and column. Each processor gets information of which blocks it needs, and then calls a subroutine to build exactly those block numbers. The subroutine builds the local parts of all differentiation matrices, which depend on N_x , N_y , possible stretching functions, and the block row and column. After this, the differential equation can be programmed as usual. At last, the relevant part of the boundary conditions are also incorporated into the matrix block. This implementation makes it easy to change both the discretization method, the governing equations, and the boundary conditions.

When the local matrices are built, a LU-factorization is performed by ScaLAPACK, and the Arnoldi loop can start. In FLUPACK, the same parallelization is used for the Arnoldi vector as for the ScaLAPACK solution vector, for convenience. In principle, different processor grids can be used for Arnoldi and ScaLAPACK, so that the Arnoldi vector would be distributed between all processors. Savings in computational time would be marginal, since most of the wall-clock time is spent in ScaLAPACK operations. Also, dividing the Arnoldi vector between all processors would pose severe restrictions for the choice of grid points, since PARPACK requires the parts of the Arnoldi vector on different processors to be equally long.

The BLACS processor grid needs to be chosen by the user. From computational point of view, quadratic grids are preferable. Each submatrix needs to be small enough to be stored on one processor (with some margin due to the other variables, that are vectors). PARPACK poses the above mentioned restriction leading to that $3 \times N_y$ needs to be dividable by the number of processor rows in the current implementation of FLUPACK.

6.3.2. *Stability in COMSOL Multiphysics*

In COMSOL Multiphysics, the global modes can also be computed in the Fluid Dynamics mode. In the present work however, they are computed in the PDE Coefficient mode, where the adjoint equations and the adjoint base flow equations presented in Sec. 6.4.1 can be easily programmed as well. The mesh is tetrahedral, and second order Lagrangian elements are used for velocity, and the first order for pressure,

with quadrature orders the double of those. COMSOL uses ARPACK for the eigenvalue computations, and the direct UMFPACK solver for the equation systems.

The version of COMSOL Multiphysics used is serial⁵. Also, COMSOL has not yet proven to be suitable for the interfacial global mode problems we aim at solving (Sec. 6.5). The advantages of COMSOL are the flexibility of FEM, and in some situations, the spatially even point distribution.

6.4. Structural sensitivity of wakes

The exact definitions of the different sensitivity measures can be found in Paper 5. Here, we focus on the numerical implementation. At this stage, it is sufficient to know that in addition to the linear global modes, we need to compute the *adjoint linear global modes*

$$[u^+, v^+, p^+] = [\hat{u}^+(x, y), \hat{v}^+(x, y), \hat{p}^+(x, y)]e^{-i\omega^+ t}, \quad (6.15)$$

governed by the equation:

$$\begin{aligned} & -U \frac{\partial u^+}{\partial x} - V \frac{\partial u^+}{\partial y} + u^+ \frac{\partial U}{\partial x} + v^+ \frac{\partial V}{\partial x} \\ & + \frac{\partial p^+}{\partial x} - \frac{1}{Re} \left(\frac{\partial^2 u^+}{\partial x^2} + \frac{\partial^2 u^+}{\partial y^2} \right) = -i\omega^+ \hat{u}^+ \end{aligned} \quad (6.16)$$

$$\begin{aligned} & -U \frac{\partial v^+}{\partial x} - V \frac{\partial v^+}{\partial y} + u^+ \frac{\partial U}{\partial y} + v^+ \frac{\partial V}{\partial y} \\ & + \frac{\partial p^+}{\partial y} - \frac{1}{Re} \left(\frac{\partial^2 v^+}{\partial x^2} + \frac{\partial^2 v^+}{\partial y^2} \right) = -i\omega^+ \hat{v}^+ \end{aligned} \quad (6.17)$$

$$\frac{\partial u^+}{\partial x} + \frac{\partial v^+}{\partial y} = 0. \quad (6.18)$$

The boundary conditions of the adjoint problem depend on the boundary conditions of the direct problem. The derivation is easily made for all sets of boundary conditions used in this thesis. For the principle of derivation, see *e.g.* Marquet *et al.* (2008) or Pralits *et al.* (2010).

The adjoint boundary conditions, with the stress-free outlet boundary condition of the direct problem in Paper 5 (Eq. 26) are:

⁵COMSOL Multiphysics can be run in parallel, but is not available on the clusters used in the present work.

1. A no slip condition on all solid boundaries:

$$\hat{u}^+ = \hat{v}^+ = 0. \quad (6.19)$$

2. An antisymmetry condition on the centerline:

$$\hat{u}^+(x, 0) = \frac{\partial \hat{v}^+}{\partial y}(x, 0) = \hat{p}(x, 0) = 0. \quad (6.20)$$

3. At the outlet:

$$\hat{p}^+ - \frac{1}{Re} \frac{\partial \hat{u}^+}{\partial x} - U \hat{u}^+ = 0. \quad (6.21)$$

$$-\frac{1}{Re} \frac{\partial \hat{v}^+}{\partial x} - U \hat{v}^+ = 0. \quad (6.22)$$

It can be shown that the eigenvalues ω^+ of the adjoint system (with the correct boundary conditions) are complex conjugates of the direct system (Eq. 6.5–6.7). This is however only true in the continuous limit. Thus, the agreement of ω and ω^+ serves as a nice resolution check of the discretized problem.

In addition, to obtain the sensitivity to a volume force, we need to solve for the *adjoint base flow* (\bar{U}^+, P^+) , satisfying:

$$-U_j \frac{\partial U_i^+}{\partial x_j} + U_j^+ \frac{\partial U_j}{\partial x_i} - \frac{\partial P^+}{\partial x_i} - \frac{1}{Re} \left(\frac{\partial U_i^+}{\partial x_j \partial x_j} \right) = \frac{\partial \hat{u}_j^*}{\partial x_i} \hat{u}_j^+ + \frac{\partial \hat{u}_i^+}{\partial x_j} \hat{u}_j, \quad (6.23)$$

$$\frac{\partial U_i^+}{\partial x_i} = 0, \quad (6.24)$$

with the following boundary conditions (again, see Marquet *et al.* (2008) or Pralits *et al.* (2010) for the derivation principle):

1. A no slip condition on all solid boundaries:

$$U^+ = V^+ = 0. \quad (6.25)$$

2. A symmetry condition on the centerline:

$$\frac{\partial U^+}{\partial y}(x, 0) = V^+(x, 0) = 0, \quad (6.26)$$

and the outlet boundary condition:

$$P^+ + \frac{1}{Re} \frac{\partial U^+}{\partial x} + U U^+ - \hat{u}^* \hat{u}^+ = 0, \quad (6.27)$$

$$\frac{1}{Re} \frac{\partial V^+}{\partial x} + U V^+ - \hat{u}^* \hat{v}^+ = 0. \quad (6.28)$$

6.4.1. *Solution of the adjoint equations in FLUPACK and Comsol*

The adjoint linearized Navier-Stokes equations (Eq. 6.16–6.18) are discretized in the exactly same way as the direct linearized Navier-Stokes equations (Eq. 6.5–6.7), both in FLUPACK (Sec. 6.3.1) and in Comsol (Sec. 6.3.2). This is the virtue of methods, where the governing equations and boundary conditions are easily manipulated.

The adjoint base flow equations are solved only in Comsol. A stationary formulation in the PDE Coefficient Form is used for this purpose.

6.5. Global stability of wakes and jets with surface tension

In computations with two fluids separated by an interface, each fluid naturally satisfies the governing equations (6.5–6.7), and wall (Eq. 6.10) and centerline (Eq. 25 or 6.9) boundary conditions. At the inlet, we keep the Dirichlet condition (Eq. 24). In Paper 3, the Neumann condition (Eq. 6.12) is set at the outlet, but for the jets in Paper 6, another condition was seen to be more appropriate. A fringe region, where the disturbance is gradually set to zero through a volume force, gave the correct stability limits for shorter domains than the Neumann condition.

In addition, a set of coupling conditions need to be satisfied on the interface between the two fluids. This requires both a multi-domain implementation, described in Sec. 6.5.1.

Let us denote the fluid closest to the centerline with index (1) and the fluid closest to the wall(s) with index (2). The conditions for the total flow field at the interface between fluids (1) and (2) are, in dimensional form:

(1–2) all velocity components are continuous at the interface:

$$U_{tot,i}^{(1)*} = U_{tot,i}^{(2)*}, \quad (6.1)$$

(3) the tangential stresses are continuous at the interface:

$$\varepsilon_{ijk} n_{tot,j}^* (\tau_{tot,km}^{(1)*} - \tau_{tot,km}^{(2)*}) n_{tot,m}^* = 0, \quad (6.2)$$

and

(4) there is a surface tension induced jump in the normal stress:

$$n_{tot,i}^* (\tau_{tot,ij}^{(1)*} - \tau_{tot,ij}^{(2)*}) n_{tot,j}^* = -\gamma^* s_{tot}^*, \quad (6.3)$$

where γ^* is the surface tension coefficient, $\mathbf{n}_{tot,j}^*$ the surface normal, $\tau_{tot,ij}^{(k)*}$ is the total stress tensor with pressure included, and s_{tot}^* is the

total surface divergence operator defined as:

$$s_{tot}^* = \frac{\partial n_{tot,j}^*}{\partial x_j^*}. \quad (6.4)$$

Here, the direction of the surface normal \mathbf{n}_{tot}^* is given by the location of the interface H_{tot} , and thus we also need an equation for H_{tot} . This comes from the assumption that the interface moves together with the fluid particles on the interface:

$$\frac{\partial(y^* - H_{tot}^*)}{\partial t^*} + U_{tot,j}^* \frac{\partial(y^* - H_{tot}^*)}{\partial x_j^*} = 0. \quad (6.5)$$

We cannot keep the time derivative of H_{tot}^* , when solving the eigenvalue problem. As for the other variables, it also needs to be Fourier transformed. Thus, we introduce:

$$H_{tot}^*(x, t) = H^*(x) + \eta^*(x, t),$$

where H^* is the position of the interface for the base flow, and η^* a small displacement.

The formulation of the linearized boundary conditions implemented in FLUPACK is valid for arbitrary density and viscosity ratios. Here, they are merely stated for density and viscosity ratios of unity, and by exploiting the fact that the base flow is computed without surface tension (for a derivation, see appendix A of Paper 6):

$$\hat{u}_i^{(1)} = \hat{u}_i^{(2)} \quad (6.6)$$

$$\begin{aligned} \left(-\hat{p}^{(1)} + \hat{p}^{(2)}\right) \delta_{ij} N_j + \frac{2}{Re} \left(\hat{e}_{ij}^{(1)} - \hat{e}_{ij}^{(2)}\right) N_j = \\ -\frac{1}{We} \left(N_i \frac{\partial \hat{n}'_j}{\partial x_j} + \hat{n}'_i \frac{\partial N_j}{\partial x_j}\right) \end{aligned} \quad (6.7)$$

$$-i\omega \hat{\eta} + \frac{\partial H}{\partial x} \hat{u} + U \frac{\partial \hat{\eta}}{\partial x} + \frac{\partial H}{\partial x} \frac{\partial U}{\partial y} \hat{\eta} - \hat{v} - \frac{\partial V}{\partial y} \hat{\eta} = 0, \quad (6.8)$$

where $\hat{n}' = \left[(-f - \frac{\partial H}{\partial x} g) \frac{\partial \hat{\eta}}{\partial x}, g \frac{\partial \hat{\eta}}{\partial x}\right]$, $\hat{e}_{ij} = \frac{1}{2}(\frac{\partial \hat{u}_i}{\partial x_j} + \frac{\partial \hat{u}_j}{\partial x_i})$, and $f = \varphi|_{\frac{\partial \eta}{\partial x}=0}$ and $g = \frac{\partial \varphi}{\partial(\frac{\partial \eta}{\partial x})}|_{\frac{\partial \eta}{\partial x}=0}$, using

$$\varphi = \frac{1}{\sqrt{\left(\frac{\partial H}{\partial x} + \frac{\partial \eta}{\partial x}\right)^2 + 1}}.$$

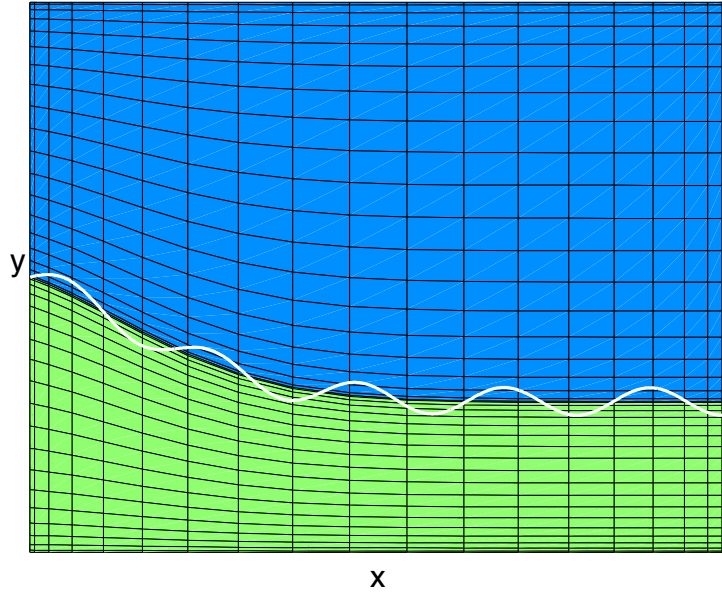


FIGURE 6.2. Illustration of the domain decomposition for wakes and jets with surface tension (w. The upper domain is blue, and the lower domain green. The computational domains are separated by the steady interface position $H(x)$. The total surface position $H_{tot}(x) = H(x) + \eta(x)$ is illustrated by the white line. The black lines illustrate the grid lines of the Chebyshev-Chebyshev grids, stretched in the y -direction.

6.5.1. Multidomain discretization in FLUPACK

The equations (6.5–6.7) are discretized using two domains that lie on top of each other in the vertical direction (see Fig. 6.2). They are stretched in the y -direction so that $y = H(x)$, the steady interface position, becomes their common boundary.

Both domains are discretized with their own sets of Chebyshev polynomials. We require that Eq. (6.5–6.7) are satisfied in both domains, and set the boundary conditions in a way similar to the one-domain case (Sec. 6.3.1). Then, the two solutions are coupled at $y = H(x)$, by imposing the five coupling conditions (Eq. 32–35) at the interface.

In the parallel implementation, the eigenvector has the following structure:

$$\mathbf{q} = (\hat{\mathbf{u}}^{(2)}, \hat{\mathbf{v}}^{(2)}, \hat{\mathbf{p}}^{(2)}, \hat{\mathbf{u}}^{(1)}, \hat{\mathbf{v}}^{(1)}, \hat{\mathbf{p}}^{(1)}, \hat{\eta}).$$

The two matrices $\mathbf{A}^{(1)}$ and $\mathbf{A}^{(2)}$ containing the governing equations for domains (1) and (2) and their outer boundary conditions are created with the same routine as in one-domain case. Afterwards, these submatrices appear along the diagonal:

$$\mathbf{A} = \begin{bmatrix} \mathbf{A}^{(2)} & 0 & 0 \\ 0 & \mathbf{A}^{(1)} & 0 \\ 0 & 0 & 0 \end{bmatrix}$$

The kinematic equation of the interface (Eq. 35) is then created by a separate routine, and replaces the zeros in the last N_x rows of the matrix. The uppermost and lowermost rows of the u - and v -momentum equations in each domain is replaced by one of Eq. (32–34), involving the flow variables in both domains and $\hat{\eta}$.

6.6. Local stability of the liquid sheet

The local stability of the liquid sheet is governed by Eq. (2.17–2.19), with ansatz (2.16). Based on the experiments, we also assume two-dimensional disturbances, so the ansatz becomes:

$$u_i = \hat{u}_i(y)e^{i\alpha x - i\omega t}.$$

Here, we take the spatial approach, where ω is real and α a complex number.

It can be shown that all unstable modes can be obtained from the *Orr-Sommerfeld equation* for v (for a derivation, see Schmid & Henningson (2001)), written for a liquid sheet as:

$$(i\alpha U - i\omega)(D^2 - \alpha^2)\hat{v}_{l,g} - i\alpha D^2 U \hat{v}_{l,g} = Re_{l,g}^{-1}(D^4 - 2\alpha^2 D^2 + \alpha^4), \quad (6.9)$$

where $D = \frac{d}{dy}$ and $Re_{l,g}$ is the Reynolds number for liquid or gas.

The Reynolds numbers are defined as:

$$Re_l = \frac{\rho_l^* U_l^* a^*}{\mu_l^*}, \quad (6.10)$$

$$Re_g = \frac{\rho_g^* U_l^* a^*}{\mu_g^*}, \quad (6.11)$$

where U_l^* is the liquid sheet velocity, a^* the half thickness of the liquid sheet, and $\rho_{l,g}^*$ and $\nu_{l,g}^*$ the density and viscosity for liquid or gas.

We have chosen to non-dimensionalize the boundary conditions with liquid quantities, as in Söderberg & Alfredsson (1998) and Söderberg (2003). This involves the following nondimensional parameters:

the Weber number:

$$We = \frac{\rho_l^* (U_l^{0*})^2 a^*}{\gamma^*}, \quad (6.12)$$

where γ^* the surface tension between the liquid and the gas, the density ratio between the gas and the liquid:

$$\tilde{\rho} = \frac{\rho_g^*}{\rho_l^*}, \quad (6.13)$$

and their viscosity ratio:

$$\tilde{\mu} = \frac{\mu_g^*}{\mu_l^*}. \quad (6.14)$$

Similarly to the global problem in Sec. 6.5, we introduce a division of the interface position into a steady and oscillating part as:

$H_{tot}^* = H^* + \hat{h}e^{i(\alpha x - \omega t)}$. After some algebra, the linearized local non-dimensional boundary conditions become (for details, see Söderberg & Alfredsson (1998)):

(1–2) Velocity continuity on the interface (comp. 21):

$$D\hat{v}_l - i\alpha\hat{h}(DU_l - DU_g) = D\hat{v}_g \quad (6.15)$$

$$\hat{v}_l = \hat{v}_g, \quad (6.16)$$

where equation (26) is the continuity of \hat{u} transformed to a condition for \hat{v} using (2.19),

(3) Continuity of the tangential stress (comp. 22):

$$(D^2 + \alpha^2)\hat{v}_l - i\alpha\hat{h}(D^2U_l - \tilde{\mu}D^2U_g) = \tilde{\mu}(D^2 + \alpha^2)\hat{v}_g \quad (6.17)$$

(4) Surface tension induced jump of the normal stress (comp. 23):

$$\begin{aligned} & [(i\alpha U_l - i\omega) - Re_l^{-1}(D^2 - 3\alpha^2)] D\hat{v}_l - i\alpha DU_l \hat{v}_l = \\ & [\tilde{\rho}(i\alpha U_g - i\omega) - \tilde{\mu}Re_l^{-1}(D^2 - 3\alpha^2)] D\hat{v}_g - i\alpha\tilde{\rho}DU_g \hat{v}_g - We^{-1}\alpha^4\hat{h}, \end{aligned} \quad (6.18)$$

and

(5) Interface equation of motion:

$$-i\omega\hat{h} + U\frac{\partial\hat{h}}{\partial x} = \hat{v}. \quad (6.19)$$

The local problem is discretized in the same way as the global problem in the previous section, with the difference that the variables only depend on y , except for h that is a constant. Thus, only a linear stretching in the y -direction is needed in this case. The local problem small

enough to be solved serially with the QR-method (Sec. 6.2), which is done using the EISPACK Software.

Summary of the results of the present work

In this chapter, the main results of Papers 1–6 will be presented. They are categorized in three parts: the effect of air co-flow on the convective instability of a plane liquid sheet (Sec. 7.1), the effect of confinement on global instability of wakes (Sec. 7.2), and the influence of surface tension on global stability of jets and wakes (Sec. 7.3).

7.1. Stabilizing effect of air co-flow on a plane liquid sheet

The effect of air flow on the stability of a plane liquid sheet (the flow case presented in Sec. 5.3) is investigated in Paper 1. In the experiments made by A. Sasaki and M. Matsubara, the liquid sheet was excited with different frequencies by loudspeakers located at the air nozzles (Fig. 5.4). Then, the inclination angle of the sheet was measured experimentally (for details about the measurement techniques see Paper 1). The spatial growth rate was extracted from the measured amplitudes over a finite interval, by plotting the amplitude curve in a logarithmic scale as a function of the spatial coordinate¹. The frequency could be converted into a wavenumber, since the experiments showed that the phase velocity of the waves was equal to the speed of the liquid. A spatial local stability computation was then performed, using an estimated base flow profile in the middle of the experimental interval.

First, the liquid sheet in stagnant air was studied. The computations were made without adjustments, using the experimental Reynolds and Weber number, density ratio, and viscosity ratio. The viscosity of both liquid and gas were included in the stability computations, and the boundary layer development in the air was taken into account. The exact shape of the air boundary layer was not possible to measure experimentally due to the flapping of the sheet, which prevented hot wire measurements in the presence of the sheet. Two similarity solutions

¹cmp. ansatz (2.16)

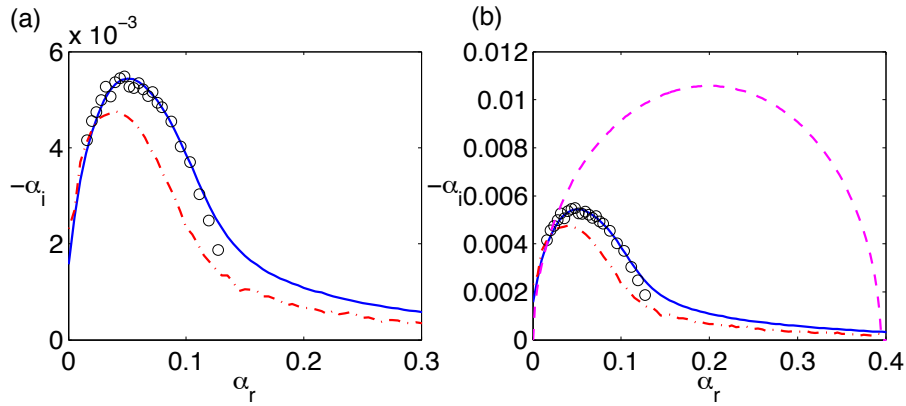


FIGURE 7.1. Liquid sheet in stagnant air. (a) Growth rate as a function of wavenumber, (o): measurements, blue (—): computation, Stokes model, dark red (-.-): computation, Sakiadis model. (b) The same as in (a), compared with the inviscid solution of Li (1993) in magenta (- -).

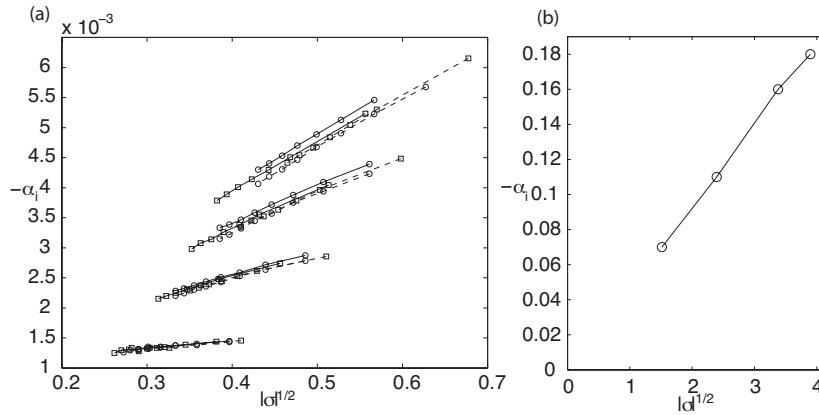


FIGURE 7.2. (a) The growth rate of the peak eigenvalues for different x -positions ($x = 400, 800, 1000, 1200, 1400, 1600, 1800$) for Stokes and Sakiadis as functions of $|\sigma|^{1/2}$, from up and down: (—□—) Sakiadis $U_g^\infty = 0, 0.2, 0.4, 0.6$, (—○—) Stokes $U_g^\infty = 0, 0.2, 0.4, 0.6$, (- -□- -) Sakiadis $U_g^\infty = 2, 1.8, 1.6, 1.4$, and (- -○- -) Stokes $U_g^\infty = 2, 1.8, 1.6, 1.4$. (b) The same scaling extracted from the data in Lozano *et al.* (2001) for $U_g^\infty = 12.5$, $Re_l = 340$, and a different base flow model.

were tested for the air boundary layer, using the nozzle exit as the virtual leading edge and the mean measurement position as the streamwise coordinate, here termed the Stokes model and the Sakiadis model.

The comparison between measurements and computations in stagnant air is shown in Fig. 7.1 (a). Here, the measured values are depicted by rings, computational values with the Stokes model by a blue solid line, and the Sakiadis model by the red dash-dotted line. The agreement is excellent for the Stokes, and fairly good for the Sakiadis model, although the latter slightly underestimates the growth rates. In Fig. 7.1 (b) both are compared to results from a previous model (Li 1993), where air is assumed to be inviscid and have a uniform profile. It is seen that the model with inviscid air overpredicts the experimental growth rate by a factor of 2, and the wavenumber for maximal growth rate by a factor of 3, while both viscous solutions are in good agreement. A further comparison of experiments and theory can be seen in Paper 1 for the case of co-flowing air, with a good agreement, although less perfect than in the stagnant case in Fig. 7.1.

The cases where $U_g > U_l$ posed difficulties for the experimental studies, due to problems to control the air flow distribution. Also, it is not straightforward to experimentally quantify the effect of the streamwise position on the growth rate. The effect of these parameters was investigated further in the theoretical framework. For moderate air speeds, with a fixed boundary layer thickness, the growth scales linearly with the velocity difference between water and air irrespective of the boundary layer model used. For fixed air speed on the other hand, the growth seems to scale as the square root of the shear from the air at the water surface (Fig. 7.2 a). The same viscous scaling due to air boundary layer was also extracted from previous work dealing with atomisation flows (Lozano *et al.* 2001) (Fig. 7.2 b).

7.2. The influence of confinement on wake instability

7.2.1. Linear global and nonlinear stability

In Paper 2, the global stability of confined plane co-flow wakes (the flow case presented in Sec. 5.1) is investigated by linear two-dimensional global modes and nonlinear direct numerical simulations (DNS).

First, the value of confinement (h) was altered for a wake at $Re = 100$, $\Lambda^{-1} = -1.2$. The growth rate (ω_i^l) as a function of h is depicted with a solid line with crosses in Fig. 15 (b). The figure shows that the growth rate of the linear global mode mostly decreases with confinement, until

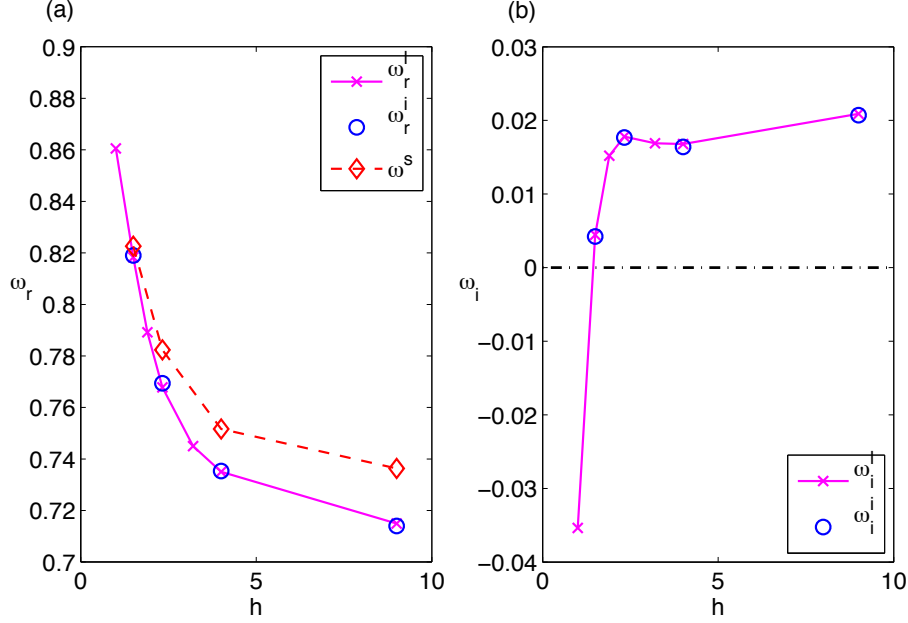


FIGURE 7.3. (a) The most unstable linear, nonlinear initial and nonlinear saturated frequency and (b) linear and nonlinear initial growth rate, as functions of confinement, at $Re = 100$, $\Lambda^{-1} = -1.2$. Linear data points: $h = 9, 4, 2.33, 1.5$ and 1 , nonlinear data points: $h = 9, 4, 2.33$, and 1.5 ($h = 1$ stable).

the flow finally stabilizes at $h = 1$. The main reason to the stabilization was found from changes of the spatial structure of the base flow — the length of the wake and the extent of the recirculation region — which both decrease with confinement.

The frequency of the linear global mode (ω_r^l) as a function of h is depicted by a solid line with crosses in Fig. 15 (a). The frequency increases monotonously with confinement, in accordance with all previous studies presented in Sec. 3.1.2 and 3.2.1.

In the DNS, a full time signal was recorded in nine points of the flow field to determine the frequency and growth of the oscillation. We extracted the frequency (circles in Fig. 15 a) and the exponent of the amplitude growth (circles in Fig. 15 b) in the initial stage, and compared those with the linear frequency and growth rate, respectively. The agreement is nearly perfect, confirming that the nonlinear oscillation develops through the computed linear global mode, thus cross-validating

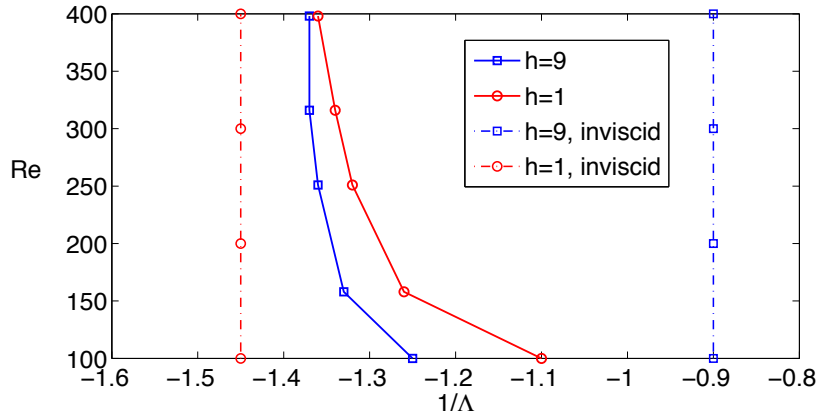


FIGURE 7.4. The neutral stability curves as a function of Λ^{-1} and Re for an unconfined ($-\square-$, blue) and confined ($-\circ-$, red) wake. The region on the right side of the curve is unstable. The inviscid solution by Juniper (2006) is also shown — unconfined ($-\square-$, blue) and confined ($-\circ-$, red).

both methods. This agreement was as good for the other wakes under study. Note that this means that the stability limits for DNS and linear global modes were always equal, also in cases where final flow states were different. For example, confinement stabilized the nonlinear flow at $h = 1$ as well.

After the initial linear regime, the growth of the nonlinear oscillation weakens and finally its amplitude *saturates* into a constant value. The frequency and shape of the fundamental Fourier mode of the saturated state were also extracted, and compared to their linear counterparts. The nonlinear saturated frequencies (diamonds connected with dashed lines in Fig. 15 a) show the same trend with confinement as the linear frequencies, but are higher for all values of h . Comparisons of linear and nonlinear mode shapes, and studies on the effect of shear ratio at $Re = 100$, are also presented in the paper.

Now, we turn into the effect of the Reynolds number. Figure 24 shows the neutral stability curves for linear global modes in $\Lambda^{-1} - Re$ -plane, for a confined ($h = 1$) and an "unconfined" ($h = 9$) wake. The confined wake is always more stable than the unconfined wake, but the stability limits approach each other at $Re = 300 - 400$. The base flows at $Re = 400$ for confined and unconfined flows were seen to be similar in the upstream region, although the total lengths of the wake region were

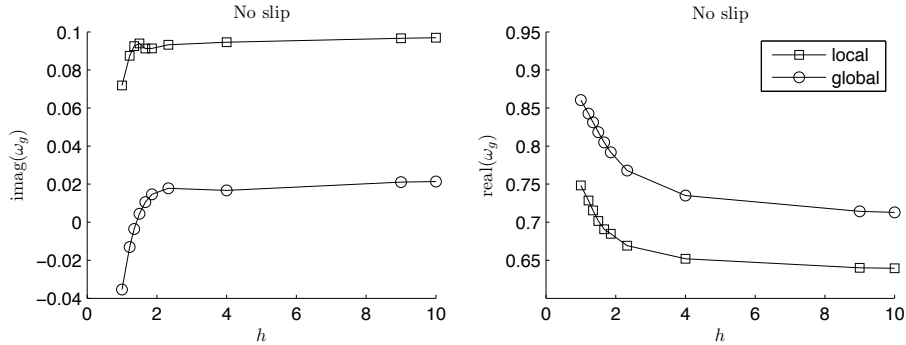


FIGURE 7.5. Growth rate, ω_{gi} (left) and frequency, ω_{gr} (right) of the linear global mode calculated with the approximate local analysis (squares) and the "true" global analysis (circles).

different. This lead to the hypothesis that the confinement affected the flow only through base flow changes in the upstream region, and that this effect would be absent for higher Reynolds numbers.

7.2.2. Linear global modes vs. weakly-non-parallel theory

The result of Paper 1, that confinement had a globally stabilizing effect on co-flow wakes, seemed to contract the previous local results (Juniper (2006), Rees & Juniper (2010)), where confinement increased the local absolute instability for co-flow wakes (see the dashed lines in Fig. 24). Also, the main conclusion from Paper 1 was that the stabilizing effect of confinement was caused by the spatial structure of the confined base flow. Therefore, the logical next step was to perform a local analysis on the same spatially developing base flows as the global analysis.

In Paper 4, a local weakly-non-parallel (WNP) analysis is made by M. P. Juniper, and the global analysis by the author of this thesis, on an extensive set of base flows. Both the growth rate, frequency and shape of the global mode can be approximated from the local analysis, as described in Sec. 2.2. These results can then be compared with the ones obtained from the "true" global analysis.

The global and local eigenvalues with respect to h are shown in Fig. 7.5: the frequency (a) and the growth rate (b). Two observations can immediately be made from the figures. The first is that the local analysis overestimates the growth rates and frequencies compared to the global analysis for all h . The difference between local and global eigenvalues is fairly constant. The second observation is that the trends

in both curves are very similar. In particular, confinement decreases the growth rate also in the local analysis. However, since the local analysis overestimates the growth rates in all cases, the local growth rate for $h = 1$ is still positive.

Shapes of local and global growth rate curves (and the same for the frequency curves) are similar in all cases under study, apart from the constant offset. Based on this, it is argued that the local analysis might be able to predict trends seen in global linear stability, despite the quantitative disagreement. Both analyses are also made on a more artificial base flow with a slip condition on the wall, in an attempt to study the influence of the wall boundary layer. Three competing effects of the confinement are found:

1. The wake length and the length of the backflow region decrease with confinement (as pointed out in Paper 1).
2. The wall boundary layer makes the profile less locally unstable.
3. The saddle point interaction (as in Juniper (2006), Rees & Juniper (2010)) acts destabilizing.

For the wakes at $Re = 100$, effects 1–2 overcome effect 3 in the local analysis, which resolves the apparent contradiction between the previous local and global results.

7.2.3. Structural sensitivity

Paper 4 deals with the structural sensitivity of co-flow wakes, concentrating on the weakly confined²wake at $h = 9$, $Re \approx 400$, $\Lambda^{-1} = -1.32$. Specific phenomena, not reported in previous works performed in other wake configurations, are highlighted. The physical background of the sensitivity approaches presented here is described in Sec. 2.4 in more detail.

First, we locate the wavemaker region, assumed to be the source of the instability (Giannetti & Luchini 2007). This is obtained by looking at the overlap of (the amplitude of) the direct and adjoint global eigenmodes. This overlap for the leading eigenmode is shown in Fig. 7.6 a. In contrary to previous results for cylinder wakes (see Sec. 3.1.1), the wavemaker has more than one local maximum: the first one in the shear layer close to the inlet, and the second one downstream, centered around $x \approx 20$. The second elongated region seems to be unique for

²In Paper 2, the wakes at $h = 9$ are called "unconfined". This is because for $h > 9$, variations in h cause only minor changes in the global eigenvalue. In Paper 6, the term "unconfined" is also sometimes used in comparisons, to distinguish from the strongly confined wake ($h = 1$).

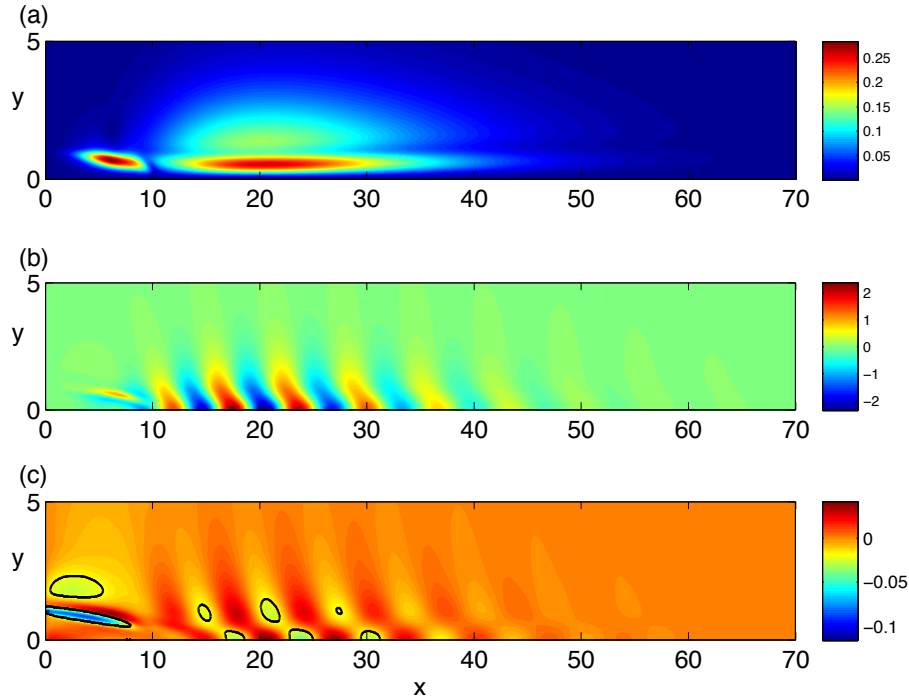


FIGURE 7.6. Theoretically predicted sensitivity of the global wake eigenvalue to small perturbations: (a) sensitivity to structural perturbations, (b) sensitivity to modifications of the streamwise base flow velocity field, (c) sensitivity to a small control cylinder (the dark contours surround regions where stabilization is predicted by the linear theory).

weakly confined wakes at high Reynolds numbers; it appears neither for strongly confined wakes, nor for weakly confined wakes at $Re \approx 100$.

Second, we look at where local modifications of the base flow velocity profile have the largest effect on the growth rate of the global mode (Marquet *et al.* 2008). This property could potentially be exploited in flow control; one could try to modify the mean flow profile experimentally in a certain position, with the goal to either suppress or enhance the global oscillations. The sensitivity to modifications in the streamwise velocity of the base flow is shown in Fig. 7.6 b. The red color indicates that a local streamwise acceleration is destabilizing, and the blue color that it is stabilizing (and since the theory is linear, a streamwise deceleration has the opposite effect).

In the region $0 < x < 10$ (the location of the upstream wavemaker in Fig. 7.6 a), the effect of base flow modifications is intuitively clear. The growth rate increases if the outer flow is accelerated, and the inner flow decelerated. Both modifications would make the shear stronger, thus enhancing the instability. The physical interpretation of the sensitivity in the region $x > 10$ is not as straightforward. Here, a periodic row of minima and maxima are seen, depending on the streamwise position of the modification. This seemingly counterintuitive theoretical result is verified by introducing a base flow modification directly in the global mode computations, for a range of streamwise positions. For small base flow modifications, the eigenvalue moves exactly as predicted by the theoretical distribution.

Further, we examine the effect of a small control cylinder on the global stability. Theoretically, this can be done by modeling the cylinder as a volume force with both steady and unsteady components (Hill (1992), Pralits *et al.* (2010)). The resulting sensitivity distribution is shown in Fig. 7.6 c. The black contours indicate regions, where a tiny control cylinder with radius $r = 0.02$ should suppress the global mode.

The validity of the theoretical prediction is tested by including a control cylinder ($r = 0.02$) in various spatial positions, and recomputing the global spectrum. The result is that all global modes can be stabilized if the control cylinder is placed inside the upstream wavemaker region. When the cylinder is placed in region $x > 10$, it fails to stabilize the flow, and instead several new unstable modes appear. The spectrum depends on the position of the control cylinder, in a similar manner as hotwires can create edge tones in shear layer experiments (Hussain & Zaman 1978).

The prediction of the theory is only valid for small enough modifications, and the force from the cylinder appears to be too large. Appearance of several modes is shown also for large generic base flow modifications, while the small base flow modifications were very consistent with the theory. Therefore, the theoretically obtained distribution in the downstream region should be valid only for small enough cylinders, but the eigenvalue would then probably not move to the stable side.

The result indicates that the flow should be controlled in the upstream region, while it is extremely sensitive to perturbations in the downstream region. In previous wake studies (mostly at lower Re), the regions of high sensitivity and controllability were always close to each

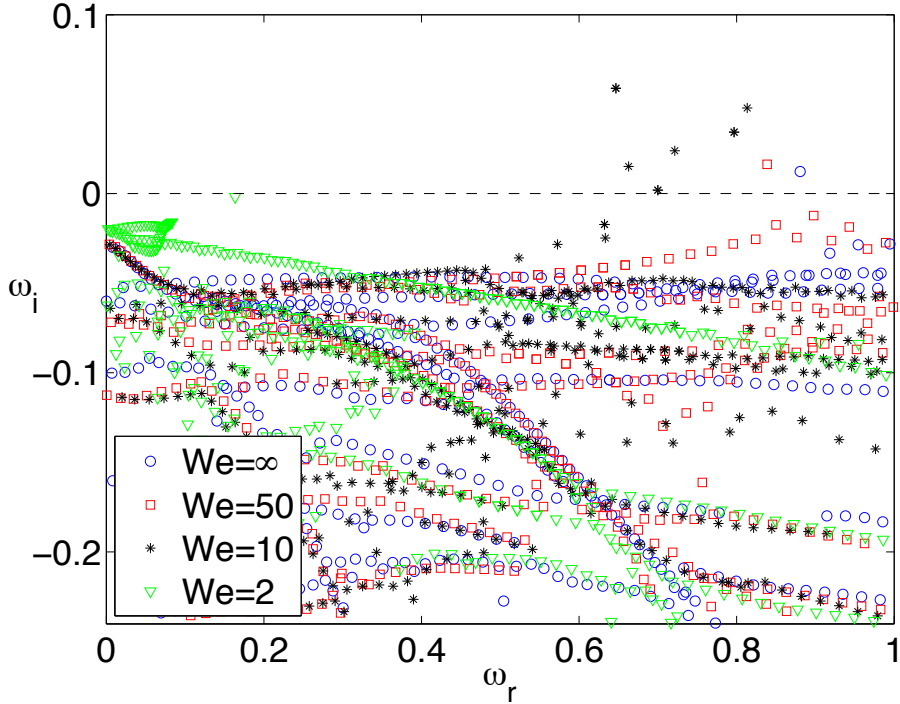


FIGURE 7.7. Spectra for different values of surface tension parameter We , for the example wake 2 in Paper 3 ($Re = 316$, $h = 1$, $\Lambda^{-1} = -1.32$).

other. Therefore, the flow case could be very interesting for studies of wake dynamics and control at moderate Reynolds numbers.

7.3. The effect of surface tension on wakes and jets

7.3.1. Changes in the spectra and modal structure of an example wake

In Paper 3, we add surface tension as a new parameter to the co-flow wake studies. Two of the slightly unstable wakes in Paper 2 are chosen, and we examine how the global modes evolve with increasing surface tension, by changing the Weber number defined in Sec. 5.2 from $We = \infty$ (no surface tension) to $We \approx 2$. In this section, some results for the second wake ($Re = 316$, $\Lambda^{-1} = -1.32$, $h = 1$) are presented³.

³The first wake in Paper 3 ($Re = 100$, $h = 1.5$, $\Lambda^{-1} = -1.2$) gives similar trends, but the effect of surface tension is smaller in that case.

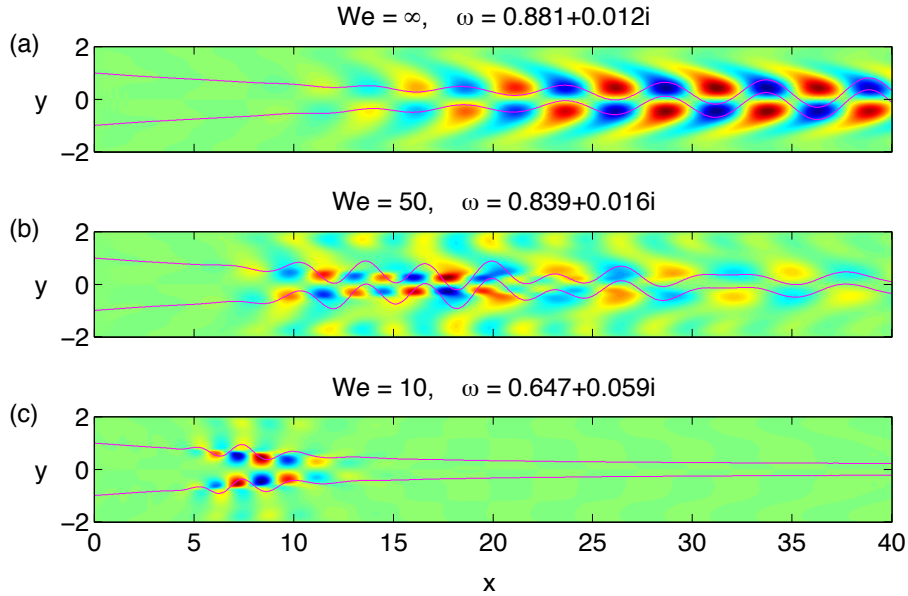


FIGURE 7.8. Streamwise disturbance velocity of the most unstable mode for different We , for the example wake 2 in Paper 3 ($Re = 316$, $h = 1$, $\Lambda^{-1} = -1.32$).

First, we look at the eigenvalue spectra for different values of surface tension, shown in Fig. 7.7. Without surface tension (blue), there is one unstable mode with nondimensional frequency $\omega_r \approx 0.88$ and growth rate $\omega_i \approx 0.012$. The mode is antisymmetric, and corresponds to the well-known von Kármán vortex street, but here in the context of a co-flow wake.

When a small amount of surface tension is added ($We \approx 50$, red), not much is changed: the unstable mode has moved to a slightly lower frequency. However, when the value of surface tension is increased to intermediate values ($We \approx 10$, black), the growth rate of the most unstable mode has increased remarkably (to $\omega_i \approx 0.059$), and five more unstable modes have shown up. All modes occur at lower frequencies than the unstable mode at $We = \infty$. A look at the mode shapes has shown that the most unstable mode at $We = 10$ is still antisymmetric, but that two of the other unstable modes are symmetric.

When the surface tension is increased further to $We \approx 4$, it is shown in Paper 3 that the most unstable mode becomes symmetric. When $We \lesssim 2$ (green), also the symmetric modes become stable.

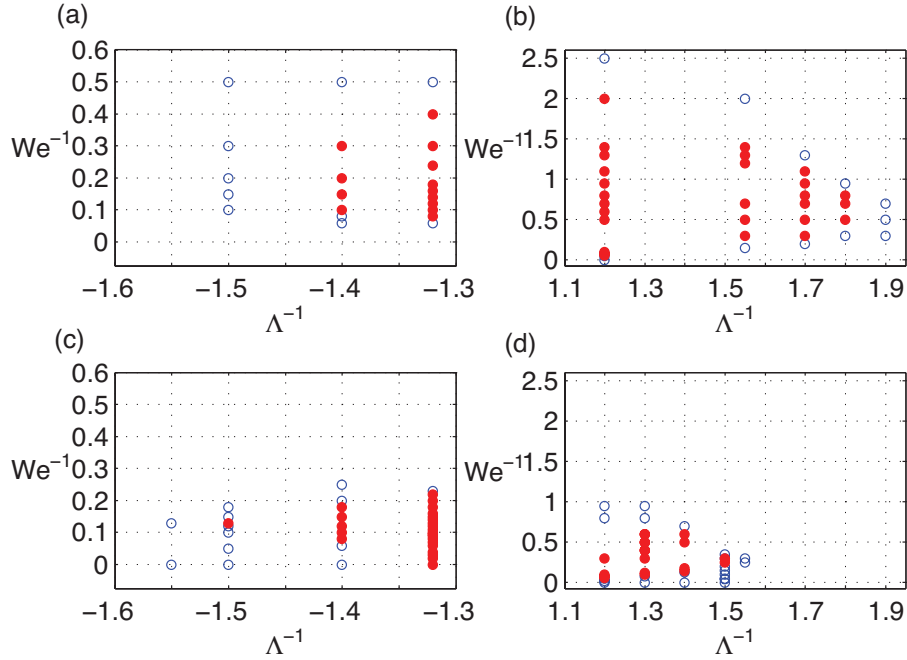


FIGURE 7.9. Global stability as a function of $1/We$ and $1/\Lambda$ for wakes (a,c) and jets (b,d). Note the different scales on vertical axis ($1/We$) for wakes and jets. Results for symmetric (a,b) and antisymmetric (c,d) are shown. Filled symbols show unstable and open show stable cases.

Examples on the effect of surface tension on the mode shapes are shown in Fig. 7.8 (for antisymmetric modes). The unstable mode without surface tension (uppermost figure) has a long wavelength and extends far outside the figure frame in the streamwise direction. Already for weak surface tension ($We = 50$, middle figure), the longer wavelength is accompanied by a shorter one in the shear layer close to the nozzle. For $We = 10$, the shorter waves have taken over, and the mode amplitude is large only over a couple of wavelengths, in a region fairly close to the nozzle.

The effect of surface tension on the example wake can be summarized as follows: Intermediate surface tension increases the growth rate of the global mode(s) in wakes, while strong surface tension stabilizes all oscillations. Further, surface tension shortens the wavelength of the unstable mode(s), and moves the oscillation region upstream.

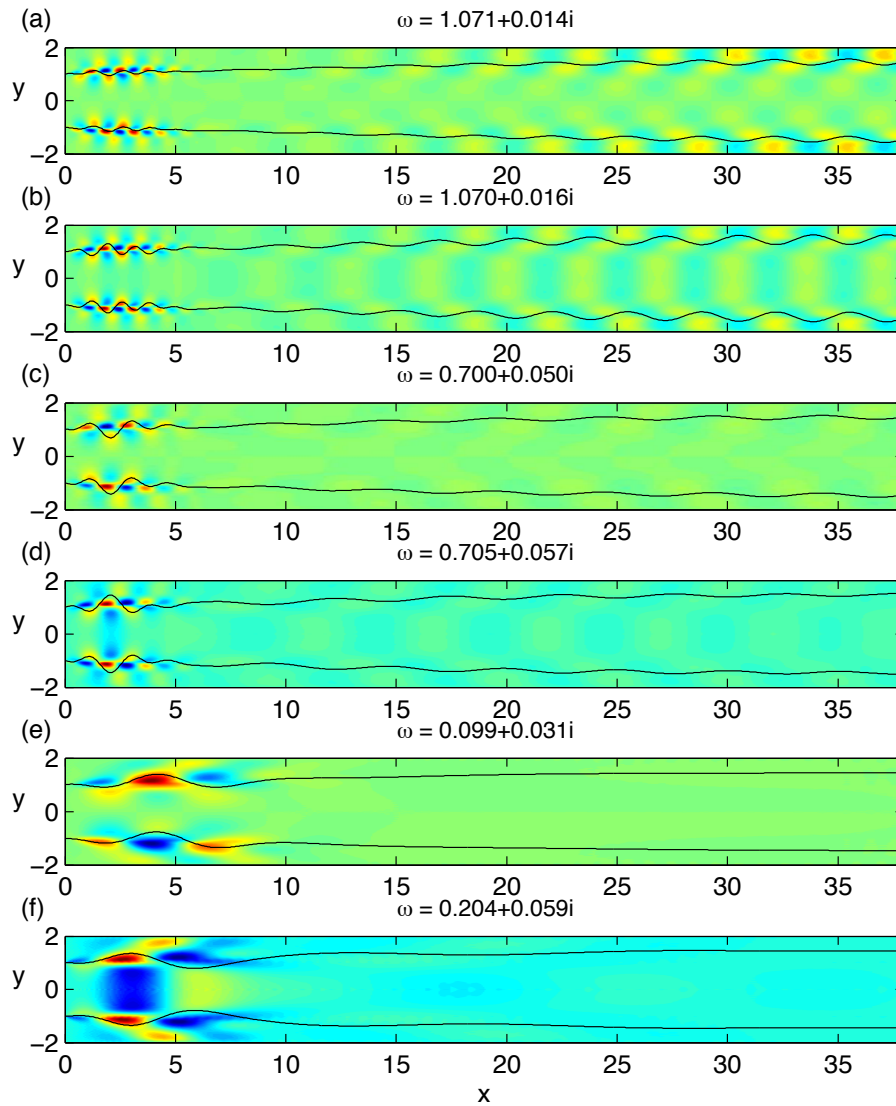


FIGURE 7.10. Modes for antisymmetric and symmetric disturbances for a jet with $1/\Lambda = 1.2$, and $1/We = 0.06, 0.1$ and 0.4 , from top to bottom.

7.3.2. Surface tension induced destabilization of jets and wakes

The investigation in Paper 3 was made for wakes that were unstable without surface tension. Although the growth rates increased, there

was no proof that surface tension could destabilize a flow field. Also, linear analysis is not expected to yield accurate results in the strongly unstable flows, but can be used to locate the bifurcation point(s), which is the focus of Paper 6.

In Paper 6, it is shown that surface tension indeed can destabilize plane wakes and jets which are stable without surface tension. The investigations are performed at $h = 1$ and $Re = 316$. In the current section, we adopt the inverse Weber number We^{-1} to characterize the importance of surface tension. This means that the case without surface tension has conveniently the value $We^{-1} = 0$.

The instability of jets is more remarkable than that of wakes, since co-flow jets do not normally have global oscillations for this low Reynolds number. The stability of jets over the $\Lambda^{-1}-We^{-1}$ -plane is shown in Fig. 7.9 (a) for antisymmetric and (b) for symmetric modes. Each dot in the figure represents one global mode computation, and the filled dots denote cases where at least one unstable mode was found. Consequently, the limits of the globally unstable parameter region are located between filled and open symbols. The jet is unstable for symmetric modes for a much larger range of shear ratios, than for antisymmetric modes (notice the different axis limit in subfigures a and b). The stability of wakes is shown in Fig. 7.9 (c-d). For wakes on the other hand, antisymmetric modes are unstable for a larger region in the parameter space than the symmetric modes. In this sense, symmetric modes dominate for jets, and antisymmetric modes for wakes.

However, the nature of the first bifurcation when surface tension is increased largely depends on the value of the shear ratio Λ^{-1} . We take the jet at $\Lambda^{-1} = 1.2$ as an example. For this jet, both symmetric and antisymmetric modes bifurcate simultaneously at $We^{-1} \approx 0.06$, and have almost the same value of ω . This indicates that the bifurcating mode is neither symmetric nor antisymmetric. Symmetric and antisymmetric eigenfunctions for this jet at different values of We , are shown in Fig. 7.10. The corresponding eigenvalue is written on top of each figure.

CHAPTER 8

Conclusions and outlook

In this chapter, the main conclusions of each paper are first presented in point-form. The conclusions are followed by a general outlook, in which the results are put in a somewhat broader perspective and some possibilities for future research and developmental work are proposed.

8.1. Conclusions

8.1.1. *Stabilizing influence of a parallel gas flow on a plane liquid sheet*

Paper 1 deals with the influence of a parallel air flow on a plane water sheet, with the air velocity at most of the same order of magnitude as the water velocity.

- The water sheet with a uniform inlet profile is convectively unstable in this regime, and responds to forcing in a consequent manner.
- Experimental spatial growth rates are measured in the region where the oscillation amplitude is small, and agree with results from local spatial stability, but only if viscosities of both phases are taken into account. The agreement is demonstrated both for the case of stagnant air, and two cases with confluent air.
- The numerical studies indicate that the growth rate is linearly proportional to the velocity difference between air and water. Also, the stabilizing influence of the air boundary layer scales as the square root of the shear at the air surface (inverse of the boundary layer thickness) in the computations.

8.1.2. *The global stability of confined wakes*

The influence of confinement on wake instability is investigated in Paper 2 and Paper 4.

- The confinement at $Re = 100$ is mainly stabilizing, both for the linear global modes and DNS.

- The stabilization is connected to the spatial development of the base flow.
- The stabilizing effect decreases with increasing Re , when the base flow becomes more parallel, and for $Re = 400$ the stability limit with respect to inlet shear is almost equal for confined and unconfined wakes.
- The stability limits for DNS and global modes are always equal, since the initial complex frequency extracted from DNS matches exactly the linear frequency.
- The saturated frequency from DNS, and its corresponding fundamental Fourier mode, are similar for some cases, but differ from the linear counterparts especially for high Reynolds numbers. Note that for co-flow wakes the inlet shear can be adjusted, and hence the high Reynolds number cases are also close to bifurcation.
- The confinement decreases the growth rate also in a local linear WNP analysis, thus resolving apparent contradictions in Paper 2 and previous works.
- The trends of the growth rate and frequency in the local analysis are evidently similar to the one of "true" linear global modes, as well as the extracted mode shape. However, the local analysis has a considerable and nearly constant offset. In particular, the local analysis overpredicts all growth rates, similarly to previous analyses of cylinder flows.

8.1.3. *Oscillatory sensitivity patterns for global modes in wakes*

For a weakly confined ($h = 9$) co-flow wake at higher Re , a region of high sensitivity is found downstream, with the center at $x \approx 20$. In Paper 5, this phenomenon is investigated in detail.

- For a wake at $h = 9$, and $Re \approx 400$, the wavemaker is split into two regions: one at the shear layer edge close to the inlet, and one further downstream. The second region does not appear for wakes at lower Reynolds numbers ($Re \approx 100$), and neither for confined wakes at $Re = 100 - 400$.
- Inside the downstream sensitivity region, it is found that small modifications in the base flow velocity profile cause either a decrease or increase of the growth rate and frequency, in a spatially periodic manner. The term "small" means that the sensitivity is

assumed to be linear with respect to the modification. The sensitivity to the base flow profile is computed using an adjoint-based approach.

- The prediction from the theory is tested by recomputing the direct eigenmodes with a small local modification in the base flow profile, in a range of streamwise positions. The oscillatory pattern is reproduced exactly for small enough base flow modifications.
- The sensitivity to a small control cylinder ($r = 0.02$) in different parts of the flow is computed by modeling the small cylinder as a volume force, similarly to previous works on sensitivity of wakes. One stabilizing region is identified inside the upstream wavemaker, and several small regions inside the downstream wavemaker.
- The theoretical prediction is tested by including a small control cylinder in the computation of direct eigenmodes. The cylinder can stabilize the flow when placed in the upstream region. Further downstream however, the force from the cylinder is too large for the linear prediction to be valid. Then instead, several unstable modes dependent on the control cylinder position are seen, similar to edge tones in shear layer experiments, or some of the global modes in a cavity.
- The flow is thus receptive for control in the upstream region, but the dynamics of the global mode is very sensitive to (both small and finite) perturbations in the downstream region. In this sense, the flow combines characteristics typical for absolute and convective instabilities.
- The downstream sensitivity could partly explain why broader spectral distributions are observed for unconfined than for confined cylinder wakes in previous works.

8.1.4. *Influence of surface tension on the global stability of wakes and jets*

In Paper 3 and Paper 6, surface tension is included in the interface between two fluids (with the same density) in global stability computations.

- Surface tension can destabilize stable jets and wakes, in the global setting.
- Intermediate amount of surface tension is globally destabilizing, while strong surface tension is globally stabilizing. The limits of the destabilizing regime depend on the flow case; wake or jet, and the value of the inlet shear ratio.

- The frequency of the global oscillation is decreased, when surface tension increases.
- Both symmetric and antisymmetric unstable modes are encountered, for both jets and wakes.
- For jets, the symmetric modes need less shear at the inlet to destabilize than antisymmetric modes. For wakes, the situation is the opposite.
- For jets, the modes with the maximal growth rate over all We are symmetric, and for wakes antisymmetric.
- The mode symmetry and structure at bifurcation (the lowest and/or highest We of the unstable regime, other parameters fixed) are different for different shear ratios.

8.2. Outlook

The wake and jet flows studied in this thesis are a family of flows showing a rich dynamical behaviour. In the light of the extensive literature on one-fluid and two-fluid shear flows, it seems reasonable that the complexity will increase if one considers different inlet profiles and inlet models, non-Newtonian fluids¹, varying viscosity and density ratios, and so on. Therefore, the thesis points out many possibilities for future studies. Nevertheless, the application window of the present results might very well carry over to related flows, as long as the results are interpreted with a good understanding of the physics. Each paper performs (more or less) a parameter study, so the conclusions are not based on one single flow setup. Also, we attempt to carefully locate the global stability limits, which is a valid application of the linear analysis, instead of characterizing the nonlinear flow regime. These related flows could be *e.g.* wakes behind a cylinder or mixing problems in the headbox jet of a papermachine.

The results on confined wakes are already validated by DNS, and relatively well understood in the current Reynolds number regime by the combination of local and global linear analysis. However, the wave-makers and sensitivities for unconfined wakes at $Re > 300$ are waiting to be studied by nonlinear simulations (and why not experiments?). If the sensitivities partially carry over to the nonlinear setup, this would have implications on experiments and/or DNS studies, depending on the cause. A deeper understanding of the underlying mechanism would therefore be desirable.

¹such as polymer flows, ink, fiber suspensions in a paper machine, to name a few.

The most immediate suggestion to future work is to validate and further quantify the considerable effects of surface tension on the global stability of wakes and jets, by experiments and nonlinear simulations. While many codes for one-phase flows can today be considered robust enough to produce results on their own, for two-fluid flows experimental validation is essential. On the other hand, in experiments it is hard to distinguish between local and global instabilities, but in a sufficiently noise-free DNS code the initial exponential growth is visible, as is shown in Paper 2. This process might involve a more accurate modeling of real experimental inlet geometries. Viscosity and density differences are already included in the global stability code, and their effect is a topic on its own. Sensitivity studies would help to further clarify the physical mechanisms. Once the current operational window of the code is carefully investigated and understood, studies of other flow cases and parameters can be undertaken. The applications for further studies could then range from ink jet printing to micro-mixing, from food to paper industry, from sprays to atomisation.

Scientists investigate that which already is; Engineers create that which has never been.

Albert Einstein (1859–1955)

CHAPTER 9

Papers and authors contributions

Paper 1

Stabilizing effect of surrounding gas flow on a plane liquid sheet

O. Tammisola (OT), A. Sasaki (AS), F. Lundell (FL), M. Matsubara (MM) & L. D. Söderberg (DS). *J. Fluid Mech.* **672**, 5–31.

This paper deals with the stabilizing effect of air co-flow around a plane water sheet in air. The sheet is excited with different frequencies by loudspeakers at the inlet. The growth rate in space is measured as a function of frequency, and this curve is compared to spatial stability computations, both in stagnant and confluent air. Then, the experimentally validated stability code is used to quantify the effect of air co-flow at moderate speeds.

The original idea of the experiment was by MM. The experiments were performed by AS under guidance of MM and input from OT and FL. The base flow computations were made by OT. The stability analysis was made by OT, using a code and method created by DS who assisted in the initial phase, and with input from FL. The writing was done by OT, with assistance from FL, and input from MM.

Paper 2

Global linear and nonlinear stability of viscous confined plane wakes with co-flow

O. Tammisola, F. Lundell, P. Schlatter (PS), A. Wehrfritz (AW) & L. D. Söderberg *J. Fluid Mech.* **675**, 397–434.

This paper deals with the effect of confinement and inlet shear ratio on the global two-dimensional stability of co-flow wakes at $Re = 100 - 400$. Both linear global modes and the final nonlinear oscillation are considered.

The base flow and linear global mode computations were performed by OT under guidance of FL, and input from PS and DS. The direct numerical simulations were performed by AW under supervision of PS and input from OT and FL. The writing was made by OT, with assistance from PS, and comments from FL.

Paper 3

Effect of surface tension on global modes of confined wake flows

O. Tammissola (OT), F. Lundell (FL) & L. D. Söderberg (DS). *Phys. Fluids* **23**, 014108.

This paper deals with the effect of surface tension on global modes in wakes. The influence on the growth rate, frequency and shape of the global mode is investigated.

The computations and writing were made by OT under supervision of FL. The manuscript was commented by DS.

Paper 4

Comparison of local and global stability properties of confined wake flows

M. P. Juniper (MJ), O. Tammissola (OT) & F. Lundell (FL). Submitted to *Journal of Fluid Mech.*

This paper deals with the comparison of true linear global modes and approximate linear global modes obtained from local weakly-non-parallel analysis, for confined wakes. Previous local computations by MJ and global computations by OT (Paper 2) gave opposite trends with respect to confinement. In this paper, the effect of confinement on spatially developing wakes at $Re = 100 - 400$ is scrutinized by both local and global methods, giving rise to several competing effects in the local setting.

The original idea for the paper was born in APS 2007 by all authors. The base flow and global mode computations were made by OT, and the local computations by MJ. The writing was made by MJ, with assistance from OT and FL.

Paper 5

Oscillatory sensitivity patterns for global modes in wakes

O. Tammissola. Submitted.

This paper deals with the structural sensitivity of very weakly confined wakes (surrounded by distant walls) at $Re \approx 400$ in a similar setup as Paper 2 and 4. Specifically, a region of high sensitivity of the "unconfined" wake located downstream is highlighted, not reported on previous works. It is shown that the downstream sensitivity pattern does not occur for confined wakes or unconfined wakes at low Reynolds number. Further, the implications on passive control are investigated.

The work has been performed by the author.

Paper 6

Surface tension induced global destabilisation of plane jets and wakes
O. Tammisola, F. Lundell & L. D. Söderberg. To be submitted.

This paper is a follow-up of Paper 3. Here, we show that globally stable co-flow jets and wakes become globally unstable in the presence of surface tension. We determine the neutral curves of global stability with respect to surface tension and inlet shear.

The computations were performed by OT. The writing was performed jointly by FL and OT, which input from DS.

Acknowledgements

The financial support from the project Ecotarget in the 6th EU Framework programme, and the Swedish Research Council through Linné FLOW Centre, is gratefully acknowledged.

First of all people, I would like to thank my present and previous supervisors: Fredrik Lundell, Daniel Söderberg and Henrik Alfredsson. Henrik accepted me as a PhD student, and was the main supervisor during the first two years. I also learnt a lot just by being around him in the Fluid Physics Lab. Daniel is my current main supervisor, and is acknowledged for a thorough introduction to the world of papermaking, as well as helping with many practical details. Last but not least, my assistant supervisor Fredrik who has followed my steps on a weekly and often even a daily basis. Thank you, Fredrik, for believing in me since I was a M.Sc. thesis student, for sharing your knowledge of different kinds of physics and engineering, your advice regarding both the project, practical matters and the future, and your always bright attitude.

I would like to thank the co-authors of papers in this thesis: Atsushi Sasaki and Masaharu Matsubara, Philipp Schlatter, Armin Wehrfritz and Matthew Juniper. The nice and smooth work with Atsushi and Matsu has also learnt me what it takes, especially from the experimental side, to obtain agreement between stability theory and experiments. I have enjoying taking part of the knowledge of Matthew about the local analysis, but also his devotion to create several methods to apply to the stability of combustion flows. I have also had the pleasure to do some work together with Gabriele Bellani, Kentaro Imagawa, Hiroshi Higuchi and Toshiyuki Hayase, on a flow problem that was not presented here.

There are several people at Mechanics who have made a scientific contribution to this work. The Paper group I have been a part of has extended my knowledge on multiphase flows and experimental methods. Philipp Schlatter is acknowledged not only for co-authorship, but also

for sharing his vast knowledge on numerical methods, and physics. The idea and way to parallelise my stability code FLUPACK was introduced by Philipp and Espen Åkervik. When I started as a PhD student, Espen was the first one to introduce me to global modes, and since then always nice and helpful. Milos Ilak is acknowledged for proofreading and commenting major parts of this thesis, as well as recent discussions on global stability. Johan Malm has advised me in Nekton-related issues. I am grateful to Dan Henningson who recently has let me participate to the meetings of his group; I have been able to keep track of the state-of-art in the stability community, as well as relevant conferences and computational clusters. The list of people who has discussed scientific matters with me during the years would be too long, but I would like to mention at least Luca Brandt, Jan Pralits, Shervin Bagheri, Lars-Uve Schrader and Vassilios Theofilis.

Also, I am very grateful to all people who have contributed to making a nice atmosphere around me here at Mechanics. I have enjoyed the lunches outside KTH and discussions about everything with Thomas, Allan, Mathias, Karl and Shintaro. Thank you, Ramis, for sharing your vast knowledge on both fluid mechanics, journals and practical things, and being a nice person. Timmy is acknowledged for helping me with practical matters, but also for being a friend. The same goes for Bengt. Lately, I enjoyed the regular coffee breaks and crazy discussions with Fredrik La, Johan F, Ylva, Markus, Malte, Emma, Niklas. Thanks also to everybody else in the lab, especially Veronica, Allan, Gabriele, Fredrik (Lu and He), Olle, Sissy, Shiho, Zohrab, Alexander, Shahab, Antonio, Ola, Henrik, Jens and Nils, and everybody in Osquars backe, especially Espen, Lars-Uve, Milos, Peter, Florian, David, Antonios, Qiang, Johan M., Shervin, Philipp, Luca, Lisa and Zeinab, and from NADA especially Oana. Also, I have greatly enjoyed the running passes with FK Studenterna which often helped me to survive the less easy periods at work, especially with Linda E, Linda J, Eva, Patrik, Sofia, Helena, Monika, Jennifer and Christin. To people in Finland: I like you, too, but the list would be too long.

Last but not least, I would like to express my deep gratitude to my family. Thank you my parents, Heljä and Jussi, and my sister Seila, for always supporting and accepting me as I am. Thanks also to my spouse Jan, only partly for his understanding and tireless work at home, without which this thesis wouldn't have happened.

Thank you Jesper and Janne, for being who you are.

References

- ÅKERVIK, E., EHRENSTEIN, U., GALLAIRE, F. & HENNINGSON, D. 2008 Global two-dimensional stability measures of the flat plate boundary-layer flow. *European Journal of Mechanics B/Fluids* **27**, 501–513.
- ALTIMIRA, M., RIVAS, A., RAMOS, J. C. & ANTON, R. 2010 Linear spatial instability of viscous flow of a liquid sheet through gas. *Physics of Fluids* **22**, 074103.
- ARNOLDI, W. E. 1951 The principle of minimized iterations in the solution of the matrix eigenvalue problem. *Quarterly of Applied Mathematics* **9**, 17–29.
- BAGHERI, S., SCHLATTER, P., SCHMID, P. J. & HENNINGSON, D. S. 2009 Global stability of a jet in cross-flow. *Journal of Fluid Mechanics* **624**, 33–44.
- BARKLEY, D., GOMES, M. G. M. & HENDERSON, R. D. 2002 Three-dimensional instability in flow over a backward-facing step. *Journal of Fluid Mechanics* **473**, 167–190.
- BARRERO, A. & LOSCERTALES, I. G. 2007 Micro- and Nanoparticles via Capillary Flows. *Annual Review of Fluid Mechanics* **39**, 89–106.
- BERKOOZ, G., HOLMES, P. & LUMLEY, J. L. 1993 The proper orthogonal decomposition in the analysis of turbulent flows. *Annual Review of Fluid Mechanics* **25**, 539–575.
- BOECK, T. & ZALESKI, S. 2005 Viscous versus inviscid instability of two-phase mixing layers with continuous velocity profile. *Physics of Fluids* **17**, 032106.
- BRIGGS, R. J. 1964 *Electron-Stream Interaction with Plasmas*. The MIT Press Classics.
- CAMARRI, S. & GIANNETTI, F. 2007 On the inversion of the von Karman street in the wake of a confined square cylinder. *Journal of Fluid Mechanics* **574**, 169–178.
- CHARALAMPOUS, G., HARDALUPAS, Y. & TAYLOR, A. M. K. P. 2010 Destabilization modes of confined coaxial liquid jets. In *Proceedings of the 7th International Conference on Multiphase Flow*.
- CHAUDHARY, K. C. & REDEKOPP, L. G. 1980 The nonlinear capillary instability of a liquid jet. Part 1. Theory. *Journal of Fluid Mechanics* **96**, 257–274.
- CHOMAZ, J.-M. 2005 Global Instabilities in Spatially Developing Flows: Non-Normality and Nonlinearity. *Annual Review of Fluid Mechanics* **37**, 357–392.
- CUBAUD, T. & MASON, T. G. 2006 Folding of Viscous Threads in Diverging Microchannels. *Physical Review Letters* **96**, 114501.

- DAVIS, R. W., MOORE, E. F. & PURTELL, L. P. 1984 A numerical-experimental study of confined flow around rectangular cylinders. *Physics of Fluids* **27**, 46–59.
- DE LUCA, L. 1999 Experimental investigation of the global instability of plane sheet flows. *Journal of Fluid Mechanics* **399**, 355–376.
- D’OLCE, M., MARTIN, J., RAKOTOMALALA, N., SALIN, D. & TALON, L. 2009 Convective/absolute instability in miscible core-annular flow. Part 1: Experiments. *Journal of Fluid Mechanics* **618**, 305–322.
- DRAZIN, P. G. & REID, W. H. 1981 *Hydrodynamic Stability*, 9th edn. Cambridge: Cambridge University Press.
- EGGERS, J. 2011 The subtle dynamics of liquid sheets. *Journal of Fluid Mechanics* **672**, 1–4.
- EHRENSTEIN, U. & GALLAIRE, F. 2005 On two-dimensional temporal global modes in spatially evolving open flows: the flat-plate boundary layer. *Journal of Fluid Mechanics* **536**, 209–218.
- GIANNETTI, F. & LUCHINI, P. 2007 Structural sensitivity of the first instability of the cylinder wake. *Journal of Fluid Mechanics* **581**, 167–197.
- GOVINDARAJAN, R. 2004 Effect of miscibility on the linear instability of two-fluid channel flow. *International Journal of Multiphase Flow* **30**, 1177–1192.
- GUILLOT, P., COLIN, A., UTADA, A. & AJDARI, A. 2007 Stability of a Jet in Confined Pressure-Driven Biphasic Flows at Low Reynolds Numbers. *Physical Review Letters* **99**, 104502.
- GUPTA, A. & KUMAR, R. 2010 Flow regime transition at high capillary numbers in a microfluidic T-junction: Viscosity contrast and geometry effect. *Physics of Fluids* **22**, 122001.
- HAGERTY, W. W. & SHEA, J. F. 1955 A study of the stability of plane fluid sheets. *Journal of Applied Mechanics* **22**, 509–514.
- HALLBERG, M. P. & STRYKOWSKI, P. J. 2006 On the universality of global modes in low-density axisymmetric jets. *Journal of Fluid Mechanics* **569**, 493–507.
- HAMMOND, D. A. & REDEKOPP, L. G. 1997 Global dynamics of symmetric and asymmetric wakes. *Journal of Fluid Mechanics* **331**, 231–260.
- HASHIMOTO, H. & SUZUKI, T. 1991 Experimental and theoretical study of fine interfacial waves on thin liquid sheet. *JSME International Series II* **34** (3), 277–283.
- HERRADA, M. A., FERRERA, C., MONTANERO, J. M. & GAÑÁN-CALVO, A. M. 2010 Absolute lateral instability in capillary coflowing jets. *Physics of Fluids* **22**, 064104.
- HILL, D. 1992 A theoretical approach for analyzing the restabilization of wakes. *AIAA Paper* pp. 92–0067.
- HOYAS, S. & JIMENEZ, J. 2006 Scaling of the velocity fluctuations in turbulent channels up to $re_\tau = 2003$. *Physics of Fluids* **18**, 011702.
- HUERRE, P. & MONKEWITZ, P. A. 1990 Local and global instabilities in spatially developing flows. *Annual Review of Fluid Mechanics* **22**, 473–537.
- HUSSAIN, A. K. M. F. & ZAMAN, Q. 1978 The free shear layer tone phenomenon and probe interference. *Journal of Fluid Mechanics* **87** (02), 349–383.
- ILAK, M., SCHLATTER, P., BAGHERI, S. & HENNINGSON, D. S. 2011 Bifurcation

- and stability analysis of a jet in crossflow. part 1: Onset of global instability at a low velocity ratio. *Submitted to Journal of Fluid Mechanics* .
- JOANICOT, M. & AJDARI, A. 2005 Droplet control for microfluidics. *Science* **309**, 887–888.
- JUNIPER, M. P. 2006 The effect of confinement on the stability of two-dimensional shear flows. *Journal of Fluid Mechanics* **565**, 171–195.
- LEIB, S. J. & GOLDSTEIN, M. E. 1986 The generation of capillary instabilities on a liquid jet. *Journal of Fluid Mechanics* **168**, 479–500.
- LESSHAFFT, L., HUERRE, P., SAGAUT, P. & TERRACOL, M. 2006 Nonlinear global modes in hot jets. *Journal of Fluid Mechanics* **554**, 393–409.
- LI, X. 1993 Spatial instability of plane liquid sheets. *Chemical Engineering Science* **48** (16), 2973–2981.
- LI, X. & TANKIN, R. S. 1991 On the temporal instability of a two-dimensional viscous liquid sheet. *Journal of Fluid Mechanics* **226**, 425–443.
- LIN, S. P., LIAN, Z. W. & CREIGHTON, B. J. 1990 Absolute and convective instability of a liquid sheet. *Journal of Fluid Mechanics* **220**, 673–689.
- LOZANO, A., BARRERAS, F., HAUKE, G. & DOPAZO, C. 2001 Longitudinal instabilities in an air-blasted liquid sheet. *Journal of Fluid Mechanics* **437**, 143–173.
- LUCHINI, P. 2004 Is a plane liquid curtain algebraically absolutely unstable? *Physics of Fluids* **16**, 2154–2157.
- LUNDELL, F., SÖDERBERG, L. D. & ALFREDSSON, P. H. 2011 Fluid mechanics of papermaking. *Annual Review of Fluid Mechanics* **43**, 195–217.
- MACK, C. J. & SCHMID, P. J. 2011 Global stability of swept flow around a parabolic body: features of the global spectrum. *Journal of Fluid Mechanics* .
- MALM, J., SCHLATTER, P. & HENNINGSON, D. S. 2011 Coherent structures and dominant frequencies in a turbulent three-dimensional diffuser flow. *To be submitted*.
- MANSOUR, A. & CHIGIER, N. 1991 Dynamic behavior of liquid sheets. *Physics of Fluids A* **3**, 2971–2980.
- MARQUET, O., LOMBARDI, M., CHOMAZ, J., SIPP, D. & JACQUIN, L. 2009 Direct and adjoint global modes of a recirculation bubble: lift-up and convective non-normalities. *Journal of Fluid Mechanics* **622**, 1–21.
- MARQUET, O., SIPP, D. & JACQUIN, L. 2008 Sensitivity analysis and passive control of cylinder flow. *Journal of Fluid Mechanics* **615**, 221–252.
- MEISTER, B. J. & SCHEELE, G. F. 1967 Generalized solution of the Tomotika stability analysis for a cylindrical jet. *AiChE Journal* **13**, 682.
- MEISTER, B. J. & SCHEELE, G. F. 1968 Drop formation at low velocities in liquid-liquid systems. *AiChE Journal* **14**, 9.
- MESTEL, A. J. 1994 Electrohydrodynamic stability of a slightly viscous jet. *Journal of Fluid Mechanics* **274**, 93–113.
- NICHOLS, J. W. & LELE, S. K. 2011 Global modes and transient response of a cold supersonic jet. *Journal of Fluid Mechanics* .
- NOACK, B. R. & ECKELMANN, H. 1994 A global stability analysis of the steady and periodic cylinder wake. *Journal of Fluid Mechanics* **270**, 297–330.

- NORMAN, B., ENGSTRÖM, G. & CO-AUTHORS 2005 *The Ljungberg Textbook - Paper Processes 2005*. Fibre and Polymer Technology, KTH.
- PARK, J., HUH, K. Y., LI, X. & RENKSIZBULUT, M. 2004 Experimental investigation on cellular breakup of a planar liquid sheet from an air-blast nozzle. *Physics of Fluids* **16** (3), 625–632.
- PIER, B. & HUERRE, P. 2001 Nonlinear self-sustained structures and fronts in spatially developing wake flows. *Journal of Fluid Mechanics* **435**, 145–174.
- PRALITS, J., BRANDT, L. & GIANNETTI, F. 2010 Instability and sensitivity of the flow around a rotating circular cylinder. *Journal of Fluid Mechanics* **650**, 513–536.
- PUJALS, G., GARCIA-VILLALBA, M., COSSU, C. & DEPARDON, S. 2009 A note on optimal transient growth in turbulent channel flows. *Physics of Fluids* **21**, 015109.
- RAYLEIGH, L. 1878 On the instability of jets. *Proceedings of the London Mathematical Society* **s1-10** (1), 4–13.
- RAYLEIGH, L. 1984 *The theory of sound*, 2nd edn. London: Macmillan.
- REES, S. J. & JUNIPER, M. P. 2009 The effect of surface tension on the stability of unconfined and confined planar jets and wakes. *Journal of Fluid Mechanics* **633**, 71–97.
- REES, S. J. & JUNIPER, M. P. 2010 The effect of confinement on the stability of viscous planar jets and wakes. *Journal of Fluid Mechanics* **656**, 309–336.
- RICHTER, A. & NAUDASCHER, E. 1976 Fluctuating forces on a rigid circular cylinder in confined flow. *Journal of Fluid Mechanics* **78**, 561–576.
- ROWLEY, C. W., COLONIUS, T. & BASU, A. J. 2002 On self-sustained oscillations in two-dimensional compressible flow over rectangular cavities. *Journal of Fluid Mechanics* **455**, 315–346.
- ROWLEY, C. W., MEZIC, I., BAGHERI, S., SCHLATTER, P. & HENNINGSON, D. S. 2009 Spectral analysis of nonlinear flows. *Journal of Fluid Mechanics* **641**, 115–127.
- SCHMID, P. J. & HENNINGSON, D. S. 2001 *Stability and Transition in Shear Flows*. New York: Springer Verlag.
- SCHUMM, M., BERGER, E. & MONKEWITZ, P. A. 1994 Self-excited oscillations in the wake of two-dimensional bluff bodies and their control. *Journal of Fluid Mechanics* **271**, 17–53.
- SELVAM, B., MERK, S., GOVINDARAJAN, R. & MEIBURG, E. 2007 Stability of miscible coreannular flows with viscosity stratification. *Journal of Fluid Mechanics* **592**, 23–49.
- SELVAM, B., TALON, L., LESSHAFFT, L. & MEIBURG, E. 2009 Convective/absolute instability in miscible core-annular flow. Part 2. Numerical simulations and nonlinear global modes. *Journal of Fluid Mechanics* **618**, 323–348.
- SHAW, T. L. 1971 Effect of side walls on flow past bluff bodies. *Journal of Hydraulics Division* **97**, 65–79.
- SIPP, D. & LEBEDEV, A. 2007 Global stability of base and mean flows: a general approach and its applications to cylinder and open cavity flows. *Journal of Fluid Mechanics* **593**, 333–358.

- SÖDERBERG, L. D. 2003 Absolute and convective instability of a relaxational plane liquid jet. *Journal of Fluid Mechanics* **493**, 89–119.
- SÖDERBERG, L. D. & ALFREDSSON, P. H. 1998 Experimental and theoretical stability investigations of plane liquid jets. *European Journal of Mechanics B/Fluids* **17** (5), 689–737.
- SORENSEN, D. C. 1996 Implicitly restarted Arnoldi/Lanczos methods for eigenvalue calculations. *Tech. Rep.*. University of Rice, tR-96-40.
- SQUIRE, H. B. 1953 Investigation of the instability of a moving liquid film. *British Journal of Applied Physics* **4**, 167–169.
- SREENIVASAN, K. R., RAGHU, S. & KYLE, D. 1989 Absolute instability in variable density round jets. *Experiments in Fluids* **7**, 309–317.
- STERLING, A. M. & SLEICHER, C. A. 1975 The instability of capillary jets. *Journal of Fluid Mechanics* **68**, 477–495.
- STRYKOWSKI, P. J. & SREENIVASAN, K. R. 1990 On the formation and suppression of vortex 'shedding' at low reynolds numbers. *Journal of Fluid Mechanics* **218**, 71–107.
- SUZUKI, H., INOUE, Y., NISHIMURA, T., FUKUTANI, K. & SUZUKI, K. 1994 Unsteady flow in a channel obstructed by a square rod (crisscross motion of vortex). *International Journal of Heat and Fluid Flow* **14**, 2–9.
- TAYLOR, G. I. 1962 Generation of ripples by wind blowing over viscous fluids. In *The scientific Papers of G. I. Taylos* (ed. G. K. Batchelor), chap. 3, pp. 244–254.
- THEOFILIS, V., HEIN, S. & DAHLMANN, U. 2000 On the origins of unsteadiness and three-dimensionality in a laminar separation bubble. *Philosophical Transactions of Royal Society of London* **358**, 3229–3246.
- TURNER, M. R., HEALEY, J. J., SAZHIN, S. S. & PIAZZESI, R. 2011 Stability analysis and breakup length calculations for steady planar liquid jets. *Journal of Fluid Mechanics* **668**, 384–411.
- UNAL, M. F. & ROCKWELL, D. 1987 On vortex formation from a cylinder. part 2. control by splitter-plate interference. *Journal of Fluid Mechanics* **190**, 513–529.
- UTADA, A. S., FERNANDEZ-NIEVES, A., GORDILLO, J. M. & WEITZ, D. A. 2008 Absolute instability of a liquid jet in a coflowing stream. *Physical Review Letters* **100**, 014502.
- VILLERMAUX, E. & HOPFINGER, E. J. 1994 Self-sustained oscillations of a confined jet: a case study for the non-linear delayed saturation model. *Physica D* **72**, 230–243.
- WEBER, C. 1931 Zum Zerfall eines Flüssigkeitsstrahles. *Zeitschrift für Angewandte Mathematik und Mechanik* **11**, 136–154.
- WEIDEMAN, J. A. C. & REDDY, S. C. 2000 A MATLAB Differentiation Matrix Suite. *Transactions on Mathematical Software* **26** (4), 465–519.
- WILLIAMSON, C. H. K. 1996 Vortex dynamics in the cylinder wake. *Annual Review of Fluid Mechanics* **28**, 477–539.
- WONG, H. Y. 1985 Wake Flow Stabilization by the Action of Base Bleed. *Journal of Fluids Engineering* **107**, 378–384.
- WOOD, C. J. 1967 Visualization of an incompressible wake with base bleed. *Journal of Fluid Mechanics* **29**, 259–272.

- YECKO, P., ZALESKI, S. & FULLANA, J.-M. 2002 Viscous modes in two-phase mixing layers. *Physics of Fluids* **14** (12), 4115–4123.
- YIH, C.-S. 1967 Instability due to viscosity stratification. *Journal of Fluid Mechanics* **27**, 337–352.
- YU, M.-H. & MONKEWITZ, P. A. 1990 The effect of nonuniform density on the absolute instability of two-dimensional inertial jets and wakes. *Physics of Fluids* **A2**, 1175–1181.
- YU, M.-H. & MONKEWITZ, P. A. 1993 Oscillations in the near field of a heated two-dimensional jet. *Journal of Fluid Mechanics* **255**, 323–347.
- YUEN, M.-C. 1968 Non-linear capillary instability of a liquid jet. *Journal of Fluid Mechanics* **33**, 151–163.

Part II

Papers

Paper 1

Stabilizing effect of surrounding gas flow on a plane liquid sheet

By **OUTI TAMMISOLA**¹,
ATSUSHI SASAKI²,
FREDRIK LUNDELL^{1,3}, **MASAHARU MATSUBARA**²
and **L. DANIEL SÖDERBERG**^{3,4}

¹ Linné Flow Centre, KTH Mechanics, Royal Institute of Technology, SE-100 44 Stockholm, Sweden

² Mechanical Systems Engineering, Shinshu University, Nagano, Japan

³ Wallenberg Wood Science Center, KTH Mechanics, Royal Institute of Technology, SE-100 44 Stockholm, Sweden

⁴ Innventia AB, BOX 5604, SE-114 86, Stockholm, Sweden

Published in *J. Fluid Mech.* **672**, 5–32, 2011

The stability of a plane liquid sheet is studied experimentally and theoretically, with an emphasis on the effect of the surrounding gas. Co-blowing with a gas velocity of the same order of magnitude as the liquid velocity is studied, in order to quantify its effect on the stability of the sheet. Experimental results are obtained for a water sheet in air at Reynolds number $Re_l = 3000$ and Weber number $We = 300$, based on the half thickness of the sheet at the inlet, water mean velocity at the inlet, the surface tension between water and air and water density and viscosity. The sheet is excited with different frequencies at the inlet and the growth of the waves in the streamwise direction is measured. The growth rate curves of the disturbances for all air flow velocities under study are found to be within 20% of the values obtained from a local spatial stability analysis, where water and air viscosity are taken into account, while previous results from literature assuming inviscid air overpredict the most unstable wavelength with a factor 3 and the growth rate with a factor 2. The effect of the air flow on the stability of the sheet is scrutinized numerically and it is concluded that the predicted disturbance growth scales with (1) the absolute velocity difference between water and air (inviscid effect) and (2) the square root of the shear from air on the water surface (viscous effect).

1. Introduction

Instability or break-up of a round or flat liquid jet entering into a gas or vacuum is important in a vast number of applications (Eggers &

Villermaux (2008) and references therein). In many cases, such as combustion, agriculture and chemical or process engineering, it is desirable that the jet breaks up and forms a spray. The reason is naturally that one wants to achieve mixing between the gas and the liquid or an efficient spreading of the liquid. We however aim at *stabilizing* a liquid jet. An application where stabilization is desirable is papermaking, where a plane jet of pulp suspension (a suspension of mainly water and cellulose fibres) is sprayed onto one or in between two permeable wires. As the water is drained, the fibres remain on the wire(s) and form the paper.

The stability of liquid jets surrounded by gas is a classical problem in fluid mechanics. The stability of round liquid jets was studied by Rayleigh (1878), who in an inviscid study concluded that all long enough round jets break down into droplets due to surface tension. The physical reason is that small waves result in an axial variation of the radius and therefore a capillary pressure gradient that makes the fluid to migrate even more to the thinner sections. Later on, Weber (1931) studied the effect of a velocity difference between liquid and gas and concluded that this should increase the instability. Plane jets, or liquid sheets, are different from round jets, since far from the rims, there is no surface force binding the upper and lower surfaces together; the equilibrium is reached when both surfaces are flat and parallel. Squire (1953) showed that liquid sheets do not possess the kind of instability caused by surface tension alone that Rayleigh (1878) found for round jets.

In order to explain instabilities of liquid sheets it is thus necessary to add more physics to the analysis. Hagerty & Shea (1955) introduced an inviscid stationary gas around the sheet and Li & Tankin (1991); Li (1993) added the viscosity of the liquid. Further on, Teng, Lin & Chen (1997) performed a linear stability analysis of a specific wall-bounded configuration including viscosity and velocity profiles of the surrounding air as well, and Söderberg & Alfredsson (1998) did the same for a free liquid sheet. The latter analysis is the basis for the theoretical part of the present work. Recently, Sander & Weigand (2008) performed a direct numerical simulation on the wave growth and break-up of a liquid jet and investigated the effects of the physical parameters, as well as initial velocity profile and turbulence intensity, on the break-up process. A very brief summary of the studies above is: (i) the instability of liquid sheets is driven by a velocity difference between liquid and gas, (ii) symmetric and antisymmetric modes can exist depending on the parameter regime, (iii) liquid viscosity has a stabilising effect in most cases, and (iv) the inlet profile has a remarkable effect on the instability.

In experiments, liquid sheets have mainly been studied through flow visualizations and measurements of integral quantities such as break-up length and spray angle. Söderberg & Alfredsson (1998) studied a liquid sheet forced by a loudspeaker, and the disturbances showed qualitative agreement with the linear stability theory. The particular case of a liquid sheet with a co-flowing gas, which is studied in the present work, has been investigated by Mansour & Chigier (1991); Lozano, Barreras, Hauke & Dopazo (2001); Park, Huh, Li & Renksizbulut (2004). In these studies, a strong blowing was applied in order to imitate the atomization process.

In the present work, a liquid sheet surrounded by gas, with and without co-flow, is generated experimentally and disturbed in a controlled manner. The growth of disturbances on the sheet is carefully quantified by measuring the variation in time of the local surface inclination. As a result, growth factors can be determined with good accuracy. The results are compared to theoretical predictions based on the method by Söderberg & Alfredsson (1998), which has been complemented to account for co-flowing air. The experimental setup and measurement techniques are presented in section 2 and the theoretical and numerical methods are explained in section 3. In section 4, the experimental results are presented and compared with the theoretical predictions. Additional observations based on the theory are made in section 5 and finally, the conclusions are summarized in section 6.

2. Experimental setup and methods

2.1. Liquid sheet facility

The experiments were performed in a liquid sheet facility at Shinshu University, Nagano, Japan. The facility consists of a nozzle unit (see figure 1) ejecting a water sheet vertically into a water basin. The coordinate system is defined in the figure, and is x^* , y^* , z^* for the streamwise, sheet-normal and spanwise directions, respectively, where stars denote dimensional quantities. The origin is located at the centre of the exit of the water nozzle. Further, the sheet half thickness is denoted by a^* , the velocity profile in the liquid by U_l^* and the velocity profile in the gas by U_g^* , while U_l^{0*} is the surface velocity of the liquid and $U_g^{\infty*}$ the free stream velocity of the gas.

The nozzle unit consists of three parts: one central nozzle for the water and two side nozzles for the co-flowing air. All of them have contractions near the outlet in order to generate as flat velocity profiles

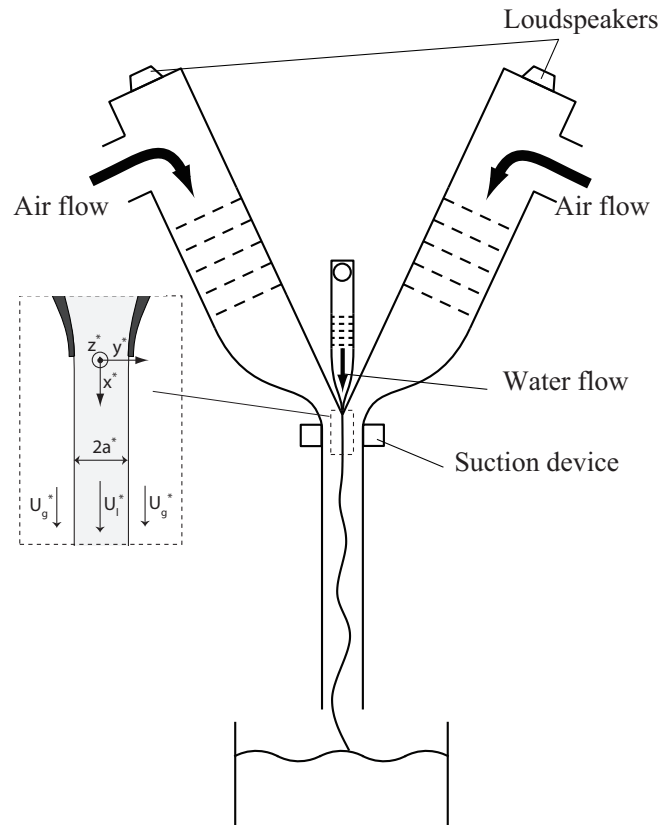


FIGURE 1. Schematic of the experimental setup: nozzles, sheet, basin and coordinate system.

as possible. The width of the exits in the z^* -direction is 400 mm and the thickness in the y^* -direction is 1 mm for the water nozzle and 50 mm for each air nozzle. Due to design constraints, the air streams have an angle of 25 degrees to the water sheet at the outlet, as indicated in figure 1.

The water is pumped in a closed loop by a centrifugal pump and the air is taken from the room and pressurized with a fan before entering the nozzles via dampers and flow regulators. The nominal velocities of air and water are the mean velocities over the cross-sections. The sheet

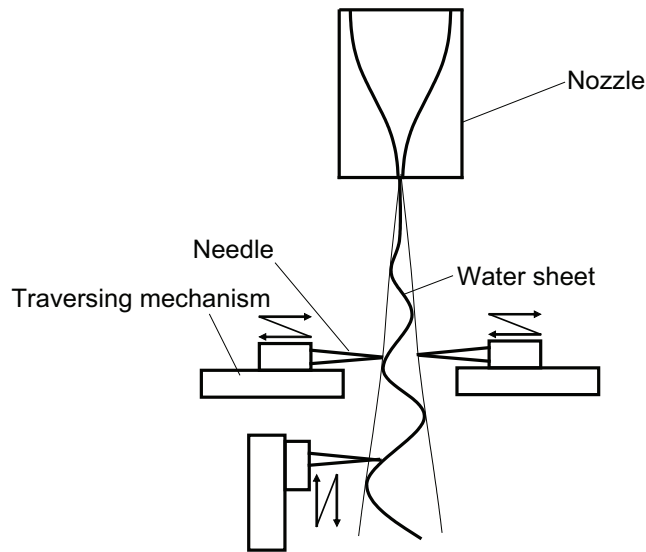


FIGURE 2. Measurement system for the thickness of the liquid sheet.

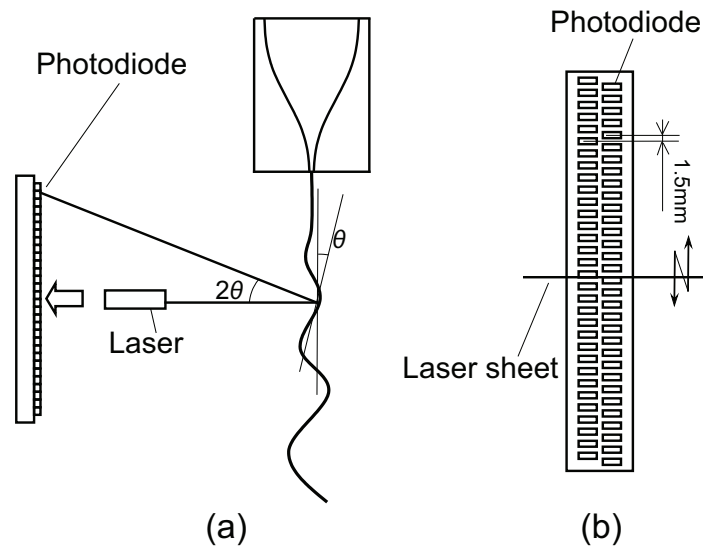


FIGURE 3. Measurement system for the local angle of the sheet surface: (a) liquid sheet and laser beam, (b) photodiode array.

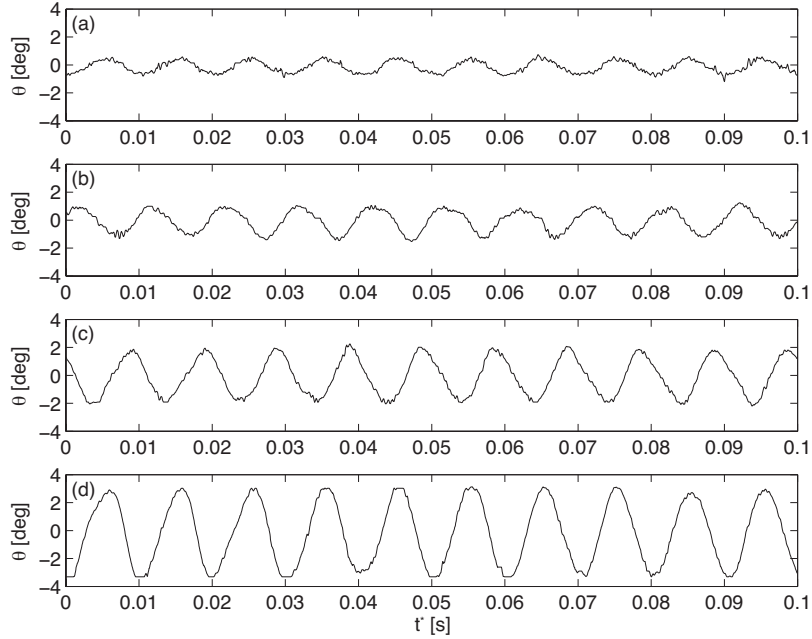


FIGURE 4. Time signals of the surface angle for a water sheet experiment. The initial disturbance frequency is 100 Hz. Measurement location: (a) $x^* = 250$ mm (non-dim. $x \approx 500$), (b) $x^* = 300$ mm (non-dim. $x \approx 600$), (c) $x^* = 350$ mm. (non-dim. $x \approx 700$), and (d) $x^* = 400$ mm. (non-dim. $x \approx 800$).

can be forced to oscillate at a given frequency by speakers mounted at the counter ends of the flow regulators.

Inclination of the air flow nozzles relative to the water sheet is a necessary design constraint, to get a sufficient contraction for the sheet prior to the nozzle. To avoid inclination of the air free stream velocity, suction is applied at the walls near the outlet. Further, the air flow is surrounded by walls of length 500 mm at a sheet-normal distance of 50 mm from the centreline, to create a constant and parallel air free stream velocity.

2.2. Experimental methods

The flow rates are monitored and adjusted by checking the pressure drops over the nozzles during all experiments. In order to verify the flow quality, velocity and thickness measurements are performed. The

velocity is measured by traversing a hot wire (air) and a total pressure tube (water) in the y^* -direction. These sensors allow the spatial variations of the mean flow to be quantified.

The thickness of the liquid sheet is measured by the system sketched in figure 2, by moving 10 pairs of sharp electrodes towards the surface of the liquid sheet from both sides with an accurate traversing mechanism. First, a reference position is determined by moving the electrodes towards a 1 mm thick gauge inserted between them until the circuit is closed. After turning on the water flow, the position of each side of the liquid sheet can be determined by moving the relevant electrode out from the liquid sheet and then traverse it towards the sheet again until it touches the surface and the circuit is closed again.

Finally, the amplitude of the sheet oscillations is measured. This is done with a laser and a photodiode array as shown in figure 3. A horizontal laser sheet is focused on the water surface by a cylindrical lens so that the measurement area is point-like. From there the light is again scattered in the spanwise direction, and the angle of reflection in the vertical direction is given by the local streamwise inclination angle of the water surface. The reflection from the measurement point thus forms a light sheet that is detected with the photodiode array. This in-house made optical system allows a continuous measurement of the inclination angle of the water surface θ , while waves pass by the measurement point.

By detecting θ over time we get time sequences as shown in figure 4. The phase velocity estimated from these example signals is 7.42 m/s, corresponding to the mean water speed 7.3 m/s. The feature that the phase velocity is almost equal to the sheet velocity is observed for a wide range of frequencies from 40 Hz to 200 Hz. The reason for the slight deviation between the phase velocity and the mean water speed ($< 2\%$) is probably that the determination of the mean water speed is somewhat less accurate than the measurement of the phase velocity.

From the time signals the local oscillation amplitude and phase can be evaluated. The growth rate is then obtained from the slope of the amplitude curve in a logarithmic diagram.

2.3. Flow characteristics

The flow quality in the apparatus is quantified in figures 5–7. The results on the liquid sheet are given without gas flow, whereas the gas flow results are taken without water — the reason for this is detailed below.

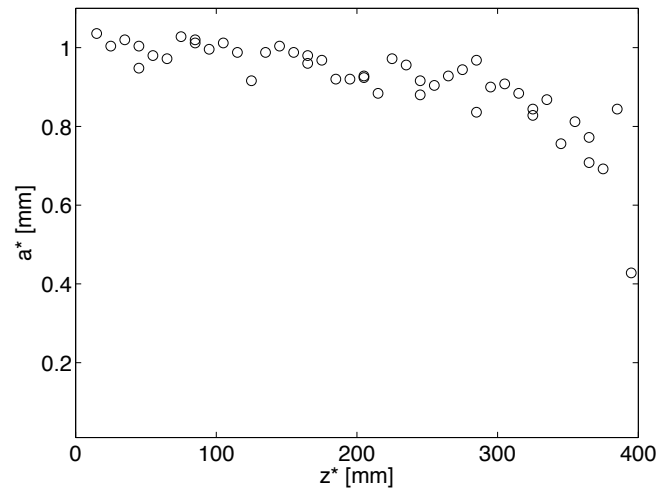


FIGURE 5. Thickness variation of the liquid sheet in the spanwise direction.

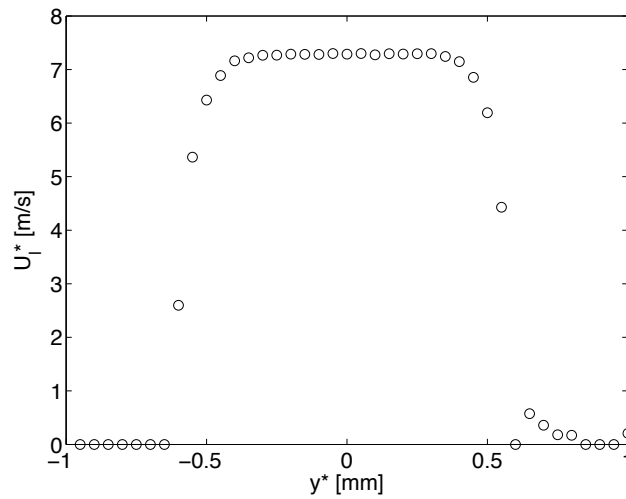


FIGURE 6. Streamwise velocity as a function of y^* right after the nozzle exit.

The thickness of the sheet as a function of the spanwise position is shown in figure 5. It varies from around $800 \mu\text{m}$ on one side to $1000 \mu\text{m}$ on the other. This variation, $\pm 10\%$, is indeed substantial.

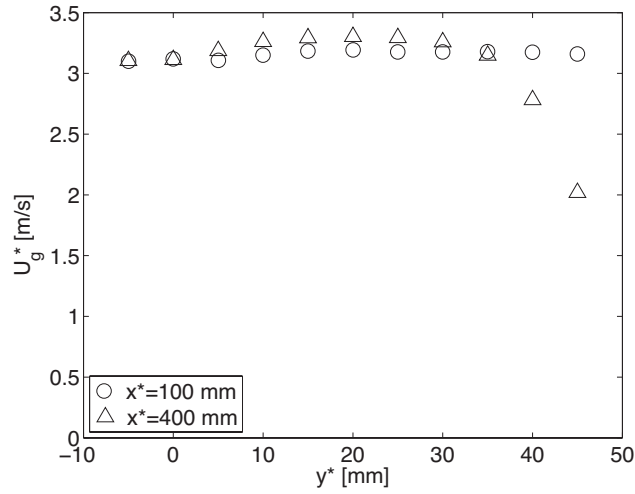


FIGURE 7. Distribution of the streamwise velocity in the air flow at two different distances from the nozzle.

Nevertheless, the flow visualizations to be shown in section 4.1 reveal that the disturbances on the sheet are very two-dimensional.

The contraction of the water nozzle prior to the outlet aims at creating a top-hat velocity profile and the water velocity data in figure 6 shows that it succeeds fairly well. The shear layers at the sides are thin and the plateau is flat. Here, it has to be mentioned that towards the rims at $y^* = \pm 0.5$ mm, small fluctuations of the position of the sheet give rise to a decrease in the mean velocity measured by the total pressure tube. This decrease occurs because the tube is intermittently exposed to air and water, respectively. Consequently, the velocity profile in figure 6 overestimates the actual shear layers of the liquid sheet. The gravitational acceleration for the sheet in the measurement region was seen to be of the order 1 %.

The velocity profile of the air as a function of y^* at two different streamwise positions is shown in figure 7. Since a hot wire is used, the measurements are taken without water flow. There are two main reasons for this. The first is that the wire might break if hit by drops, and the second is that the heat transfer from the wire to the air, which is used to determine the air velocity U_g^* , changes with the air humidity. Thus, in order to get accurate data of the air velocity, the sheet cannot be present.

Figure 7 shows that the air velocity is constant and fairly parallel to the sheet in the region $y^* = -5$ mm to $y^* = 5$ mm (remember the sheet thickness 1.1 mm). The deviation in the free stream velocity is of the order 3 % in this region. Further out from the sheet there is a difference of 0.1 m/s between the two streamwise stations.

The observed shear in the air free stream will be of secondary importance, since the deviation between water and air velocity will always be an order of magnitude larger in all cases that are studied in detail. Near the walls surrounding the air flow, located at $y^* = \pm 50$ mm, there is a clear boundary layer development and therefore a velocity decrease at $x^* = 400$ mm. However, this boundary layer is far enough from the sheet so that the free stream velocity near the sheet remains unaffected in the measurement region.

3. Theoretical and numerical methods

The velocities are non-dimensionalized with U_l^{0*} and the lengths with a^* , again all dimensional quantities marked with stars. In the following, we denote the non-dimensional liquid velocity profile by $U_l(y)$, the gas velocity profile by $U_g(y)$, and the free stream velocity of the gas (normalised by liquid velocity) by U_g^∞ . Recall from figure 1 that x is the streamwise, y the sheet-normal and z the spanwise direction.

In this way, the problem is characterised by the following four non-dimensional parameters:

Firstly, we have the overall Reynolds number

$$Re_l = \frac{U_l^{0*} a^*}{\nu_l^*} \quad (1)$$

and the Weber number

$$We = \frac{\rho_l^* (U_l^{0*})^2 a^*}{\gamma^*}, \quad (2)$$

where ν_l^* is the kinematic viscosity of the liquid, ρ_l^* its density and γ^* the surface tension between the liquid and the gas. We describes the ratio between inertia and capillary forces, and will enter the problem through the interface boundary conditions as will be explained in section 3.2. We also need the density ratio between the gas and the liquid,

$$\tilde{\rho} = \frac{\rho_g^*}{\rho_l^*} \quad (3)$$

and similarly, the viscosity ratio:

$$\tilde{\mu} = \frac{\mu_g^*}{\mu_l^*}. \quad (4)$$

In two-dimensional linear stability, all flow variables are divided into a steady base flow (capital letters) and a disturbance (small letters) as follows:

$$\begin{aligned} \mathbf{U}_{tot}(x, y, z, t) &= \mathbf{U}(x, y) + \mathbf{u}(x, y, z, t), \\ P_{tot}(x, y, z, t) &= P(x, y) + p(x, y, z, t). \end{aligned}$$

In the following subsections we will explain how both of them are obtained.

3.1. Determination of the base flow

The base flow in the liquid is assumed to be uniform, based on the experimental profiles — the deviation from uniform velocity was estimated to be less than 1 %, and the shape of the liquid velocity profile was hard to calculate numerically with that accuracy.

Since it was not possible to measure the air boundary layer in the presence of the liquid sheet, it has to be modelled. We present results for two alternative models in this paper, denoted as Sakiadis and Stokes boundary layers. The first one is formally a solution to the boundary layer equations, whereas the second one is not, but admits a convenient analytical solution.

3.1a. *Model I: Modified Sakiadis boundary layer.* This profile is obtained from the similarity solution for the boundary layer equations in a manner analogous to the Blasius boundary layer over a flat plate. We introduce a non-dimensional streamfunction f such that

$$f'(\eta) = U_g(y), \quad \eta = (y - 1)\sqrt{\frac{Re_g}{x}}, \quad (5)$$

where

$$Re_g = \frac{\tilde{\rho} Re_l}{\tilde{\mu}}. \quad (6)$$

The boundary layer equation and the boundary conditions ($U_g = 1$ on the sheet surface and $U = U_g^\infty$ far away from the sheet) then read:

$$f f'' + 2f''' = 0, \quad (7)$$

$$f'(1) = 1 \quad (8)$$

and

$$f'(\infty) = U_g^\infty. \quad (9)$$

This equation coupled with the boundary condition $U_g^\infty = 0$ was first studied by Sakiadis (1961a), and is therefore termed Sakiadis boundary layer in this paper.

3.1b. *Model II: Modified Stokes layer.* This model was used in Söderberg (2003) and is based on the Stokes first problem: the flow above an instantaneously started plate. The solution to this problem is analytical, and therefore especially easy to include also in problems with a varying liquid velocity profile in the streamwise direction, as in Söderberg (2003). In this case, the air velocity is obtained as:

$$U_g^* = U_l^{0*} + (U_g^{\infty*} - U_l^{0*})\text{erf}(\eta^*/2), \quad (10)$$

where erf is the error function, and:

$$\eta^* = (y^* - a^*)/\sqrt{\nu_g^* t^*},$$

where ν_g^* is the kinematic viscosity of the gas. To be able to use this solution, we must define t^* as a function of x^* in a way that gives a qualitatively correct growth of the gas boundary layer in the streamwise direction. The choice here is:

$$t^* = \frac{U_l^{0*}}{x^*}. \quad (11)$$

The resulting equation is in non-dimensional form:

$$U_g = 1 + (U_g^\infty - 1)\text{erf}(\eta/2), \quad (12)$$

where, as before,

$$\eta = (y - 1)\sqrt{\frac{Re_g}{x}}. \quad (13)$$

3.1c. *Parameterization of the base flow profiles.* As mentioned, the liquid base flow profile was assumed to be uniform. The experimental velocity profile of the water right after the nozzle exit is shown in figure 6. The boundary layers are thin enough that this profile should have relaxed to a uniform one at all measurement positions, located at least 300 jet thicknesses downstream from the nozzle.

The uniformity also means that the non-dimensional parameters Re_l and We for the liquid sheet are constant in the streamwise direction.

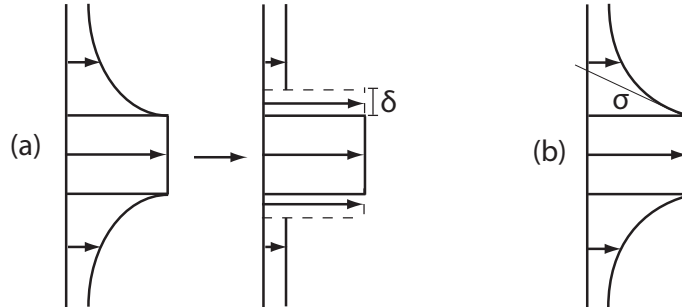


FIGURE 8. (a): Physical interpretation of the boundary layer thickness δ (equation 14). (b): Illustration of σ .

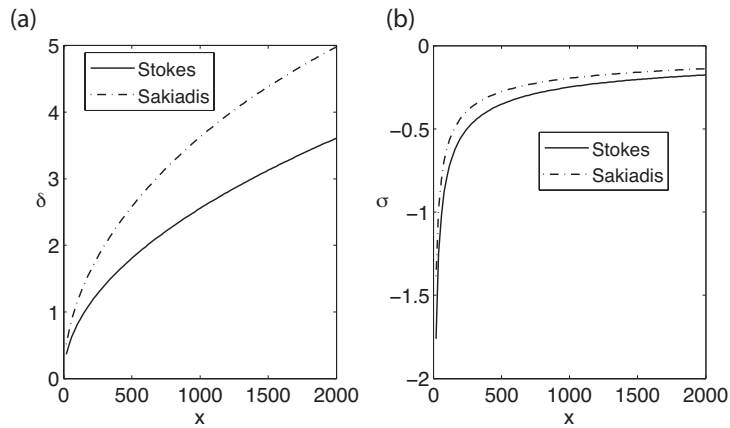


FIGURE 9. (a): The boundary layer thickness δ as a function of the streamwise distance x for the Stokes (—) and Sakiadis (- -) base flow models, $U_g^\infty = 0$. (b): σ , the shear from air at the surface, as a function of x , Stokes (—) and Sakiadis (- -), $U_g^\infty = 0$.

While Re is indeed constant due to mass conservation, the small gravitational acceleration of the sheet in the measurement region (section 2.3) results in an increase of We of the order 1%. This variation is of the same order as the uncertainty due to *e.g.* temperature fluctuations, and was therefore not considered.

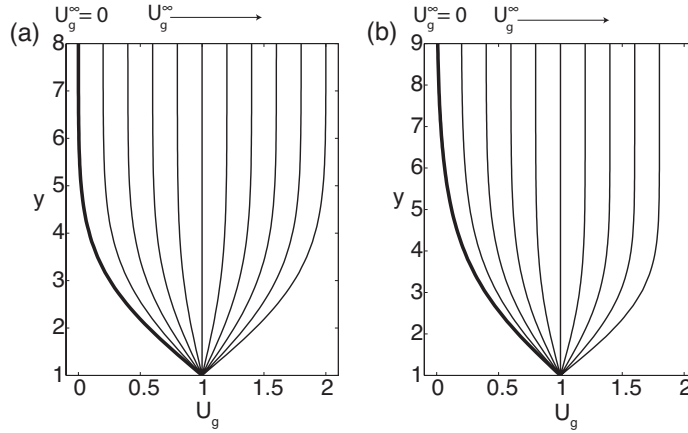


FIGURE 10. The base flow profiles with different amount of "blowing" for (a) Stokes model (b) Sakiadis model. The profile for $U_g^\infty = 0$ is drawn with a thick line, and thereafter $U_g^\infty = 0.2, 0.4, \dots, 2$. For the Stokes model in (a) the profiles are exactly symmetric with respect to the difference between the liquid and gas velocities, while for the Sakiadis model in (b) they are not.

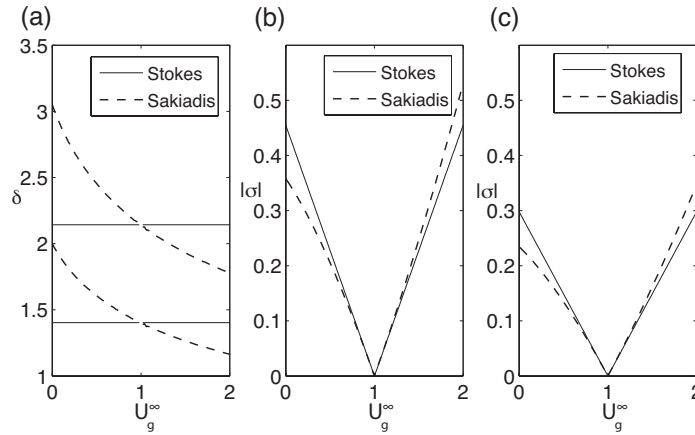


FIGURE 11. (a) The boundary layer thickness δ as a function of blowing velocity U_g^∞ for the Stokes (—) and Sakiadis (- -) base flow models for two different x -positions, $x = 300$ (lower) and $x = 700$ (upper). The absolute value of the shear from air at the surface as a function of U_g^∞ , Stokes (—) and Sakiadis (- -): (b) $x = 300$ and (c) $x = 700$.

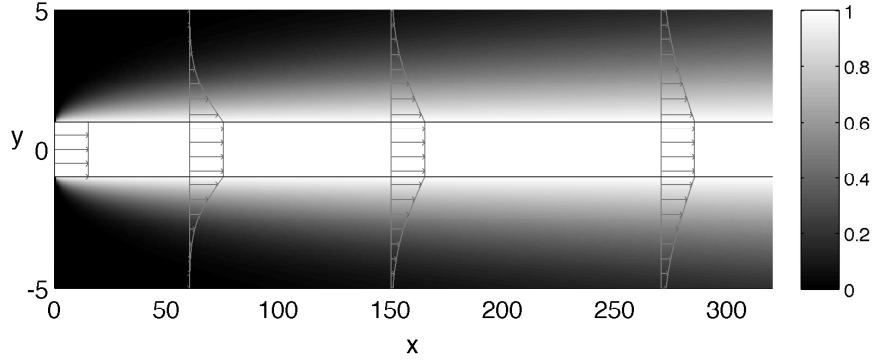


FIGURE 12. The streamwise velocity of the base flow with Stokes gas flow model in grayscale, values indicated by the colorbar. The velocity profiles at $x = 0$, $x = 60$, $x = 150$ and $x = 270$ are plotted with grey arrows on top of the picture. The boundary between the liquid and gas phases is marked by a dark solid line. The liquid velocity profile is uniform all way through, and the streamwise development of the gas boundary layer is seen.

The streamwise development of the whole flow can thus be characterised by one additional parameter, *e.g.* the boundary layer thickness δ that we define by:

$$\delta = \int_1^{\infty} \frac{(U_g(y) - U_g^{\infty})}{(1 - U_g^{\infty})} dy. \quad (14)$$

This δ is similar to the displacement thickness for a boundary layer around a solid body in the way that it gives the height by which the liquid sheet should be extended in the sheet-normal direction to get the same total volume flow, if both liquid and gas flows were considered inviscid. In a real inviscid calculation, it might be desirable to keep the total mass flow constant instead of volume flow, in which case the height of the extensional region is effected by the density ratio. However, we prefer to define the boundary layer thickness based on the gas properties.

The same definition of δ was also used by Sakiadis (1961*b*) in the stagnant air case, and termed displacement thickness in that paper. However, we would like to point out that it does not have a physical interpretation in terms of displacement of streamlines like for the Blasius

boundary layer, but rather represents a displacement of the free stream region.

Another alternative to characterise the flow that will be considered is the shear on the liquid surface, σ . Both parameters are illustrated in figure 8. The Sakiadis solution has a larger δ and a larger absolute value of σ than Stokes at the same streamwise position, as detailed in figure 9.

When the air velocity U_g^∞ is added as a parameter, the shape of the Stokes profile only depends on the absolute velocity difference between water and air, while the Sakiadis profiles are different for $U_g^\infty < 1$ and $U_g^\infty > 1$ (figure 10). This difference is also reflected in δ and σ (figure 11). The resulting full base flow field $U(x, y)$ for $U_g^\infty = 0$ and the Stokes model is shown with grayscale in figure 12.

3.2. Linear stability analysis

In the linear stability analysis, two separate sets of equations are solved — one for the liquid and one for the gas phase, with $Re = Re_l$ and $Re = Re_g$, respectively. Both of them share the same form, presented below. These equations are then coupled together by the interface conditions presented in section 3.2a.

The Navier–Stokes equations, linearized around a two-dimensional base flow

$(\mathbf{U}(x, y), P(x, y))$ and with pure base flow terms subtracted, become:

$$-\frac{\partial u}{\partial t} - U \frac{\partial u}{\partial x} - V \frac{\partial u}{\partial y} - u \frac{\partial U}{\partial x} - v \frac{\partial U}{\partial y} + \frac{\partial p}{\partial x} + \frac{1}{Re} \left(\frac{\partial^2 u}{\partial x^2} + \frac{\partial^2 u}{\partial y^2} + \frac{\partial^2 u}{\partial z^2} \right) = 0 \quad (15)$$

$$-\frac{\partial v}{\partial t} - U \frac{\partial v}{\partial x} - V \frac{\partial v}{\partial y} - u \frac{\partial V}{\partial x} - v \frac{\partial V}{\partial y} + \frac{\partial p}{\partial y} + \frac{1}{Re} \left(\frac{\partial^2 v}{\partial x^2} + \frac{\partial^2 v}{\partial y^2} + \frac{\partial^2 v}{\partial z^2} \right) = 0 \quad (16)$$

$$-\frac{\partial w}{\partial t} - U \frac{\partial w}{\partial x} - V \frac{\partial w}{\partial y} + \frac{\partial p}{\partial z} + \frac{1}{Re} \left(\frac{\partial^2 w}{\partial x^2} + \frac{\partial^2 w}{\partial y^2} + \frac{\partial^2 w}{\partial z^2} \right) = 0 \quad (17)$$

$$\frac{\partial u}{\partial x} + \frac{\partial v}{\partial y} + \frac{\partial w}{\partial z} = 0 \quad (18)$$

The stability analysis is based on the assumption that the base flow variations occur on a much longer length scale than the typical wavelength of the disturbances, *i.e.* *locally parallel flow*. The choice of a local method is supported by the fact that in the experiments the growth rate is changing very slowly in the streamwise direction. Both the sheet-normal velocity and all streamwise derivatives of the base flow are neglected, considering only base flow velocity profiles of type:

$$\mathbf{U} = (U(y), 0, 0)$$

This results in that all coefficients in front of the disturbance quantities in equations (15–18) are independent of both x and t . Thus, we can Fourier-transform in x and t , making the well-known local Ansatz:

$$\mathbf{u}(x, y, t) = (\hat{u}(y), \hat{v}(y))e^{i(\alpha x - \omega t)}, \quad (19)$$

and similarly for p , where α is the wavenumber in the streamwise direction. The spanwise wavenumber is set to zero, as well as the spanwise velocity component, which is justified by the two-dimensional nature of the disturbances in the present experiment.

This is further converted to the velocity–vorticity formulation, which gives the well-known Orr–Sommerfeld equation for the sheet-normal disturbance velocity v (for a derivation, see Schmid & Henningson (2001)) for gas and liquid:

$$(i\alpha U - i\omega)(D^2 - \alpha^2)\hat{v}_{l,g} - i\alpha D^2 U \hat{v}_{l,g} = Re_{l,g}^{-1}(D^4 - 2\alpha^2 D^2 + \alpha^4), \quad (20)$$

where $D = \frac{d}{dy}$ and $Re_{l,g}$ is the Reynolds number in liquid or gas (given by equations 1 and 6, respectively). The two sets of equations are coupled by the interface boundary conditions that will be presented in section 3.2a. We select the centreline of the sheet ($y = 0$) to be the lower boundary of the computational domain and set an antisymmetry condition there, and a no slip condition at the upper boundary located in the gas free stream. The upper boundary is chosen to be sufficiently far away from the sheet in order to make the results independent of this boundary condition.

The local spatial growth rates for the base flows represented in section 3.1 are calculated numerically with a Chebyshev-discretization in the sheet-normal direction. In spatial analysis, the frequency ω is assumed real while the spatial growth rate and wavenumber are sought.

This is similar to the experiments, where the sheet is forced at a given temporal frequency and the spatial growth rate is measured. With this approach, the equations constitute a generalized polynomial eigenvalue problem with the complex eigenvalue $\alpha = \alpha_r + i\alpha_i$, where the real part α_r gives the wavenumber of a disturbance, while the growth rate $-\alpha_i$ is given by the imaginary part. The disturbance shape corresponding to each eigenvalue comes from the complex eigenfunctions $\hat{v}_{l,g}$.

This fourth order polynomial generalized eigenvalue problem is converted to a first order one by a straightforward procedure suggested in Schmid & Henningson (2001). The problem can then be solved by standard methods for eigenvalue calculations. In this work, the EISPACK Fortran Package was used, since it had been used previously for this code (in Söderberg (2003), Söderberg & Alfredsson (1998)), and also because of good numerical stability properties compared to some other solvers for this particular problem. The solver is based on the QR-algorithm and therefore solves for all eigenvalues and eigenvectors simultaneously.

Finally, for each frequency ω , the eigenvalue with the largest spatial growth rate is extracted from the calculations, since we assume that only the most amplified wavenumber is observed in the experiments. This hypothesis is supported by the fact that in the experiments the phase speed for each excitation frequency is constant, indicating one single (and constant) wavelength. The growth rate of the most amplified wavelength is plotted as a function of the frequency, and compared with the experimental growth rates.

3.2a. *Boundary conditions on the interface* . To close the two sets of equations presented in the previous section, we need to couple the velocities and pressures in the different phases together. These coupling conditions are derived from the flow physics.

The boundary conditions for the total flow field at the interface between gas and liquid are, in dimensional form:

(1–2) all velocity components are continuous at the interface:

$$\mathbf{U}_{l,tot}^* = \mathbf{U}_{g,tot}^*, \quad (21)$$

(3) the tangential stresses are continuous at the interface:

$$\mathbf{n}_{tot}^* \times (\boldsymbol{\tau}_{l,tot}^* - \boldsymbol{\tau}_{g,tot}^*) \cdot \mathbf{n}_{tot}^* = 0, \quad (22)$$

and

(4) there is a surface tension induced jump in the normal stress:

$$\mathbf{n}_{tot}^* \cdot (\boldsymbol{\tau}_{l,tot}^* - \boldsymbol{\tau}_{g,tot}^*) \cdot \mathbf{n}_{tot}^* = -\gamma s_{tot}^*, \quad (23)$$

where γ is the surface tension coefficient, \mathbf{n}_{tot}^* the surface normal, $\tau_{p,tot}^*$ is the total stress tensor with pressure included, and s_{tot}^* is the total surface divergence operator defined as:

$$s_{tot}^* = (\nabla \cdot \mathbf{n}_{tot}^*). \quad (24)$$

Here, the direction of the surface normal \mathbf{n}_{tot}^* is given by the location of the interface H_{tot} , and thus we also need an equation for H_{tot} . This comes from the assumption that the sheet-normal displacement of the interface follows the sheet-normal displacement of a fluid particle on the interface:

$$\frac{\partial H_{tot}^*}{\partial t} + (\mathbf{U}_{tot}^* \cdot \nabla) H_{tot}^* = V_{tot}^*. \quad (25)$$

To non-dimensionalize the boundary conditions with liquid quantities, as before, we need We (2), $\tilde{\rho}$ (3) and $\tilde{\mu}$ (4).

Similarly to the other variables, we introduce a division of the interface position into a steady and oscillating part as: $H_{tot}^* = H^* + \hat{h}e^{i(\alpha x - \omega t)}$. After some algebra, the linearized non-dimensional boundary conditions become (for details, see Söderberg & Alfredsson (1998)):

(1–2) Velocity continuity on the free surface (comp. 21):

$$D\hat{v}_l - i\alpha\hat{h}(DU_l - DU_g) = D\hat{v}_g \quad (26)$$

$$\hat{v}_l = \hat{v}_g, \quad (27)$$

where equation (26) is the continuity of \hat{u} transformed to a condition for \hat{v} using (18),

(3) Continuity of the tangential stress (comp. 22):

$$(D^2 + \alpha^2)\hat{v}_l - i\alpha\hat{h}(D^2U_l - \tilde{\mu}D^2U_g) = \tilde{\mu}(D^2 + \alpha^2)\hat{v}_g \quad (28)$$

(4) Surface tension induced jump of the normal stress (comp. 23):

$$\begin{aligned} & [(i\alpha U_l - i\omega) - Re_l^{-1}(D^2 - 3\alpha^2)] D\hat{v}_l - i\alpha DU_l \hat{v}_l = \\ & [\tilde{\rho}(i\alpha U_g - i\omega) - \tilde{\mu}Re_l^{-1}(D^2 - 3\alpha^2)] D\hat{v}_g - i\alpha\tilde{\rho}DU_g \hat{v}_g - We^{-1}\alpha^4\hat{h}, \end{aligned} \quad (29)$$

and

(5) Interface equation of motion:

$$-i\omega\hat{h} + U\frac{\partial\hat{h}}{\partial x} = \hat{v}. \quad (30)$$

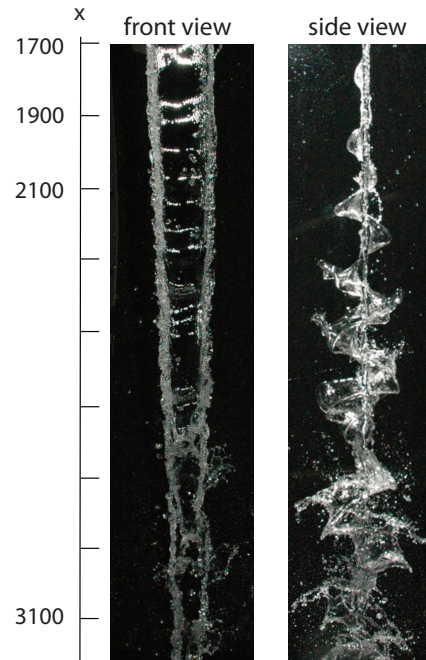


FIGURE 13. The natural oscillation of the water sheet in stagnant air ($x = 1700\text{--}3200$ measured from the nozzle exit), $Re_l \approx 3000$, $We \approx 350$.

4. Experimental results and comparison with theory

4.1. A plane liquid jet into stagnant air

The visualisations shown in this section were performed with a prototype jet facility with 150 mm width for the water sheet and no air flow nozzles. In figure 13 the sheet is shown in the xz (front) and xy (side) planes. The oscillations of the sheet are directly seen in the side view (right photo) and as variations of the reflected light in the front view (left). The front view shows that also under natural conditions without forcing, the disturbances developing on the sheet are distinctively two-dimensional and independent of z . This can be concluded from the horizontal nature

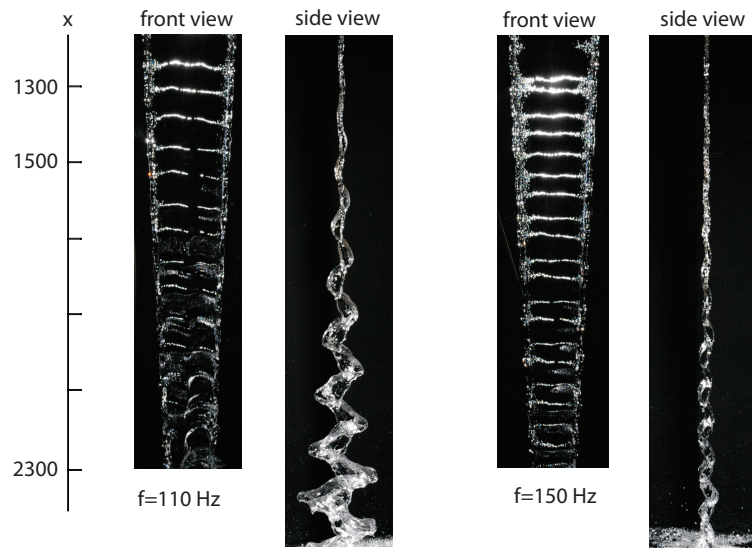


FIGURE 14. The forced water sheet oscillation for two different excitation frequencies: 110 Hz (left), 150 Hz (right).

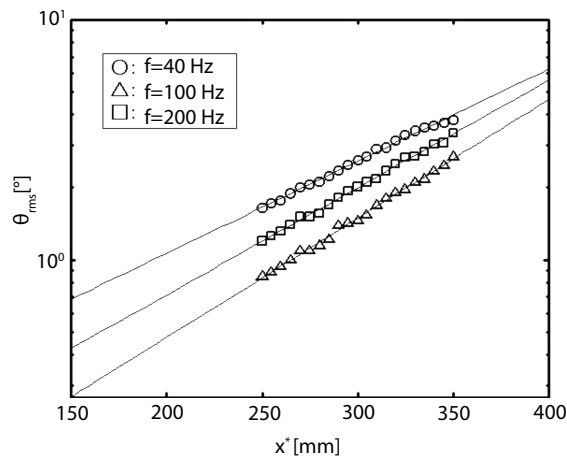


FIGURE 15. The amplitude of the disturbance in the region $x^* = 250\text{--}350$ mm (non-dim. $x \approx 500\text{--}700$).

of the reflections in the sheet. From the side view it is clear that the dominant oscillation is sinusoidal.

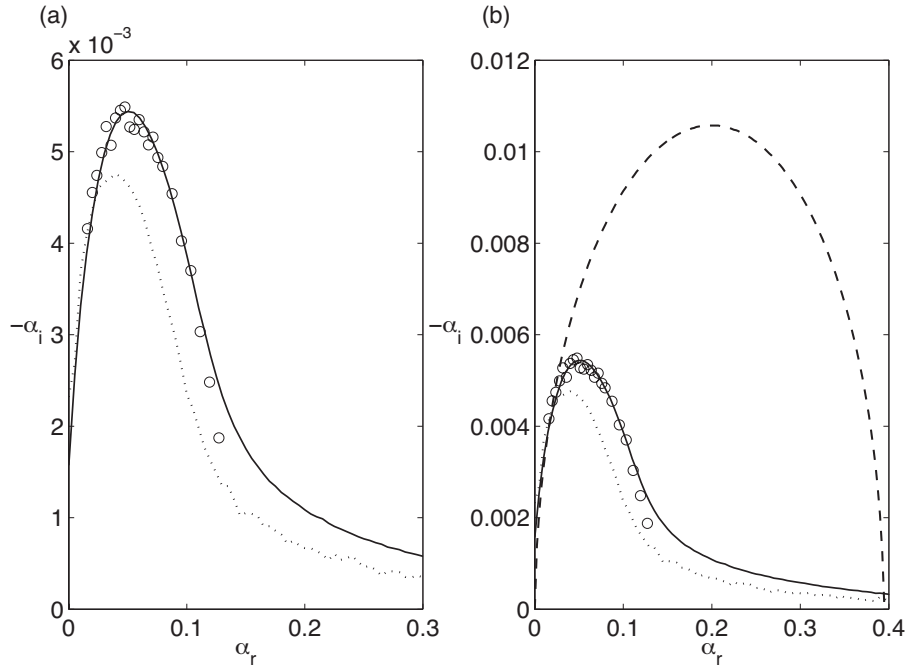


FIGURE 16. (a) The experimental (o) and theoretical spatial growth rates as functions of wavenumber in stagnant air ($Re_l = 2910$, $We = 350$): Stokes model (solid line) and Sakiadis model (dotted line). The computations are performed in the middle of the measurement interval, at $x = 600$, using the nozzle outlet as a virtual leading edge for both models. (b) All three growth rate curves compared to a solution where air is assumed inviscid (Li (1993), dashed line). The inviscid solution clearly overestimates the experimentally observed growth rates and wavelengths, whereas the viscous solutions are in good agreement.

If the flow instead is disturbed at a given frequency with the loudspeakers, the sheet picks up this frequency. This is illustrated in figure 14 where front and side views for frequencies $f^* = 110$ and 150 Hz are shown to the left and to the right, respectively. First it is noted that the irregular oscillations of figure 13 are replaced by oscillations with a well-defined wavelength. The reflections in the front views again show a distinct two-dimensionality of the disturbances and it is also seen that the wavelength is shorter for the higher frequency. Furthermore,

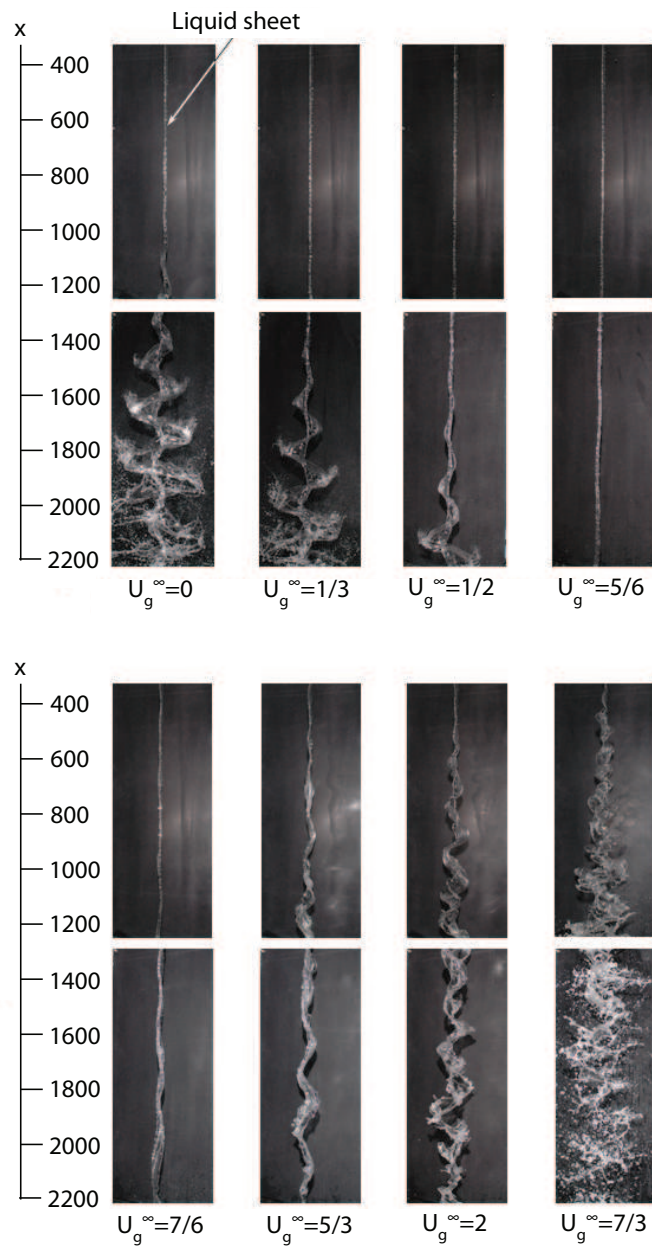


FIGURE 17. Visualisation of the liquid jet over a long distance without guiding walls for the air flow, for different gas blowing velocities.

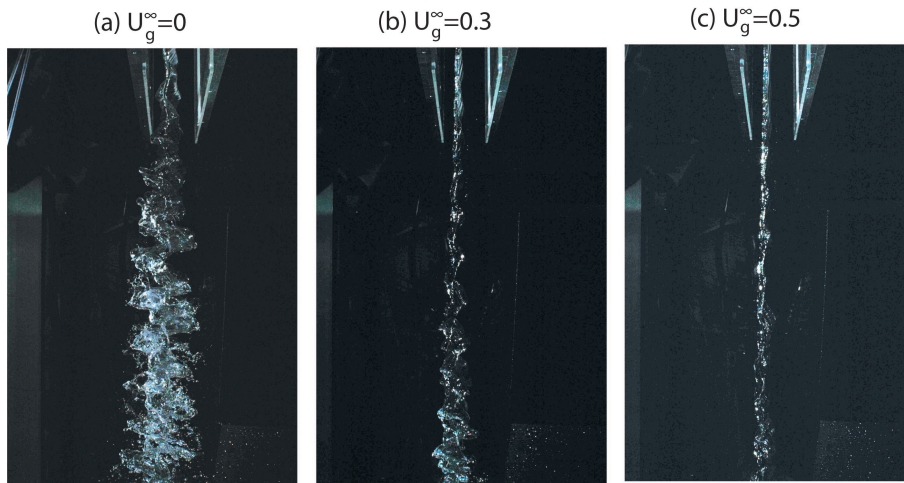


FIGURE 18. Visualisation of the break-up process, far from the inlet, with guiding walls guaranteeing uniform air flow, for different gas blowing velocities.

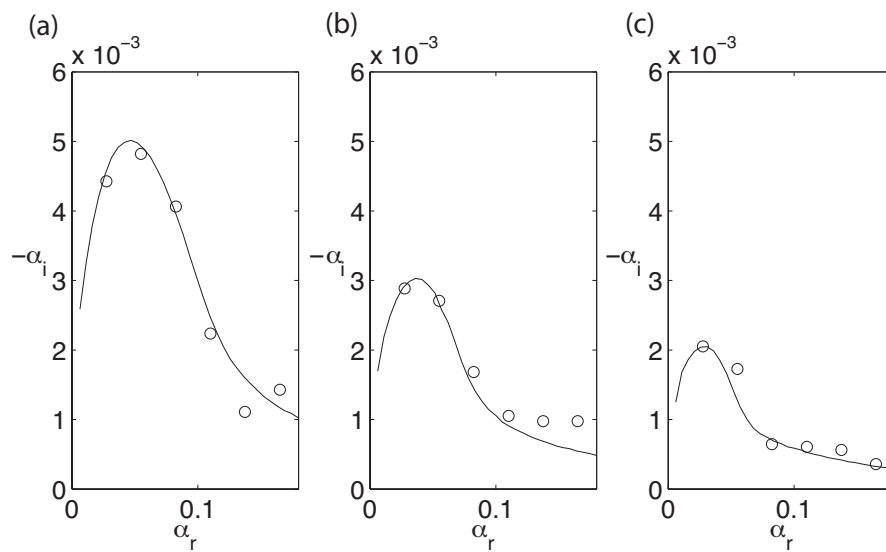


FIGURE 19. The experimental (\circ) and theoretical (-) spatial stability results ($Re_l = 3170$, $We = 312$, Stokes model), with different gas co-blowing velocities : (a) $U_g^\infty = 0$, (b) $U_g^\infty = 0.3$ and (c) $U_g^\infty = 0.5$.

the side-views show that the disturbances are sinusoidal and that the growth is considerably stronger for 110 Hz (left) than for 150 Hz (right).

The disturbance growth rate is quantified by looking at the root mean square of the surface angle (θ_{rms}) at different streamwise positions (cf. figure 4). An example of such curves for three different frequencies is shown in figure 15. The root mean square of θ is seen to grow exponentially and for each frequency, a growth factor can be readily determined as the slope of the respective line. The surface oscillation amplitude h has the same exponential growth rate. Note that the initial disturbance amplitude varies depending both on the exact level of forcing and receptivity, and only the growth rate is of interest in our analysis. It deserves to be mentioned that the fact that the sheet picks up the disturbance frequency and amplifies it with a distinct growth rate demonstrates that the disturbances are of a convective nature, and can be analysed by the local spatial approach used in this work. Furthermore, the angular phase of the measured wave in different streamwise positions showed that the phase speed of the disturbances is constant and equal to the water velocity, a feature that is confirmed by the linear stability analysis. Note that the growth rates for curves such as the ones in figure 15 were obtained further upstream (and thus at lower disturbance amplitudes) than the visualisations in figure 14. This was to ensure that the measurements were taken in the regime of linear growth, while it was difficult to obtain visualisations where the disturbance amplitude was very small.

Experimental growth rates are compared with theoretical ones for the Stokes and Sakiadis boundary layer models in figure 16(a). The spatial growth rate $-\alpha_i$ is shown as a function of the wavenumber α_r . At each real frequency ω , a spectrum of α is calculated and the one with largest growth (largest $-\alpha_i$) is plotted in the figure; the curve is obtained by performing the eigenvalue analysis for a sequence of ω . Since the experiments are measured over an interval in the spanwise direction while the theoretical analysis is local, a choice regarding the position at which to perform the analysis has to be made. Here, the centre of the interval used in measurements was chosen. For the experimental values, the spatial growth rate is obtained from lines similar to the ones in figure 15 and the wavenumber is given by the frequency and the velocity of the sheet (*i.e.* the phase speed as discussed above).

The comparison in stagnant air yields excellent agreement for the Stokes boundary layer model as seen in figure 16(a). The experimental data (circles) follows the theoretical curve (solid line) over the peak,

until it falls slightly below at $\alpha_r = 0.12$. Higher frequencies could not be measured at the same x -position due to the low amplitude. For the Sakiadis model (dotted line), the agreement is no more than satisfactory. In figure 16 (b) the results are drawn together with the analytic solution assuming inviscid air by Li (1993) (dashed line), obtained from the expression given in Appendix 6. The inviscid solution overestimates the growth rate and wavenumber of the peak by a factor of 2–3, while the viscous solutions reproduce the experimental behaviour.

The difference between Stokes and Sakiadis is distinct although not substantial and shows the relative importance of correct models for the boundary layer in the air in order to pinpoint the growth rate exactly. Even though the Sakiadis model includes more physics (specifically the development in the streamwise direction) than the somewhat ad-hoc Stokes model, the latter compares better with the experiments. This could be a result of the fact that there are aspects of the air flow, such as the inevitable re-circulation in the room, that neither the Stokes nor the Sakiadis model account for. However, it will be shown later that for the same characteristic parameters (boundary layer thickness or shear from air at the interface) both models produce nearly identical results, and therefore a correct choice of these for the measurement position under study should be more important than the choice of the model.

It should be noted that no parameters have been adjusted for the comparison; the physical constants are extracted from tables using the measured mean temperature for water and air, and the air boundary layer profiles computed by taking the middle of the measurement interval as the distance from the virtual leading edge for both models. Since the water profile has boundary layers at the nozzle exit, there is a reason to believe that the streamwise development of the air boundary layer is delayed. If the virtual leading edge is actually located downstream from the outlet, this would explain why the Sakiadis model somewhat underestimates the growth rates.

4.2. *A plane liquid jet with confluent air*

To visualise the effect of gas flow the whole way from the nozzle to breakup, some initial experiments were performed without the guiding walls and thus without suction for the air flow around the water sheet. Although the uniformity of the air flow profile was not as good as in the later experiments with walls, the pictures provide a good qualitative measure of how blowing air in parallel to the liquid sheet affects the stability.

The oscillating liquid sheet with different amounts of air co-flow is seen in figure 17. The non-dimensional gas velocity is varied between $U_g^\infty = 0$ and $U_g^\infty = 7/3$. It is clear that the air co-flow has a considerable effect on the stability. Going from the stagnant case $U_g^\infty = 0$ to $U_g^\infty = 5/6$ the oscillation is almost totally suppressed. When the gas velocity is increased above the liquid velocity, the sheet destabilises again. This is consistent with previous and present theoretical findings (see sections 1 and 5.2). The liquid sheet seems to be slightly more unstable and have a more irregular shape for overflow ($U_g^\infty > 1$), but this might be an effect of difficulties to control the air flow distribution in the overflow case. For the same reason, experimental growth rates will be presented only for $U_g^\infty < 1$.

The second visualisation concentrating on the breakup process (figure 18) is made in the current experimental setup. With the walls, it is not possible to observe the whole wave growth process. However, the breakup is seen to be delayed considerably, when air flow velocity is increased from 0 (stagnant air) to half of the liquid velocity.

The growth rates for six different forcing frequencies are seen in figure 19, for three values of the gas velocity: $U_g^\infty = 0, 0.3$ and 0.5 . While the shapes of the growth rate curves are similar, the liquid sheet becomes less unstable for all frequencies by the gas flow. The agreement in the stagnant case is good, but not as excellent as in the previous section, probably because the measurement region is longer ($x = 468$ – 755), and therefore the experimental growth rates are averaged over a longer streamwise interval.

When confluent air is considered, the computed solution also predicts the trends seen in the experiments. In the same figure, the computed growth rate curves from the Stokes' model are drawn with solid lines. The air flow is stabilising for all frequencies, and the peak growth rates are within 10% relative and 0.4×10^{-3} absolute accuracy. Sometimes the theory slightly overpredicts, sometimes under-predicts the experimental growth rates. One reason might be that it is difficult to obtain a homogeneous air flow when blowing, due to the inclination of the air flow nozzles, as indicated in the previous section (figure 7). Also small modelling errors, such as the uncertainty in temperature that affects the values of Re and We , and the shape of the velocity profiles for both water and air, contribute to the difference.

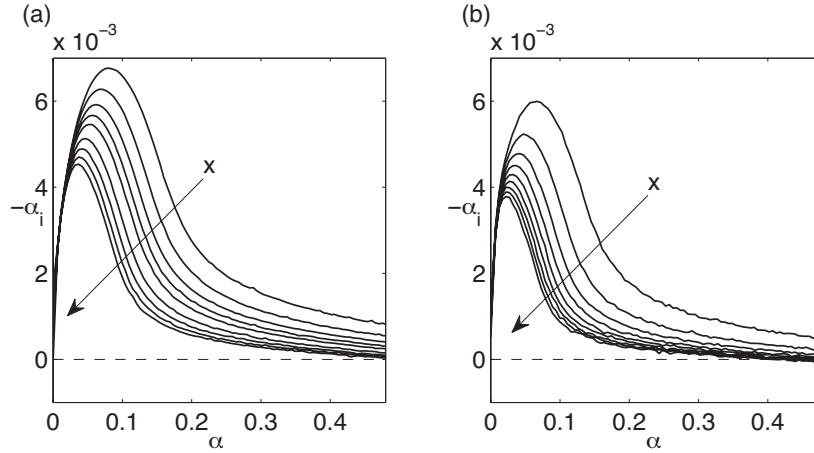


FIGURE 20. Growth rate curves at $Re = 3200$ and $We = 340$ from the (a) Stokes and (b) Sakiadis air flow model, $U_g^\infty = 0$, for different streamwise positions: $x = 200, 400, 600, \dots, 1800$. In both cases the peak moves towards longer wavelengths and the growth rate decreases downstream.

5. Theoretical consideration

Based on the inviscid studies, we expect the relative velocity between gas and liquid to be one important parameter, but we are also looking for viscous parameters that would quantify the difference from the inviscid result. The air boundary layer thickness δ represents the global scale of a viscous modification, and the shear at the liquid surface σ is a local scale near the surface.

5.1. Liquid jet in the stagnant air

In figure 20 eigenvalue curves in stagnant air ($U_g^\infty = 0$) are shown for different streamwise positions, for the Stokes (a) and Sakiadis (b) boundary layer models. The results for the two models share several common features. It is clearly seen that for both cases the growth rate of the most unstable mode and its wavenumber decrease when going downstream. This decrease is most pronounced for the upstream x -positions, while the curves for the downstream positions are near each other. The appearance of the whole eigenvalue curve is similar.

The most unstable wavenumber for each x -position (position of the peak) and its growth rate (height of the peak) differ by 5–10 % between the two models in the streamwise region under study, starting from

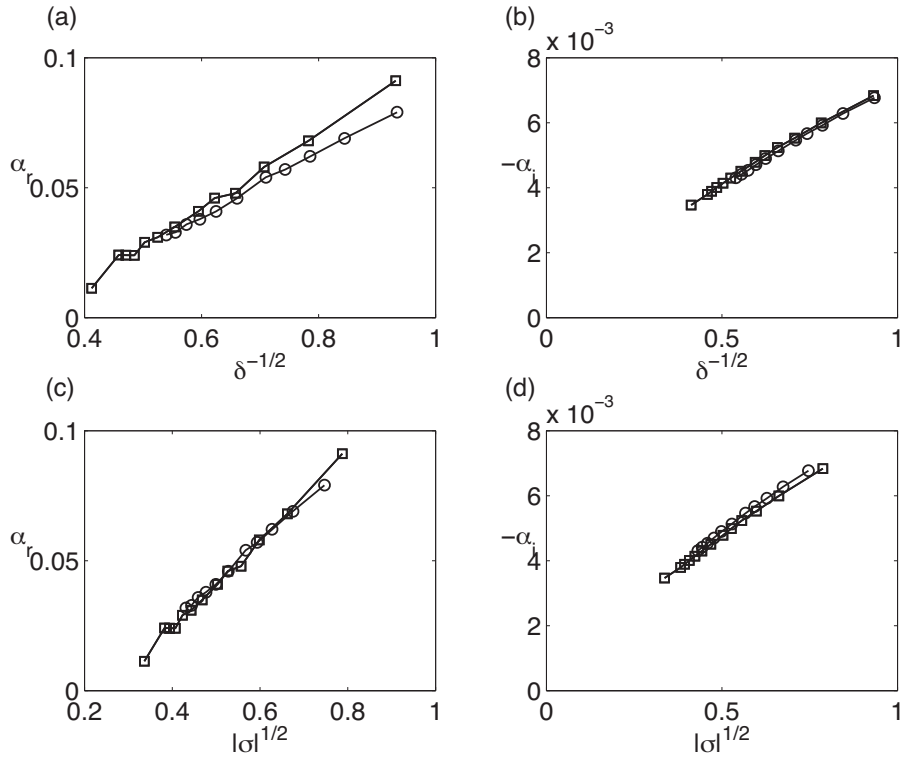


FIGURE 21. The peak eigenvalues for each x -position ($x = 200, 400, 600, \dots, 1800$) from figure 20 for Stokes (-o-) and Sakiadis (-□-) as functions of $\delta^{-1/2}$ and $|\sigma|^{1/2}$: (a) most unstable wavenumber α_r against inverse square root of boundary layer thickness $\delta^{-1/2}$ (b) growth rate $-\alpha_i$ against $\delta^{-1/2}$, (c) most unstable wavenumber against $|\sigma|^{1/2}$, (d) growth rate against $|\sigma|^{1/2}$.

$x = 200$, which corresponds to a distance 10 cm from the nozzle exit in the experiments. Remember that it was shown in figure 9 that the viscous parameters (δ and σ) at a given streamwise position have both slightly larger absolute value for the Sakiadis than for the Stokes model.

The stabilisation of the sheet with the viscous development of the base flow is expected already from an inviscid stability analysis, since the vorticity thickness of the air increases. Since the basic instability mechanism of the liquid sheet is the same as for the Kelvin–Helmholtz instability of a vortex sheet (Chandrasekhar 1961), the stabilisation can

be seen as an analogy to the classical piece-wise mixing layer: it is known that the stability curve of a piece-wise mixing layer deviates from the linear Kelvin–Helmholtz curve at a cut-off wavenumber inversely proportional to the vorticity thickness. However, this comparison should not be taken too far, since the liquid sheet problem involves more physics; even the appearance of the inviscid curve without taking the vorticity thickness into account is fundamentally different from the Kelvin–Helmholtz curve.

Indeed, the growth rate seems to be inversely proportional to the square root of δ , or directly proportional to the square root of σ . In figure 21 the growth and wavenumber for both cases are compared as functions of $|\sigma|^{1/2}$ and $\delta^{-1/2}$. In these scalings, the two models almost collapse. Especially, the growth rate displays a linear dependence on $|\sigma|^{1/2}$ in figure 21(d). In (a) and (c), the wave number also seems to have a linear dependence on the same quantities, although it is obvious from the figure that the slope cannot stay constant when $\delta \rightarrow \infty$.

5.2. Effect of gas flow on disturbance growth

The inviscid instability of a liquid sheet is known to be of aerodynamic nature. The co-flow of gas stabilises the sheet, if the relative speed between gas and liquid is decreased. In other words, an increasing gas free stream velocity U_g^∞ leads to a more stable sheet to the point when gas velocity is equal to liquid velocity ($U_g = 1$), in which case the sheet is stable. When the gas velocity is increased over the liquid velocity, the sheet destabilises again.

This feature is clearly seen in the eigenvalue curves from the Stokes and Sakiadis models in figure 22. For Stokes in (a, c) the difference between $U_g^\infty - 1 = 1$ and $U_g^\infty - 1 = -1$ is only 5 %, so the curves are nearly symmetric with respect to the velocity difference. For Sakiadis in (b, d) the same difference is 17 %. The reason can be understood by looking at the base flow profiles in figure 10 and the development of δ and σ for different U_g^∞ in figure 11. For Stokes the parameters are symmetric with respect to $(U_g^\infty - 1)$, but for Sakiadis asymmetric. Although measurements were not made for $U_g^\infty > 1$, the visualisations in figure 17 give some support to the Sakiadis result in this case, since the wave growth seems to be faster for the over-blowing case. However, it has to be kept in mind that this particular visualisation was made without the guiding vanes guaranteeing uniform air flow.

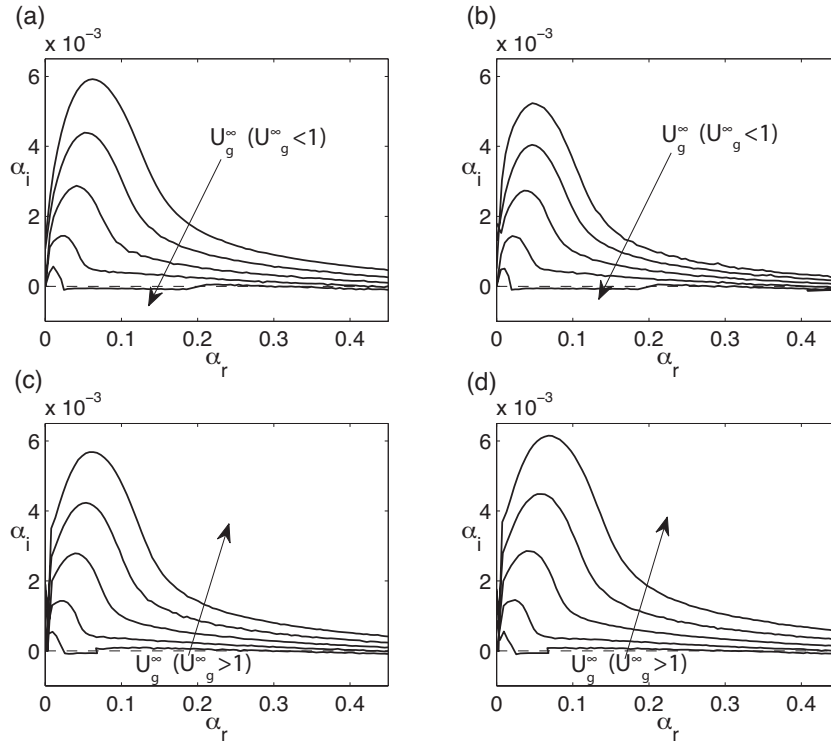


FIGURE 22. Growth rate curves (at $Re = 3200$, $We = 340$, $x = 200$) for different air velocities, (a): Stokes, $U_g^\infty = 0, 0.2, 0.4, 0.6, 0.8$ ($U_g^\infty < 1$), (b): Sakiadis, $U_g^\infty = 0, 0.2, 0.4, 0.6, 0.8$ ($U_g^\infty < 1$), (c) Stokes, $U_g^\infty = 1.2, 1.4, 1.6, 1.8, 2$ ($U_g^\infty > 1$), (d) Sakiadis, $U_g^\infty = 1.2, 1.4, 1.6, 1.8, 2$ ($U_g^\infty > 1$). Increasing air velocity is stabilising if $U_g^\infty \leq 1$, and destabilising otherwise.

The growth rate of the most unstable mode as a function of the relative velocity $U_g^\infty - 1$ is seen for both models in figure 23. Dependence on this parameter is expected from the inviscid analysis, as for Kelvin–Helmholtz-type instability. In the inviscid analysis the dependence on the growth rate of $U_g^\infty - 1$ can be shown to be quadratic — the growth rate curve based on uniform velocity in water and air is shown with dotted curve in the same figure, and derived in Appendix 6. In our study, the growth rate scales linearly for $|U_g^\infty - 1| \geq 0.4$ and the best fit is shown as a line in the figure together with the data points. A similar

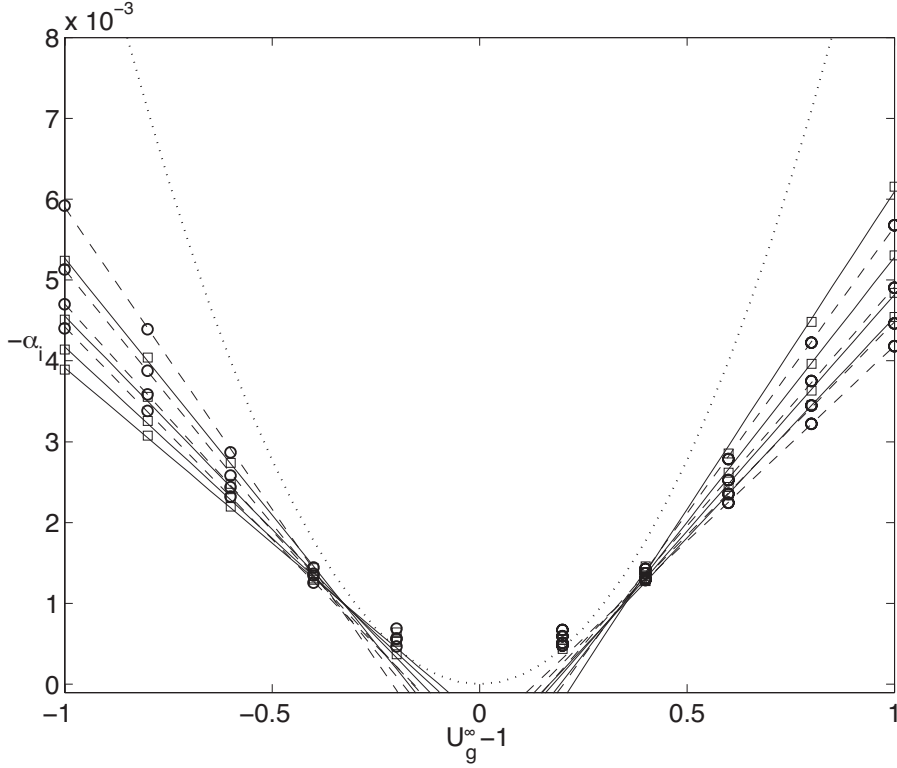


FIGURE 23. The largest growth rate at $Re = 3200$, $We = 340$ as a function of the velocity difference $U_g^\infty - 1$ at different x -positions ($x = 0.2, 0.4, 0.6, 0.8$) for Sakiadis (—□—) and Stokes (- -o-) model. The markers represent calculated values, while lines are linear fits for $|U_g^\infty| > 0.4$. A temporal solution assuming inviscid air and water is given by the dotted curve.

deviation from the inviscid analysis was noticed in the viscous analysis of Lozano *et al.* (2001), who looked at the frequency for the most unstable mode as a function of air velocity — the frequency increased linearly, instead of a quadratic dependence predicted by the inviscid analysis.

The slopes of the lines for Sakiadis model (solid) are different for negative ($U_g^\infty < 1$) and positive velocity differences, with $U_g^\infty > 1$ being slightly more unstable. For Stokes model (dashed) the same linear dependency is seen, but the slopes are symmetric with respect to the velocity difference. For all cases, the lines in figures 23 intersect at a point in the region $|U_g^\infty| = 0.3\text{--}0.4$. The data points at $|U_g^\infty - 1| = \pm 0.2$

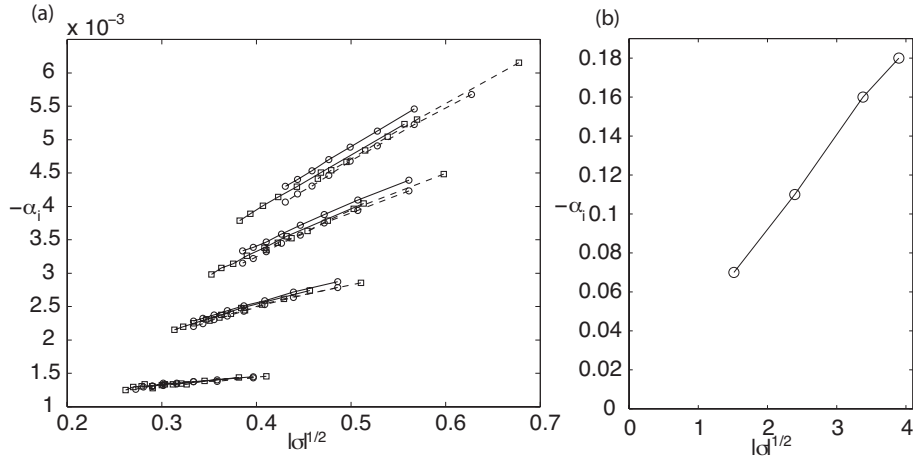


FIGURE 24. (a) The growth rate of the peak eigenvalues for different x -positions ($x = 400, 800, 1000, 1200, 1400, 1600, 1800$) for Stokes and Sakiadis as functions of $|\sigma|^{1/2}$, from up and down: ($-\square-$) Sakiadis $U_g^\infty = 0, 0.2, 0.4, 0.6$, ($-\circ-$) Stokes $U_g^\infty = 0, 0.2, 0.4, 0.6$, ($- \square -$) Sakiadis $U_g^\infty = 2, 1.8, 1.6, 1.4$, and ($- \circ -$) Stokes $U_g^\infty = 2, 1.8, 1.6, 1.4$. (b) The same scaling extracted from the data in Lozano *et al.* (2001) for $U_g^\infty = 12.5$, $Re_l = 340$, and a different base flow model.

that were not used for the linear fit are all above their respective lines. The intersection of the lines and deviation from the linear fit for low velocity differences is an interesting feature. It is natural to believe that for these very long waves, the viscous and inviscid solution approach each other, *i.e.* the Kelvin-Helmholtz instability mechanism gradually weakens and is overtaken by neutrally stable capillary waves. We also note that there is more scattering in the eigenvalues for $|U_g^\infty - 1| = 0.2$ than at larger velocity differences.

Furthermore, the slopes of the lines in figure 23 decrease with the streamwise position. However, the linear relation persists. This is only possible if the dependence of the growth rate on the x -position is of the same form for different blowing velocities. Figure 24 confirms that there is a nearly linear scaling with $|\sigma|^{1/2}$ for blowing velocities that differ from the liquid velocity by a factor larger than or equal to 0.4, as in the stagnant air case. Again, if the profiles with the same characteristic parameters are considered, the difference between Sakiadis and Stokes is

very small. Moreover, when the data is drawn as a function of $\sigma^{1/2}$ like in this figure, especially for the Sakiadis case, points with the same absolute velocity difference ($|U_g^\infty - 1|$) for both underflow and overflow line up on the same line. This was not as obvious if $\delta^{-1/2}$ was considered. Therefore we consider $\sigma^{1/2}$ to be the most attractive parameter to quantify the viscous scaling.

Remarkably, we could find the same viscous scaling from the literature, by extracting the maxima from the temporal growth rate curves drawn as a function of air boundary layer thickness in figure 7 of Lozano *et al.* (2001). Their base flow model and parameter region are completely different: Their non-dimensional gas velocity (in our coordinates) is $U_g^\infty = 12.5$, and water Reynolds number $Re_l = 340$. The scaling is shown in figure 24 b. The derivation of σ for the model of Lozano *et al.* (2001) is given in Appendix 6.

When it comes to the wave numbers for different U_g^∞ , we could not find universal scaling laws. One reason might be that the plateau in the growth rate curves is rather flat, making the uncertainty in the wavenumber bigger than that in the growth rate. Though, for $U_g^\infty > 1$ both models seem to approach a linear dependency between shear and wavenumber, the latter exchangeable to frequency in our case, in consistence with the experimental and numerical results of Lozano *et al.* (2001) for high blowing velocities.

6. Conclusions

The disturbance growth for plane liquid sheets with air co-flow has been analyzed experimentally and theoretically. Unlike many other studies, that have a rapid breakup as a goal, our aim is to quantify the stabilising effect of an air flow with a similar speed as the liquid flow.

Experiments have been conducted for a water sheet ($Re_l \approx 3000$, $We \approx 300$), both in stagnant air and with different amounts of co-flow. The liquid sheet was excited with different frequencies by acoustic forcing at the nozzle exit. The time-varying inclination of the water surface was measured at different streamwise positions. With this method, we could extract the spatial growth rate along with the frequency of the waves.

A linear spatial stability analysis has been made using two different air flow models — the theoretically correct Sakiadis model obtained by solving the boundary layer similarity equations, and an analytical

Stokes model based on Stokes' solution of the flow above an instantaneously started plate, where the time dependency was changed to an x -dependency. The liquid velocity was assumed to be uniform.

It was shown that the dependence of the growth rate on the inviscid stability parameter — relative velocity between air and water — is retained for viscous gas, even if the viscous growth rates can be smaller by several orders of magnitude. The dependence of this parameter is approximately linear, instead of a quadratic dependence predicted by a fully inviscid analysis. The two boundary layer models were shown to produce very similar results, which justifies the use of Stokes model in other (Söderberg 2003; Söderberg & Alfredsson 1998) and future studies. The viscous effect was investigated in terms of two parameters — δ , the boundary layer thickness for the air flow quantifying the scale of the total viscous modification, and σ , the shear from air at the interface representing the viscous effect near the surface. As a function of these parameters both models nearly collapse, and show a linear dependence between the growth rate and the square root of $|\sigma|$ starting some distance downstream from the nozzle exit.

The Stokes model was compared with experiments. The results are in very good agreement for the stagnant air case, while the previous inviscid solution of Li (1993) overestimates the most unstable wavenumber and its growth rate by more than a factor of 2. For the case of air co-flow, the trends are the same, and the quantitative agreement between experiments and theory is also very good, but not perfect. We believe this is due to experimental uncertainties concerning both the exact shape and magnitude of the air flow and the non-dimensional numbers involved.

In the theoretical studies, the Stokes model gives an almost symmetric growth rate curve with respect to velocity difference, irrespectively if underflow ($U_g^\infty < 1$) or overflow ($U_g^\infty > 1$) is applied. For the more physical Sakiadis model, the slope is changed if overflow is applied. At this point, experimental growth rates have not been obtained for $U_g^\infty > 1$ and the experimental confirmation of this has to be left for a future study. A linear dependence between the growth rate and $U_g^\infty - 1$ is obtained for both cases for $|U_g^\infty - 1| > 0.4$. As functions of σ or δ , the models collapse. This means that for the same σ , the influence of velocity difference is symmetric. So this leaves us with two parameters: absolute value of the velocity difference $|U_g^\infty - 1|$ (inviscid) and shear from air at the surface σ (viscous).

Since the viscous parameter σ also changes with gas velocity, it would be tempting to try to characterise the stability in terms of this parameter only. Our results show that for different values $U_g^\infty - 1$ the same shear at the surface leads to different growth rates, underlining the importance of the inviscid parameter. However, when $U_g^\infty - 1$ is kept constant, the same linear dependence on $|\sigma|^{1/2}$ is obtained for the two different boundary layer models, and also extracted from a previous result found in literature with a strong overflow in air.

In future work, it would be interesting to test the validity of these scalings experimentally. In order to do this, it is crucial to accurately measure the air (and water) boundary layer profile at different stream-wise positions. Also, it could be interesting to repeat the theoretical analysis using inviscid stability in air but taking into account the vorticity thickness of the air boundary layer. The aim would be to determine if the viscous stabilisation can be explained by the base flow modification alone. Alternatively, a complete viscous stability analysis (as presented here) is necessary.

The authors gratefully thank Mr. Masamichi Tosaki, Mr. Yuta Wakabayashi and Mr. Akihiko Mori for their support in arranging the water jet facility and the experiments.

Appendix A: Spatial stability of a viscous liquid sheet in an inviscid stagnant gas

A previous solution assuming viscous liquid and inviscid gas is compared with our experiments and numerical solution with viscous gas in figure 16. The dispersion relation for sinuous disturbances is given by equation 5 in Li (1993):

$$\left[(m - \Omega) - i \frac{4m^2}{R} \right] (m - \Omega) \tanh(m) + \frac{4m^3}{R^2} [S \tanh(S) - m \tanh(m)] + \rho \Omega^2 - \frac{m^3}{\beta^2} = 0 \quad , \quad (31)$$

where $m = k^* a^*$, $\Omega = \omega^* a^* / U^*$, $\beta = We^{1/2} = U^* / (\sigma^* a^* \rho_l^*)^{1/2}$, $\rho = \rho_g^* / \rho_l^*$, $R = \rho_l^* U^* a^* / \mu_l^*$, and $S = [m^2 + iR(m - \Omega)]^{1/2}$.

The solution for our parameter values can be obtained by making the substitutions: $m = \alpha$, $\Omega = \omega$, $\beta = We^{1/2}$, $R = Re_l$.

Appendix B: Fully inviscid temporal stability of a liquid sheet in a confluent gas

The derivation here is based on the solution of Squire (1953) for an inviscid liquid sheet in inviscid stagnant gas, both with uniform velocity profiles. For the case of long waves compared to the thickness of the liquid sheet, he recovers maximum of the dimensional growth rate:

$$\omega_{i,max}^* = \frac{\tilde{\rho}U_l^{*2}}{2\sqrt{\frac{\gamma^*h^*}{\rho_l^*}}}. \quad (32)$$

Since in the inviscid equations there is a slip boundary condition, they can be translated without affecting the sheet-normal velocity of the disturbance, and thus the growth rate. The only quantity with the streamwise velocity U^* that will appear in the equations and boundary conditions is $\alpha^*U - \omega^*$. Consequently, if we transform the equations into a coordinate system where the gas is stagnant, $\tilde{U}^* = U^* - U_g^*$, the maximal growth rate will have the same value as in the untransformed system, as will the wavenumber α_{max}^* for which this growth rate occurs. The frequency, however, will be shifted by an amount of $\alpha_{max}^*U_g^*$, since the phase velocity is shifted by U_g^* .

The dimensional growth rate in our case is, consequently:

$$\omega_{i,max}^* = \frac{\tilde{\rho}(U_l^* - U_g^*)^2}{2\sqrt{\frac{\gamma^*h^*}{\rho_l^*}}}. \quad (33)$$

The non-dimensional growth rate in our system becomes:

$$\omega_{i,max} = \frac{h^*}{U_l^*} \frac{\tilde{\rho}(U_l^* - U_g^*)^2}{2\sqrt{\frac{\gamma^*h^*}{\rho_l^*}}} = \frac{1}{2}\tilde{\rho}(U_g - 1)^2\sqrt{We}. \quad (34)$$

To convert between the temporal and spatial formulations, we also need to approximate the phase velocity. We get from Squire (1953), for stagnant air:

$$c_{r,max}^* = \frac{U_l^*}{1 + \tilde{\rho}\coth(\alpha h)} \approx U_l^* \quad (35)$$

for water in air. Applying the transformation to get the solution in moving air, and shifting the phase velocity by U_g^* , we simply get:

$$c_{r,max}^* = (U_l^* - U_g^*) + U_g^* = U_l^*$$

or in non-dimensional formulation:

$$c_{r,max} = 1. \quad (36)$$

Appendix C: Derivation of shear at the surface for the model of Lozano *et al.* (2001)

The dimensional velocity profile of Lozano *et al.* (2001) in air is:

$$U_2^*(y^*) = b_0^* + b_1^* \frac{(y^* - h^*)}{\delta^*} + b_2^* \left(\frac{(y^* - h^*)}{\delta^*} \right)^2 \quad (37)$$

where b_0^* , b_1^* and b_2^* are constants (dependent on δ^*).

The dimensional y^* -derivative of this becomes:

$$\frac{dU_2^*}{dy^*} = \frac{b_1^*}{\delta^*} + \frac{2b_2^*}{\delta^*} \frac{(y^* - h^*)}{\delta^*} \quad (38)$$

of which the second term vanishes on the interface between water and air at $y^* = h^*$.

The non-dimensional form of this at the interface ($y = 1$) becomes:

$$\frac{dU_2}{dy}(y = 1) = \frac{b_1^* h^*}{\langle U_1^* \rangle \delta^*} = \frac{b_1^*}{\langle U_1^* \rangle \delta} \quad (39)$$

where the vertical mean of the water velocity $\langle U_1^* \rangle$ is the velocity scale and h^* the length scale. It is given that

$$b_1^* = (U_2^{*\infty} - \langle U_1^* \rangle) \frac{\delta^*}{h^* (2/3\mu_r + \frac{\delta^*}{h^*})} = (U_2^{*\infty} - U_1^*) \frac{\delta}{(2/3\mu_r + \delta)} \quad (40)$$

and μ_r is the air/water viscosity ratio.

Finally:

$$\sigma = \frac{dU_2}{dy}(y = 1) = \frac{(U_2^{\infty} - 1)}{(2/3\mu_r + \delta)}. \quad (41)$$

Since $\mu_r \approx 0.01$, this implies in practice that $\delta \sim 1/\sigma$.

References

- CHANDRASEKHAR, S. 1961 *Hydrodynamic and Hydromagnetic Stability*, 3rd edn. New York: Dover Publications (copyright Oxford University Press).
- EGGERS, J. & VILLERMAUX, E. 2008 Physics of liquid jets. *Reports on Progress in Physics* **71**, 036601.
- HAGERTY, W. W. & SHEA, J. F. 1955 A study of the stability of plane fluid sheets. *Journal of Applied Mechanics* **22**, 509–514.
- LI, X. 1993 Spatial instability of plane liquid sheets. *Chemical Engineering Science* **48** (16), 2973–2981.
- LI, X. & TANKIN, R. S. 1991 On the temporal instability of a two-dimensional viscous liquid sheet. *Journal of Fluid Mechanics* **226**, 425–443.
- LOZANO, A., BARRERAS, F., HAUKE, G. & DOPAZO, C. 2001 Longitudinal instabilities in an air-blasted liquid sheet. *Journal of Fluid Mechanics* **437**, 143–173.
- MANSOUR, A. & CHIGIER, N. 1991 Dynamic behavior of liquid sheets. *Physics of Fluids A* **3**, 2971–2980.
- PARK, J., HUH, K. Y., LI, X. & RENKSIZBULUT, M. 2004 Experimental investigation on cellular breakup of a planar liquid sheet from an air-blast nozzle. *Physics of Fluids* **16** (3), 625–632.
- RAYLEIGH, L. 1878 On the instability of jets. *Proceedings of the London Mathematical Society* **s1-10** (1), 4–13.
- SAKIADIS, B. C. 1961*a* Boundary-Layer behaviour on continuous solid surfaces: I. Boundary-Layer Equations for Two-Dimensional and Axisymmetric Flow. *AIChE Journal* **7** (1), 26–28.
- SAKIADIS, B. C. 1961*b* Boundary-Layer behaviour on continuous solid surfaces: II. The Boundary Layer on a Continuous Flat Surface. *AIChE Journal* **7** (2), 221–225.
- SANDER, W. & WEIGAND, B. 2008 Direct numerical simulation and analysis of instability enhancing parameters in liquid sheets at moderate Reynolds numbers. *Physics of Fluids* **20**, 053301.
- SCHMID, P. J. & HENNINGSON, D. S. 2001 *Stability and Transition in Shear Flows*. New York: Springer Verlag.
- SÖDERBERG, L. D. 2003 Absolute and convective instability of a relaxational plane liquid jet. *Journal of Fluid Mechanics* **493**, 89–119.

- SÖDERBERG, L. D. & ALFREDSSON, P. H. 1998 Experimental and theoretical stability investigations of plane liquid jets. *European Journal of Mechanics B/Fluids* **17** (5), 689–737.
- SQUIRE, H. B. 1953 Investigation of the instability of a moving liquid film. *British Journal of Applied Physics* **4**, 167–169.
- TENG, C. H., LIN, S. P. & CHEN, J. N. 1997 Absolute and convective instability of a viscous liquid curtain in a viscous gas. *Journal of Fluid Mechanics* **332**, 105–120.
- WEBER, C. 1931 Zum Zerfall eines Flüssigkeitsstrahles. *Zeitschrift für Angewandte Mathematik und Mechanik* **11**, 136–154.

Paper 2

Global linear and nonlinear stability of viscous confined plane wakes with co-flow

By **OUTI TAMMISOLA**¹,
FREDRIK LUNDELL^{1,2}, **PHILIPP SCHLATTER**¹,
ARMIN WEHRFRITZ¹,
and **L. DANIEL SÖDERBERG**^{2,3}

¹ Linné FLOW Centre, KTH Mechanics, Royal Institute of Technology, SE-100 44 Stockholm, Sweden

²Wallenberg Wood Science Center, KTH Mechanics, SE-100 44 Stockholm, Sweden

³Innventia AB, BOX 5604, SE-114 86, Stockholm, Sweden

Published in *Journal of Fluid Mechanics* **675**, 397–434, 2011

The global stability of confined wakes is studied numerically, using two-dimensional linear global modes and nonlinear direct numerical simulations (DNS). The wake inflow velocity is varied between different amounts of co-flow (base bleed), while the density and viscosity are assumed to be constant everywhere in the flow domain. In accordance with previous studies, we find that the frequencies of both the most unstable linear and the saturated nonlinear global mode increase with confinement. Here, we also find that for wake Reynolds number $Re = 100$, the confinement is stabilising. It decreases both the growth rate of the linear and the saturation amplitude of the nonlinear modes. We conclude that the dampening effect is connected to the streamwise development of the base flow, and for higher Reynolds numbers this effect decreases, since the flow becomes more parallel. The linear analysis reveals that the critical wake velocities below which the flow becomes unstable are almost identical for unconfined and confined wakes at $Re \approx 400$. Also, the present results are compared with literature data for an inviscid parallel wake due to the similarity of inflow profile. The confined wake is found to be more stable than its inviscid counterpart, while the unconfined wake is more unstable than the inviscid wake. The main reason to both can be explained by the base flow development. A detailed comparison of the linear and nonlinear results reveals that the most unstable linear global mode gives an excellent prediction of the initial nonlinear behaviour and therefore the stability boundary, in all cases. However, the nonlinear saturated state is quite different in particular for higher Reynolds numbers. For $Re = 100$, the saturated frequency also differs less than 5% from the linear frequency, and trends regarding confinement observed in the linear analysis are confirmed.

1. Introduction

A wake is formed when a local region with lower velocities than its surroundings is present in a flow. In many such cases, the flow in the wake features a temporally periodic oscillation around a specific mean flow, like in the well-known example of a von Kármán vortex street behind a solid cylinder. Then the wake is said to be unstable, and often this instability is solely dependent on the flow geometry (*e.g.* location of confining walls) and characteristic parameters (for example Reynolds number), and is independent on the level of disturbances in the environment; wakes are often globally unstable. Wake instability and the related mixing process are important in many industrial applications ranging from combustion to food industry. Wakes behind solid obstacles in two and three dimensions have grasped the attention of many researchers, due to their relation to the aerodynamic drag imposed on the obstacle. Confined wakes, *i.e.* wakes between near-lying walls, occur *e.g.* when two streams of fluid mix in a narrow channel, or when cylinders are introduced into a channel in order to increase the heat transfer. In most applications, efficient mixing is desired and therefore knowledge of wake instabilities is essential. In other cases it might be desirable to stabilise the flow, and the self-sustained oscillations potentially introduced by wake instabilities should be avoided. One example of the latter type occurs in the beginning of the papermaking process: a suspension consisting of 99% water and 1% cellulose fibres flowing through a sharply convergent nozzle, where different pulp streams can be separated by either solid or water-filled plates, and the globally unstable wakes behind these may cause unwanted mixing.

In the present contribution, we investigate the global instability of viscous wakes with co-flow, where one inner and two outer streams with different velocities enter into a channel and mix with each other. The configuration is symmetric in the vertical direction, and the inner stream is assumed to have a lower velocity. When the streams meet, a wake region appears, which gradually diminishes as the parabolic channel flow profile develops for the mean flow (figure 1). We study the global stability of this flow as a function of shear, *i.e.* velocity difference between the inner and outer streams at the inflow, and different degrees of confinement, for low to moderate Reynolds numbers. The investigation is performed using two different methods. Firstly, we determine the

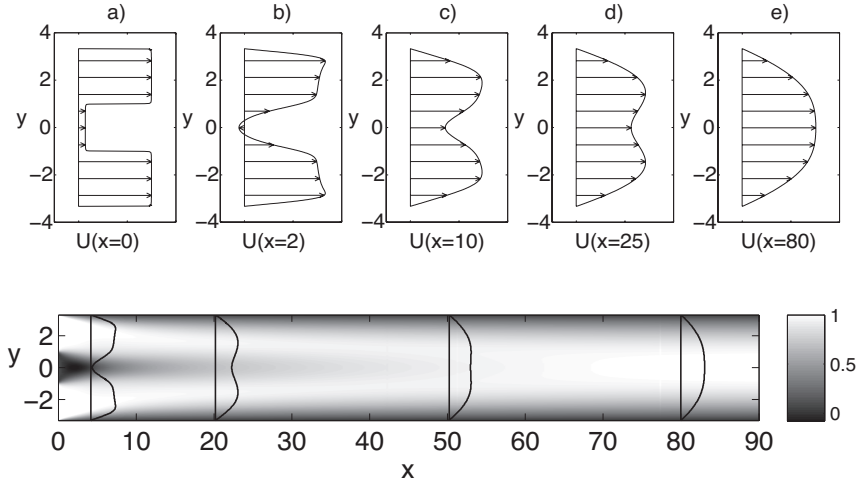


FIGURE 1. An example base flow for a typical wake in this study, *i.e.* the equilibrium point for the linear analysis ($Re = 100$, $h = 2.33$, $\Lambda^{-1} = -1.2$). The mean flow in the nonlinear simulations is qualitatively similar. Top: Streamwise velocity profiles for the base flow at different downstream stations: a) $x = 0$, b) $x = 2$, c) $x = 10$, d) $x = 25$, and e) $x = 80$. Bottom: Greyscale representation of the streamwise velocity pertaining to the complete base flow field. Dark regions have low or reverse velocity and light regions high velocity. The profiles b) to e) are superimposed with solid lines.

growth rates of the linear global modes. These states oscillate periodically around the chosen mean flow (base flow) that the problem is linearised around. The modes either grow or decay in time, and growing modes represent self-sustained oscillations. Secondly, we extract frequencies and oscillation shapes from nonlinear direct numerical simulations (DNSs).

According to our knowledge, neither the two-dimensional linear stability nor nonlinear development have been computed previously for this flow configuration. However, in parallel with the present work, direct numerical simulations have been performed by another group for a similar flow case; wakes confined in a channel with a slip condition at the walls (Biancofiore *et al.* 2010). Their results will be discussed and compared to our results in section 6.

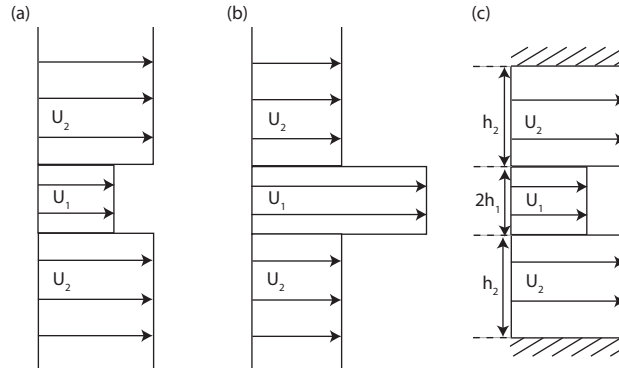


FIGURE 2. Velocity profiles in the study of absolute instability of inviscid parallel wakes and jets by Huerre & Monkewitz (1990): (a) wake and (b) jet. The geometry is assumed infinite in both the vertical and horizontal directions. In contrast, (c) gives the geometry in the study of Juniper (2006), confined by walls in the vertical direction.

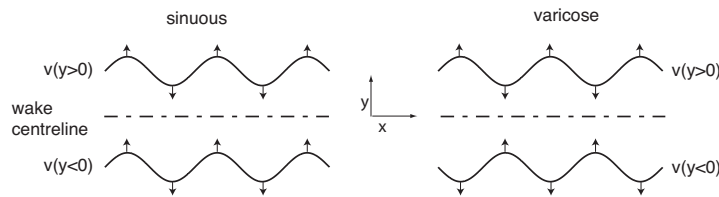


FIGURE 3. Definition of a sinuous and varicose mode in terms of the vertical disturbance velocity.

On the other hand, there are a number of studies based on the theory for weakly-nonparallel flows (WNP) dealing with the stability of co-flow wakes. Many of these consider fluid streams of different density. In the present work, we study flows with uniform density and the review below reflects this basic assumption. According to the WNP theory (Huerre & Monkewitz 1990), local streamwise velocity profiles can be used to find an approximation of the frequencies, growth rates and shapes of the linear global modes. A finite region of *local absolute instability* can then be shown to be a requirement for a growing linear global mode to exist, and therefore absolute instability of velocity profiles potentially occurring in *e.g.* a wake is of interest. Consequently, many studies

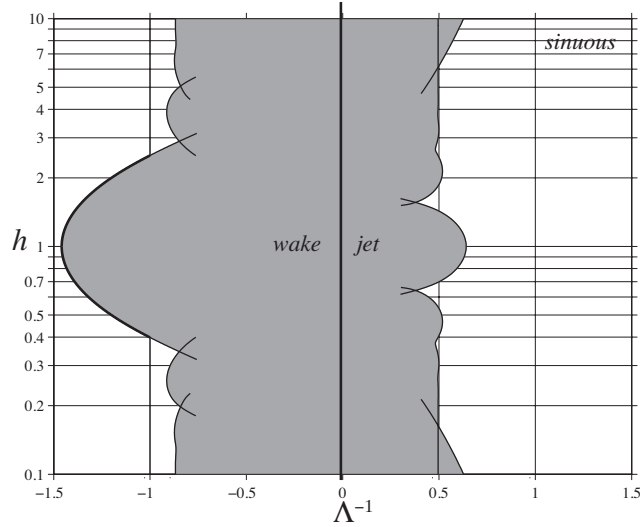


FIGURE 4. The gray area shows the region of absolute instability for sinuous disturbances and uniform density in the inviscid study of Juniper (2006) with respect to confinement h (1) and inverse shear ratio Λ^{-1} (2) (figure provided by M. Juniper.)

have concentrated on searching for *absolute instability* (Briggs 1964) of different model velocity profiles.

Already Huerre & Monkewitz (1990) discussed local absolute instability on plane “wakes and jets” (figure 2 a and b), which also could be called inviscid symmetric mixing layers, with constant velocity and density inside the inner and outer layers. They concluded that the absolute instability is enhanced by a high velocity difference for both wakes and jets. In the wake the sinuous (antisymmetric for streamwise, symmetric for vertical velocity) von Kármán vortex street becomes unstable first, while in the jet it is always a varicose (streamwise symmetric) mode (figure 3). Almost at the same time, Yu & Monkewitz (1990) analysed the effect of viscosity, and they concluded that the absolute instability for wakes and jets is caused by the interaction of the two shear layers and not by viscous effects.

The effect of confinement on the absolute instability of wakes and jets, represented by the same type of symmetric model profiles as in the previous studies, was conducted by Juniper (2006). The stability analysis was still inviscid, and the base flow profile step-like, without

shear and boundary layers. A sketch of the flow configuration together with parameter definitions is given in figure 2 (c). This problem can be described by two nondimensional parameters, which were chosen as the confinement parameter h :

$$h = \frac{h_2}{h_1}, \quad (1)$$

and the shear ratio λ :

$$\lambda = \frac{(U_1 - U_2)}{(U_1 + U_2)}. \quad (2)$$

The boundary between absolute and convective instability in the h - Λ^{-1} -plane obtained by Juniper (2006) is shown in figure 4 for the sinuous case (the setting relevant for the present work), for confinements $0.1 < h < 10$. It is shown that in the inviscid limit, wakes are most unstable when $h = 1$. In a very recent paper (Rees & Juniper 2010), the analysis was extended to viscous stability of velocity profiles with finite shear layer thickness, although the slip condition on the wall was retained for both the base flow and the (linear) disturbance in the stability analysis. The destabilising effect of confinement observed in the inviscid case was still present, but somewhat weaker for viscous wakes, and the most unstable case was observed for higher h .

Traditionally, stability problems have been formulated based on the so-called local approach. The use of such local methods was motivated by the fact that solving the several-dimensional linear stability problem requires extensive computational resources, which have not been available until recently. Also, according to some recent theories, the frequency selection of the final nonlinear state for weakly non-parallel flows might occur in the most upstream locally absolutely unstable point (Chomaz 2005). However, since the WNP theory assumes locally parallel flow neglecting streamwise gradients of the base flow, it is therefore only applicable to finding linear global modes around base flows that are weakly developing in the streamwise direction.

The studies with non-local methods have until now been concentrated on wakes behind solid obstacles. Hammond & Redekopp (1997) performed DNS on wakes behind an unconfined solid plate subject to suction at the trailing edge at $Re = 160 - 400$ based on the plate thickness and the free stream velocity. The appearance of self-sustained oscillations as a function of Reynolds number was investigated for different suction velocity distributions. The authors concluded that strong suction stabilised the wake for a range of Reynolds numbers, due to the decrease of length of the wake region. They also found that the frequency

matched the frequency prediction by the WNP analysis at $Re = 160$ within 1% for symmetric and 8% for asymmetric wakes. It should be noted that the linearisation was performed around the mean flow obtained from the nonlinear simulation, instead of the true steady solution of Navier-Stokes equations.

The importance of the length of the wake is also highlighted by *e.g.* Camarri & Giannetti (2007), who observed that the point of inversion of the vortices observed for confined wakes was connected to the length of the wake for the nonlinear mean flow. Also, the length of the reverse flow region is generally known to be important for the onset of global oscillations. Further below, these two quantities (length of the wake and reverse flow region) will be used to characterise and classify the wake flows under consideration.

There are also a number of experiments and nonlinear simulations studying the effect of confinement on wakes behind cylindrical obstacles, see *e.g.* the classical studies Shaw (1971), Davis *et al.* (1984) and Richter & Naudascher (1976). Similarities and differences between such flows and wakes with co-flow will be further discussed in section 6.

1.1. *Structure of the paper*

It is the aim of the present contribution to study the stability of viscous, spatially developing wake flows through global linear stability analysis and nonlinear DNS. The paper is organised as follows: The characteristic parameters, governing equations and definitions of linear and nonlinear global modes are introduced in section 2, and the numerical methods used for linear and nonlinear analysis are introduced in section 3. Section 4 presents results pertaining to the linear and nonlinear simulations of an unconfined reference wake ($h = 9$) in greater detail, while section 4 contains the results for confined wakes, which are further discussed and linked to the results from previous studies in section 6. Finally, section 7 summarises the present findings. Further technical details on the boundary conditions, grid independence and numerical convergence are given in Appendix 7, whereas details of the signal processing related to the nonlinear results are summarised in Appendix 7.

2. Problem definition

2.1. *Characteristic parameters*

The flow problem at hand is parameterised in a straight-forward way based on the inflow profile of the wake (see figures 2 c above and 7

below). For a complete description of the viscous confined problem, three nondimensional parameters are needed, as detailed below. Two of them are chosen as in the inviscid case by Juniper (2006) — the confinement parameter h (equation 1) and the shear ratio Λ (equation 2). As the third parameter, we choose the Reynolds number based on the wake width and outer stream velocity:

$$Re = Re_{wake} = \frac{U_2 h_1}{\nu}, \quad (3)$$

Holding Re_{wake} constant while confining the flow, can be seen as placing a thin plate above the wake/jet without altering the flow velocity. This could therefore be described as a confined wake in a free stream.

Note that a number of other studies, in particular dealing with cylinder wakes, base their Reynolds number on the channel width: $Re_{ch} = \frac{U_2 h_2}{\nu}$. We would like to point out that the stability boundary in our parameter regime depends on the type of confinement, *i.e.*, the definition of Reynolds number, as further discussed in section 6.

2.2. Linear and nonlinear global modes

In the following, x denotes the streamwise, y the vertical and z the spanwise direction. The nondimensionalisation is performed based on h_1 as the length and U_2 as the velocity scale, in accordance with the definition of Reynolds number in the previous section. Unless explicitly stated otherwise, all quantities from now on are nondimensional. The nonlinear simulations are performed by solving the full time-dependent, incompressible Navier-Stokes equations:

$$\frac{\partial \mathbf{U}}{\partial t} + \mathbf{U} \cdot \nabla \mathbf{U} = -\nabla P + \frac{1}{Re} \nabla^2 \mathbf{U} \quad (4)$$

$$\nabla \cdot \mathbf{U} = 0 \quad (5)$$

In the following subsections we introduce the equations that are solved in the linear analysis, and define the concepts of linear and nonlinear global modes. Further details of their computation are presented in section 3, including the boundary conditions needed to close the equation systems. The detailed procedure of extracting the nonlinear global modes from the simulation data is described in Appendix 7.

2.2a. *Linear global modes*. As common in stability analysis, the flow variables are divided into a steady and a time-varying part:

$$\mathbf{U}_{tot}(x, y, z, t) = \mathbf{U}(x, y, z) + \mathbf{u}(x, y, z, t)$$

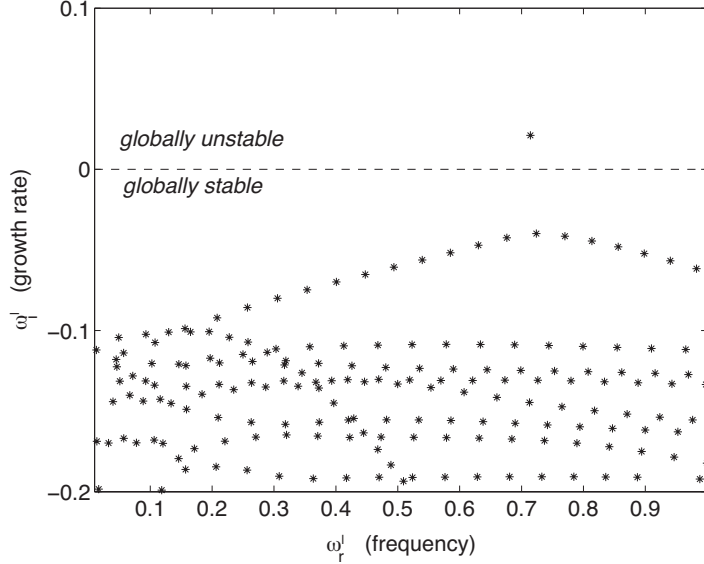


FIGURE 5. The global linear eigenvalue spectrum of the unconfined reference wake ($Re = 100$, $h = 9$, $\Lambda^{-1} = -1.2$). There is one eigenvalue with a positive growth rate ($\omega_i^l > 0$), indicating an unstable global mode.

$$P_{tot}(x, y, z, t) = P(x, y, z) + p(x, y, z, t),$$

where $(\mathbf{U}_{tot}, P_{tot})$ is the total time-dependent flow field, $(\mathbf{U}(x, y, z), P(x, y, z))$ the steady base flow, and $(\mathbf{u}(x, y, z, t), p(x, y, z, t))$ a *disturbance*, *i.e.* a deviation from the base flow. We take as a base flow the solution to the steady nonlinear Navier-Stokes equations, *i.e.* equations (4)-(5) without the time derivative.

If the disturbance magnitude is small enough compared to that of the base flow, and if it is smooth enough, the governing equations can be linearised in the disturbance quantities about the steady state, yielding the *linearised Navier-Stokes equations*, LNSE. Due to linearity in time, the equations can be transformed from the time domain to a frequency domain by a Fourier ansatz. If the base flow does not vary in all coordinate directions, or varies slowly in certain directions, then these directions can be Fourier transformed as well. Our base flow is Cartesian 2D — independent of the spanwise coordinate z — which leads to the

ansatz:

$$\mathbf{u}(x, y, z, t) = (\hat{u}(x, y), \hat{v}(x, y), \hat{w}(x, y), \hat{p}(x, y)) e^{i\beta z - i\omega^l t}, \quad (6)$$

where β is a wavenumber in the spanwise direction, and ω^l is the complex frequency; the superscript l indicates a frequency from linear analysis. In this paper, only disturbances with $\beta = 0$ are discussed, which automatically leads to a vanishing cross-flow disturbance velocity \hat{w} . This approximation is made for two reasons: the first bifurcation of our wakes is probably two-dimensional, as for cylinder wakes, and it makes the parameter studies we aim at considerably easier. For further details about linear stability and the modal ansatz, see *e.g.* Drazin & Reid (1981), Schmid & Henningson (2001) and Theofilis (2003).

Inserting ansatz (6) into the LNSE gives (assuming $\beta = 0$):

$$\begin{aligned} & -U \frac{\partial \hat{u}}{\partial x} - V \frac{\partial \hat{u}}{\partial y} - \hat{u} \frac{\partial U}{\partial x} - \hat{v} \frac{\partial U}{\partial y} + \\ & - \frac{\partial \hat{p}}{\partial x} + \frac{1}{Re} \left(\frac{\partial^2 \hat{u}}{\partial x^2} + \frac{\partial^2 \hat{u}}{\partial y^2} \right) = -i\omega^l \hat{u} \end{aligned} \quad (7)$$

$$\begin{aligned} & -U \frac{\partial \hat{v}}{\partial x} - V \frac{\partial \hat{v}}{\partial y} - \hat{u} \frac{\partial V}{\partial x} - \hat{v} \frac{\partial V}{\partial y} + \\ & - \frac{\partial \hat{p}}{\partial y} + \frac{1}{Re} \left(\frac{\partial^2 \hat{v}}{\partial x^2} + \frac{\partial^2 \hat{v}}{\partial y^2} \right) = -i\omega^l \hat{v} \end{aligned} \quad (8)$$

$$\frac{\partial \hat{u}}{\partial x} + \frac{\partial \hat{v}}{\partial y} = 0. \quad (9)$$

The linearised equations (8–11) constitute a $2D$ eigenvalue problem for ω^l . Linear temporal global modes are obtained when discretizing and solving this problem without further simplifications. The eigenfunctions then represent possible two-dimensional disturbance shapes $(\hat{u}(x, y), \hat{v}(x, y), \hat{p}(x, y))$, together with corresponding frequencies and growth rates given by the real and complex part of $\omega^l = \omega_r^l + i\omega_i^l$, respectively. The corresponding eigenfunction with a non-zero amplitude in any point will be amplified by a factor $\exp(\omega_i^l t)$ and grow at all times in that point. Convective instabilities, which are convected downstream while growing in amplitude, are in this setting represented by a sum of stable eigenfunctions, as in *e.g.* Ehrenstein & Gallaire (2005). An example of such a global eigenvalue spectrum for the unconfined reference wake (reference case $h = 9$, further discussed in section 4), is shown in figure 5.

An eigenfunction-eigenvalue pair is called a mode. A general disturbance can usually be expressed as a sum of the eigenfunctions with the largest growth rates:

$$u(x, y, t) = \sum_{k=1}^N c^k \hat{u}^k(x, y) e^{-i\omega^{l,k}t}, \quad (10)$$

where c^k is a complex amplitude (similarly for v and p).

A finite number of the most unstable modes can then be used to approximate the dynamics of the flow. How many modes that are needed (the value of N) to capture the relevant behaviour at finite times, *i.e.* the structures that dominate the flow dynamics, is problem-dependent (Schmid & Henningson 2001). If the initial condition is known, the values for the unknown coefficients c^k can be obtained by projecting the initial condition to eigenmodes of the adjoint linearised system (Schmid & Henningson 2001), which requires a solution of another eigenvalue problem. However, if there are *unstable* global modes ($\omega_i^{l,k} > 0$), it is often sufficient to include these in order to catch the physical behaviour after initial transients, and the initial condition becomes irrelevant. In particular, unstable global modes mean that the flow eventually will deviate from the steady state.

The interpretation of the linear global results, computed from the system (8-11) with the above ansatz, is fairly straight-forward. In the cases presented here, there is at most one mode with a positive growth rate. When presenting the results, unless stated otherwise, ω^l always describes the linear complex eigenvalue for the most unstable mode.

2.2b. *Nonlinear global modes*. When simulating the flow in a nonlinear setting, after an initial transient behaviour the flow field will feature periodic oscillations around its mean. In the following, the oscillation frequencies in this time-periodic state are denoted by ω^s , denoting the nonlinear *saturated* frequencies. A typical nonlinear frequency spectrum is shown in figure 6. This spectrum is obtained from the final time-periodic part of the simulation data as described in Appendix 7. It contains a peak for the mean flow at $\omega^s = 0$, a high energy peak for the fundamental frequency, and several lower energy peaks for the harmonics located at multiples of the fundamental.

Among several possibilities to define a nonlinear global mode, we have chosen the following definition. If a discrete Fourier transform is

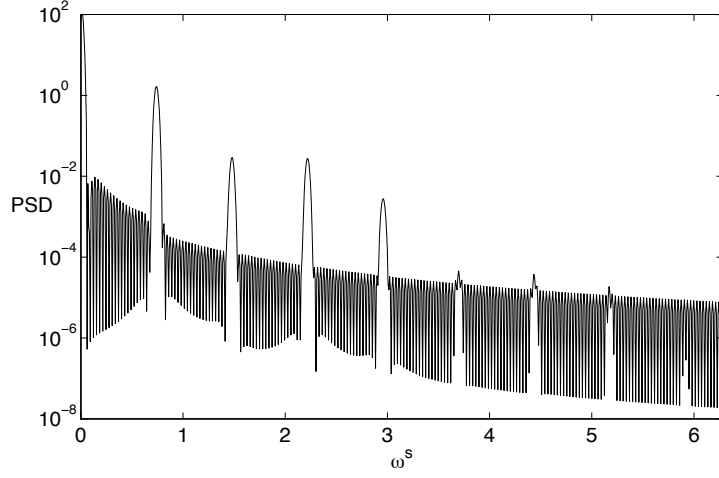


FIGURE 6. Frequency spectrum extracted from the saturated nonlinear velocity fluctuations (time signal shown in figure 29) for the unconfined reference wake ($Re = 100, h = 9, \Lambda^{-1} = -1.2$). The first nonzero peak $\omega^s \approx 0.73$ corresponds to the nonlinear global mode, and the other visible peaks to its harmonics.

performed based on the oscillation period T of the flow field:

$$\hat{u}(x, y, \omega) = \sum_{k=0}^{\infty} u_k(x, y) e^{(ik2\pi t/T)}, \quad (11)$$

the nonlinear global mode is the term with $k = 1$ in this expansion, *i.e.* the one oscillating with the fundamental frequency $2\pi/T$. The frequency of the nonlinear global mode is thus real-valued. The coefficient $u_1(x, y)$ gives the spatial shape of the nonlinear global mode. Note that for our flow case, this mode coincides with the Koopmann mode with highest amplitude (Rowley *et al.* 2009), and its spatial shape also with the most energetic POD mode (Berkooz *et al.* 1993). When presenting the results, unless otherwise stated, ω^s is the frequency, and the spatial shape (\hat{u} , \hat{v} and \hat{p}) the coefficient of this fundamental Fourier mode.

In addition to this saturated nonlinear global mode, we also extract the oscillation frequency and logarithmic slope of the amplitude curve in the initial part of the nonlinear simulation, where an exponential growth is seen. These quantities together form the *initial nonlinear frequency* ω^i , which is complex-valued. Thus it and can be compared to

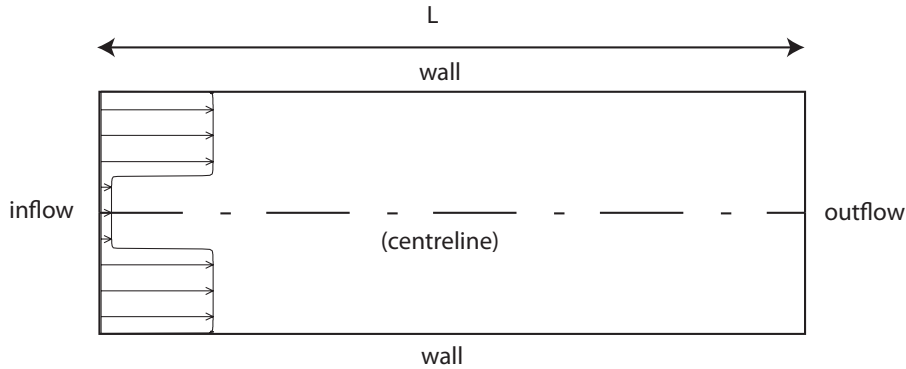


FIGURE 7. Illustration of the nonlinear computational domain with following boundaries : the upper and lower walls (no slip), the inflow (condition 9), and the outflow (Neumann condition with constant pressure).

the (complex) frequency obtained for the linear global mode, ω^l . Mode shapes are not extracted for this oscillation stage.

3. Numerical methods

3.1. Solution of the nonlinear system

The solution to the nonlinear Navier-Stokes equations (4-5) is computed using a Legendre polynomial based spectral-element method (SEM) (Fischer 1997), implemented in the code `nek5000`. In this method, as in the case of the finite-element method (FEM), the governing equations are cast into weak form and discretised in space by the Galerkin approximation, where the test and trial spaces are restricted to certain (and different) velocity and pressure spaces respectively, following the $\mathbb{P}_N - \mathbb{P}_{N-2}$ SEM discretisation by Maday & Patera (1989). The velocity space is spanned by N th-order Lagrange polynomial interpolants, based on tensor-product arrays of Gauss-Lobatto-Legendre (GLL) quadrature points in a local element. The individual elements take the shape of hexahedra, allowing a general coordinate mapping of both the element boundaries and the collocation points inside the elements. Time advancement is achieved by an explicit second-order extrapolation (EXT2) for the advection terms and an implicit second-order backward differentiation scheme (BDF2) for the viscous terms.

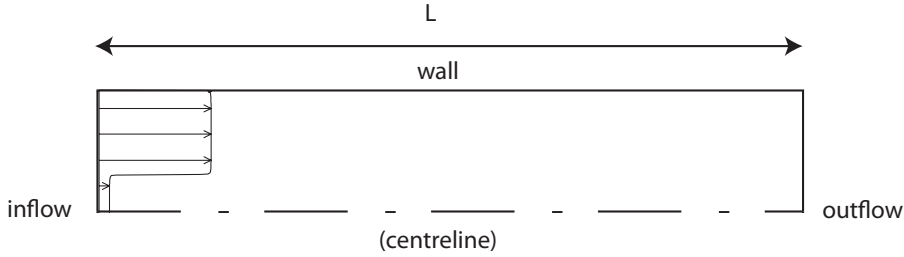


FIGURE 8. Illustration of the computational domain for the base flow with following boundaries: the wall (no slip), the wake centreline (symmetry), the inflow (condition 9, $y > 0$), and the outflow (Neumann condition with constant pressure).

The computational domain together with boundary conditions is illustrated in figure 7. It consists of a rectangular box, discretised with non-equidistantly distributed but structured spectral elements, and four boundaries, representing the inflow, outflow and the two surrounding walls. For the inflow, a slightly modified inviscid double mixing layer profile, symmetric around the centreline, is imposed as a Dirichlet boundary condition. Since the spectral method is based on high-order polynomial interpolation, sharp gradients could cause unphysical oscillations near the inflow boundary. Therefore, the gradients of the inviscid top-hat profile were slightly smoothed. The shape of the inflow profile is shown in figure 7, and is given by the following analytic expression:

$$\begin{aligned}
 U(0, y < 0) &= 1/\pi [\arctan(500(y + h + 1)) + \pi/2] + \\
 &\quad 2 [\pi (\Lambda^{-1} - 1)]^{-1} [\arctan(500(y + 1)) + \pi/2] \\
 U(0, y > 0) &= 1/\pi [\arctan(500(h + 1 - y)) + \pi/2] + \\
 &\quad 2 [\pi (\Lambda^{-1} - 1)]^{-1} [\arctan(500(1 - y)) + \pi/2]
 \end{aligned} \tag{12}$$

Note that the inflow profile is C^2 -continuous. No-slip conditions were applied at the walls, and a homogeneous Dirichlet condition for the pressure together with a homogeneous Neumann condition for the velocities was chosen at the outflow boundary. Further details on convergence properties are given in Appendix 7.

3.2. Base flows for linear stability

The base flows are steady solutions to the Navier-Stokes equations, and were obtained with the same code as the time-dependent flow field. In our flow case, the only unstable mode for moderate Reynolds numbers was known to be antisymmetric. Therefore, by applying a symmetry

condition at the wake centreline, the oscillations could effectively be eliminated, and the DNS converged to a stationary solution.

The computational domain for the base flow calculations and its boundaries are illustrated in figure 8. The inflow profile is the upper half of the nonlinear one (equation 9). The condition at the wall (no-slip) and the outflow boundary condition were the same as in the nonlinear case (section 3.1). As the specific outflow condition could potentially have an effect on the stability results, the base flow domain was always chosen long enough to avoid this.

The evolution of the streamwise velocity of the base flow for a specific choice of parameters has already been shown in figure 1. In the upper part, velocity profiles at different streamwise stations are shown. Starting from an almost plug-like inflow profile in both the wake and the outer streams, the base flow quickly develops boundary layers at the solid walls and gradually approaches a parabolic profile at $x = 80$. There is a small backflow region near the inflow boundary, and the recirculation is strongest around $x = 2$. The whole streamwise velocity field is shown with greyscale in the lower part of the figure.

3.3. Solution of the linear system

In the global linear analysis, equations (8)–(11) are discretised in space by a spectral method, using Chebyshev-polynomials in both streamwise and vertical directions:

$$\hat{u}(x, y) \approx \sum_{i=1}^{N_x} \sum_{j=1}^{N_y} c_{ij} \phi^i(x) \phi^j(y) \quad (13)$$

where ϕ^k is the k^{th} Chebyshev polynomial. The values of the unknown coefficients c_{ij} are obtained by requiring the discretised equations to be satisfied exactly at the $N_x \times N_y$ collocation points, which are selected as the Gauss-Lobatto points to assure an exponential convergence rate (Weideman & Reddy 2000). A linear transformation of the domain from $[-1, 1] \times [-1, 1]$ to $[0, L_x] \times [0, h_1 + h_2]$ is applied.

The eigenvalue problem of a continuous operator is thus transformed into a generalised matrix eigenvalue problem:

$$\mathbf{A}q = \omega^l \mathbf{B}q, \quad (14)$$

where $q = (\hat{u}, \hat{v}, \hat{p})$ is the eigenvector and ω^l the eigenvalue. The system matrices of the local and global discretised problem share the same structure. A basic property for the present two-dimensional eigenvalue

problem is that the left-hand side matrix A grows as $9N_x^2N_y^2$, compared to only N_y^2 in the one-dimensional formulation. For instance, at $Re = 400$ we need $N_x = 500$ and $N_y = 70$ to obtain a converged most unstable mode, resulting in a dense matrix with $(105000)^2$ elements. To store such a matrix in double precision 88 GB of RAM is needed. Thus, a parallel code FLUPACK was developed, in which the matrix is built in smaller pieces on each processor. Then the eigenvalue problem is solved using PARPACK (Maschhoff & Sorensen 1996), a mathematical library containing a parallel version of the Arnoldi algorithm based on Krylov subspace iterations (Lehoucq *et al.* (1998)), where a chosen number of eigenvalues and eigenvectors near a chosen location, the *shift*, are recovered. Complex shifts are used to reduce the necessary number of eigenvalues, which doubles the memory need mentioned above. All incoming vector operations and equation system solving are made in parallel with the mathematical library ScaLAPACK.

The code scales well with the number of processors in the sense that computational times remain within a few hours independently of problem size. The amount of processors used is thus dictated by the memory need alone, where the system matrix has the biggest contribution. For problems of reasonable size, the computational time is spent mostly and almost in equal amounts in two types of ScaLAPACK operations: (a) the LU-factorization of the system matrix, and (b) repeated back-substitutions of the LU-decomposed matrix inside the Arnoldi loop. The FLUPACK code is not yet fully optimized in terms of memory and speed. Here we outline some differences between FLUPACK and the well optimized and documented similar code of Rodriguez & Theofilis (2009). Both use machine-optimized versions of the ScaLAPACK library, while in the code of Rodriguez & Theofilis (2009), the algorithm for the Arnoldi loop is implemented manually. Presumably, this improves the performance, since the combination of distributed and non-distributed arrays can be chosen as is appropriate for two-dimensional global mode computations. Also, this opens the possibility for more dynamic allocations. It seems at the first sight that the way the system matrix is created in FLUPACK is already quite efficient; in the code of Rodriguez & Theofilis (2009) this operation takes 20% of the computational time regardless the problem size, while in FLUPACK the building of the system matrix (and postprocessing) give only marginal contributions to the time spent. In the code of Rodriguez & Theofilis (2009) a looping over the elements of the global matrix is performed at this stage, while in FLUPACK each processor calls a subroutine to build the blocks it needs.

3.4. Boundary conditions for the disturbance

The boundary conditions at the wall and the centreline are determined by the problem setup. At the confining wall, we set a no slip condition:

$$\hat{u}(x, h + 1) = 0, \quad \hat{v}(x, h + 1) = 0. \quad (15)$$

As was mentioned in section 3.2, it is known that for wakes a sinuous von Kármán-type of mode always becomes unstable first. So it is sufficient to consider antisymmetric modes:

$$\hat{u}(x, 0) = 0, \quad \frac{\partial \hat{v}}{\partial y}(x, 0) = 0, \quad \hat{p}(x, 0) = 0, \quad (16)$$

where the condition on the pressure is used to specify both the required symmetry condition and setting the (undetermined) level of the disturbance pressure.

The boundary conditions in the streamwise direction are not as straightforward, as the only natural boundary condition for the global mode is to decay at infinity. The standard choice was made by taking a Dirichlet condition at the inflow boundary, and a Neumann condition at the outflow boundary:

$$\hat{u}(0, y) = 0, \quad \hat{v}(0, y) = 0, \quad (17)$$

$$\frac{\partial \hat{u}}{\partial x}(L, y) = 0, \quad \frac{\partial \hat{v}}{\partial x}(L, y) = 0. \quad (18)$$

It was then verified that the chosen streamwise boundary conditions did not affect the stability characteristics, by assuring that the most unstable eigenvalue converged in terms of domain length. However, the most unstable eigenvalue showed a weak dependence on the upstream condition, but this was considered to be of secondary importance. Further details on the convergence studies are presented in Appendix 7.

Finally, the remaining seven spurious pressure modes inherent in a Chebyshev-Chebyshev discretisation are removed by setting specially designed boundary conditions in seven near-corner points, *i.e.*, homogeneous Neumann conditions to remove the four so-called corner modes:

$$\begin{aligned} \left(\frac{\partial p}{\partial x} + \frac{\partial p}{\partial y} \right)_{1,1} &= \left(\frac{\partial p}{\partial x} + \frac{\partial p}{\partial y} \right)_{1,N_x} = \\ \left(\frac{\partial p}{\partial x} + \frac{\partial p}{\partial y} \right)_{N_y,1} &= \left(\frac{\partial p}{\partial x} + \frac{\partial p}{\partial y} \right)_{N_y,N_x} = 0, \end{aligned} \quad (19)$$

where the subscripts give the indices of the grid point in y and x -directions, and conditions for the three modes oscillating between grid

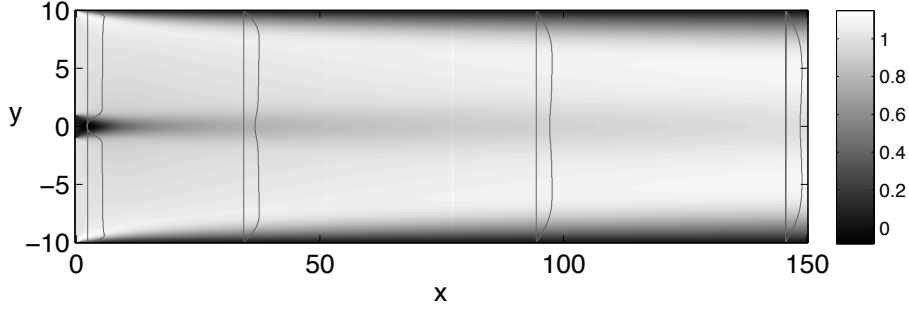


FIGURE 9. Streamwise velocity of the base flow for the unconfined reference wake ($h = 9$, $\Lambda^{-1} = -1.2$) indicated with greyscale — light tones represent high velocity and dark tones low velocity or reverse flow. Note that the figure has to be stretched by a factor of 3 in the streamwise direction to get the physical aspect ratio.

points:

$$\sum_{i,j} (-1)^i m_{i,j} p(i,j) = \sum_{i,j} (-1)^j m_{i,j} p(i,j) = \sum_{i,j} (-1)^{i+j} m_{i,j} p(i,j) = 0, \quad (20)$$

where $m_{i,j} = (1 - 0.5\delta_{i,1})(1 - 0.5\delta_{i,N_y})(1 - 0.5\delta_{j,1})(1 - 0.5\delta_{j,N_x})$.

4. Results for an unconfined reference wake

For comparison with the confined cases, we chose a wake with walls sufficiently far away so that the wall distance no longer affects the stability. This situation was seen to occur for $h \approx 9$, *i.e.* when the total channel width is ten times the width of the wake, for a wake that has a weak co-flow at the upstream boundary, $\Lambda^{-1} = -1.2$.

When viewing the results in this and following sections, recall from sections 2.2a and 2.2b that the complex frequency extracted from the linear analysis is denoted by ω^l , the real saturated nonlinear frequency ω^s , and the initial complex frequency near the onset of the nonlinear oscillation ω^i .

4.1. Linear results

The base flow development for this reference wake can be seen in figure 9. The inflow profile is step consisting of two layers with constant velocity, and the boundary layers grow until the parabolic profile is reached at $x \approx 170$.

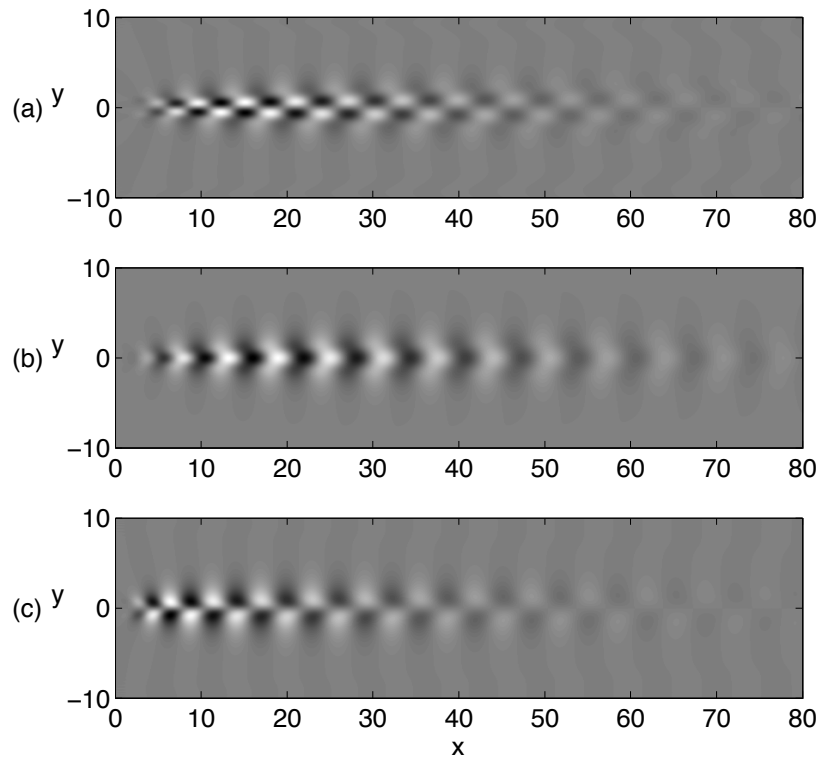


FIGURE 10. Real part of the eigenfunction of the unstable mode in figure 5 ($Re = 100$, $h = 9$, $\Lambda^{-1} = -1.2$): (a) \hat{u} , (b) \hat{v} and (c) \hat{p} . Light regions represent positive and dark regions negative values. This is an instantaneous picture of the disturbance distribution in space. The colormap in all pictures is scaled with the maximum amplitude of the eigenfunction.

For this case, one unstable mode is found with nondimensional oscillation frequency $\omega_r^l = 0.714$, and growth rate $\omega_i^l = 0.021$ (the eigenvalue spectrum was already shown in figure 5). The spatial shape of the unstable mode can be seen in figure 10. Figure 10 (a) shows the streamwise component of the oscillation \hat{u} at one instant in time. The mode oscillates back and forth around the base flow (figure 9). The symmetric vertical component \hat{v} and antisymmetric pressure component \hat{p} are provided in figures 10 (b) and (c). The mode is an antisymmetric (sinuous) mode.

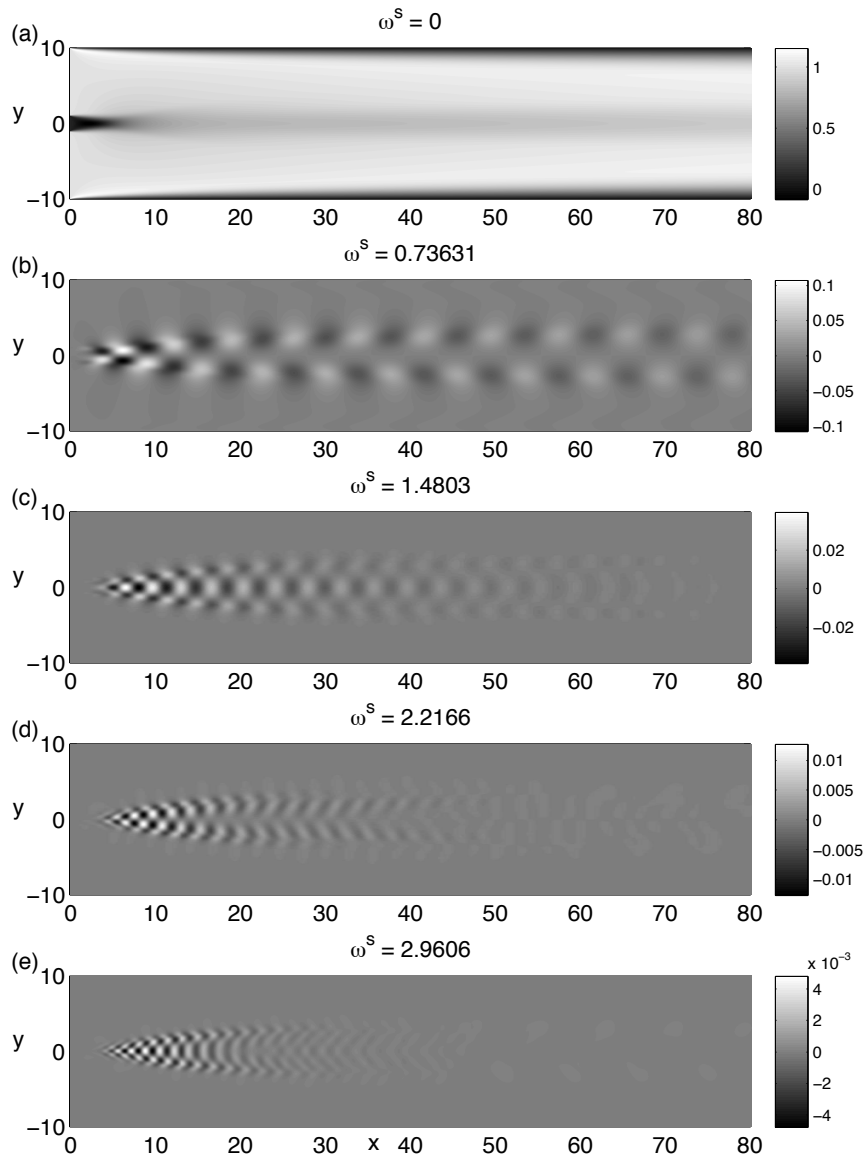


FIGURE 11. Reference case ($Re = 100$, $h = 9$, $\Lambda^{-1} = -1.2$) — the streamwise velocity for: (a) the nonlinear mean flow (compare to figure 9 for the steady base flow), (b) the saturated nonlinear global mode, and (c)–(e) the first harmonics. The saturated frequency for each mode is given above respective plot.

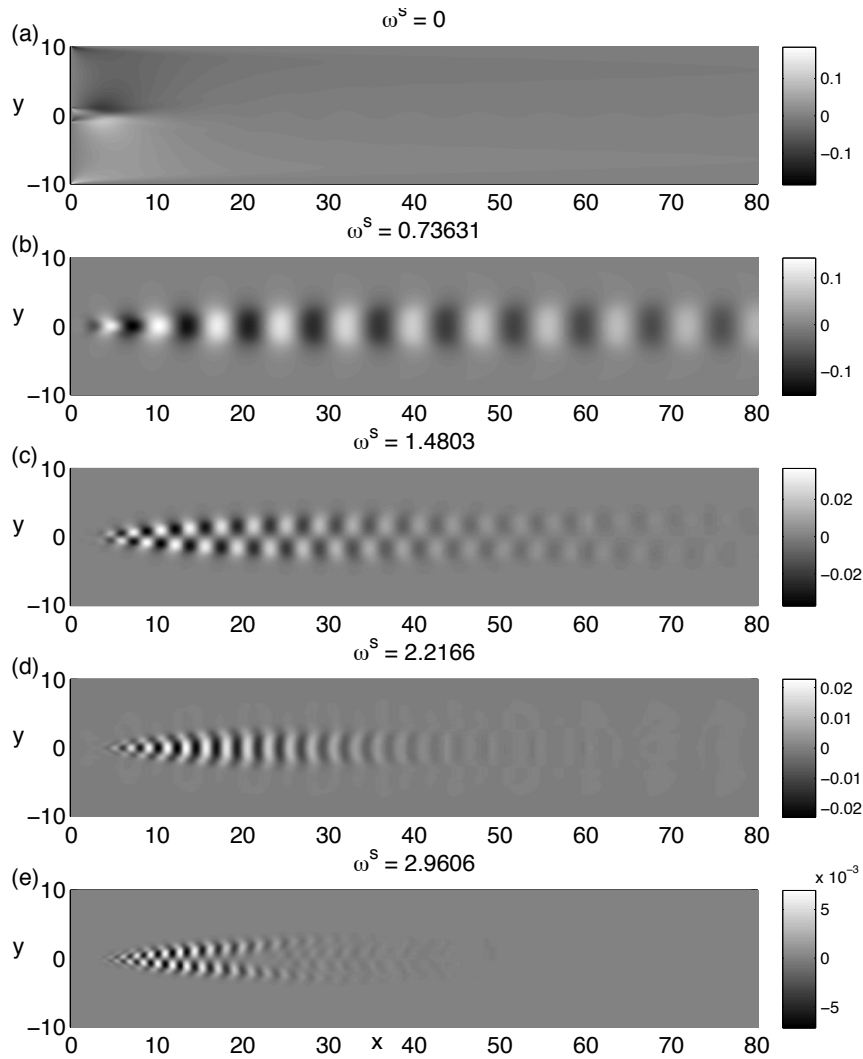


FIGURE 12. Reference case ($Re = 100$, $h = 9$, $\Lambda^{-1} = -1.2$) — the vertical velocity for: (a) the nonlinear mean flow, (b) the saturated nonlinear global mode, and (c)–(e) the first harmonics. The saturated frequency for each mode is given above respective plot.

4.2. Nonlinear results and comparison

The spectral density (PSD) distribution of the velocity signals for the reference wake (shown in figure 6) contains several peaks. The highest

peak is located at $\omega = 0$, with energy density PSD ≈ 100 , and it belongs to the mean flow. The next highest peak at $\omega^s \approx 0.73$ corresponds to the nonlinear global mode, and has the value PSD ≈ 1.6 . The first harmonic has twice the frequency of the global mode, and is almost equal in energy with the second harmonic, PSD ≈ 0.03 for both. The third harmonic has again an order of magnitude lower energy density (PSD ≈ 0.003), while the fourth and fifth are equal in amplitude at PSD ≈ 0.0004 .

It is described in section 7 how the spatial shapes of the mean flow, the global mode and its harmonics can be obtained by a Fourier-decomposition in time of the velocity and pressure fields. The streamwise velocity of the mean flow is shown in figure 11 (a), and is very similar to the steady solution shown in figure 9. An instantaneous streamwise velocity distribution of the nonlinear global mode is shown in figure 11 (b), and is similar, but not identical, to the real part of the streamwise velocity of the linear global mode in figure 10 (a). The wavelength and upstream shape of the linear and nonlinear global modes match, but further downstream the nonlinear one moves towards the walls and becomes more diffuse, in contrast to the linear one. However, their frequencies are very close, $\omega^l = 0.714$ and $\omega^s = 0.736$.

The streamwise velocity of the first harmonic is shown in figure 11 (c). It is symmetric, and positioned along the contours of the nonlinear global mode in the vertical direction, but it has a more refined spatial structure than the global mode — the phase changes sign twice in the vertical direction. Also, it is located closer to the inflow than the global mode. The same development continues when comparing the first harmonic to the antisymmetric second harmonic (figure 11 d) and the symmetric third harmonic (11 e). The vertical velocities of the mean flow, global mode and the same harmonics are seen in figure 12 (a–e). From the amplitude distributions shown by the colorbars it can be seen that the global mode provides an almost equal contribution to the total vertical velocity as the mean flow does. Notice also the shape of the vertical velocity for the nonlinear global mode. It is evidently similar to the vertical velocity of the linear global mode in figure 10 (b), but extends further downstream. Since the linear and nonlinear global mode are the focus of the present work, the harmonics will not be considered further.

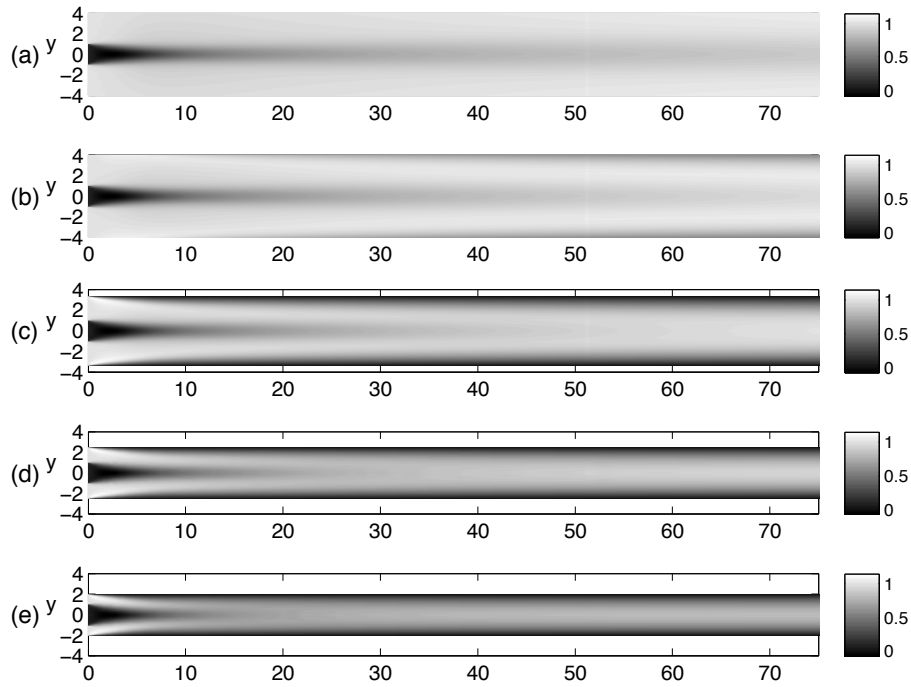


FIGURE 13. Base flows for different values of confinement ($Re = 100$, $\Lambda^{-1} = -1.2$): (a) $h = 9$, (b) $h = 4$, (c) $h = 2.33$, (d) $h = 1.5$, (e) $h = 1$. The plots show distributions of streamwise velocity, where high velocity regions are light, and low or reverse velocity regions dark. For ease of comparison, all plots have the same vertical and streamwise length scales, *i.e.* for the two uppermost wakes the walls are located outside the axis limits. The figures need to be stretched by a factor 2.5 in the streamwise direction to get the physical aspect ratio.

5. Stability results for confined wakes

5.1. Stability vs. confinement

In this section the stability of the wake is studied with different values of confinement while holding both the Reynolds number $Re_{wake} = 100$ and the shear $\Lambda^{-1} = -1.2$ constant. The confinement parameter ($h = h_1/h_2$, see figure 2) goes from the almost unconfined $h = 9$, where the total channel width ($h_1 + h_2$) is ten times the wake width (h_1), to $h = 1$, where the channel is only twice as wide as the wake. For all wakes, the

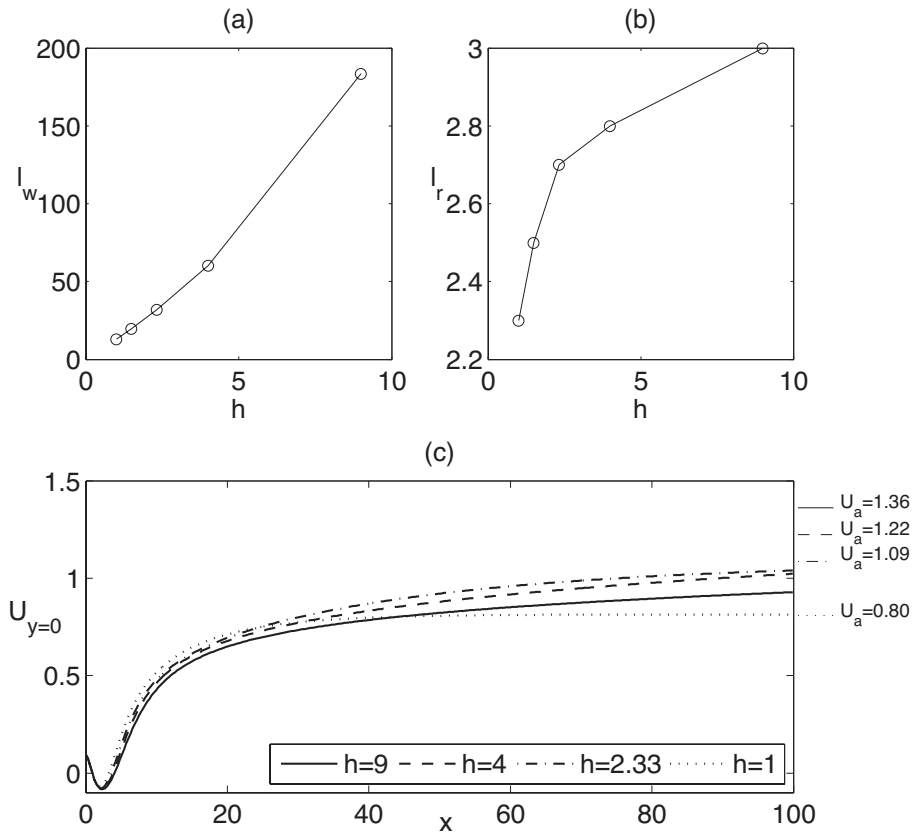


FIGURE 14. Characteristics of the base flow for different degrees of confinement at $Re = 100$, $\Lambda^{-1} = -1.2$: (a) the wake length, (b) the length of the reverse flow region, and (c) the centreline velocity. The asymptotic values of the centreline velocity far downstream assuming parabolic velocity profile (U_a) are given with respective line style to the right of (c).

inflow profile mimics the inviscid shear layer, but the development of the viscous flow field is altered by confinement in several ways.

Base flows for different confinements are shown in figures 13 a-e, with decreasing h (more confined wake) from top to bottom. We quantify the wake length l_w as the point where the streamwise velocity of the centreline has reached 75 % of the value for a fully developed channel flow profile, where the threshold value is chosen arbitrarily. The wake length is shown in figure 14 (a) and decreases monotonously with confinement,

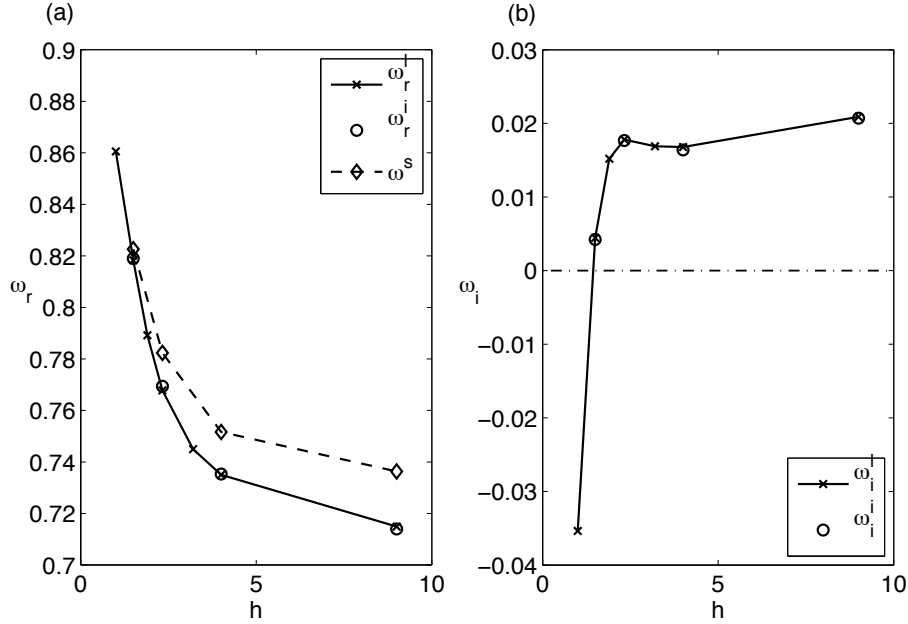


FIGURE 15. (a) The most unstable linear, nonlinear initial and nonlinear saturated frequency and (b) linear and nonlinear initial growth rate, as functions of confinement, at $Re = 100$, $\Lambda^{-1} = -1.2$. Linear data points: $h = 9, 4, 2.33, 1.5$ and 1 , nonlinear data points: $h = 9, 4, 2.33$, and 1.5 ($h = 1$ stable).

from $l_w \approx 183$ for $h = 9$ to $l_w \approx 60$ for $h = 4$, and further to $l_w \approx 13$ for $h = 1$. At the same time, the length of the reverse flow region l_r shrinks from $l_r = 3$ to $l_r = 2.3$ with confinement (figure 14 b), while the minimum value of the velocity (in the point of maximal reverse flow) increases slightly from $U_r = -0.08$ to $U_r = -0.07$. In figure 14 (c), the centreline velocity of the base flow is shown inside the domain for the stability calculations, from $x = 0$ to $x = 100$. It can be seen that the shortening of the wake leads to an increased centreline velocity for $h = 4$ and $h = 2.33$ in this region, compared to the unconfined wake.

These changes of the base flow clearly have an influence on the global stability of the wake: This is exemplified by the crosses connected by a solid line in figure 15 depicting ω_r^l (left) and ω_i^l (right) for the most unstable eigenvalue for linear global modes in each case. As the confinement parameter h goes from 9 to 1, the general trend is that the growth rate ω_i^l decreases (the flow is stabilised), and the frequency ω_r^l

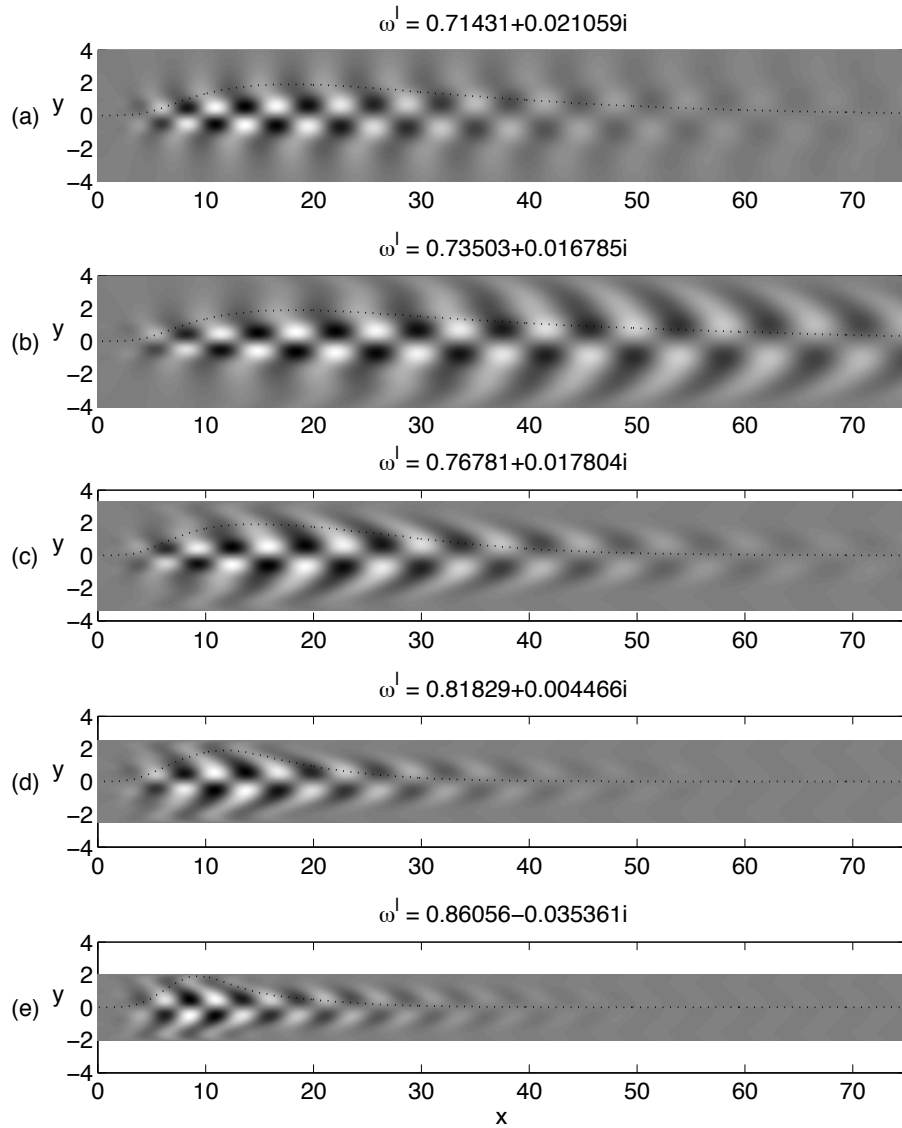


FIGURE 16. Real part of the streamwise disturbance velocity \hat{u} corresponding to the linear eigenvalues ω^l in figure 15, from up and down: $h = 9, 4, 2.33, 1.5$ and 1 . In other words, the walls move closer to the wake from up and down. The amplitude distribution of \hat{u} , scaled with 1.99 times the maximum amplitude, is given by the dotted line on top of each figure. The colormap in all figures is scaled with the maximum amplitude of \hat{u} . The figures need to be stretched by a factor 2.5 in the streamwise direction to get the physical aspect ratio.

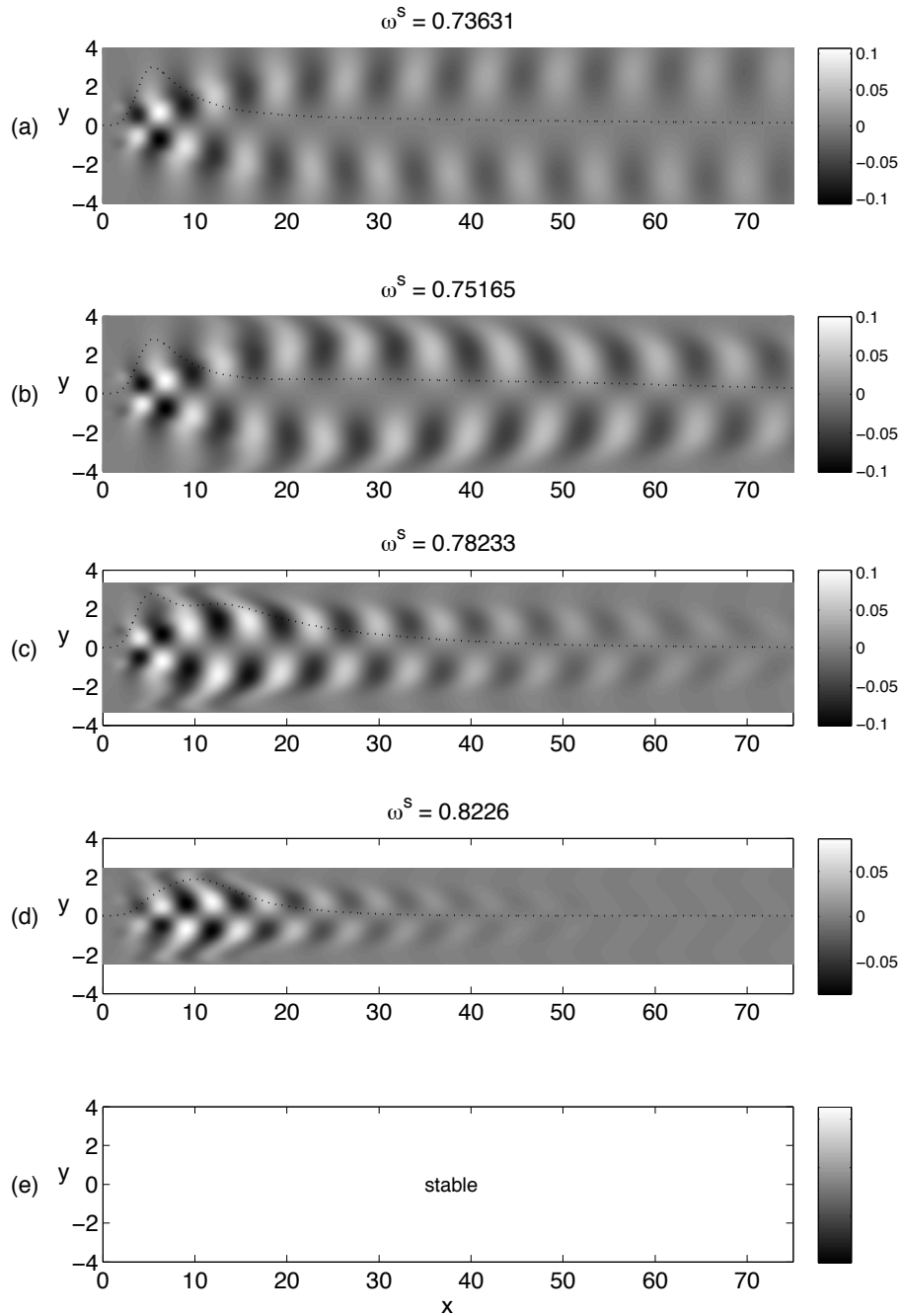


FIGURE 17. An instantaneous streamwise velocity of the non-linear global mode, corresponding to ω^s in figure 15, from up and down: $h = 9, 4, 2.33$, and 1.5 . As indicated in the figure, the case $h = 1$ is stable. The amplitude distribution of the streamwise velocity of the global mode, scaled with 3 times the maximum amplitude for the unconfined wake, is given by the dotted line on top of each figure.

increases, the latter in agreement with previous studies. For $h = 1$, the wake becomes stable. Observe in the previous figures that there is still a considerable amount of reverse flow for this wake, so the length or strength of the reverse flow region seems not to be the only criterion to determine the stability. Note also that as h goes from 4 to 2.33, the wake is actually slightly destabilised by the confinement.

Figure 16 shows the real part of the streamwise velocity distribution of the disturbance, \hat{u} , for the five wakes. Also here, two different trends are observed as the flow is confined. Focus first on the development from $h = 4$ to 1 (the four lower panels). The wavelength of the mode, *i.e.* the streamwise distance between two consecutive peaks, decreases with confinement (and thus with the increasing frequency, indicating a nearly constant phase velocity). The *envelope*, *i.e.* the streamwise extent of the mode, is seen to be generally shorter for the more confined flows. This is further illustrated by the dotted lines on top of the figures representing the distribution of $\max_y |\hat{u}(y)|$ in the streamwise direction. The envelope can be assumed to reflect the balance between energy production and convection, which would mean that the reason for stabilisation with confinement is rather a decrease in production, than an increase in convection speed. This is in agreement with our hypothesis, that the slow-down of the high-speed fluid and a faster relaxation to the parabolic profile is the main cause of stabilisation. However, at the initial stages of confinement, when h is changed from 9 to 4 (the two top panels), both the wavelength and envelope of the mode increase. The latter is possibly related to the increased streamwise velocity of the base flow at the centreline (figure 14 c) for $h = 4$ compared to $h = 9$. This might in turn lead to that the convection velocity is increased. For $h = 2.33$ the centreline velocity is also strong, but the wake is slightly destabilised (increased production), and therefore the convection becomes less important, resulting again in a shorter mode. For the most confined wake, the convection velocity is lower than in other cases, and the mode stays localised even if it is stable.

For the nonlinear case, we have investigated the saturated frequency ω^s and the shape of the saturated oscillation, for the same parameters as in the linear case. In addition, the frequency and initial growth rate when the oscillation sets in (ω_r^i and ω_i^i) were determined, to see whether the transition happened via a state determined by the linear analysis.

The real and complex part of ω^i extracted from the initial phase of the nonlinear simulation are depicted by rings in figures 15, left and right. The agreement with linear analysis is excellent. Note that the values for $h = 1$ could not be determined, since this case was stable even in the nonlinear simulation. The saturated frequencies ω^s are also shown in the left figure. The trend is the same as in the linear case, frequency increases with confinement, and the values are within 5% from the linear frequency. The saturated frequency (the diamonds in figure 15 a) is somewhat lower than the linear one, with best agreement for small h . Note that the saturated state does not involve any temporal growth so that figure 15 (b) only contains ω_i^l and ω_i^i .

The instantaneous streamwise velocity of the saturated nonlinear global mode for each case is shown in figure 17. Even here, the envelope and wavelength of the mode become shorter with confinement, apart from $h = 4$. In the nonlinear case, also the amplitude of the saturated state has a physical meaning, and from the colorbars it is clear that the amplitude is smaller for the most confined wake near the stability boundary, but nearly constant otherwise. In the cases with a long envelope and a high saturation amplitude of the nonlinear global mode ($h = 4$ and $h = 9$), the shear layers in the mean flow are smoothed by nonlinear diffusion, and consequently the nonlinear modes are displaced towards the walls. For the most confined wakes, this effect is less important.

5.2. Influence of base bleed

It is known that base bleed, *i.e.* increasing the velocity of the inner part of the inflow to the wake, has a stabilising effect on unconfined wakes. Here we investigate the same phenomenon for a moderately confined wake ($h = 1.5$). The wake inflow velocity is increased so that the inverse shear ratio decreases from $\Lambda^{-1} = -1$ to $\Lambda^{-1} = -1.3$. A decreasing inverse shear ratio means reduced shear, *i.e.* a smaller velocity difference between the wake and the outer streams. Although not shown here, the wake length increases slightly with decreasing shear for these wakes, but the dominating effect is that the extent of the reverse flow region is reduced towards zero. The mean velocity also increases, resulting in a stronger convection. Figure 18 shows linear, initial nonlinear, and nonlinear saturated frequencies, for different shear ratios. As the shear is decreased, the flow is stabilised as expected. The growth rate of the linear mode and the amplitude of the nonlinear mode given by the relative maxima of the dotted lines decrease, until the wake is stable

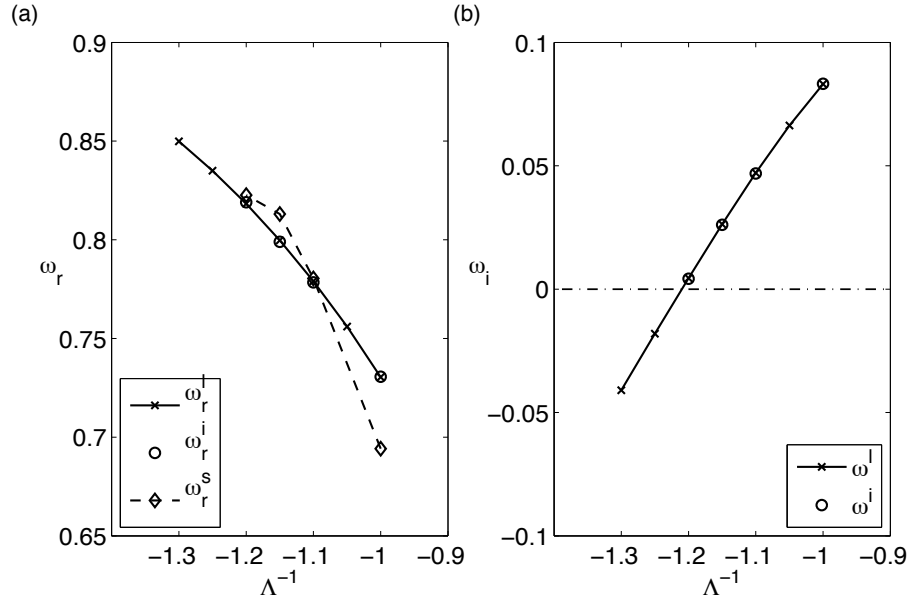


FIGURE 18. (a) The most unstable linear, nonlinear initial and nonlinear saturated frequency and (b) linear and nonlinear initial growth rate as functions of shear of the inflow Λ^{-1} , for $Re = 100$, $h = 1.5$. Data points for linear case: $\Lambda^{-1} = -1, -1.05, -1.1, -1.15, -1.2, -1.25$ and -1.3 , data for nonlinear DNS: $\Lambda^{-1} = -1, -1.1, -1.15$ and -1.2 ($\Lambda^{-1} = -1.3$ stable).

at $\Lambda^{-1} = -1.3$. Also, the frequency increases monotonously in both cases. The agreement between the linear and initial nonlinear frequency is very good, and the saturated frequency stays within 5 % of the linear frequency: it is slightly higher for $\Lambda^{-1} = -1.15$, and lower for $\Lambda^{-1} = -1$. As expected, the deviation increases when moving further from the neutral stability boundary (located at $\Lambda^{-1} \approx -1.21$).

The real part of the streamwise disturbance velocity distribution for the linear modes is shown in figure 19, and for the saturated nonlinear modes in figure 20. The effect of base bleed is monotonous and consistent: the disturbance envelope becomes more elongated and the maximum moves further away from the inflow, while the wavelength is nearly constant; less production and enhanced convection results in longer modes. This is more apparent for the linear than for the nonlinear modes, again due to the fact that the mean flow becomes slightly more diffusive than the base flow when the mode saturates. As the frequency

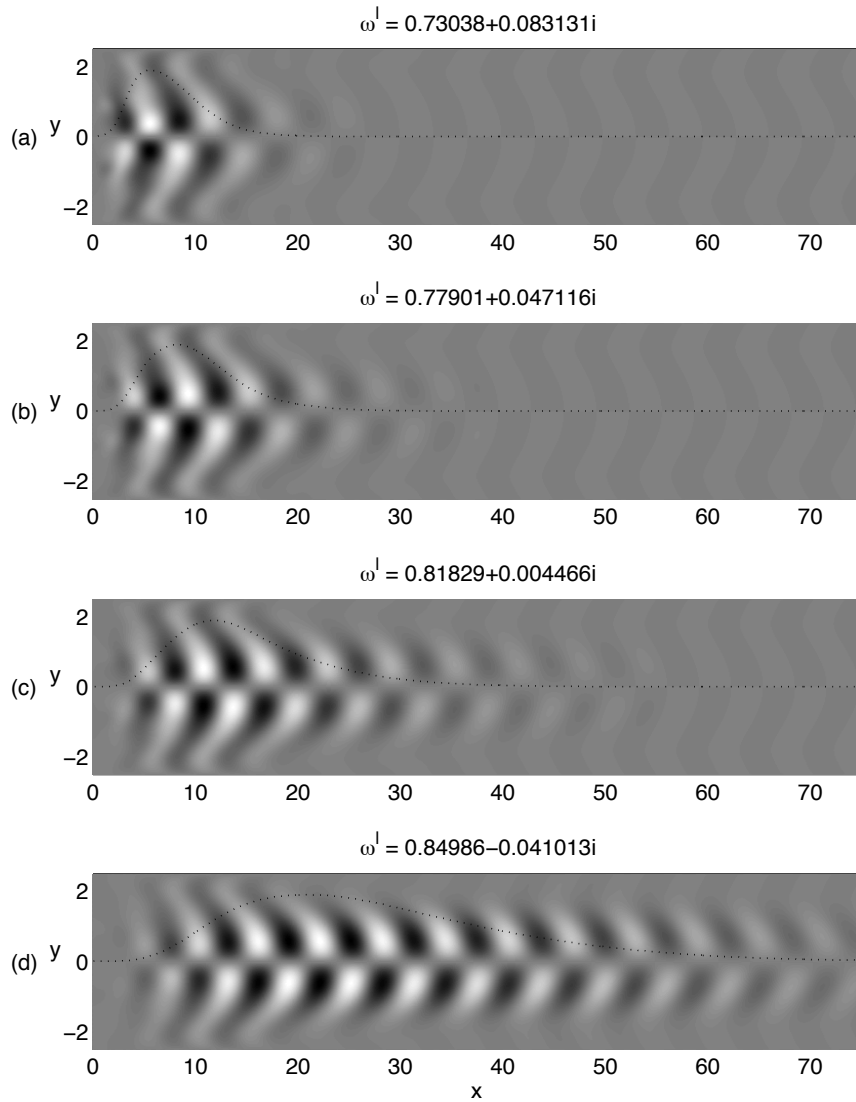


FIGURE 19. Real part of the streamwise disturbance velocity corresponding to the linear eigenvalues ω^l in figure 18 for different shear ratios, from top to bottom: $\Lambda^{-1} = -1, -1.1, -1.2,$ and -1.3 . In other words, the velocity of the outer streams U_1 increases from top to bottom. The amplitude distribution of \hat{u} , scaled with 1.99 times the maximum amplitude, is given by the dotted line. The colormap in all figures is scaled with the maximum amplitude of \hat{u} . The figures need to be stretched by a factor 2.5 in the streamwise direction to get the physical aspect ratio.

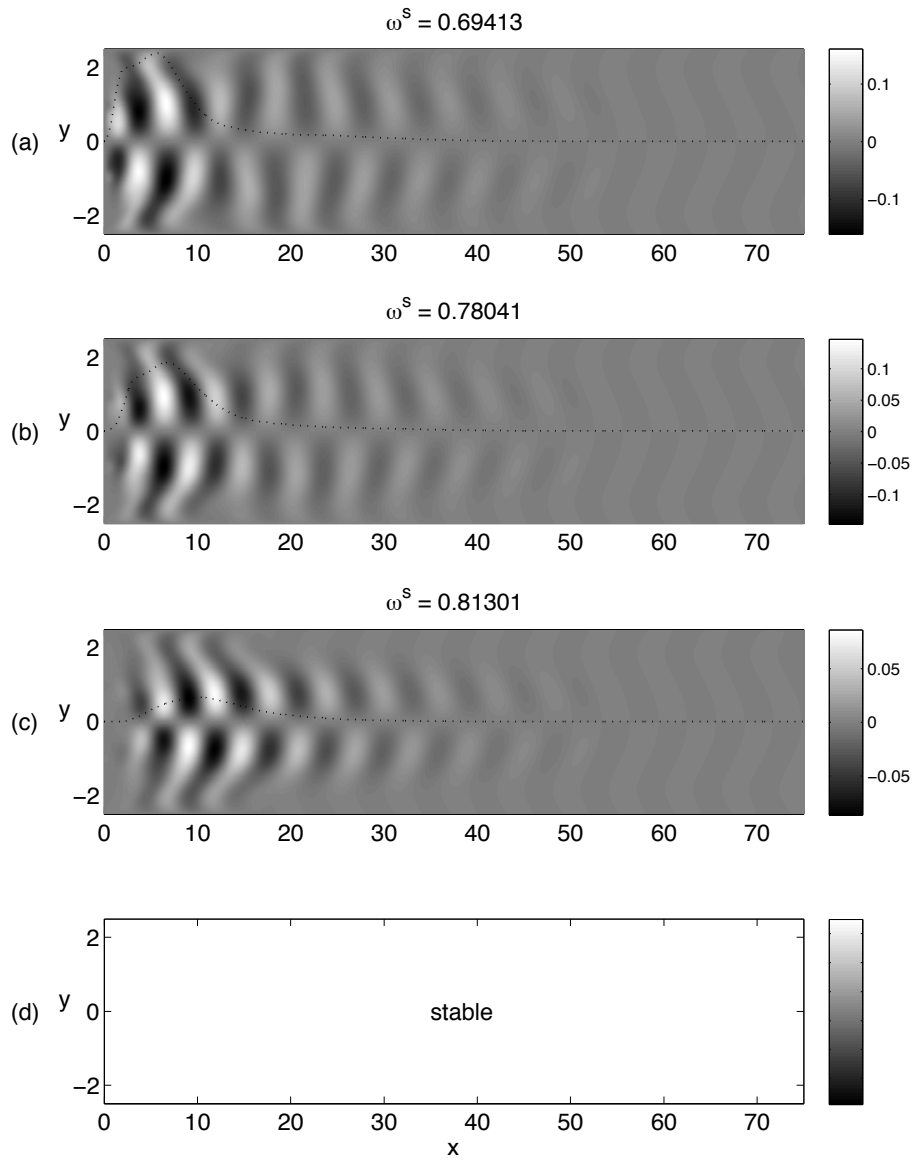


FIGURE 20. Instantaneous streamwise velocity of the nonlinear global mode, corresponding to ω^s in figure 18, from up and down: $\Lambda^{-1} = -1, -1.1, -1.2$ (case $\Lambda^{-1} = -1.3$ is stable). The amplitude distribution of the streamwise velocity of the global mode, scaled with 2.44 times the maximum amplitude without co-flow ($\Lambda^{-1} = -1$), is given by the dotted line.

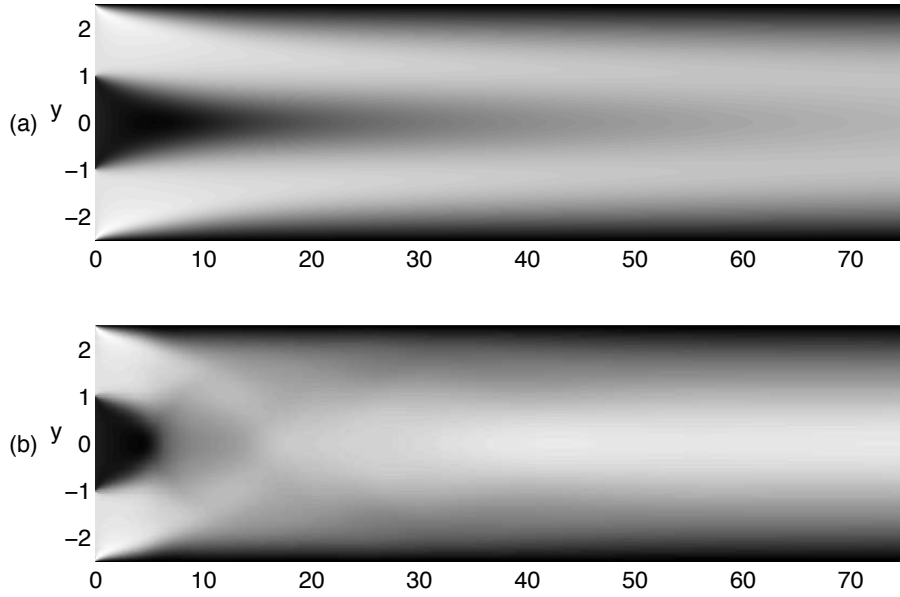


FIGURE 21. (a) Base flow and (b) nonlinear mean flow at $Re = 316$, $\Lambda^{-1} = -1.35$, $h = 1.5$.

increases, so does the phase speed of the waves, in accordance with common knowledge of local temporal instability in shear layers (the phase speed $c = (U_1 + U_2)/2$ for Kelvin-Helmholtz instability).

5.3. Increasing Reynolds number

For wakes at $Re = 100$ the linear analysis provided an excellent prediction of the initial nonlinear behaviour. Next, we will look at how the linear global stability limit evolves for higher Reynolds numbers, and the applicability of linear analysis in this parameter regime needs to be investigated.

We compare the linear and nonlinear result in a case near the global linear stability boundary (neutral curve): $Re = 316$, $h = 1.5$, $\Lambda^{-1} = -1.35$. At first sight, the comparison does not appear promising. The steady base flow and nonlinear mean flow are shown in figure 21. This wake is very close to the linear stability boundary (as will be shown, the growth rate is very small), but there is still a substantial nonlinear modification of the mean flow field. This is even reflected in the fact that the saturated frequency $\omega^s = 0.91$ and the linear frequency $\omega_r^l = 0.8392$ differ by almost 10 %, which is more than at lower Re . There are also

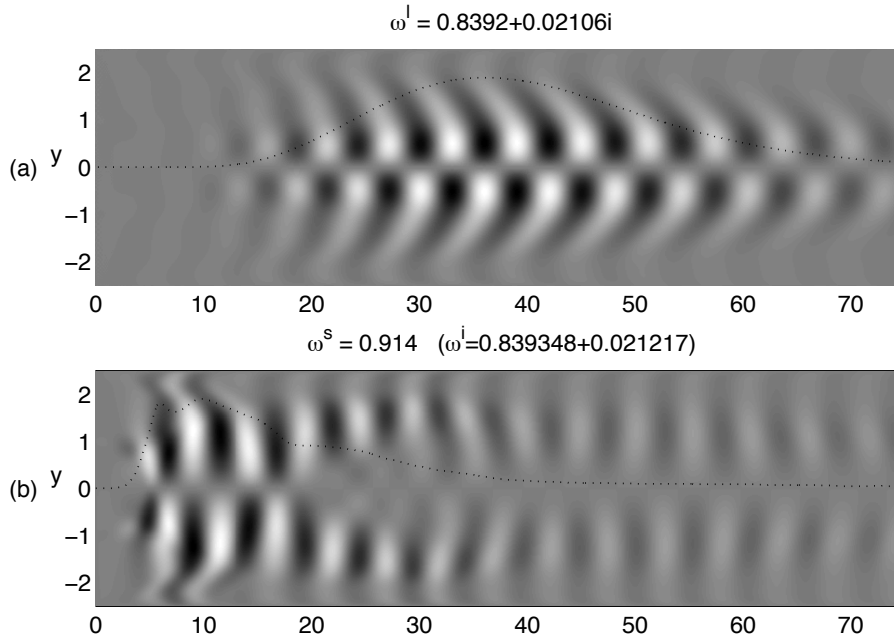


FIGURE 22. The instantaneous streamwise velocity of the (a) linear and (b) nonlinear global mode at $Re = 316$, $\Lambda^{-1} = -1.35$, $h = 1.5$. The amplitude distributions, scaled with 1.99 times the maximum amplitude in each case, are given by the dotted lines.

clear differences in the mode shape — the nonlinear global mode has a maximum amplitude at $x \approx 10$, while the entire linear global mode is located more downstream, the maximum lying at $x \approx 40$ (figure 22 a). In addition, the nonlinear mode is located further from the centreline than the linear one, due to the diffusion of the shear layers by means of the Reynolds stresses in the nonlinear setting. Recall that the same tendencies regarding mode shape were visible, but less apparent, for the two least confined wakes at $Re = 100$ (the uppermost plates in figures 16 and 17).

However, when we look at the initial frequency and growth rate in the nonlinear simulation (ω^i above the picture), they are again in excellent agreement with the linear analysis, up to three digits. When we repeated the analysis for another wake close to the linear stability boundary, $Re = 316$, $\Lambda^{-1} = -1.33$, we got the values $\omega^l = 0.8358 + 0.0333i$, $\omega^i = 0.8362 + 0.0329i$. Thus, we conclude that our linear global modes

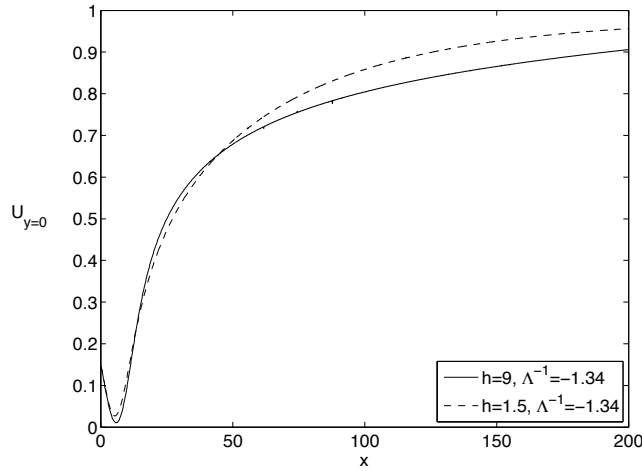


FIGURE 23. Development of the streamwise velocities at the centreline for a confined ($h = 1.5$) and unconfined ($h = 9$) wake at $Re = 316$, $\Lambda^{-1} = -1.34$.

still give an excellent prediction of the initial nonlinear behaviour, and consequently the stability boundary, of confined wakes also at $Re = 316$.

The confined wakes were seen to be more stable than the unconfined wakes for $Re = 100$. When comparing the previously defined base flow quantities again, for an unconfined ($h = 9$) and confined ($h = 1.5$) wake with the same value of inverse shear ratio ($\Lambda^{-1} \approx -1.34$), one finds that the wake length is still much larger in the unconfined case: $l_w > 350$ for $h = 9$ and $l_w = 59$ for $h = 1.5$. The centreline velocities are shown in figure 23 – notice also that none of these two wakes contains any reverse flow (compare figure 14 c).

Both wakes are slightly and almost equally unstable ($\omega_i^l \approx 0.02$), which seems to contradict the wake length analysis. However, looking at the velocities at the centreline in figure 23, we see that in a large streamwise region, between $x = 0$ and $x = 50$ they are very close, and differ from each other by maximum 2 % of the reference velocity. This could be compared to the case $Re = 100$, where the difference in the centreline velocity between wakes with $h = 9$ and $h = 1.5$ was of the order 10 % already in the interval $x = 0$ to $x = 5$. So, although the asymptotic decay rates for unconfined and confined wakes are still very different at higher Reynolds numbers, as are the entrainment lengths for the two channels, it is clear that the wake length effect is decoupled

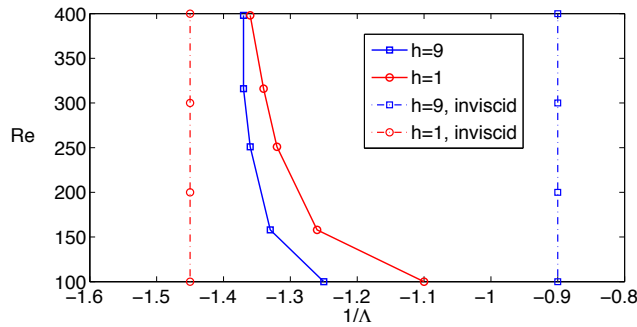


FIGURE 24. The neutral stability curves as a function of Λ^{-1} and Re for an unconfined ($-\square-$) and confined ($-\circ-$) wake. The region on the right side of the curve is unstable. The inviscid solution is also shown — unconfined ($--\square--$) and confined ($--\circ--$).

from the wake development in the upstream region of high shear. Either this is the most important region deciding the stability of the flow, or there are other competing mechanisms. This also confirms what was previously seen for $Re = 100$, that neither the wake length nor the length or strength of the reverse flow region alone is enough to completely characterise the stability behaviour.

To further quantify the effect of confinement on the stability limit, we compare one confined wake ($h = 1$) with an unconfined wake ($h = 9$) at a few different Reynolds numbers. Figure 24 shows the neutral stability curves for both in the Λ^{-1} - Re -plane. The region on the right side of all curves is unstable. As was shown in the previous sections, for $Re = 100$ the stability limit of the unconfined wake is at higher inflow velocities than the confined one; the unconfined wake is more unstable. This is also the case for the higher Reynolds numbers tried, $Re = 150$ – 400 , but the stability limits gradually approach each other.

6. Discussion

The wake developing from our inflow profile often has a region of reverse flow and is unstable even for low Reynolds numbers, and by changing the defining parameters many different wakes with varying characteristics can be generated. For this reason the present wake flow provides a suitable flow case for comparison of local weakly non-parallel (WNP), global linear and nonlinear stability results. A specific goal of the present work is to demonstrate the general agreement between global linear and nonlinear methods as well as to point out the differences. This work

therefore also provides a firm base for a future comparison with a local WNP analysis using the same base flow fields.

The basic mechanism behind local absolute instability in jets and wakes is known to be of inviscid nature (Yu & Monkewitz 1990), and the absolute instability of parallel, inviscid co-flow wakes has been well characterised: unconfined (*e.g.* Huerre & Monkewitz (1990)) and confined (Juniper 2006). However, the spatial development of the flow field caused by viscosity can still be important when determining the global stability limits for real confined wakes and jets. In the linearised setting, this influence can be divided into two parts:

- (1) the degree and type of confinement has a considerable effect on the base flow profiles, and
- (2) also the disturbance itself satisfies a no-slip condition at the confining walls, and this might affect the shape of the disturbance and consequently the stability properties.

Our results indicate that the mechanism (1) dominates for co-flow wakes in the studied parameter regime. In particular, the length of the high shear or reverse flow region is known to be important for the onset of global instability, and this length is clearly influenced by the base flow development. Below, we discuss four aspects (the relation between linear and nonlinear stability, the effect of boundary condition at the walls, the relation between local absolute and global stability, and finally similarities to confined cylinder wakes) of wake instability in the light of our present results and the literature.

6.1. Linear and nonlinear stability

The differences in the shapes of linear and nonlinear global modes especially at the higher Re (see *e.g.* figure 22) might be in accordance with local nonlinear theory. This theory, summarised *e.g.* by Chomaz (2005), predicts that the frequency selection and saturated shape of the nonlinear global mode is determined in a station upstream of the linear global mode. For nonlinear modes of the so-called pulled-front type, the selection occurs at the first locally absolutely unstable point. Chomaz (2005) further suggests that the efficiency of linear global modes as predictors of flow dynamics is dependent on the normality of the global linear operator (higher degree of non-normality gives a worse predictor). Consequently, the linear global modes should be better suited for strongly non-parallel flows than for almost parallel flows.

In our case, the frequency agrees well at low Re but differs approximately 10% between the linear global method and nonlinear simulations

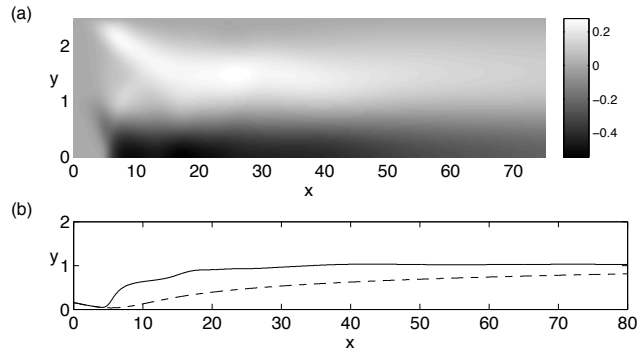


FIGURE 25. (a) The spatial distribution of the deviation between the streamwise velocity of the base flow and mean flow shown in grayscale; case $Re = 316$, $h = 1.5$ and $\Lambda^{-1} = -1.35$. Both wakes are symmetric with respect to the centerline, and only the upper half is shown here. Dark regions indicate that the base flow velocity is slower than the mean flow velocity, and light regions the other way around. (b) The streamwise velocity at the centerline: nonlinear (solid line) and linear (dashed line).

at $Re = 316$. The base flow becomes more parallel for higher Reynolds numbers, and the mode in figure 22 (b) indeed resembles the pulled-front nonlinear global mode, the dynamics of which was suggested to be described by local nonlinear theory by Chomaz (2005). For the Ginzburg-Landau equation, it has been shown that the nonlinear global mode can occur even when all linear modes are stable (Pier, Huerre & Chomaz 2001). It is possible that the final frequency is indeed selected by a local mechanism for our flow. However, the initial nonlinear frequency and growth rate was captured exactly by our linear analysis also for this case, cross-validating the two very different numerical approaches. The route to transition from a steady flow to a saturated oscillation is through the unstable linear global mode in our DNS, and does not occur if the global modes are stable. This confirms that properly converged linear global modes can predict the stability limit also for fairly parallel flows.

Several authors have connected the nonlinear behaviour of wakes to local or global linear analysis performed around the mean flow (Hammond & Redekopp (1997), Camarri & Giannetti (2007)) rather than around the steady solution to Navier-Stokes that has been used in the

present work. This approach often yields good agreement between linear and nonlinear results for cylinder wakes (Camarri & Giannetti 2007), but not for *e.g.* open cavities, as shown by Sipp & Lebedev (2007). The deviation between the stationary base flow and the nonlinear mean flow is shown in figure 25 for $Re = 316$, $h = 1.5$ and $\Lambda^{-1} = -1.35$. Due to the Reynolds stresses in the nonlinear (oscillatory) flow, the wake shortens, which is especially visible in the centerline velocities shown in figure 25 (b). Also, the boundary layers develop faster. Thus, these differences could explain the differences between the linear mode in figure 22 (a) and the nonlinear mode in 22 (b). However, preliminary studies indicate that the linear global mode computed around the mean flow as such does not coincide with the nonlinear global mode in this case. It is possible that the Reynolds stresses not only affect the mean flow shape, but also the disturbance, and that these has to be accounted for in the stability analysis.

6.2. Relation to wakes with slip condition at the walls

Recently, Biancofiore *et al.* (2010) performed DNS on confined wakes with a slip condition at the channel walls. They concentrated on defining the parameter regions for which the nonlinear oscillation appears, for two different wake Reynolds numbers: $Re = 100$ and $Re = 500$. In contrast to our results based on no-slip conditions, they find that confinement is weakly destabilising for $Re = 100$, while for $Re = 500$ the stability limits for unconfined and confined wakes approach each other, in agreement with our findings. We suggest that the different base flow development, resulting from the change in wall condition, is the dominant factor behind the discrepancy at $Re = 100$. This suggestion is supported by linear global mode analysis of base flows with slip and no-slip at $Re = 100$ by Tammissola (2009). In this comparison, it was seen that with increased confinement (decreasing h), the wake length increases for the slip case but decreases for the no-slip case. This base-flow difference was reflected in the linear global modes. Longer wakes give longer amplitude distributions, higher growth rates and lower frequencies.

Biancofiore *et al.* (2010) also track the appearance of local absolute instability in their base flow for selected flow cases. For the six example cases chosen at $Re = 500$, a nonlinear oscillation is observed if and only if there is absolute instability. In some applications, a rough approximation of the stability boundary is sufficient, while in others one would like to have quantitative description of the neutral curve, frequencies, and

possibly mode shapes. Their result is however promising for the local method, and promotes a WNP study of the whole flow field for our as well as their flow.

6.3. Relation to local absolute instability of inviscid wakes

As mentioned in the introduction, the inviscid local stability of our inflow profiles was studied by Juniper (2006). In figure 24 the stability limits of Juniper (2006) (limits of the gray region in figure 4 at $h = 9$ and $h = 1$) are shown with vertical lines. Our global confined wake ($h = 1$) is more stable than the local inviscid wakes. The main reason to this is clear: the wakes get weaker as the viscous flow develops towards the full parabolic profile. This development occurs in a shorter streamwise distance for the confined cases. On the other hand, the unconfined viscous wake ($h = 9$) is more unstable than the inviscid wake. This is probably due to a region of reverse flow that appears one or two wake heights downstream from the inflow in the viscous developing flow. However, it is intriguing to see that even the unconfined wakes without reverse flow are unstable for higher Re , while in the inviscid analysis the neutral stability limit goes to $\Lambda^{-1} = -0.9$. In Rees & Juniper (2010) it was shown that thicker shear layers than in the inviscid profile result in a slightly broader instability region for unconfined wakes. Another reason to the deviation could be that the flow is still more than weakly non-parallel, also at higher Re . Further comparisons with the viscous model profiles by Rees & Juniper (2010) are omitted here, since their parameter combinations are not representative for our inflow profile.

6.4. Relation to confined cylinder wakes

While co-flow wakes have been mostly studied by employing the local approach, the effect of confinement on a wake behind a cylinder has been widely investigated by direct numerical simulations and experiments in a global sense.

Experiments on wake instability behind cylindrical rods confined in a channel were performed by Shaw (1971) and Davis *et al.* (1984) for a rectangular cross-section of the rod, and by Richter & Naudascher (1976) for a circular cross-section. The inflow velocity to the channel was kept fixed, while the cylinder-to-channel diameter ratio was varied from 0.05 to 0.35 (Shaw 1971) and 0.167 to 0.5 (Richter & Naudascher 1976). All studies report a substantial increase in the non-dimensional frequency for confined flows compared to unconfined ones, up to 12 %. This is consistent with our results (figure 15). In the linear analysis for

$Re = 100$, we observed a monotoneous increase from $\omega^r = 0.72$ ($h = 9$) to $\omega = 0.86$ ($h = 1$), and the nonlinear results are in good agreement.

When it comes to stability, Richter & Naudascher (1976) reports increased amplitude of the lift-force oscillations with confinement, which could be coupled to destabilisation. Furthermore, a DNS study of square cylinders by Suzuki *et al.* (1994) reported that the critical Reynolds number (based on the cylinder height) decreased with confinement; if, instead, Re was based on total channel height, the trend was the opposite. When comparing results from confined flow around obstacles with the present co-flow wakes, several issues arise. For flow around obstacles, the Reynolds number is typically based on the mean velocity in the channel and the height of either the channel or the obstacle. In our case, the Reynolds number is based on the outer velocity U_2 , which would correspond to the velocity of the accelerated flow in between the obstacle and the wall. Furthermore, the wakes behind obstacles typically have no co-flow in the wake (a special case of the present work) and the separation point might fluctuate. Nevertheless, the present results on co-flow wakes suggests that the complete mean flow development, including wake length and reverse flow regions (*e.g.* Richter & Naudascher (1976) report an increase of reverse flow velocity with a factor of 15 at a flow case corresponding to $h = 2$), has to be documented in order to understand and explain the effects of confinement on wakes behind obstacles. Further interpretation of our results in this context is out of the scope of the present work

7. Conclusions

In this paper, global stability of spatially developing co-flow wakes has been analysed as a function of confinement and shear of the inflow for low to moderate wake Reynolds numbers ($Re = 100 - 400$), with linear global modes and direct numerical simulations. The main results are:

- Base flow development is important for the linear stability of the confined co-flow wakes in this parameter regime.
- For $Re = 100$ the flow is stabilised by confinement due to a faster relaxation of the confined wake towards a parabolic profile, compared to an unconfined wake.
- For $Re = 300 - 400$ the base flow upstream for confined and unconfined wakes is similar, and the stability limits approach each other.

- For $Re = 100$ the nonlinear saturated frequencies differ from the linear ones by at maximum 5%.
- For $Re = 300 - 400$ the difference between linear and nonlinear saturated frequency is of the order 10%, even close to the stability limit.
- Nonlinear stability limits and initial nonlinear frequency and growth of the oscillation in perfect agreement with the linear ones for all wakes at all Re under study.
- The saturated nonlinear oscillation shape is similar, but its amplitude distribution differs from the linear one, in increasing amount for higher Reynolds numbers, when the mean flow becomes more parallel (as well as the base flow).

Our results indicate that the extension of a region with high shear in the flow is the most important factor for deciding the stability of confined co-flow wakes at low to moderate wake Reynolds numbers. Since the flow development for co-flow wakes, in contrast to cylinder wakes, seems to be unaffected by confinement for moderate Reynolds numbers, it would be of interest to see whether this is true for high Reynolds numbers as well, by tracking the wake length and reverse flow region, as well as invent better measures to characterise the high shear region in the flow. Base flows as well as nonlinear flow fields could rather easily be computed for higher Reynolds numbers than presented here.

We also conjecture that confinement by decreasing channel height while keeping the flow rate constant could be destabilising, due to increasing shear ratio, as well as increasing wake length. However, for our Reynolds numbers, we could not identify the inviscid destabilising mechanism of confinement proposed by Juniper (2006), and neither could this be seen in the DNS of Biancofiore *et al.* (2010). This mechanism might still appear, and possibly be dominant, for high Reynolds number co-flow wakes.

In future work, it would also be interesting to consider the adjoint linear global modes and the associated wavemaker region to these wakes, to confirm the observations regarding base flow development and confinement effects, and for comparison with cylinder wakes. A full comparison between local and global analysis (linear as well as nonlinear in both cases) is also a logical next step, to further elucidate to which extent the local methods can be applied to real spatially developing co-flow wakes.

N_x	N_y	$h = 1$ & $\Lambda^{-1} = -1.15$	$h = 1$ & $\Lambda^{-1} = -1.35$
100	60	$0.838540 - 0.012176i$	$0.915644 - 0.108935i$
150	60	$0.838547 - 0.012185i$	$0.915917 - 0.109439i$
180	60	$0.838549 - 0.012165i$	$0.915932 - 0.109460i$
N_x	N_y	$h = 9$ & $\Lambda^{-1} = -1.2$	
100	60	$0.714911 + 0.020903i$	
150	60	$0.714383 + 0.021059i$	
180	60	$0.714349 + 0.021082i$	

TABLE 1. Convergence of the most unstable linear eigenvalue ω^l with grid refinement in x -direction ($d = 0$, $L = 80$).

The authors would like to thank Prof. M.P. Juniper for providing figure 3, where an absolutely unstable region in his analysis is shown. O. Tammisola also would like to thank Johan Malm at KTH Mechanics for introducing her to the Nek5000 software. The project has been financed by the project Ecotarget in the 6th EU Framework Programme, and the Swedish Research Council (VR).

Appendix A. Convergence analysis

The linear and nonlinear results were verified with respect to grid refinement and streamwise boundary conditions. In tables 1–2, the most unstable linear eigenvalues for three example wakes can be found:

- (1) A marginally globally unstable confined wake: $h = 1$ and $\Lambda^{-1} = -1.15$,
- (2) a globally stable confined wake: $h = 1$ and $\Lambda^{-1} = -1.35$, and
- (3) a globally unstable very weakly confined wake: $h = 9$ and $\Lambda^{-1} = -1.2$.

Convergence is obtained at least for two decimal places for both frequency and growth rate in all cases, which shows that the results are convergent to this amount with respect to grid refinement (table 1) and length of the computational box, L , *i.e.* independent of the outflow boundary condition (table 2).

The linear results proved to be quite insensitive on the number of collocation points in the vertical y -direction (N_y), while in the streamwise x -direction the necessary number of polynomials (N_x) increased rapidly with increasing domain length. Therefore, we emphasise the results for the resolution check in the x -direction in table 1.

L	N_x	N_y	$h = 1$ & $\Lambda^{-1} = -1.15$	$h = 9$ & $\Lambda^{-1} = -1.2$
80	100	60	$0.838540 - 0.012176i$	$0.714911 + 0.020903i$
120	150	60	$0.838538 - 0.012174i$	—
120	200	60	—	$0.714315 + 0.021059i$

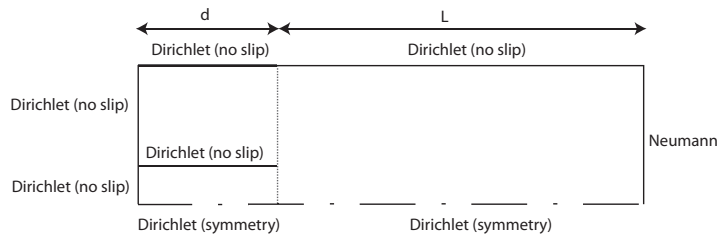
TABLE 2. Convergence of ω^l with box length ($d = 0$).

FIGURE 26. Illustration of the parameters and disturbance boundary conditions in the test domain used for the second boundary condition independency test, performed with COMSOL Multiphysics.

To see the effect of the inflow boundary condition we initially performed a simulation with a different software, COMSOL Multiphysics, that was able to handle most of the unstable flow cases. A damping region was introduced by moving the inflow boundary to the stability problem upstream from the actual computational domain, and creating two channels (figure 1 a) for the outer stream and wake, respectively, where the base flow velocity in each channel was set to a constant value, equal to 1 in the outer and $U_2 = (\Lambda^{-1} + 1)/(\Lambda^{-1} - 1)$ in the inner channel. To prevent any shear layer instability due to this extensional region a no slip condition (cmp. splitter plate) was set between the two channels. The test configuration along with boundary conditions is illustrated in figure 26. The aim was purely to see whether a change in the location of the upstream boundary condition would alter the stability. This together with the outflow boundary condition gave us two variables: domain length L and length of the damping region d , and the effects could be analysed and compared.

The most unstable eigenvalue was calculated as a function of Λ for a weakly confined wake ($h = 10$), for varying L and d . The growth rate ω^i is shown as a function of Λ^{-1} in figure 27. It is seen that the length

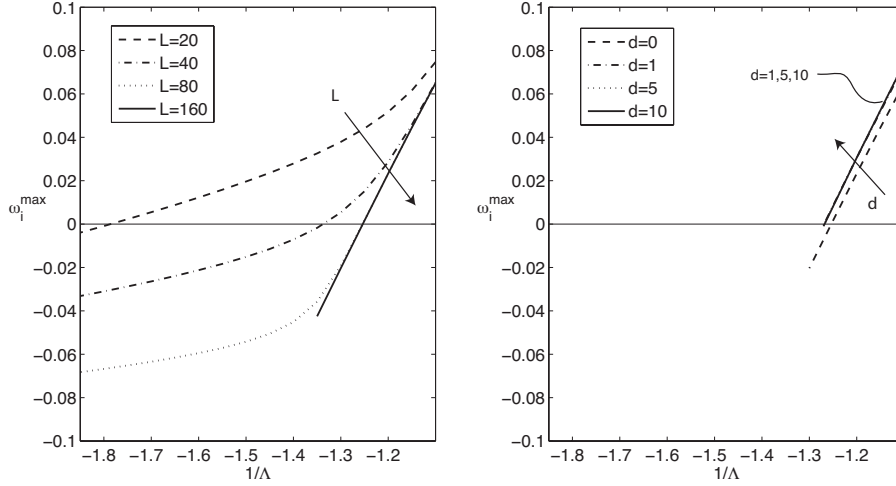


FIGURE 27. The convergence of the most unstable linear eigenvalue ω^l and the stability limit, with respect to L (left) and d (right) for a weakly confined wake: $h = 10$.

N_x	N_y	$\omega^{s,1}$	$\omega^{s,2}$	$\omega^{s,3}$
26	15	0.8015	1.6068	2.4083
36	20	0.8053	1.6162	2.4215
52	30	0.8130	1.6183	2.4314

TABLE 3. Convergence of the frequencies of the nonlinear global mode and first two harmonics with h -refinement, at $Re = 100$, $h = 1.5$ and $\Lambda^{-1} = -1.2$. Domain length $L_x = 100$ and polynomial order $N = 7$. N_x and N_y denote the number of elements in the respective coordinate directions.

of the domain is of considerable importance for the stability. Stable modes can be forced to be unstable with a too short domain; $L = 20$ gives a largely overestimated instability region ($\Lambda^{-1} \lesssim -1.75$), while for $L = 80$ the stability limit is converged ($\Lambda^{-1} \lesssim -1.27$). We believe that this is an effect of an unphysical disturbance outflow condition only, and not due to that the base flow development far downstream would have implications on stability.

The results for the length of the damping region d are shown in figure 27 (b). There is a minor effect on the location of the neutral curve in the

$h\Lambda$ -plane — a convergent result was obtained for $d = 1$. For smaller h , the effect was slightly larger, and a region of length $d = 2$ was required for convergence. However, the change was not considered to be large enough to require an implementation of the extensional region in the actual Chebyshev-Chebyshev stability code. Such a region in that code would require a multi-domain approach in the stability problem, and result in a considerably increased complexity. In addition, the damping region concept would have been difficult to realise in the nonlinear simulations.

In the nonlinear case, the domain length was chosen with the linear results as a guideline. For a few specific cases, the adequacy of the chosen grid was verified by both a grid refinement study as well as by changing the domain length, see table 3. In a first series, a h -refinement, *i.e.* an increase of the number of spectral elements, was performed on an example wake with $h = 1.5$, $\Lambda^{-1} = -1.15$, $Re = 100$, $L = 100$ using three non-equidistantly distributed grids and a fixed polynomial order $N = 7$. The finest grid used in this convergence study (or a grid with a similar resolution for weakly confined wakes) is then used for runs in the present paper. To further ensure that the nonlinear results are not affected by the numerical choice, an additional p -refinement test (increasing polynomial order) for a wake with $h = 4$, $\Lambda^{-1} = -1.2$, $Re = 100$ was performed, where in addition the box length was changed from $x = 100$ to $x = 160$. The computed frequencies did not change for these latter cases given the temporal resolution of the PSD calculation. This indicates that the grid for the nonlinear DNS (extent, number of elements and polynomial order) is indeed appropriate.

Appendix B: Determination of the nonlinear oscillation characteristics

In the following, we will go through the numerical procedure for extracting the nonlinear result from the simulation data in detail. For illustration, we use the flow case where $Re = 100$, $h = 9$ and $\Lambda^{-1} = -1.2$, *i.e.* the practically unconfined reference wake to which all confined wakes are compared in the coming sections.

In each flow case, an initial simulation is performed, where the time signal in nine selected points of the flow field (the points depicted by rings in figure 28) is followed more carefully. To obtain a temporal high-resolution signal and avoid aliasing errors, the velocity data in these points is stored in double precision binary format at every 10 time steps. One of these time signals (recorded at $x = 10$, $y = -1$) for the example

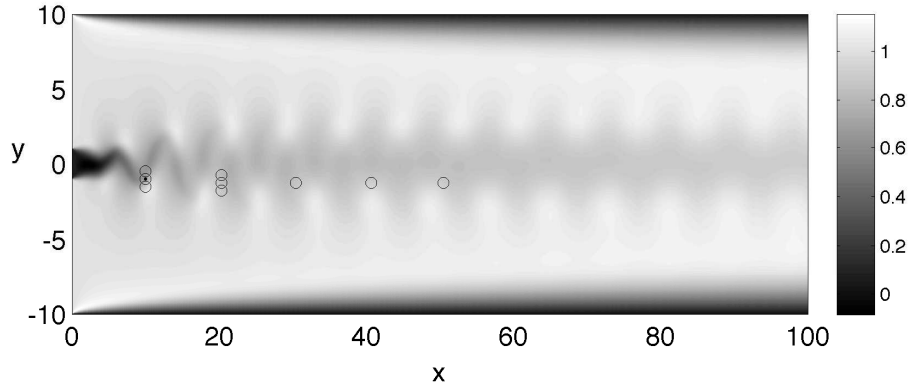


FIGURE 28. The whole instantaneous streamwise velocity field with fluctuations at $t=2000$ ($Re = 100$, $h = 9$, $\Lambda^{-1} = -1.2$). Rings depict points where time signal history was collected. The time signal from the position marked with a dot inside the ring is shown in figure 29.

flow case is shown in figure 29 (a). The obtained time signal contains the whole history of the flow simulation for the spatial point where it was recorded, and can be divided into three phases. In the initial phase, the signal remains seemingly steady for a comparably long time, until an oscillation appears at $t \approx 600$. During the following transient phase the oscillation grows in time, until it finally reaches a constant finite amplitude due to nonlinear effects. Then the flow has reached what will be called the saturated state in this work. Note that although the self-sustained oscillations start around the steady state, the mean flow that the saturated state fluctuates around is in general different, as can be clearly seen for the given example. The development is similar in all unstable flow cases, *i.e.* whenever an oscillation appears in the nonlinear simulation. To obtain a good resolution of the oscillation frequencies there has to be a long enough period of the saturated state. Note that such a simulation typically required a few hundred CPU hours to complete.

The power spectral density (PSD) spectrum is calculated for the saturated state, for each of these nine signals. For this purpose the Welch modified periodogram method is used. Since the noise level of the signal is low and resolution high, the influence of the window functions is not significant and splitting the data into several segments and averaging the periodograms has only small advantages. Thus the usual Hamming

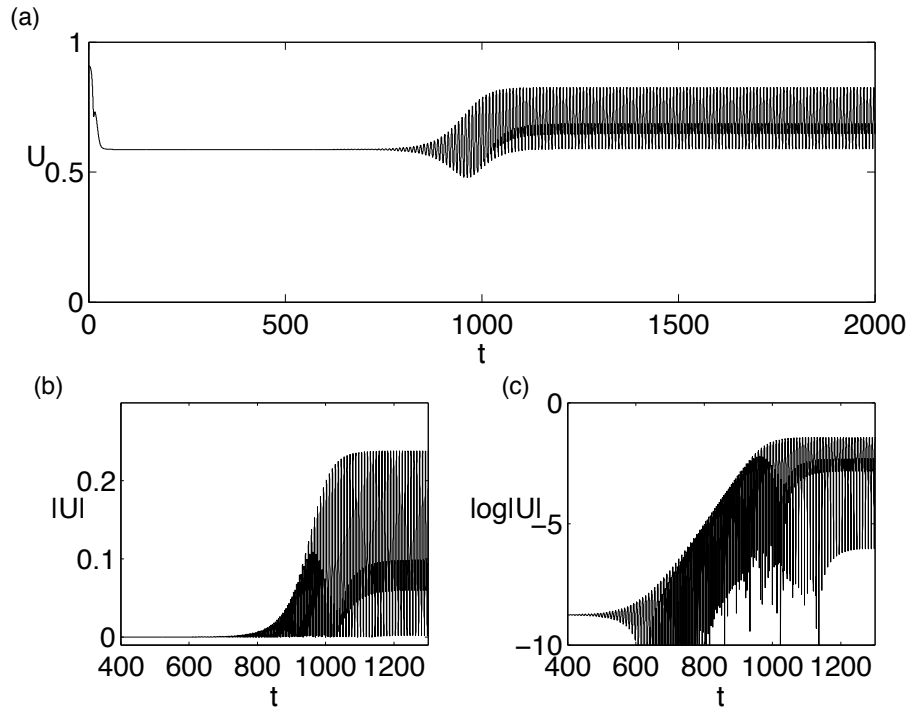


FIGURE 29. Time signal of the streamwise velocity in point $x = 10, y = -1$ (marked with a dot-ring in figure 28): (a) The original time signal, where U_{steady} is the level from which the oscillation starts to grow, (b) the absolute value of $U - U_{steady}$ in linear scale and (c) in logarithmic scale. The slope of the line in the last picture indicates the extracted growth rate in the linear regime.

window is chosen and the data is split up into two segments with 50% overlap. The data of each segment is zero-padded to four times the segment length. The highest peak in the PSD spectrum is always located exactly at zero frequency and represents the mean flow energy. The second highest peak corresponds to the energy in the nonlinear global mode, and other peaks are its harmonics. The harmonics have usually, but not always, monotonically decreasing energy levels. An accurate determination of the global mode frequency from the spectrum is crucial for the further analysis. The global mode frequencies based on the signals in the nine different sampling points in figure 28 were, as expected, identical.

When the global mode frequency has been identified from the spectra, a new simulation is performed starting from a converged saturated state, and the whole flow field is saved during exactly four periods of oscillation of the global mode. A Fourier transform of the data from the second simulation is then performed. The spatial shape of the mean flow is obtained as a coefficient to the Fourier mode with zero frequency in this expansion. The shape of the global mode is given by the fifth coefficient, since the transform was performed over four periods. If the global mode frequency is denoted by ω_1^s , then the n^{th} harmonic has per definition the frequency $\omega_n^s = (n + 1)\omega_1^s$, and its spatial shape is consequently given by the Fourier coefficient number $4(n + 1) + 1$. These shapes will be called Fourier modes of the flow field, and are naturally dependent on the time period used for the transform. A similar method has been previously used by *e.g.* Rowley *et al.* (2002) to visualise two acoustic eigenmodes for a resonant cavity obtained from a direct numerical simulation — the time period of the Fourier decomposition was then chosen to be a multiple of both frequencies. Of course, if many different peaks in the energy spectrum can be identified, or if there are no clear peaks, this approach becomes cumbersome and possibly ill-defined. Other methods to characterise and visualise structures obtained from a nonlinear simulation include the eigenmodes of the time-averaged auto-correlation matrix of the velocities, *i.e.* the *POD modes* (*e.g.* Berkooz *et al.* (1993)) containing the most energetic structures of the flow, and the eigenmodes of the Koopman operator associated with the nonlinear evolution operator, the *Koopman modes* (Rowley *et al.* 2009). However, since the spectrum in our case was clearly dominated by one (periodic) global mode and its harmonics, all of these approaches are equivalent, and Fourier modes proved to be an adequate and simple method to extract the structures of interest. The obtained mode shapes will be further discussed in the coming sections.

Finally, to get a good picture of how closely the initial development of the flow field corresponds to the calculated linear stability characteristics, we can again look at the time signal. Typically, we expect the initial development of the flow field, when the deviation of the steady state is small, to be governed by linear dynamics. Therefore, the disturbance that initially grows in the flow field should be the most unstable linear global mode. It should have an exponential growth rate, which along with its shape and frequency can be determined by the linear stability calculation, described in the next section.

There is indeed a time interval during the transient phase of the nonlinear signal where the growth is exponential. This can be seen in *e.g.* figure 29 c, where the absolute value of the velocity signal is drawn in a logarithmic diagram, and the slope is approximately linear at $700 < t < 900$ in this example case. The slope of this curve can be directly compared with the growth rate of the linear global mode obtained from the linear stability calculation. This frequency and growth rate form the real and complex part of the initial nonlinear frequency ω^i .

References

- BERKOOZ, G., HOLMES, P. & LUMLEY, J. L. 1993 The proper orthogonal decomposition in the analysis of turbulent flows. *Annual Review of Fluid Mechanics* **25**, 539–575.
- BIANCOFIORE, L., GALLAIRE, F. & PASQUETTI, R. 2010 Influence of confinement on a two-dimensional wake. *Under consideration for publication to Journal of Fluid Mechanics* .
- BRIGGS, R. J. 1964 *Electron-Stream Interaction with Plasmas*. The MIT Press Classics.
- CAMARRI, S. & GIANNETTI, F. 2007 On the inversion of the von Karman street in the wake of a confined square cylinder. *Journal of Fluid Mechanics* **574**, 169–178.
- CHOMAZ, J.-M. 2005 Global Instabilities in Spatially Developing Flows: Non-Normality and Nonlinearity. *Annual Review of Fluid Mechanics* **37**, 357–392.
- DAVIS, R. W., MOORE, E. F. & PURTELL, L. P. 1984 A numerical-experimental study of confined flow around rectangular cylinders. *Physics of Fluids* **27**, 46–59.
- DRAZIN, P. G. & REID, W. H. 1981 *Hydrodynamic Stability*, 9th edn. Cambridge: Cambridge University Press.
- EHRENSTEIN, U. & GALLAIRE, F. 2005 On two-dimensional temporal global modes in spatially evolving open flows: the flat-plate boundary layer. *Journal of Fluid Mechanics* **536**, 209–218.
- FISCHER, P. F. 1997 An Overlapping Schwarz Method for Spectral Element Solution of the Incompressible Navier-Stokes Equations. *Journal of Computational Physics* **133**, 84–101.
- HAMMOND, D. A. & REDEKOPP, L. G. 1997 Global dynamics of symmetric and asymmetric wakes. *Journal of Fluid Mechanics* **331**, 231–260.
- HUERRE, P. & MONKEWITZ, P. A. 1990 Local and global instabilities in spatially developing flows. *Annual Review of Fluid Mechanics* **22**, 473–537.
- JUNIPER, M. P. 2006 The effect of confinement on the stability of two-dimensional shear flows. *Journal of Fluid Mechanics* **565**, 171–195.
- LEHOUCQ, R. B., SORENSEN, D. C. & YANG, C. 1998 *ARPACK users' guide : solution of large-scale eigenvalue problems with implicitly restarted Arnoldi methods*. Philadelphia: SIAM.

- MADAY, Y. & PATERA, A. T. 1989 Spectral element methods for the Navier-Stokes equations. In *State-of-the-art surveys on computational mechanics* (ed. A. Noor), pp. 71–143. ASME.
- MASCHHOFF, K. J. & SORENSEN, D. 1996 P_ARPACK: An Efficient Portable Large Scale Eigenvalue Package for Distributed Memory Parallel Architectures. In *Applied Parallel Computing: Industrial Computation and Optimization* (ed. J. Wasniewski), pp. 478–486. Berlin /Heidelberg: Springer.
- PIER, B., HUERRE, P. & CHOMAZ, J.-M. 2001 Bifurcation to fully nonlinear synchronized structures in slowly varying media. *Physica D* **148**, 49–96.
- REES, S. J. & JUNIPER, M. P. 2010 The effect of confinement on the stability of viscous planar jets and wakes. *Journal of Fluid Mechanics* **656**, 309–336.
- RICHTER, A. & NAUDASCHER, E. 1976 Fluctuating forces on a rigid circular cylinder in confined flow. *Journal of Fluid Mechanics* **78**, 561–576.
- RODRIGUEZ, D. & THEOFILIS, V. 2009 Massively parallel solution of the biglobal eigenvalue problem using dense linear algebra. *AIAA Journal* **47** (10).
- ROWLEY, C. W., COLONIUS, T. & BASU, A. J. 2002 On self-sustained oscillations in two-dimensional compressible flow over rectangular cavities. *Journal of Fluid Mechanics* **455**, 315–346.
- ROWLEY, C. W., MEZIC, I., BAGHERI, S., SCHLATTER, P. & HENNINGSON, D. S. 2009 Spectral analysis of nonlinear flows. *Journal of Fluid Mechanics* **641**, 115–127.
- SCHMID, P. J. & HENNINGSON, D. S. 2001 *Stability and Transition in Shear Flows*. New York: Springer Verlag.
- SHAW, T. L. 1971 Effect of side walls on flow past bluff bodies. *Journal of Hydraulics Division* **97**, 65–79.
- SIPP, D. & LEBEDEV, A. 2007 Global stability of base and mean flows: a general approach and its applications to cylinder and open cavity flows. *J. Fluid Mech.* **593**, 333–358.
- SUZUKI, H., INOUE, Y., NISHIMURA, T., FUKUTANI, K. & SUZUKI, K. 1994 Unsteady flow in a channel obstructed by a square rod (crisscross motion of vortex). *International Journal of Heat and Fluid Flow* **14**, 2–9.
- TAMMISOLA, O. 2009 Linear stability of plane wakes and liquid jets: global and local approach. *Licentiate thesis, Royal Institute of Technology, Stockholm, Sweden*.
- THEOFILIS, V. 2003 Advances in global linear instability analysis of nonparallel and three-dimensional flows. *Progress in Aerospace Sciences* **39**, 249–315.
- WEIDEMAN, J. A. C. & REDDY, S. C. 2000 A MATLAB Differentiation Matrix Suite. *Transactions on Mathematical Software* **26** (4), 465–519.
- YU, M.-H. & MONKEWITZ, P. A. 1990 The effect of nonuniform density on the absolute instability of two-dimensional inertial jets and wakes. *Physics of Fluids* **A2**, 1175–1181.

Paper 3

3

Effect of surface tension on global modes of confined wake flows

By O. Tammisola¹, F. Lundell^{1,2} and L. D. Söderberg^{2,3}

¹ Linné FLOW Centre, KTH Mechanics, Royal Institute of Technology, SE-100 44 Stockholm, Sweden

² Wallenberg Wood Science Center, KTH Mechanics, SE-100 44 Stockholm, Sweden

³ Innventia AB, BOX 5604, SE-114 86, Stockholm, Sweden

Published in *Physics of Fluids* **23**, 014108, 2011

Many wake flows are susceptible to self-sustained oscillations, such as the well-known von Kármán vortex street behind a cylinder, that makes a rope beat against a flagpole at a distinct frequency on a windy day. One appropriate method to study these global instabilities numerically is to look at the growth rates of the linear temporal global modes. If all growth rates for all modes are negative for a certain flow field then a self-sustained oscillation should not occur. On the other hand, if one growth rate for one mode is slightly positive, the oscillation will approximately obtain the frequency and shape of this global mode. In our study, we first introduce surface tension between two fluids to the wake-flow problem. Then we investigate its effects on the global linear instability of a spatially developing wake with two co-flowing immiscible fluids. The inlet profile consists of two uniform layers, which makes the problem easily parametrisable. The fluids are assumed to have the same density and viscosity, with the result that the interface position becomes dynamically important solely through the action of surface tension. Two wakes with different parameter values and surface tension are studied in detail. The results show that surface tension has a strong influence on the oscillation frequency, growth rate and shape of the global mode(s). Finally, we make an attempt to confirm and explain the surface-tension effect based on a local stability analysis of the same flow field in the streamwise position of maximum reverse flow.

1. Introduction

This paper analyses the global stability of plane immiscible two-dimensional wakes. In our model configuration, an inner and two outer fluid streams with different velocities enter into a channel, introducing a region of local velocity deficit, *i.e.* a wake, which gradually recedes as a parabolic channel flow profile develops downstream. The development of the flow

field in time and space is determined by the inflow profile, densities and viscosities of the fluids, as well as the surface tension between them.

Here, we concentrate on the effect of surface tension on the stability of planar wakes. The density and viscosity of the two fluids is kept equal and uniform to exclude other effects, but a density and viscosity ratio could easily be included in subsequent analysis ¹ albeit not introduced in this work. We assume small perturbations, and apply the method of 2D linear global modes around the time-independent solution of Navier-Stokes equations, to determine for which parameter values the global oscillation appears.

The global stability of wakes and jets has grasped the attention of many researchers due to its importance in mixing and heat transfer related problems. The wake behind a solid circular or rectangular cylinder has served as a model problem in a large number of studies, since the transition to global instability happens at a low value of the Reynolds number making the global problem computationally tractable (see *e.g.* Williamson (1996) with references, Giannetti & Luchini (2007), Pier & Huerre (2001), Camarri & Giannetti (2007)). Planar wakes where fluid streams with two different velocities mix have also been a topic of several previous studies. Our starting point is the local stability of inviscid parallel flow in a symmetric configuration with one inner and two outer fluid streams, and uniform velocities in each Huerre & Monkewitz (1990). This flow profile is also used as the inlet profile in the present work. It has been concluded Huerre & Monkewitz (1990) that the velocity ratio is destabilizing and that high density wakes and low-density jets are more unstable. Later studies include wakes and jets surrounded by walls (Juniper 2006), *i.e.* confined wakes, and confined wakes with surface tension (Rees & Juniper 2009), with the conclusions that both intermediate confinement and intermediate surface tension have a destabilizing effect.

In the case of a weakly non-parallel flow, the stability limits from a local approach might be similar to the ones obtained with linear global modes. However, for strongly non-parallel flows, this is not the case. In such cases, a global approach is necessary in order to determine the stability of the flow.

Linear global modes for viscous confined wakes starting from the inlet profile of Juniper (2006) and developing in the streamwise direction,

¹The special case of a water sheet in air has been shortly considered in Tammisola (2009) and Tammisola, Lundell, Söderberg, Sasaki & Matsubara (2009).

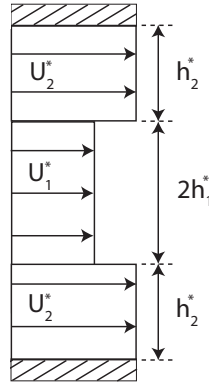


FIGURE 1. The inlet profile with illustration of the (dimensional) parameters h_1^* , h_2^* , U_1^* and U_2^* .

for different parameter values but without surface tension, have also been calculated (Tammisola 2009). It was shown that confinement was stabilizing for low Reynolds numbers ($Re < 400$), due to the more rapid mean flow development in the streamwise direction imposed by the shear at the confining walls. In this paper we extend this work to confined wakes with surface tension, but without examining the coupling between surface tension and the confinement effects.

2. Flow case

Figure 1 shows the inlet profile: it consists of two fluid layers with a uniform velocity in each. An inlet profile similar to this can in principle be obtained experimentally by a sharp contraction prior to the inlets. The profile is easily parametrizable as shown in the figure, we choose h_1^* (the asterisk indicate dimensional parameters) to be half the width of the inner layer (wake half width at the inlet), and h_2^* to be the height of the outer streams, and similarly, U_1^* is the inlet velocity of the wake and U_2^* that of the outer streams.

Since the densities and viscosities of the two fluids are equal, the problem is characterized by the following four nondimensional parameters:

- The *Reynolds number* describing the ratio between inertia and viscous forces

$$Re = \frac{U_2^* h_1^*}{\nu^*}, \quad (1)$$

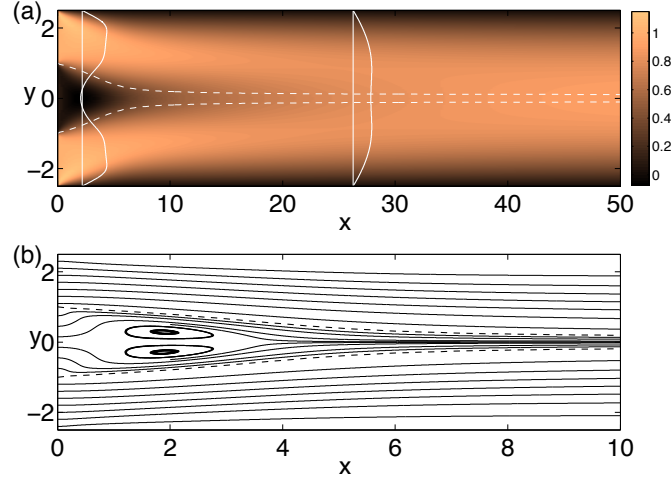


FIGURE 2. Base flow velocity field for study case 1, $Re = 100$, $h = 1.5$, $\Lambda^{-1} = -1.2$. The dashed curves show the streamlines separating the inner and outer fluids. (a) Streamwise velocity shown by colors, with example velocity profiles drawn on top of the figure.

(b) Streamlines close to the inlet. Observe that the aspect ratio is different from (a).

where ν^* is the kinematic viscosity of the fluids.

- The *Weber number* representing the ratio between inertia and capillary forces

$$We = \frac{\rho^* (U_2^*)^2 h_1^*}{\gamma^*}, \quad (2)$$

where ρ^* is the density of the fluids and γ^* the surface tension coefficient between them.

- The *shear ratio* describing the strength of the shear between the fluids at the inlet compared to their momentum

$$\Lambda = \frac{(U_1^* - U_2^*)}{(U_1^* + U_2^*)}. \quad (3)$$

- The *confinement* characterizing the distance to the walls:

$$h = \frac{h_2^*}{h_1^*}. \quad (4)$$

All these parameters are based on the inlet profile. However, the flow development downstream for a confined wake can also differ considerably depending on the choice of parameters. In this paper, we present example results for two cases:

- Case 1: $Re = 100$, $h = 1.5$ and $\Lambda^{-1} = -1.2$, and
- Case 2: $Re = 316$, $h = 1$ and $\Lambda^{-1} = -1.32$.

These two cases were chosen to give an illustration of the effects surface tension can have on the wake instability. Both wakes are slightly unstable without surface tension (Tammissola 2009), and the growth rates with different amounts of surface tension are examined here. More extensive parameter studies are left to the future, including a determination of the neutral stability limits, where linear global modes serve as a proper tool.

3. Methods

In the following, we denote the streamwise coordinate by x^* , wall-normal coordinate by y^* and spanwise coordinate by z^* . The problem is nondimensionalized with h_1^* and U_2^* as scaling parameters.

In general in linear stability, the flow variables are divided into one steady and one timevarying part. This concerns both the velocity vector:

$$\bar{U}_{tot}(x, y, z, t) = \bar{U}(x, y) + \bar{u}(x, y, z, t),$$

the pressure field:

$$P_{tot}(x, y, z, t) = P(x, y) + p(x, y, z, t),$$

and in the case of immiscible fluids, the position of the interface between them:

$$H_{tot}(x, z, t) = H(x) + \eta(x, z, t).$$

Here \bar{U}_{tot} , P_{tot} and H_{tot} determine the total time dependent flow field, $\bar{U}(x, y, z)$ and $P(x, y, z)$ the time-independent base flow, and $(\bar{u}(x, y, z, t), p(x, y, z, t), \eta(x, z, t))$ a *disturbance*, *i.e.* a deviation from the base flow. The stationary (time independent) solution to the 2D Navier-Stokes equations is taken as a base flow. We also assume two-dimensional disturbances, hence the z -dependence is removed from the problem.

3.1. Base flow

A typical base flow field, here for case 1, is shown in Fig. 2. Starting from the inlet profile at $x = 0$, the flow first develops a reverse flow region around to $x \approx 2$ (clearly seen in the streamline plot in Fig. 2 b),

whereafter the wake gradually disappears and the velocity profile goes towards a parabolic shape downstream. It is known that for the lowest Reynolds numbers ($Re = 100$), not only the shear ratio but also the confinement plays a considerable role for the development of the base flow, and therefore for the global stability (Tammisola 2009). For higher Reynolds numbers (*e.g.* $Re = 316$) the base flow development is more similar for confined and unconfined wakes, over a long distance upstream from the inlet.

In both cases, the curvature of the interface given by the streamline originating from $(x, y) = (0, \pm 1)$ for the base flow is small except in the immediate vicinity of the inlet ($x < 0.1$)². Thus, surface tension is assumed not to have a considerable effect on the shape of the stationary solution. To simplify the problem, the base flow is therefore calculated without surface tension. We have checked the validity of this assumption a posteriori by computing the capillary pressure gradient along the interface that would exist for case 1, $We^{-1} = 0.1$. This pressure gradient was of the order 10^{-4} , *i.e.* two orders of magnitude smaller than pressure gradients occurring in the flow field.

To obtain the base flow, the steady Navier-Stokes equations are solved using Nek5000 DNS spectral element code provided by Paul Fischer MCS, Argonne National Laboratory, Argonne, USA³. The code is based on rectangular blocks with Legendre polynomials in both the vertical and streamwise directions (Deville *et al.* 2002).

Preliminary studies showed that for these wakes, the only unstable mode has an antisymmetric streamwise velocity, while the base flow wake is symmetric around the centerline. Therefore, by using only the upper half of the domain and imposing a symmetry condition at the lower boundary, the DNS converges in time to the steady solution. The condition at the wall is no slip and for the outlet we choose the standard Nek5000 outlet condition with $P = 0$.

The outflow condition could potentially have an effect on the stability results. Therefore, the base flow domain is always chosen to be much longer than the domain used in the stability analysis described in the next subsection. It was ensured that changing the domain length for the base flow calculations does not affect the stability results.

²To define a fully physical curvature of the interface at the inlet would require contact line modelling, which is out of the scope of this work.

³The code can be accessed from <https://nek5000.mcs.anl.gov>.

3.2. Stability

In the stability problem, the computational domain is divided into two parts in the vertical direction, coinciding with the regions each fluid occupies in the steady state, with the steady position of the interface given by $(x, y) = (x, H(x))$ as the common boundary. These regions are referred to as domains 1 and 2. In each region, the coordinates are transformed from the physical domain to a rectangular one by stretching in the vertical direction.

The stability analysis is made by assuming small disturbances, so that the Navier-Stokes equations can be linearized around the steady state, the base flow (\bar{U}, P, H) . Further, we assume two-dimensional disturbances, independent of the z -coordinate⁴. We also transform the problem from a time frame to a frequency frame, by making the well-known normal mode ansatz:

$$u_k(x, y, t) = \hat{u}_k(x, y)e^{-i\omega t}, \quad (5)$$

$$v_k(x, y, t) = \hat{v}_k(x, y)e^{-i\omega t}, \quad (6)$$

$$p_k(x, y, t) = \hat{p}_k(x, y)e^{-i\omega t}, \quad (7)$$

$$\eta(x, t) = \hat{\eta}(x)e^{-i\omega t}, \quad (8)$$

where ω is the complex angular frequency and the subscript k refers to flow domain 1 and 2. The division into two domains and introduction of η is necessary in order to include the effect of surface tension on the interface, as described in the next subsection. In the following, this subscript is often skipped and in these cases \hat{u} , \hat{v} and \hat{p} refer to the disturbance distributions in the full domain.

Inserting the ansatz (3-6) into the *linearized Navier-Stokes equations* (LNSE) gives:

$$-U \frac{\partial \hat{u}}{\partial x} - V \frac{\partial \hat{u}}{\partial y} - \hat{u} \frac{\partial U}{\partial x} - v \frac{\partial U}{\partial y} \quad (9)$$

$$-\frac{\partial \hat{p}}{\partial x} + \frac{1}{Re} \left(\frac{\partial^2 \hat{u}}{\partial x^2} + \frac{\partial^2 \hat{u}}{\partial y^2} \right) = -i\omega \hat{u} \quad (10)$$

$$-U \frac{\partial \hat{v}}{\partial x} - V \frac{\partial \hat{v}}{\partial y} - \hat{u} \frac{\partial V}{\partial x} - \hat{v} \frac{\partial V}{\partial y} \quad (11)$$

$$-\frac{\partial \hat{p}}{\partial y} + \frac{1}{Re} \left(\frac{\partial^2 \hat{v}}{\partial x^2} + \frac{\partial^2 \hat{v}}{\partial y^2} \right) = -i\omega \hat{v} \quad (12)$$

⁴This assumption is valid for wakes at low Re , e.g. the flow in a wake behind a circular cylinder becomes three-dimensional at $Re \approx 180$.

$$\frac{\partial \hat{u}}{\partial x} + \frac{\partial \hat{v}}{\partial y} = 0. \quad (13)$$

Equations (8–11), together with appropriate boundary conditions shortly described in the next section, constitute a 2D eigenvalue problem for ω . The eigenfunctions represent possible 2D disturbance shapes $(\hat{u}(x, y), \hat{v}(x, y), \hat{p}(x, y), \hat{\eta}(x))$, together with corresponding frequencies and growth rates given by the real and complex part of the eigenvalue $\omega = \omega_r + i\omega_i$. Each eigenvalue-eigenfunction pair is called a *global mode*, and the analysis is distinguished from its local counterpart by two-dimensionality of the eigenfunction.

We discretize this problem using a spectral collocation technique based on Chebyshev polynomials in both the streamwise and vertical directions. In order to handle a storage issue generated by the resulting huge matrix, that appears in global mode calculations, we have parallelized them: we build the matrix in pieces on different processors, and the LU-factorization and eigenvalue calculation are accomplished with the aid of mathematical libraries ScaLAPACK (Blackford *et al.* 1997) and P_ARPACK (Maschhoff & Sorensen 1996).

3.2a. *Boundary conditions.* To complete the set of equations above, we also need boundary conditions for the disturbance. The condition at the upper wall is no slip:

$$\hat{u}_2(x, h + 1) = \hat{v}_2(x, h + 1) = 0, \quad (14)$$

and at the centerline, for antisymmetric modes:

$$\hat{u}_1(x, 0) = \frac{\partial \hat{v}_1}{\partial y}(x, 0) = \hat{p}_1(x, 0) = 0, \quad (15)$$

and symmetric modes:

$$\frac{\partial \hat{u}_1}{\partial y}(x, 0) = \hat{v}_1(0) = \frac{\partial \hat{p}_1}{\partial y}(x, 0) = 0. \quad (16)$$

In order to be able to include capillary forces in the problem, we also need to satisfy physical constraints at the interface $y = H + \eta$, presented below. To make the expressions simple and the physics clear, we only write down the nonlinear conditions before the linearization steps here. They are presented in tensor form, where $\hat{u}_{k,i}$ now represents the streamwise disturbance velocity for $i = 1$ and the vertical disturbance velocity for $i = 2$. The conditions are:

1. Continuity of the velocities at the interface

$$U_{1,i} + u_{1,i} = U_{2,i} + u_{2,i}. \quad (17)$$

2. Continuity of the tangential force at the interface

$$\tilde{t}_i S_{1,ij} \tilde{n}_j = \tilde{t}_i S_{2,ij} \tilde{n}_j, \quad (18)$$

where \tilde{t} is the tangent vector of the interface (that depends on both H and η), \tilde{n} the normal vector, and S the stress tensor with pressure included.

3. Jump in the normal stress due to surface tension, dependent on local surface curvature:

$$\tilde{n}_i S_{1,ij} \tilde{n}_j = \tilde{n}_i S_{2,ij} \tilde{n}_j - \frac{1}{We} \left(\frac{\partial \tilde{n}_j}{\partial x_j} \right). \quad (19)$$

4. The interface displacement follows the vertical displacement of a particle at the interface⁵:

$$\frac{\partial \eta}{\partial t} + (U_1 + u_1) \frac{\partial}{\partial x} (H + \eta) = V_1 + v_1. \quad (20)$$

The surface normal in the stress conditions above contains both H and η , so these conditions need to be linearized not only with respect to \hat{u} , \hat{v} and \hat{p} , but also $\hat{\eta}$. Furthermore, since the surface position varies in time, all conditions also have to be linearized to yield at $y = H$, the stationary position of the interface. Consequently, the interface boundary conditions will involve many base flow terms in combination with $\hat{\eta}$, and disturbance terms in combination with H , and their exact form is omitted here due to extensive length. More details can be found in Tammissola (2009), where the linearized conditions at the interface are presented for an arbitrary density and viscosity ratio between the fluids. A similar method has been used previously to obtain the local stability of a water sheet in air, solving the Orr-Sommerfeld equations with a coupling at the interface (Söderberg 2003), (Tammissola *et al.* 2010). This approach yielded an excellent agreement with experiments in a globally stable (locally unstable) flow (Tammissola *et al.* 2010).

Finally, a Dirichlet no slip condition was chosen at the inlet:

$$\hat{u}_{k,i}(0, y) = \hat{\eta}(0) = 0, \quad (21)$$

and a Neumann condition at the outlet:

$$\frac{\partial u_{k,i}}{\partial x} = 0, \quad (22)$$

⁵By Eq. 15, this condition has exactly the same appearance if formulated in terms of variables in domain 2.

where $k = 1, 2$.

Unstable global modes are per definition localized in space, so the disturbance should vanish at infinity. However, there is no physical argument that would a priori justify a restriction of the disturbance to any particular finite interval in the streamwise direction. Therefore, it needs to be investigated whether the results are independent on the streamwise boundary conditions. For the outlet condition, this is easily established by making the domain longer until the unstable eigenvalues have converged to the desired precision. A domain length of $L = 100$ for the first, and $L = 200$ for the second wake, were seen to be sufficient in order to obtain a convergence of the first three decimal places for both the real and imaginary part of the unstable eigenvalues. To investigate the influence of the inlet condition, we have tested a procedure involving a *damping region* upstream of $x = 0$ (Tammisola *et al.* 2011). This amounts to extending the computational domain for the velocity and pressure variables upstream from the actual inlet, with a parallel base flow profile equal to the inlet profile, and a splitter plate between the two fluid streams, in order not to enhance the instability⁶. A Dirichlet condition as above (Eq. 21) is then set at the inlet of the damping region, at $x = -d$, instead of $x = 0$. The only purpose of the damping region is to allow the disturbance to start more smoothly, and the results were seen to be insensitive to both the chosen base flow profile in this region and the length of the damping region, except from the appearance of some additional unstable modes for case 2. These were one weakly unstable varicose mode at intermediate values of surface tension and two strongly unstable sinuous modes at weak surface tension ($We > 500$). The antisymmetric modes appear neither without surface tension nor with stronger surface tension than $We = 500$, and the symmetric mode always has the lowest growth rate of all modes. Thus, they do not affect the main conclusions of the present investigation. A complete study of the effect of the upstream boundary condition is left for a future study.

4. Results

4.1. Case 1

The base flow for case 1 is shown in Fig. 2. It contains a region of reverse flow with a maximum at $x \approx 2$. Without surface tension ($We = \infty$),

⁶Our investigations have shown that the form of base flow profile in the damping region does not affect the solution, as long as there is a splitter plate so that the wake region is not extended upstream. The possibility for the disturbance to decay smoothly is more important, but is required only if the modes have a high amplitude close to the inlet.

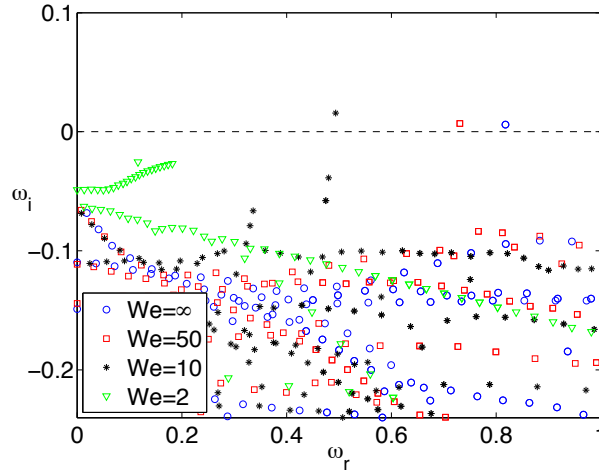


FIGURE 3. Spectra for different We . Case 1: $Re = 100$, $h = 1.5$, $\Lambda^{-1} = -1.2$.

it is known (Tammissola *et al.* 2011) that there is one slightly unstable mode, with $\omega = 0.818 + 0.006i$.

Eigenvalue spectra for different values of We are shown in Fig. 3. For very weak surface tension, $We = 50$, the growth rate (ω_i) of the unstable mode remains almost constant, while its frequency decreases to $\omega_r = 0.731$. For stronger surface tension, $We = 10$, the growth rate of the unstable mode increases noticeably (to $\omega_i = 0.016$), and the frequency is much lower, $\omega_r = 0.494$. However, when the surface tension is increased further to $We = 2$, all global modes are stable. The growth rate of the eigenvalue (ω_i) is shown in Fig. 4 (b), when the inverse Weber number We^{-1} changes continuously from 0 to 0.28 ($We = \infty \rightarrow 3.6$), and it shows two local peaks. The maximum growth rate is seen to occur at $We^{-1} \approx 0.14$ ($We \approx 7$), while a second maxima is observed at $We^{-1} = 0.06$ ($We \approx 16$). The frequency as a function of We^{-1} is quantified in Fig. 4 (a), and is monotonously decreasing.

The eigenfunctions of the most unstable modes for $We = \infty$, $We = 50$ and $We = 10$ are presented in Fig. 5. We start by looking at the real part, *i.e.* an instantaneous field, of the streamwise disturbance velocity. The usual wake mode for $We = \infty$ (Fig. 5 a) has a long *envelope*, *i.e.* a streamwise region where its amplitude is not vanishingly small (compared to its maximum amplitude). This can be seen in that there are red (high velocity) and blue (low velocity) regions over a long distance.

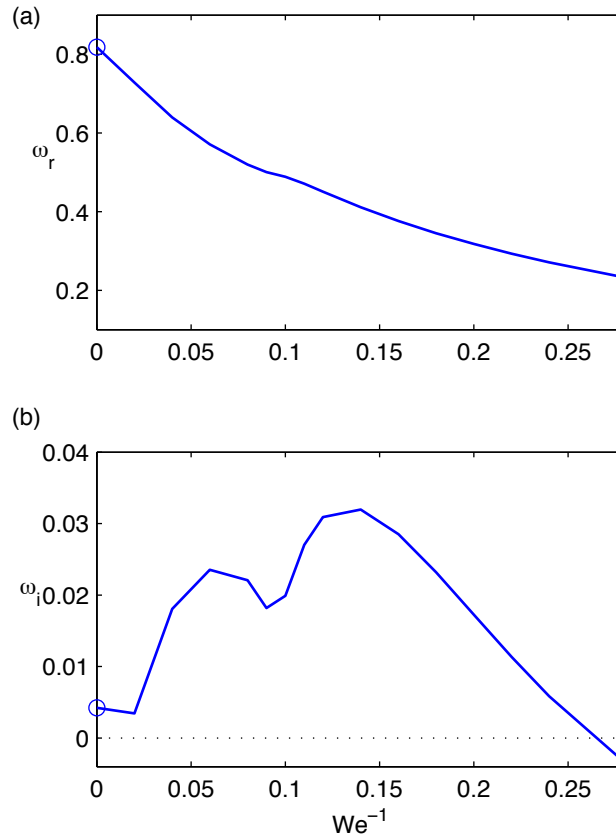


FIGURE 4. (a) The frequency ω_r , and (b) the growth rate ω_i as a function of We^{-1} for the unstable mode at $Re = 100$, $h = 1.5$, $\Lambda^{-1} = -1.2$.

Naturally, the mode finally decays upstream and downstream, a localization that is characteristic for unstable global modes. The amplitude for the velocity disturbance reaches a maximum at $x \approx 12$. If the mean distance between two consecutive peaks of the oscillation (*e.g.* the centers of the red regions at $x = 9$, $y = 0.5$ and $x = 15$, $y = 0.5$) is seen as a wavelength, then the wavelength of this mode is of the order 6, which gives a wavenumber slightly greater than unity. The instantaneous oscillation of the interface is shown with a magenta line on top of the mode picture, and its phase is seen to follow that of the streamwise velocity

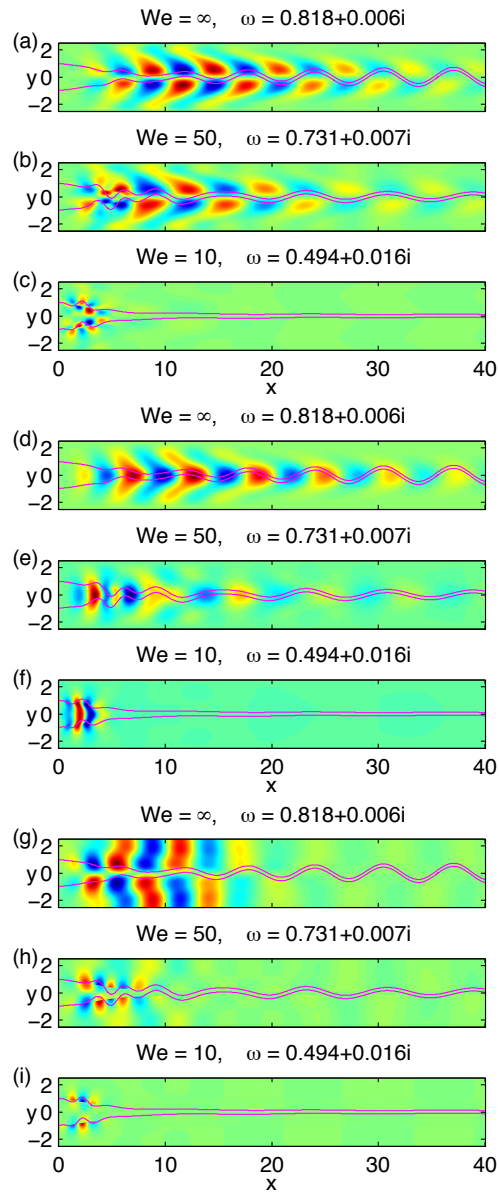


FIGURE 5. Spatial shape of the most unstable mode for different We , at $Re = 100$, $h = 1.5$, $\Lambda^{-1} = -1.2$: (a)-(c) the streamwise disturbance velocity, (d)-(f) the vertical disturbance velocity, (h)-(i) the pressure disturbance. Red color represents positive values, blue color negative values and the figures has to be stretched a factor of 1.25 in the horizontal direction to get the physical aspect ratio.

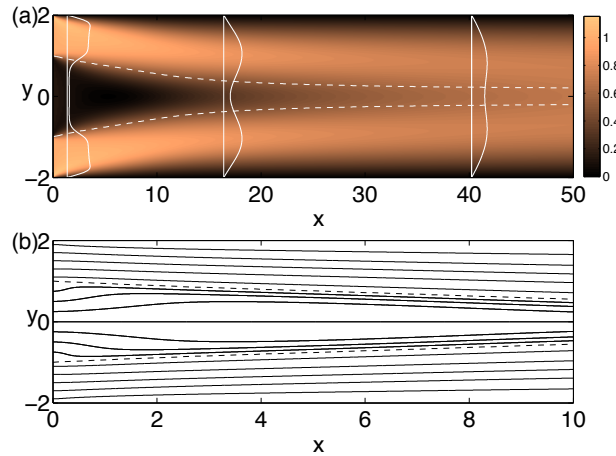


FIGURE 6. Base flow streamwise velocity field, at $Re = 316$, $h = 1$, $\Lambda^{-1} = -1.32$. The boundary between inner and outer fluid is marked with a dashed curve. (a) Velocity field shown by colors, example velocity profiles are drawn on top of the figure. (b) Streamlines close to the inlet. Observe that the aspect ratio is different from (a).

oscillation. However, it should be mentioned that the interface perturbation starts to decay first at $x \approx 50$. The slower decay of the interface perturbation is due to its ability to be convected with the mean flow, further described in section 5.

For $We = 50$ in Fig. 5 (b), the shape of the mode downstream is similar, but more irregular structures are seen to appear in the wake close to the inlet. The envelope is shorter, maximum being where the new structures appear, at $x \approx 6$. The amplitude of the oscillation of the interface (the magenta line) is largest near the inlet and decays downstream, and does not follow the phase of the streamwise velocity oscillation there. The wavelength of the mode downstream is longer, as one would intuitively expect, since in local stability surface tension damps the short wavelengths.

However, for $We = 10$ (Fig. 5 c) the mode is completely dominated by short waves close to the inlet. The maximum is at $x \approx 3$ and the streamwise velocity oscillation is concentrated on both sides of the interface, with the same wavelength as the interface oscillation. One has to look carefully to find traces of a long wavelength wake oscillation downstream.

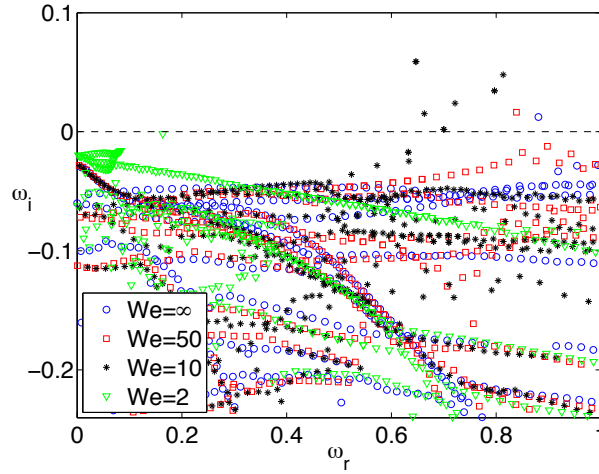


FIGURE 7. (Color online) Spectra for different We , at $Re = 316$, $h = 1$, $\Lambda^{-1} = -1.32$.

For the vertical disturbance velocity \hat{v} shown in Fig. 5 (d)–(f) the conclusions are similar, but for $We = 50$ (Fig. 5 e) it is seen that the phase of the vertical velocity is equal to that of the interface close to the inlet. This localized vertical interface movement is the reason why the wake structure in Fig. 5 (b) becomes distorted. Figures 5 (g)–(i) show the pressure disturbance, and here the effect of surface tension is clear. Without surface tension, the pressure changes smoothly over the interface, and follows the low wavelength structures seen in the velocity modes in this case. For $We = 50$, capillary force introduces a “pressure jump”, a discontinuity over the interface. The amplitude of the pressure is clearly highest where the distortion of the wake mode appears (near $x \approx 6$). Furthermore, the pressure variation seems to have a high amplitude in the high speed fluid and low in the low speed fluid in that region, a feature that is common for all modes with surface tension presented here. The reason for this is not obvious. However, it means that the pressure is interacting both with the interface and with the velocity fields. A pure pressure jump due to the oscillation of the interface is seen by careful scrutiny of the middle figure longer downstream, where the pressures below and above the interface are exactly out of phase.

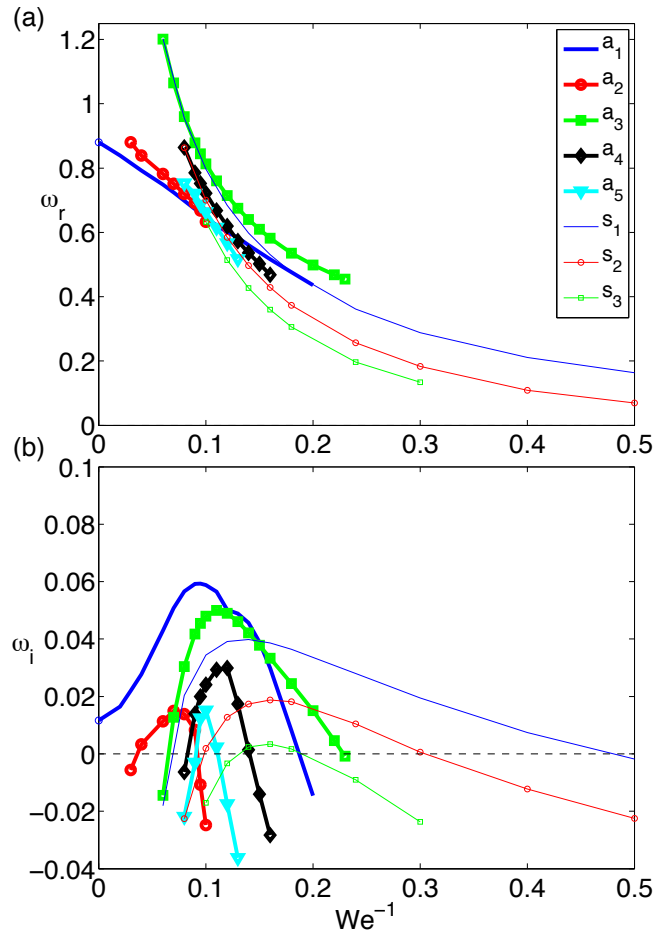


FIGURE 8. (Color online) (a) The frequency ω_r , and (b) the growth rate ω_i as a function of We^{-1} for the unstable modes at $Re = 316$, $h = 1$, $\Lambda^{-1} = -1.32$: antisymmetric (a_1 - a_5) and symmetric (s_1 - s_3).

4.2. Case 2

Case 2 is different in several ways. Firstly, the base flow (Fig. 6) contains no reverse flow region. Therefore, also the streamline at $y = 0$ is continuous (Fig. 6 b), without stagnation points. Secondly, it is more confined than the first case, which is known to be stabilizing for the wake without surface tension for similar parameter values (Tammisola 2009). There is less shear at the inlet ($\Lambda^{-1} = -1.32$), which is also

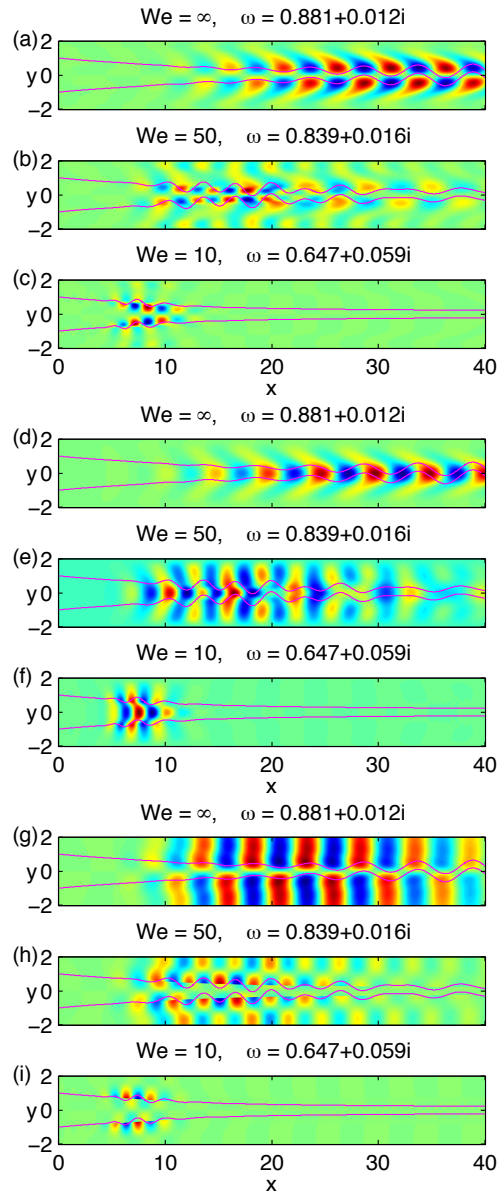


FIGURE 9. Spatial shape of mode a_1 for different We , at $Re = 316$, $h = 1$, $\Lambda^{-1} = -1.32$: (a)-(c): the streamwise disturbance velocity, (d)-(f) the vertical disturbance velocity, and (g)-(i) the pressure disturbance. Red color represents positive values, blue color negative values and the figures has to be stretched a factor of around 1.5 in the horizontal direction to get the physical aspect ratio.

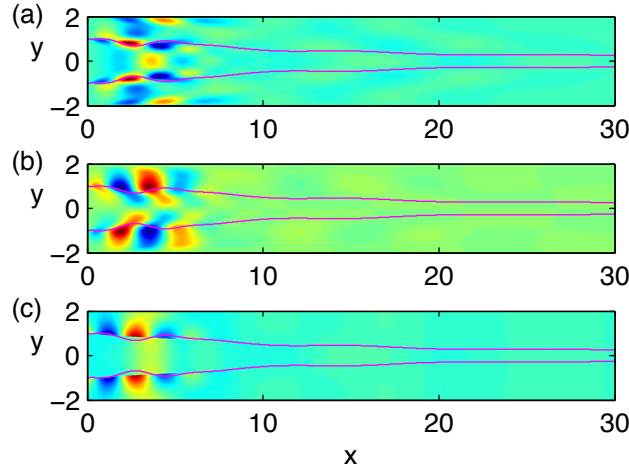


FIGURE 10. The symmetric most unstable mode at $We = 4.2$ ($We^{-1} = 0.24$), $Re = 316$, $h = 1$, $\Lambda^{-1} = -1.32$: (a) \hat{u} , (b) \hat{v} and (c) \hat{p} . Red color represents positive values, blue color negative values and the figures has to be stretched a factor of around 1.3 in the horizontal direction to get the physical aspect ratio.

stabilizing. However, the Reynolds number ($Re = 316$) is higher than in case 1, which makes the high shear region longer, and consequently there is still one unstable mode without surface tension.

Eigenvalue spectra for the same four values of We are shown in Fig. 7 (compare with Fig. 3 for case 1). At $We = 50$, no major changes in the frequency or growth rate of the one unstable mode are seen. However, at $We = 10$ the change in the spectrum is dramatic: six different unstable low frequency modes show up. In fact, even in case 1 (Fig. 3) there were modes separating from the main branch at $We = 10$ and becoming less stable, but they all still had negative growth rates. Despite this destabilization for $We = 10$, at $We = 2$ all modes are once again stable. The study of the eigenvalue spectra when We^{-1} changes continuously from 0 to 0.5 ($We = \infty \rightarrow 2$) reveals in total eight unstable modes, five of which are antisymmetric, and three symmetric (Fig. 8). For an intermediate range of Weber numbers ($We^{-1} = 0.25 - 0.47$) the most unstable mode is symmetric. It is remarkable that symmetric unstable modes can dominate the antisymmetric ones for a wake, when surface tension is introduced. This confirms that the trend seen in inviscid local

analysis (Rees & Juniper 2009), that moderate surface tension considerably extends the parameter region where a varicose (symmetric) mode is absolutely unstable, is relevant also for viscous spatially developing flows.

The real part of the streamwise disturbance velocity of the most unstable mode for the same We as in case 1 is seen in Fig. 9 (a)–(c). The mode without surface tension (Fig. 9 a) is very elongated, the maximum being at $x \approx 35$. The wavelength is comparable to the one observed for case 1. When weak surface tension is introduced ($We = 50$, Fig. 9 b), the mode shape is very different, even if the frequency and growth rate were similar. Short wavelength oscillation appears downstream from $x = 10$, with maximum amplitude at $x \approx 18$, and the maximum oscillation amplitude is suddenly moved from the outer to the inner fluid. Modes localized on each side of a sheared interface with surface tension have been noted in previous studies (Yecko *et al.* 2002). In the downstream end the oscillation again retains a similar shape as in the $We = \infty$ case in (a), but with a lower relative amplitude. For $We = 10$ the small wavelength oscillations are again completely dominant. The most unstable mode is shown, but all antisymmetric unstable modes (Fig. 7) have a similar structure.

The most noticeable change in the vertical disturbance velocity (Fig. 9 d–f) with surface tension is that the mode for $We = 50$ in (e) extends almost the whole way up to the wall in the high-speed fluid, whereas for $We = \infty$ in (d) it lies closer to the shear layer and low speed fluid. This could mean that confinement has a stronger influence on the mode shape when surface tension is introduced, as was also indicated by previous local studies (Rees & Juniper 2009). Notice that in case 1 with slightly weaker confinement, the v -mode was still more concentrated in the low speed fluid (Fig. 5 e). For the wake pressure disturbance without surface tension, the phase is constant from the shear layer and up to the closest wall (Fig. 9 g). But with surface tension, in particular $We = 50$, we observe a phase change for the pressure in the vertical direction. Finally, in Fig. 10 an example of the shape of a symmetric mode is shown: the most unstable mode at $We = 4.2$. This mode is similar to the antisymmetric ones regarding envelope and wavelength. It is located even closer to the inlet, and the amplitude of the \hat{u} -eigenfunction has a secondary peak near the wall, indicating that this mode is influenced by confinement. The shape near the inlet is close to the antisymmetric modes at the same wavenumbers (not shown), but the symmetric mode

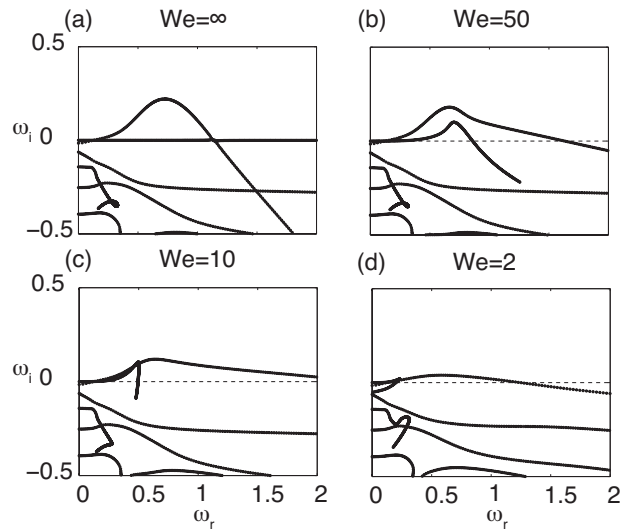


FIGURE 11. Temporal spectra for $x = 2$, different We , at $Re = 100$, $h = 1.5$, $\Lambda^{-1} = -1.2$.

is more localized, since it is more unstable, and does not contain traces of the usual wake mode downstream.

4.3. Summary

Even weak surface tension has a complicated influence on the global stability of plane wakes. This is the case even when other physical parameters of the two-fluid problem such as different densities and viscosities of the two fluids are not included. Surface tension changes the global spectrum and mode structures in different ways depending on the other parameter values, and the full influence of confinement, Reynolds number and shear ratio to this effect is yet to be determined. In the next section we will try to explain why weak surface tension has a destabilizing influence.

5. Physical reason for destabilization

To understand global mode results better and to verify them, it is good practice to compare some of them with results obtained with a different method. The verification is especially important in the case of global modes with surface tension, since the linearized interface boundary conditions are rather complicated.

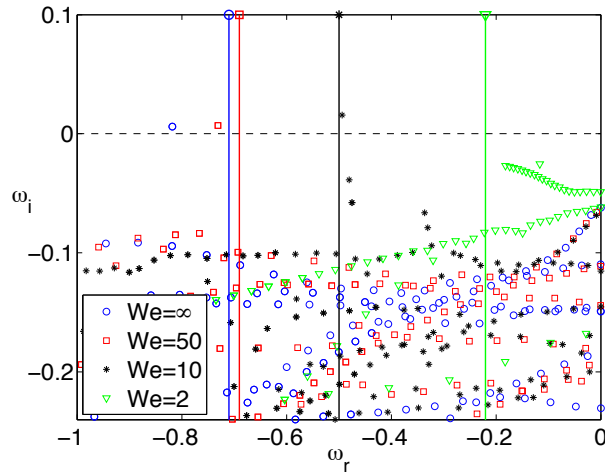


FIGURE 12. (Color online) The absolute frequencies at $x = 2$, at $Re = 100$, $h = 1.5$, $\Lambda^{-1} = -1.2$, given by vertical lines on top of the global eigenvalue spectra for different We . Each marker on top of the line (and color online) represent the same We as that of the global spectrum.

This will now be done for Case 1. We start by investigating the base flows with the *local* linear stability method (*e.g.* Drazin & Reid (1981)). In brief, this means that the flow is assumed to be *locally parallel*, *i.e.* the base flow is assumed to evolve in the streamwise direction on a scale that is much longer than the wavelength of the disturbance, and therefore for each streamwise position, it is sufficient to look at the base flow profile at that position. Consequently, the base flow field is of the form $(\bar{U}, P) = (\bar{U}(y), P(y))$, and all streamwise derivatives of the base flow disappear from the equations. With this simplification, it becomes possible to make the local ansatz:

$$\bar{u} = \hat{u}(y)e^{i(\alpha x - \omega t)}, \quad (23)$$

where we can look at the development for different streamwise wavenumbers α separately. The equations to solve are then a simplified form of Eqs. (8–11) and the boundary conditions stated in Eqs. (12–18). With this approach, the interface boundary conditions become much simpler, and it is relatively easy to verify the local stability code against existing results.

We first take the *temporal* approach, by setting a real wavenumber α , and obtain the complex ω (the frequency and growth rate in time)

for this wavenumber by solving the eigenvalue problem. When this is done for many different α , we get lines of eigenvalues in ω -space. One example is shown in Fig. 11 (a). It is now convenient to denote each of these lines (over all α) as a mode. For parallel and weakly non-parallel flows, local temporal instability is a necessary condition to get an unstable global mode (Huerre & Monkewitz 1990). This condition is not sufficient, but means that modes that are temporally stable will not become globally unstable for weakly nonparallel flows. Therefore, even if our flow is spatially developing, temporally unstable modes could give a first indication of the physics behind the destabilization with surface tension.

For $We = \infty$, there is one unstable mode, as shown in Fig. 11 (a). This mode reaches a maximal temporal growth rate of $\omega_i = 0.22$ for the frequency $\omega_r = 0.73$ and wavenumber $\alpha = 1.2$. This has to be the mode that develops to an unstable global mode without surface tension, *i.e.* the usual wake mode. The maximal temporal growth rate of this mode is much higher than the global mode growth rate, which is to be expected from the theory. However, the frequency and wavenumber are in the same range as what is seen in the global mode pictures without surface tension (Figs. 5 a, d, g). In addition, there is one neutrally stable mode. A closer examination shows that the eigenfunction of the neutrally stable mode only involves an interface displacement $\hat{\eta}$, with vanishing velocity and pressure components. In addition, by tracking the *phase speed* $c = \frac{\omega_r}{k_r}$ of this mode, we have seen that it travels with the base flow velocity at the surface. In other words, the kinematic equation of the interface, Eq. (18), reduces to:

$$\frac{\partial \eta}{\partial t} + U(H) \frac{\partial \eta}{\partial x} = 0, \quad (24)$$

where an initial interface displacement is convected with the base flow speed without changing its amplitude. Since there is no velocity associated with this interface displacement, viscosity will not stabilise it, and the mode is neutrally stable. Without surface tension, this mode lacks physical meaning, and is purely due to our choice to introduce η as a variable in a problem which also could be solved in terms of velocity and pressure disturbance only.

However, when surface tension is introduced, the interface position suddenly becomes dynamically important. It is clear that with the presence of surface tension no pure convection of the disturbed interface

position can exist, since an interface displacement introduces a pressure perturbation. This in turn induces a vertical velocity field, which emerges in the kinematic equation of the interface possibly rendering the mode stable or unstable.

Now look at the temporal spectrum for $We = 50$ and $x = 2$ in Fig. 11 (b). The wake mode still has the highest amplitude, but the "interface convection mode" has become unstable for certain wavenumbers. It reaches a maximal temporal growth rate $\omega_i = 0.1$ at $\omega_r = 0.71$ for wavenumber $\alpha = 1.6$. A shorter wavelength appearing near the inlet was also seen in the shape of the global mode (Figs. 5 b, e, h). At the same time, the usual wake mode has been slightly stabilized and the maximum moved to longer wavelengths ($\alpha = 1$). The same development clearly continues for $We = 10$ and $We = 2$ as seen in Fig. 11 (c) and (d), although the maximal temporal growth rates of both modes decrease. The local temporal pressure and velocity eigenfunctions are now nonvanishing for all values of α for the interface convection mode, as they should be due to the capillary action. But otherwise, the nature of this mode is very much dependent on the value of α . For very long waves (small α) the effect of surface tension (which acts through the interface curvature) is so weak that the interface displacement is still mostly convected with the mean velocity: the growth rates are nearly zero and the phase speed is very close to the base flow surface speed. Surface tension clearly damps very short waves. What is most interesting is the destabilization for some intermediate wavenumbers.

Our suggestion is that this can be seen as an interplay between capillary waves and the base flow shear. In a stagnant base flow, the two interfaces with surface tension support neutrally stable capillary waves. For long waves, the capillary force is very weak, and very short capillary waves are damped by viscosity. Thus, there should be an intermediate range of wavelengths, where the dynamical relevance of capillary waves is maximum. On the other hand, shear layers support Kelvin-Helmholtz type instability, where the maximal growth rate and its associated wavelength depend on both the strength and thickness of the shear layer. When the wavelength and frequency of the capillary waves, simultaneously convected by the base flow, is suitable, these may also extract energy from the base flow shear by the Kelvin-Helmholtz mechanism. The shorter wavelengths approaching the thickness of the shear layer, which would be damped otherwise, may be promoted by capillarity. Also, the lower frequency of the interfacial mode helps to counteract

viscous stabilisation for short wavelengths. The hypothesis of a Kelvin-Helmholtz mechanism is supported by the fact that for high surface tension, the frequency-growth rate curve for the interfacial mode seems to follow closely that of the usual wake mode for low frequencies. When the wavelength becomes short enough, the growth rate and frequency of the interfacial mode suddenly drop, as could be expected due to a strong capillary force.

A new local temporal mode cannot explain a destabilisation in the global spectrum. A more important question to be answered is: Can we get any indications from the local analysis that this interfacial mode, or the usual wake mode, becomes more globally unstable with surface tension? To do this, we have to take the local analysis a bit further.

It is known (Huerre & Monkewitz 1990) that for weakly nonparallel flows a region of so-called local absolute instability, *i.e.* the existence of unstable zero group velocity modes in the local stability problem, is a necessary condition for an unstable 2D global mode to exist. The locally unstable frequency is identified from the frequency at a saddle point with a positive growth rate in the complex frequency-wavenumber-plane. Although temporal instability is also a necessary condition for global instability, it is not the temporal frequencies but rather the frequency of the complex saddle point that might give a prediction of the frequency of the 2D global mode. This frequency should be determined in the whole streamwise region where local absolute instability exists, whereafter a prediction of the global mode frequency can be established by techniques based on analytic continuation. This has been done in the inviscid wake and jet analyses based on model velocity profiles (Huerre & Monkewitz 1990; Juniper 2006; Rees & Juniper 2009).

We limit ourselves to obtaining the local absolute frequencies in the streamwise point where counterflow and therefore absolute instability without surface tension is strongest, at $x = 2$, to get a first indication of whether the trends seen in the global analysis can be confirmed by the local analysis. Observe that to get a full comparison between local and global methods, the analysis have to be extended to a wider streamwise region (Huerre & Monkewitz 1990).

The result is shown in Fig. 12, where the absolute frequencies are represented by vertical lines (with the corresponding marker on top) and compared to the global spectra. For $We = \infty$ and $We = 50$ the zero group velocity mode turned out to be the usual wake mode, and for $We = 10$ and $We = 2$ the interfacial mode. The absolute growth

rates determined in one spatial point do not give a good approximation of the global mode growth rate; however, the absolute growth rate in this point was highest for $We = 10$ and lowest for $We = 2$.

The local absolute frequencies at $x = 2$ are far from identical to global frequencies, but the same trend is seen in both: the frequency increases with the surface tension. The wavenumber also goes in the right direction, but the wavelength predicted is still longer than the wavelength seen in the global mode by a factor 2 (not shown). In a previous inviscid local study (Rees & Juniper 2009) a short wavelength mode was also seen to appear in the presence of surface tension, but with a wavelength one order of magnitude smaller than our global mode wavelength. These local studies together confirm that the phenomena seen in the global analysis are physical and not a result of *e.g.* upstream or downstream boundary conditions. Furthermore, they indicate that a global linear analysis might be necessary to accurately predict the frequency and stability limits of global modes with surface tension.

6. Conclusions

Global stability of plane wakes consisting of inner and outer fluid layers with surface tension on the interfaces has been analyzed by 2D linear global modes. Surface tension was modified by changing the value of the nondimensional parameter We describing the ratio between inertia and capillary forces. This parameter was varied and the global eigenvalue spectrum investigated for values between $We = \infty$ (no surface tension) and $We = 2$ (inertia twice as strong as surface tension). It was shown that surface tension has an influence on both the growth rate, appearance, and number of unstable global modes. The most unstable configurations for the two example wakes presented in this paper were found to occur for intermediate surface tension at $We = 7$ (case 1, $Re = 100$) and $We = 11$ (case 2, $Re = 316$). Both wakes had one slightly unstable mode without surface tension. For the first wake, only one mode was observed to be unstable, while for the second wake, seven new unstable modes appeared with surface tension, three of which are varicose (symmetric), which is unusual for wake instability. However, when surface tension was increased further to $We = 2$, both wakes became stable. In light of these results, there is a strong reason to believe that intermediate surface tension will destabilize also wakes that would be stable without surface tension.

A possible physical explanation for the influence of surface tension was indicated by a local stability analysis performed on the first wake in

the streamwise position where the counterflow was strongest, at $x = 2$. Without surface tension, in addition to the well-known wake mode, there was a neutrally unstable mode in the temporal spectrum. This mode corresponded to a pure convection of a small interface displacement by the mean flow. When surface tension was introduced, the mode became temporally unstable for certain wavenumbers, and for $We = 10$ and $We = 2$ it also became the most absolutely unstable mode. A similar situation, where a neutrally stable "invisible" interfacial mode in Poiseuille flow was rendered temporally unstable by viscosity stratification, has been observed previously (Yih 1967). Our hypothesis is that with capillarity, energy can be extracted from the local mean flow shear at the surface at different scales than without surface tension. A saddle point associated with the shear layer activated by surface tension was even found for inviscid flow (Rees & Juniper 2009).

An interfacial saddle is assumed to interact with the wake saddle and therefore influence the frequency and mode shape for our first wake. Oscillations with a small wavelength, in accordance with the local analysis, are seen to appear in the global mode in the shear layer close to the inlet, and for higher surface tension these oscillations become dominant. For the second wake no local analysis was made, but the trends seen in the global modes, and the appearance of varicose modes, confirms that the wake instability changes character when surface tension is added. The wake instability moves closer to the inlet and becomes a shear layer instability for intermediate surface tension.

The absolute instability thus has all the same trends as global linear instability with surface tension, confirming that there is a physical mechanism behind the phenomena. However, the frequency, growth rate and wavelength are not identical. The local analysis was performed only in one streamwise position, and more refined methods need to be applied to get real predictions from it (Huerre & Monkewitz 1990). Also, a fully global analysis might be necessary to get an accurate description of the influence of surface tension in this and similar flow cases.

The ordinary wake instability without surface tension, similar to the von Kármán instability behind the cylinder, has its origin in the low speed or recirculation region inside the wake. The linear global analysis shows clearly that when surface tension is introduced, this instability is gradually replaced by a new type of global modes located closer to the inlet, where the shear near the surface is strongest. The destabilization is strongest in the slowly developing example wake (higher Re),

containing a longer region of high shear at the surface. Both symmetric and antisymmetric modes were observed for this wake, further indicating that the new modes are shear layer modes rather than wake modes, and might therefore be observed in jets as well.

Ass. Prof. Philipp Schlatter and Dr. Espen Åkervik are acknowledged for assistance with the development of the parallel eigenvalue solver. This work was supported by the Swedish Research Council, Linné FLOW Centre and the European Union FP6 project EcoTarget, contract number 500345 (NMP2-CT-2004-500345).

References

- BLACKFORD, L. S., CHOI, J., CLEARY, A., D'AZEVEDO, E., DEMMEL, J., DHILLON, I., DONGARRA, J., HAMMARLING, S., HENRY, G., PETITET, A., STANLEY, K., WALKER, D. & WHALEY, R. C. 1997 *ScaLAPACK Users' Guide*. Philadelphia, PA: Society for Industrial and Applied Mathematics.
- CAMARRI, S. & GIANNETTI, F. 2007 On the inversion of the von Karman street in the wake of a confined square cylinder. *Journal of Fluid Mechanics* **574**, 169–178.
- DEVILLE, M. O., FISCHER, P. F. & MUND, E. H. 2002 *High-Order Methods for Incompressible Fluid Flow*. Cambridge: Cambridge University Press.
- DRAZIN, P. G. & REID, W. H. 1981 *Hydrodynamic Stability*, 9th edn. Cambridge: Cambridge University Press.
- GIANNETTI, F. & LUCHINI, P. 2007 Structural sensitivity of the first instability of the cylinder wake. *Journal of Fluid Mechanics* **581**, 167–197.
- HUERRE, P. & MONKEWITZ, P. A. 1990 Local and global instabilities in spatially developing flows. *Annual Review of Fluid Mechanics* **22**, 473–537.
- JUNIPER, M. P. 2006 The effect of confinement on the stability of two-dimensional shear flows. *Journal of Fluid Mechanics* **565**, 171–195.
- MASCHHOFF, K. J. & SORENSEN, D. C. 1996 P_arpac: An efficient portable large scale eigenvalue package for distributed memory parallel architectures. In *Proceedings of the Third International Workshop on Applied Parallel Computing, Industrial Computation and Optimization*, pp. 478–486. London, UK: Springer-Verlag.
- PIER, B. & HUERRE, P. 2001 Nonlinear self-sustained structures and fronts in spatially developing wake flows. *Journal of Fluid Mechanics* **435**, 145–174.
- REES, S. J. & JUNIPER, M. P. 2009 The effect of surface tension on the stability of unconfined and confined planar jets and wakes. *Journal of Fluid Mechanics* **633**, 71–97.
- SÖDERBERG, L. D. 2003 Absolute and convective instability of a relaxational plane liquid jet. *Journal of Fluid Mechanics* **493**, 89–119.
- TAMMISOLA, O. 2009 Linear stability of plane wakes and liquid jets: global and local approach. *Licentiate thesis, Royal Institute of Technology, Stockholm, Sweden*.
- TAMMISOLA, O., LUNDELL, F., SCHLATTER, P., WEHRFRITZ, A. & SÖDERBERG,

- L. D. 2011 Global linear and nonlinear stability of viscous confined plane wakes with co-flow. *Accepted for Journal of Fluid Mechanics* .
- TAMMISOLA, O., LUNDELL, F., SÖDERBERG, L. D., SASAKI, A. & MATSUBARA, M. 2009 Global stability of a plane liquid jet. In *Seventh IUTAM Symposium on Laminar-Turbulent Transition* (ed. P. Schlatter and D. S. Henningson), *IUTAM BOOKSERIES*, vol. 18, pp. 403–408. 233 Spring street, New York, NY 10013, United States: Springer, Proceedings of the Seventh IUTAM Symposium of Laminar-Turbulent Transition, Stockholm, Sweden, June 23-26, 2009.
- TAMMISOLA, O., SASAKI, A., LUNDELL, F., MATSUBARA, M. & SÖDERBERG, L. D. 2010 Stabilizing effect of surrounding gas flow on a plane liquid sheet. *Accepted for publication in Journal of Fluid Mechanics* .
- WILLIAMSON, C. H. K. 1996 Vortex dynamics in the cylinder wake. *Annual Review of Fluid Mechanics* **28**, 477–539.
- YECKO, P., ZALESKI, S. & FULLANA, J.-M. 2002 Viscous modes in two-phase mixing layers. *Physics of Fluids* **14** (12), 4115–4123.
- YIH, C.-S. 1967 Instability due to viscosity stratification. *Journal of Fluid Mechanics* **27**, 337–352.

Paper 4

4

The local and global stability of confined planar wakes at intermediate Reynolds number

By M. Juniper¹, O. Tammisola² and F. Lundell^{2,3}

¹Department of Engineering, University of Cambridge, CB2 1PZ, U.K.,

²Linné FLOW Centre, KTH Mechanics, Royal Institute of Technology, SE-100 44 Stockholm, Sweden

³Wallenberg Wood Science Center, KTH Mechanics, SE-100 44 Stockholm, Sweden

To appear in *Journal of Fluid Mechanics*.

At high Reynolds numbers, wake flows become more globally unstable when confined within a duct or between two flat plates. At Reynolds numbers around 100, however, global analyses suggest that such flows become more stable when confined, while local analyses suggest that they become more unstable. The aim of this paper is to resolve this apparent contradiction. In this theoretical and numerical study, we combine global and local stability analyses of planar wake flows at $Re = 100$ to determine the effect of confinement. We find that confinement acts in three ways: it modifies the length of the recirculation zone if one exists, it brings the boundary layers closer to the shear layers, and it can make the flow more locally absolutely unstable. Depending on the flow parameters, these effects work with or against each other to destabilize or stabilize the flow. In wake flows at $Re = 100$ with free slip boundaries, flows are most globally unstable when the outer flows are 50% wider than the half-width of the inner flow because the first and third effects work together. In wake flows at $Re = 100$ with no slip boundaries, confinement has little overall effect when the flows are weakly confined because the first two effects work against the third. Confinement has a strong stabilizing effect, however, when the flows are strongly confined because all three effects work together. By combining local and global analyses, we have been able to isolate these three effects and resolve the apparent contradictions in previous work.

1. Introduction

In this theoretical and numerical paper, we describe the effect of confining a viscous planar wake between two flat plates at $Re = 100$. In particular, we examine how the destabilizing effect of confinement is influenced by the boundary layers that are generated by the confining

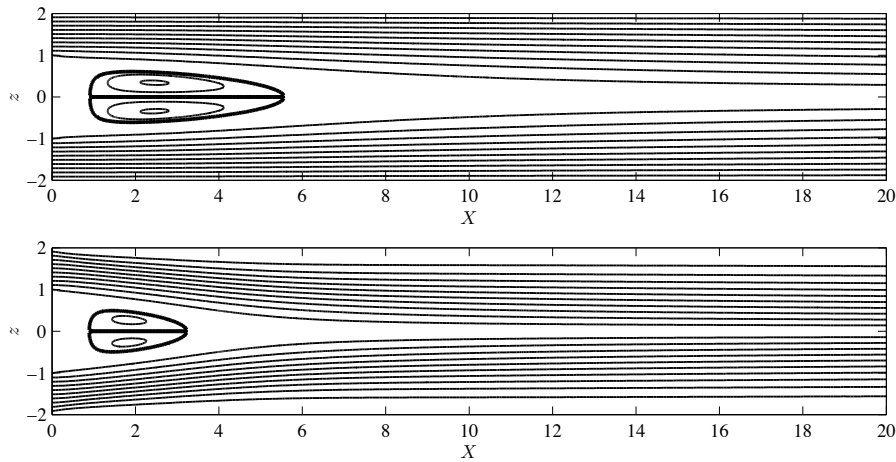


FIGURE 1. Streamlines of two of the confined wake flows studied in this paper. Both flows have inverse shear ratio $\Lambda^{-1} = -1.2$ and confinement parameter $h = 1$. The top flow has free slip at the boundaries. The bottom flow has no slip at the boundaries.

walls. Unlike our previous analyses, this analysis combines a local stability analysis with a global stability analysis over a wide range of confinements and shear ratios. This provides more information than can be obtained with independent local and global analyses.

Confined wake flows are frequently found in industry and in model problems. Our previous research into the effect of confinement has been motivated partly by instabilities that appear in paper manufacturing, Lundell, Söderberg & Alfredsson (2011) and Tammissola, Lundell, Schlatter, Wehrfritz & Söderberg (2011), and partly by instabilities that appear in rocket and aircraft engines, Juniper & Candel (2003).

The above flows tend to be at high Reynolds numbers, for which confinement increases global instability. This is seen particularly clearly in the experimental study of Richter & Naudascher (1976). They examined the fluctuating forces on a confined circular cylinder at $10^4 < Re < 10^6$ and found that the fluctuating cross-stream force, which arises from sinusoidal vortex shedding, increases markedly as the flow is confined. The same effect was observed in a numerical study by Kim, Yang & Senda (2004), by Bearman & Zdravkovich (1978) and Hwang & Yao (1997)

for the half-confined case, and by Healey (2007) for a confined rotating disk boundary layer. Confinement destabilizes wake flows at intermediate Reynolds numbers as well, as is seen, for example, in Davis, Moore & Purtell (1983) at $Re = 750$.

The effect of confinement is less well understood at low and moderate Reynolds numbers. In this paper, we examine viscous wake flows, such as those shown in Fig. 1, at $Re = 100$. Two incompressible flows with uniform viscosity are injected through the left boundary: a fast-moving outer flow and a slow-moving inner flow. When the inner flow is sufficiently slow-moving, a recirculation zone forms just downstream of the injection plane. The whole flow is confined between two flat plates. The ratio of the width of the outer flow to the half-width of the inner flow, which is labelled h , turns out to have a strong influence on the flow's stability.

Local stability analyses of jets and wakes with piecewise-linear velocity profiles, such as Juniper (2006) and Juniper (2007), show that inviscid flows become more absolutely unstable when confined. Co-flow inviscid planar jets are convectively unstable at all h but they become marginally absolutely unstable to a varicose mode at $h = 2.79$. Co-flow inviscid planar wakes are convectively unstable at large h but they become absolutely unstable to a sinuous mode at $h = 2.79$ and reach maximum absolute instability at $h = 1$, when the outer flow has exactly half the width of the inner flow. This result is exploited in cryogenic rocket engines in order to enhance break-up of the slow-moving liquid oxygen stream by the fast-moving hydrogen stream, Juniper & Candel (2003).

Although the effect of confinement is clear for inviscid flows, our previous studies of viscous flows at $Re \sim 10^2$ seem to contradict each other. On the one hand, a local stability analysis of viscous planar wakes without boundary layers, Rees & Juniper (2010), shows that the destabilizing effect of confinement persists down to $Re = 10$, although it becomes attenuated at lower Reynolds numbers because the instability itself becomes attenuated by viscosity. This destabilizing effect, attenuated by viscosity, is also seen at $Re = 500$ and $Re = 100$ in the nonlinear DNS of Biancofiore, Gallaire & Pasquetti (2011). On the other hand, linear global stability analyses of confined viscous planar wakes with boundary

layers, Tammisola *et. al* (2011), show that wakes at $Re = 100$ become more globally stable when confined. This is observed both for the linear global modes and in nonlinear DNS. At first sight, these results seem to contradict those of Rees & Juniper (2010) because stronger absolute instability should imply a stronger global instability. In this paper, we examine these confined flows in more detail in order to explain this apparent contradiction and to highlight the influence of the boundary layers, which was not considered in detail in Rees & Juniper (2010).

2. Methodology

In this paper, we perform two types of analysis on two types of flow. The first type of flow has free slip at the confining walls. The second type of flow has no slip at the confining walls. In the second type of flow, the boundary layers affect the stability of the shear layers and also block the flow near the wall, which shortens the recirculation bubble by forcing the flow to speed up near the centreline. By considering both flows with both analyses, we can separate the effect of confinement from the two effects caused by the boundary layers.

The properties of each flow are characterized by the conditions on the left boundary, where the inner flow has velocity U_1^* and width h_1^* and the outer flow has velocity U_2^* and width h_2^* . The shear between the two flows is quantified by the inverse shear ratio $\Lambda^{-1} \equiv (U_1^* - U_2^*) / (U_1^* + U_2^*)$. The confinement is quantified by the ratio $h \equiv h_2^* / h_1^*$. (In Rees & Juniper (2010), it was quantified by $h_{RJ} \equiv (h_2^* - h_1^*) / (h_2^* + h_1^*) = (h - 1) / (h + 1)$.) The viscosity is quantified by the Reynolds number, which is defined as $Re \equiv U_2^* h_1^* / \nu^*$. (In Rees & Juniper (2010), it was quantified by $Re_{RJ} \equiv (U_1^* + U_2^*) (h_1^* + h_2^*) / (2\nu^*) = (1 + h) / (1 - \Lambda) Re$.) For each type of flow we vary Λ^{-1} at $h = 1$ in order to test the effect of Λ^{-1} and then we vary h at $\Lambda^{-1} = -1.2$ in order to test the effect of h .

Our first type of analysis is a linear global stability analysis, Tammisola *et. al* (2011). The Navier–Stokes equations are linearized about the steady but unstable base flow and small perturbations are assumed of the form $\tilde{\mathbf{u}}(x, z) \exp(-i\omega_g t)$. The evolution operator for the perturbations is discretized and expressed as a matrix acting on the discretized state vector $\tilde{\mathbf{u}}(x, z)$. The global modes of the linearized system are the eigenmodes of this matrix. Each eigenmode consists of an eigenvalue, ω_g , which describes the frequency and growth rate, and an eigenvector, $\tilde{\mathbf{u}}(x, z)$, which describes the mode shape. The procedure for finding the

eigenmodes of this matrix is described in §3.

Our second type of analysis is a linear local stability analysis, Huerre & Monkewitz (1990). As for the global analysis, the Navier–Stokes equations are linearized about the steady but unstable base flow. The WKBJ approximation is applied, *i.e.* the base flow is assumed to be locally parallel and small local perturbations are assumed of the form $\hat{\mathbf{u}}(z) \exp(i(kx - \omega t))$. The absolute frequency ω_0 is calculated at each slice and the frequency and growth rate of the linear global mode, ω_g , are estimated by analytical continuation into the complex x -plane. The response of each slice at ω_g is then calculated and the WKBJ approximation is inverted in order to obtain the mode shape $\tilde{\mathbf{u}}(x, z)$. This procedure is described in §4.

3. The global analysis

3.1. Construction of the global analysis

The flow is assumed to be governed by the Navier–Stokes (N–S) equation and the incompressibility condition:

$$\frac{\partial \mathbf{U}_{tot}}{\partial t} + \mathbf{U}_{tot} \cdot \nabla \mathbf{U}_{tot} = -\nabla P_{tot} + \frac{1}{Re} \nabla^2 \mathbf{U}_{tot}, \quad (1)$$

$$\nabla \cdot \mathbf{U}_{tot} = 0. \quad (2)$$

Following our previous studies, the flow is assumed not to vary in the spanwise direction, y . The total velocity and pressure fields are divided into steady and time-varying components:

$$\mathbf{U}_{tot}(x, z, t) = \mathbf{U}(x, z) + \mathbf{u}(x, z, t), \quad (3)$$

$$P_{tot}(x, z, t) = P(x, z) + p(x, z, t). \quad (4)$$

The steady base flow $(\mathbf{U}(x, z), P(x, z))$ is the solution to the N–S equations (1–2) without time derivatives. The unsteady perturbation is assumed to take the form:

$$\mathbf{u}(x, z, t) = \tilde{\mathbf{u}}(x, z) \exp(-i\omega_g t). \quad (5)$$

The N–S equations are linearized around the base flow by ignoring quadratic terms in perturbation quantities, to give the Linearized N–S equations (LN–S):

$$\begin{aligned} -U\partial_x\hat{u} - V\partial_z\hat{u} - \hat{u}\partial_xU - \hat{v}\partial_zU \\ -\partial_x\hat{p} + \frac{1}{Re}(\partial_{xx}\hat{u} + \partial_{zz}\hat{u}) = -i\omega_g\hat{u} \end{aligned} \quad (6)$$

$$\begin{aligned} -U\partial_x\hat{v} - V\partial_z\hat{v} - \hat{u}\partial_xV - \hat{v}\partial_zV \\ -\partial_z\hat{p} + \frac{1}{Re}(\partial_{xx}\hat{v} + \partial_{zz}\hat{v}) = -i\omega_g\hat{v} \end{aligned} \quad (7)$$

$$\partial_x\hat{u} + \partial_z\hat{v} = 0. \quad (8)$$

The LN–S equations (8–11) constitute a 2D eigenvalue problem for ω_g . This set of equations is satisfied only for certain eigenvalues, ω_g , which give the growth rates and frequencies of the linear global modes. (We call ω_g the *complex frequency*.) Each ω_g has an associated eigenfunction $\tilde{\mathbf{u}}(x, z)$, which describes the shape of the global mode.

A finite number of the most unstable modes can approximate the dynamics of the flow, as described in Schmid (2007). In most of the cases presented in this paper, there is only one mode with positive growth rate, which dominates the dynamics after the initial transients have died away. In this paper, we focus only on this global mode.

3.2. Solution of the global analysis

The base flow is obtained from Direct Numerical Simulation (DNS) using a Legendre polynomial-based spectral-element method (SEM) implemented in the code `nek5000`, Fischer (1997). The inlet velocity has a slightly-smoothed top hat profile with slower velocity in the inner flow:

$$U(0, z > 0) = \frac{1}{\pi} \left[\arctan(500(h+1-z)) + \frac{\pi}{2} \right] + \frac{2}{\pi(\Lambda^{-1}-1)} \left[\arctan(500(1-z)) + \frac{\pi}{2} \right] \quad (9)$$

A symmetry condition is imposed along the centreline, $z = 0$. For these base flows, all the unstable modes are antisymmetric, which means that the DNS converges naturally to the steady (but antisymmetrically-unstable) solution.

At the wall boundary ($z = h + 1$), we set either a no slip condition or a free slip condition (Fig. 1). At the downstream boundary, we set a homogeneous Neumann condition for the velocities and a homogeneous

Dirichlet condition for the pressure. The possible influence of the downstream boundary condition is eliminated by using substantially longer domains for the base flow than are used in the stability problem. For more details about the code and base flow computations, see Tammisola *et. al* (2011).

To calculate the linear global modes, (8–11) are discretized in space using Chebyshev-polynomials in both the streamwise and cross-stream directions:

$$\hat{u}(x, z) \approx \sum_{i=1}^{N_x} \sum_{j=1}^{N_z} c_{ij} \phi^i(x) \phi^j(z) \quad (10)$$

where ϕ^k is the k^{th} Chebyshev polynomial. The values of the unknown coefficients c_{ij} are obtained by requiring the discretized equations to be satisfied exactly at the $N_x \times N_z$ collocation points. The domain is linearly transformed from $[-1, 1] \times [-1, 1]$ to $[0, L_x] \times [0, h_1 + h_2]$.

For all base flows, whether they have free slip or no slip at the confining walls, we set a no slip condition for the perturbation:

$$\hat{u}(x, h + 1) = 0, \quad \hat{v}(x, h + 1) = 0. \quad (11)$$

For the wake flows in this paper, it is sufficient to consider only antisymmetric modes:

$$\hat{u}(x, 0) = 0, \quad \partial_z \hat{v}(x, 0) = 0, \quad \hat{p}(x, 0) = 0. \quad (12)$$

The truncation of the domain in the streamwise direction is problematic because the only natural streamwise boundary condition for unstable global modes is to decay at infinity. We impose a Dirichlet condition at the inlet and a Neumann condition at the outlet:

$$\hat{u}(0, z) = 0, \quad \hat{v}(0, z) = 0, \quad (13)$$

$$\partial_x \hat{u}(L, z) = 0, \quad \partial_x \hat{v}(L, z) = 0. \quad (14)$$

We check that these boundary conditions do not affect the stability by ensuring that the most unstable eigenvalue is not sensitive to the domain length and that the upstream influence of the Dirichlet condition is small, Tammisola *et. al* (2011).

Using these techniques, the eigenvalue problem of a continuous operator (8-11) with boundary conditions (13-14) is transformed into a

generalised matrix eigenvalue problem:

$$\mathbf{A}\mathbf{q} = \omega_g \mathbf{B}\mathbf{q}, \quad (15)$$

where $\mathbf{q} = (\hat{u}, \hat{v}, \hat{p})$ is the eigenvector and ω_g the eigenvalue. The number of elements of the left-hand side matrix \mathbf{A} grows as $9N_x^2 N_z^2$ (compared to N_z^2 in the local analysis) and the required memory increases correspondingly. To handle this, the matrix is built in parallel and the eigenvalue problem solved using parallel versions of the Arnoldi algorithm, with linear algebra operations from ScaLAPACK, Tammisola *et. al* (2011).

4. The local analysis

4.1. Construction of the local analysis

As for the global analysis, the velocity and pressure fields are decomposed into a steady base flow, $(\mathbf{U}(x, z), P(x, z))$, and a small perturbation, $(\mathbf{u}(x, z, t), p(x, z, t))$. For the local analysis, however, we assume that the flow exhibits two well-separated length scales: an instability wavelength, λ , and a length scale that characterizes the stream-wise non-uniformity of the base flow, L . The ratio λ/L , which must be small for a local analysis to be rigorously valid, is labelled ε .

The development in this paper follows Monkewitz, Huerre & Chomaz (1993), which is summarized pedagogically in Huerre & Monkewitz (2000) §4. The LN–S equations for the small perturbation contain terms that scale with ε^0 , terms that scale with ε^1 and terms, which are neglected, that scale with higher orders of ε . The ε^0 terms represent a streamwise succession of locally parallel problems, which are solved with the technique described in §4.2. The complex frequency, ω_g , of the linear global mode and the position of the wavemaker region, X_s , are calculated with the technique described in §4.3. The corresponding global mode shape is calculated in §4.4 by integrating

$$\mathbf{u}(x, z, t) \sim A_0(X) \hat{\mathbf{u}}^\pm(z; X) \exp\left(\frac{i}{\varepsilon} \int_0^X k^\pm(X'; \omega) dX' - \omega_g t\right), \quad (16)$$

where, at the X -position of each slice, k^+ is the local wavenumber downstream of X_s , k^- is the local wavenumber upstream of X_s , and $\hat{\mathbf{u}}^\pm(z; X)$ is the corresponding eigenfunction. The ε^1 terms of the LN–S equations describe the evolution of the slowly-varying amplitude $A_0(X)$ but, for the simple local analysis in this paper, we assume that A_0 is a constant.

4.2. Solution of the locally-parallel problem

The planar LN–S equations for the perturbation are expressed as three PDEs in three primitive variables, (u, v, p) . At each X -position, the perturbations are expressed as Fourier modes such as

$$u(x, z, t) = \hat{u}(z) \exp\{i(kx - \omega t)\}$$

which converts the three PDEs into three ODEs. The ODEs are discretized on a Chebyshev-spaced grid in the z -direction, which produces a generalized matrix eigenvalue problem of the form

$$\mathbf{A}(k)\phi = \omega\mathbf{B}(k)\phi \quad (17)$$

where ϕ is a column vector representing the discretized values of \hat{u} , \hat{v} and \hat{p} . This is satisfied for certain (ω, k) pairs and represents the dispersion relation for this slice of the flow. In this paper, 108 Chebyshev-spaced points are used between the centreline and top wall, which is sufficient that the eigenvalues change by $\sim 10^{-5}$ when the resolution is increased.

A temporal stability analysis is performed on a slice near the entry plane to find the maximum temporal growth rate, which corresponds to the growth rate of the centre of the impulse response in a parallel flow, Juniper (2007). A spatio-temporal stability analysis is then performed by finding the saddle points of $\omega(k)$ that are also k^+/k^- pinch points. (In a flow with mean mass flux in the positive x -direction, the perturbation with maximum temporal growth rate lies on the k^+ branch and the algorithm used in this paper finds all the k^- branches that pinch with it.) In wake flows such as those studied here, there can be up to three such k^+/k^- saddles, Juniper (2006). The highest saddle is labelled the *dominant* saddle point. These saddle points are then followed as the base flow changes. The absolute complex frequency of the dominant saddle, ω_0 , as a function of streamwise distance, X , is stored for the algorithm in §4.3. An example of $\omega_{0i}(X)$ is shown in Fig. 2(b).

4.3. Calculating the frequency and growth rate of the linear global mode

It is assumed that the absolute complex frequency $\omega_0(X)$ can be continued analytically into the complex X -plane. The complex frequency of the linear global mode, ω_g , is given at leading order in ε by the saddle point of $\omega_0(X)$, which is labelled $\omega_s(X_s)$, Chomaz, Huerre & Redekopp (1991). In this paper, the position of the saddle point X_s is estimated by selecting the region of $\omega_0(X)$ around the maximum of $\omega_{0i}(X)$ and then fitting Padé polynomials to these values. (Padé polynomials take the

form $P^n(x)/Q^m(x)$, where $P^n(x)$ and $Q^m(x)$ are polynomials of order n and m respectively.) Padé polynomials have two advantages over standard polynomials: they can fit $\omega_0(X)$ accurately at relatively low order, and they are better behaved in the complex plane, Cooper & Crighton (2000).

Initially, the saddle position, X_s , is found for $n = m = 2$ by considering a small region around $\omega_{0i}(X)$. The saddle is then followed as n and m are increased to 8 and the threshold value of ω_{0i} is lowered until the polynomials fit a wide range of $\omega_0(X)$ around the absolutely unstable region. This gives the complex frequency ω_g of the global mode and the position of the wavemaker region X_s . If n and m are increased further, there is no systematic change in the saddle position but its variance around the value at $n = m = 8$ increases. From this, we conclude that, for larger n and m , the saddle position becomes unduly influenced by small errors in $\omega_0(X)$, without becoming more accurate.

These results can be compared with those from other local analyses. For the steady but unstable flow behind a cylinder at $Re = 50$, Pier (2002) found the real part of ω_g to be 0.78, while Giannetti & Luchini (2007) found $\omega_g = 0.779 + 0.09i$. The process used in this study finds $\omega_g = 0.789 + 0.0918i$ for the same flow. Given that the calculated value of ω_g varies slightly with n and m and with the streamwise extent of $\omega_0(X)$ that is sampled, this is sufficiently close for us to have confidence in the procedure.

These results can also be compared with those from global analyses (§3). Giannetti & Luchini (2007) compared a linear global analysis with a linear local analysis of the flow behind a cylinder at $15 < Re < 100$ and showed that the local analysis always over-predicts ω_{gi} . At $Re = 50$, their global analysis predicts $\omega_g = 0.747 + 0.0125i$, showing that their local analysis over-predicts ω_{gi} by 0.08. At $Re = 100$, which is the value used for most of the results in this paper, their local analysis over-predicts ω_{gi} by 0.059. Given that the flows in this paper are very similar to the flow behind a cylinder, we expect a similar over-prediction in this paper.

4.4. Calculating the 2D global mode shape

The 2D global mode shape is calculated by investigating how the flow responds to an oscillation with complex frequency ω_g applied at X_s , so that the integral (16) can be evaluated. To do this, the values of k that satisfy (17) when $\omega = \omega_g$ are calculated and the two that correspond to the k^+ and k^- branches in the X -plane are selected. The global mode is estimated from (16) by integrating the k^- branch upstream of X_s and the k^+ branch downstream of X_s . The z -dependence is obtained by multiplying the result by the eigenfunction of the k^- branch upstream of X_s and that of the k^+ branch downstream of X_s .

5. Comparison of local and global results

In this section, results from the global analysis are compared with those of the local analysis for two wake flows: one at $Re = 400$ and the other at $Re = 100$.

5.1. $Re = 400$

Figure 2 shows local and global results for a confined wake flow at $Re = 400$ with $h = 1$, $\Lambda^{-1} = -1.2$ and a free slip condition at the walls. There is a recirculation zone between $2.36 < X < 22.29$. Taking the length of this recirculation zone as a characteristic streamwise evolution lengthscale, L , we obtain $L \approx 20$. The absolutely unstable region lies between $0.06 < X < 28.42$. Continuing ω_0 analytically into the complex X -plane, the complex global frequency is found to be $\omega_g(\text{loc}) = 0.6547 + 0.1306i$. The k^+ and k^- branches are calculated at $\omega_g(\text{loc})$ and are plotted in Fig. 2(c,d) alongside the complex local wavenumber, k , extracted from the global analysis. The complex local wavenumber, k , closely follows the k^- branch upstream of the wave-maker region and the k^+ branch downstream, as expected.

The global analysis gives a complex global frequency of $\omega_g(\text{glob}) = 0.6659 + 0.1133i$, which is slightly more stable than that of the local analysis, as expected from §4.3. (Being at $Re = 400$, however, the difference is quite small.) The global analysis gives the 2D eigenfunction in Fig. 2(e), while, by integrating (16), the local analysis gives the 2D eigenfunction in Fig. 2(f), which is very similar. The slightly higher growthrate in the local analysis causes the centre of its global mode to be slightly further upstream. This is a general feature of the global mode predicted

by the local analysis. Having calculated the k^\pm branches and the mode shapes, we can estimate that $\lambda \approx 5.0$, which means that $\varepsilon \approx 0.25$. The local analysis works well at this value of ε .

Figure 3 shows the k^+ and k^- branches and the 2D eigenfunctions calculated by the local analysis, but at the complex frequency calculated by the global analysis, $\omega_g(\text{glob})$. The results are almost identical, which shows that the only significant defect of the local analysis is its over-prediction of ω_{gi} .

In summary, the global analysis gives the more accurate prediction of the absolute frequency and the 2D eigenfunctions because it does not make the parallel flow assumption. However, the local analysis gives the more useful qualitative information about the flow. For instance it shows that, although the global mode has a maximum amplitude at $X = 28.36$, it is actually driven by a wavemaker region at $X = 12.43$, which arises from the absolutely unstable region between $0.06 < X < 28.42$, which is centred on the recirculation zone. The flow downstream of the recirculation zone is simply responding to the forcing from this region.

5.2. $Re = 100$

Fig 4 shows results for a confined wake flow at $Re = 100$ with $h = 1$, $\Lambda^{-1} = -1.2$ and a free slip condition at the walls. There is a recirculation zone between $0.91 < X < 5.57$. Taking the length of this recirculation zone as a characteristic streamwise evolution lengthscale, L , we obtain $L \approx 6$. The absolutely unstable region lies between $0.17 < X < 6.69$. From this, the complex global frequency is found to be $\omega_g(\text{loc}) = 0.6538 + 0.08594i$. The k^+ and k^- branches are calculated at $\omega_g(\text{loc})$ and are plotted in Fig. 4(c,d) alongside the complex local wavenumber, k , extracted from the global analysis. The complex local wavenumber, k , follows the k^- branch upstream of the wavemaker region and the k^+ branch downstream, but is not as close as it was in the $Re = 400$ case.

The global analysis gives a complex global frequency of $\omega_g(\text{glob}) = 0.6613 + 0.02665i$, which is 0.059 more stable than that of the local analysis, as expected from §4.3. The global analysis gives the 2D eigenfunctions in Fig. 4(e), while the local analysis gives the 2D eigenfunctions

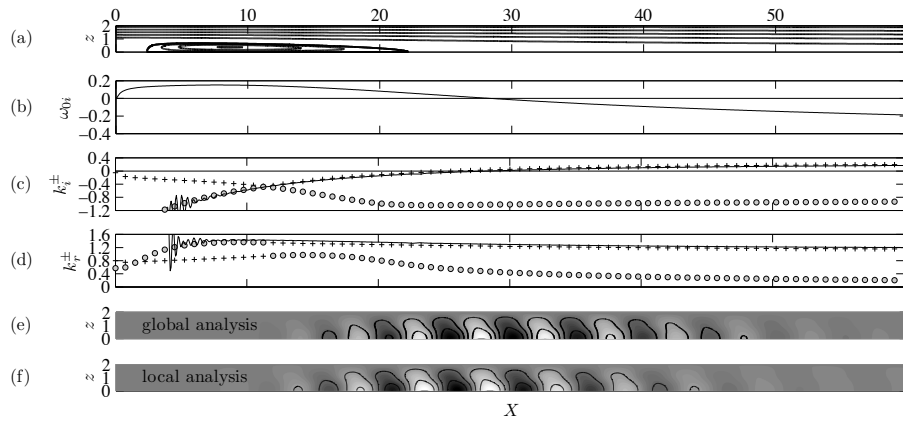


FIGURE 2. The base flow (a), local stability properties (b–d) and global modes (e–f) of a confined planar wake with $h = 1$, $\Lambda^{-1} = -1.2$, $Re = 400$ and free slip boundaries; (a) streamlines; (b) absolute growth rate, ω_{0i} ; (c) spatial growth rates, k_i^+ (+) and k_i^- (o), calculated with the local analysis, compared with k_i^- (–) extracted from the global analysis (the latter is noisy at the upstream end because the amplitude is small); (d) as for (c) but for the spatial wavenumber, k_r ; (e) $\tilde{v}(x, z)$ of the first eigenmode calculated with the global analysis; (f) $\tilde{v}(x, z)$ of the first eigenmode calculated with the local analysis;

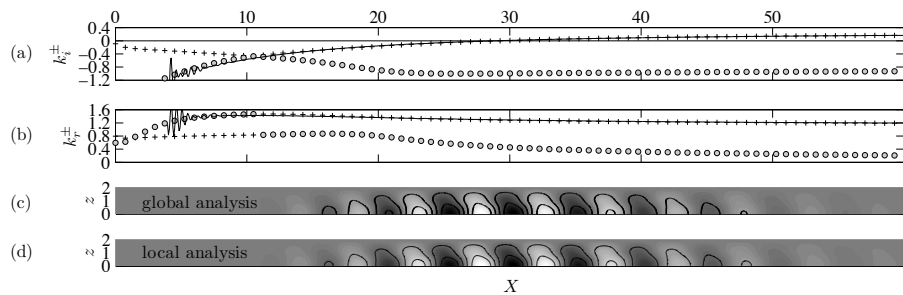
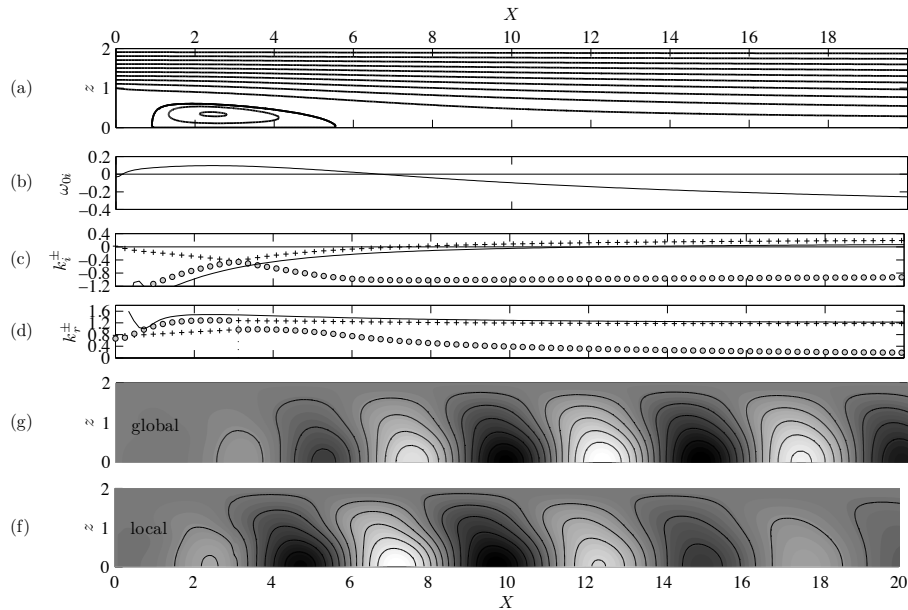


FIGURE 3. As for Fig. 2(c–f) but with k^\pm calculated at the complex frequency of the global analysis, $\omega_g(\text{glob})$, rather than that of the local analysis, $\omega_g(\text{loc})$.

in Fig. 4(f). The agreement is reasonable but not excellent. Again, the higher growthrate in the local analysis causes the centre of its global mode to be slightly further upstream. Having calculated the k^\pm branches

FIGURE 4. As for Fig. 2, but for $Re = 100$.

and the mode shapes, we can estimate that $\lambda \approx 5.1$, which means that $\varepsilon \approx 0.8$. This is too large to expect the WKBJ analysis to be accurate.

Figure 5 shows the k^+ and k^- branches and the 2D eigenfunctions calculated with the local analysis, but at the complex frequency calculated with the global analysis, $\omega_g(\text{glob})$. This gives a more accurate prediction of the 2D eigenfunction than was obtained with $\omega_g(\text{loc})$. This shows that, for this flow, the inaccuracy in the local analysis lies in the prediction of ω_g , rather than in the calculation of the k^\pm branches downstream. This is because the local analysis is less accurate in the upstream regions, which determine ω_g , because the flow is locally non-parallel there. By contrast, the local analysis is accurate in the downstream regions because the flow is nearly locally parallel there.

6. Effect of shear ratio

The growth rate and frequency of the linear global mode are plotted in Fig. 6 and table 1 for flows with $Re = 100$, $h = 1$ and varying Λ^{-1} . The top frames show flows with free slip at the boundaries. The bottom frames show flows with no slip at the boundaries. As the co-flow increases (as Λ^{-1} becomes more negative), the global modes become more

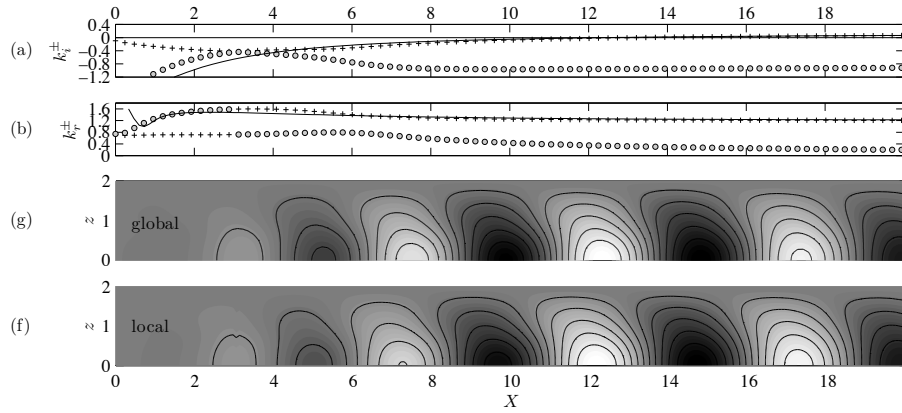


FIGURE 5. As for Fig 3, but for $Re = 100$.

stable and oscillate at higher frequencies. We will use the local analysis to find the physical origin of these trends.

There is a nearly systematic off-set between the complex frequencies calculated with the local analysis and those calculated with the global analysis, very similar to that found by Giannetti & Luchini (2007). The real part of this offset is smaller for the free slip case, for which $\varepsilon \approx 0.8$, than it is for the no slip case, for which $\varepsilon \approx 1.5$, probably because the free slip case is closer to being locally parallel. The imaginary part of this offset is always around 0.059.

The streamlines, the absolutely unstable regions (light grey), and the wavemaker region (dark grey) are shown in Fig 7(a) for the case with free slip and in Fig 8(a) for the case with no slip. The local absolute growth rate, ω_{0i} , and the local k_i^+ and k_i^- branches are shown in Figs 7(b) and 8(b).

For low co-flow (bottom frames) the region of absolute instability creates a globally unstable flow, whose wavemaker region lies just downstream of the centre of the recirculating zone. As the co-flow increases (i.e. as Λ^{-1} becomes more negative), the recirculating zone becomes smaller and the flow becomes more stable.

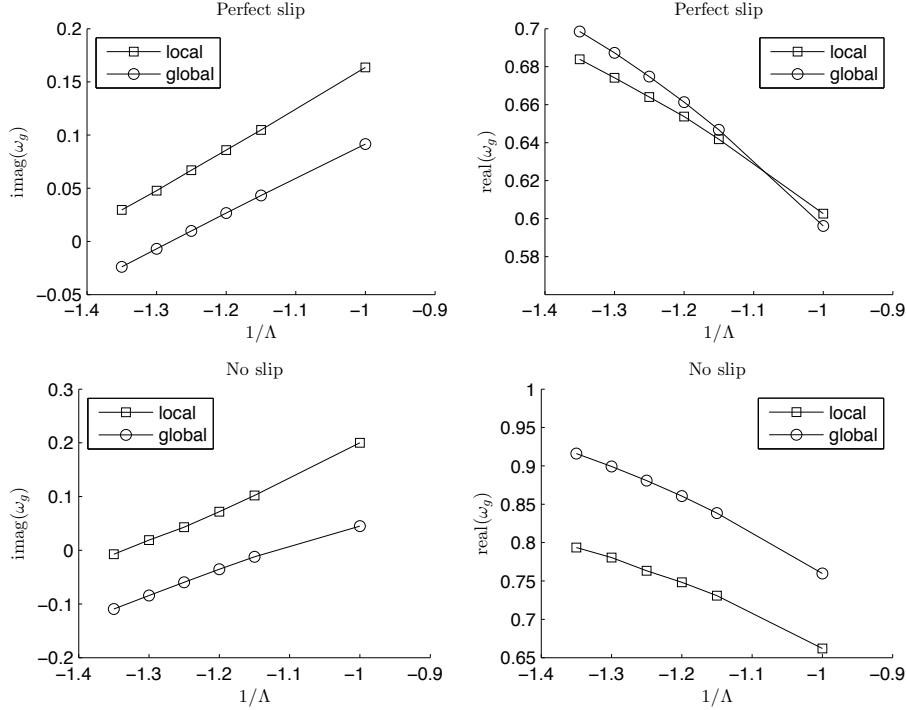


FIGURE 6. Growth rate, ω_{gi} (left) and frequency, ω_{gr} (right) of the linear global mode calculated with the local analysis (squares) and the global analysis (circles) for free slip boundaries (top) and no slip boundaries (bottom).

The cases with no slip have smaller recirculation zones than the corresponding cases with free slip. This is the first reason why the cases with no slip are more globally stable than the cases with free slip, but it is not the only reason.

In the case with free slip, the absolutely unstable region extends into the co-flow region on both sides of the recirculation zone, similar to the results of Pier (2002) for an unconfined flow behind a cylinder. In the case with no slip, however, the absolutely unstable region does not extend into the co-flow region downstream of the recirculation zone. We can conclude that the second reason that the cases with no slip are more globally stable than the cases with free slip is that the proximity of the boundary layer to the shear layer makes the shear layer less locally

Perfect slip		
Λ^{-1}	$\omega_g(\text{loc})$	$\omega_g(\text{glob})$
-1.00	0.6026 + 0.163657i	0.5961 + 0.091515i
-1.15	0.6418 + 0.104847i	0.6468 + 0.043247i
-1.20	0.6538 + 0.085942i	0.6613 + 0.026651i
-1.25	0.6641 + 0.066963i	0.6748 + 0.009889i
-1.30	0.6742 + 0.047717i	0.6873 - 0.006971i
-1.35	0.6839 + 0.029651i	0.6985 - 0.023865i

No slip		
Λ^{-1}	$\omega_g(\text{loc})$	$\omega_g(\text{glob})$
-1.00	0.6621 + 0.200105i	0.7597 + 0.044896i
-1.15	0.7307 + 0.101872i	0.8385 - 0.012174i
-1.20	0.7482 + 0.071893i	0.8606 - 0.035369i
-1.25	0.7632 + 0.042795i	0.8807 - 0.059537i
-1.30	0.7805 + 0.018816i	0.8992 - 0.084329i
-1.35	0.7936 - 0.007261i	0.9159 - 0.109491i

TABLE 1. Data in Fig. 6

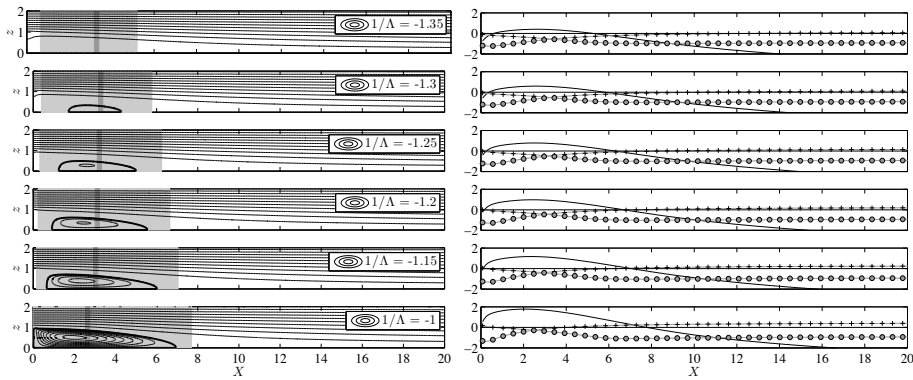


FIGURE 7. Streamlines (right) and ω_{0i} (-), k^+ (+) and k^- (o) (left) for the free slip case at $h = 1$ as Λ^{-1} varies. The absolutely unstable region is shown in light grey. The position of the wavemaker region is shown in dark grey. As the co-flow increases (top to bottom), the recirculation zone strengthens and the flow becomes more absolutely unstable.

unstable.

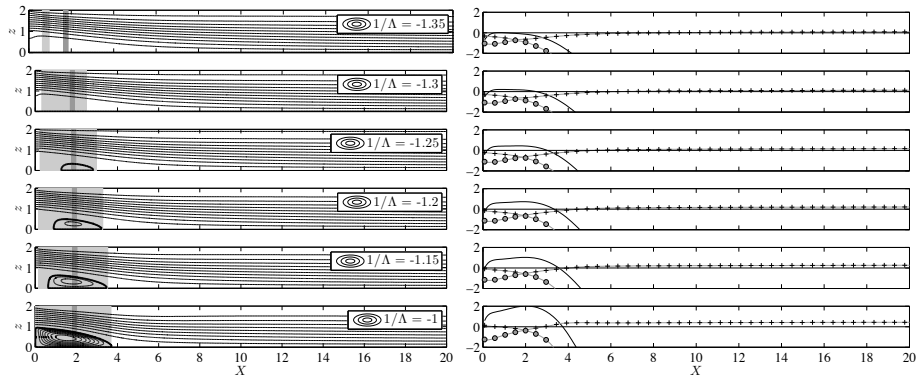


FIGURE 8. As for Fig. 7 but for the no slip case. The same effect is seen at the upstream end of the recirculation bubble but the flow quickly becomes convectively unstable at the downstream end due to the boundary layers.

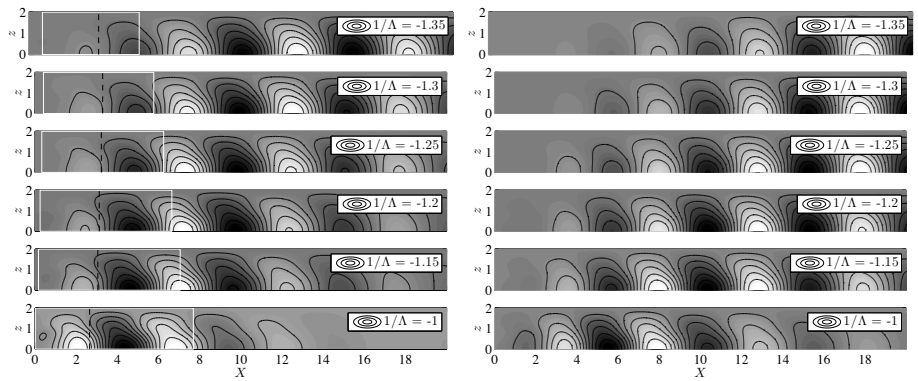


FIGURE 9. $\tilde{v}(x, z)$ eigenfunctions for the free slip cases calculated with a local analysis (left) and a global analysis (right). The global mode lies further upstream for the local analysis because of its higher growth rate.

The eigenfunctions from the local analysis are compared with those from the global analysis in figure 9 (free slip) and 10 (no slip). They have the same qualitative structure and behaviour but there are some quantitative differences. When compared with the corresponding eigenfunction of the global analysis, each eigenfunction of the local analysis always has a slightly longer wavelength, more rapid growth at the upstream end, more rapid decay at the downstream end, and a centre that

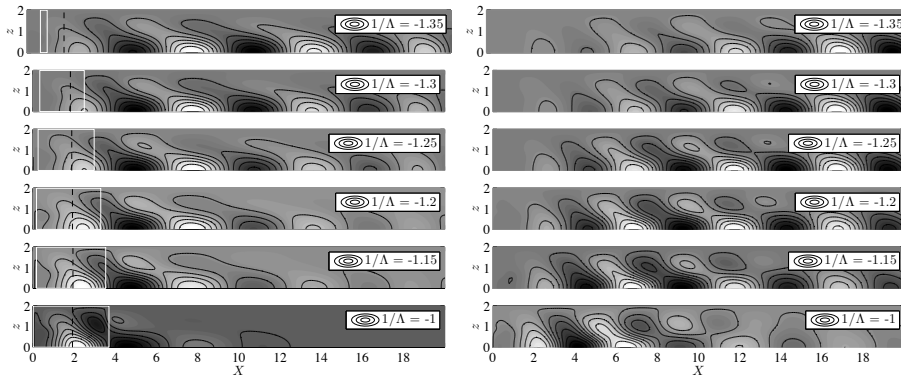


FIGURE 10. As for Fig. 9 but for the no slip cases.

is further upstream. This is because each eigenfunction from the local analysis has a lower $k_r(X)$ and a higher $k_i(X)$ than the corresponding eigenfunction from the global analysis. This is exactly the trend seen in Fig. 4. and, when Fig. 4 is compared with Fig. 5, it is seen that this arises because the local analysis over-predicts the global growth rate (see Fig. 6). When the local analysis is repeated using the complex frequency derived from the global analysis, as in Fig. 5, the eigenfunctions from the local analysis are almost identical to those from the global analysis. As already mentioned, this over-prediction is a common feature of wake flows at this Reynolds number ($Re \sim 100$), Giannetti & Luchini (2007). This defect of the local analysis arises because the flow is locally non-parallel. The local analysis becomes more accurate as the Reynolds number increases because the flow becomes more locally parallel.

7. Effect of confinement

The growth rate and frequency of the linear global mode are plotted as a function of h in Fig. 11 for flows with $\Lambda^{-1} = -1.2$ and $Re = 100$ with free slip and no slip at the boundaries. For the free slip cases, the flow is most unstable when $h \approx 1.5$. For the no slip cases, the flow is barely affected by confinement when $h > 2$ but is strongly stabilized when $h < 2$. We will use the local analysis to find the physical origin of these trends.

The streamlines, the absolutely unstable regions, and the position of the wavemaker region are shown in Fig 12(a) for the case with free slip and in Fig 13(a) for the case with no slip. The local absolute growth

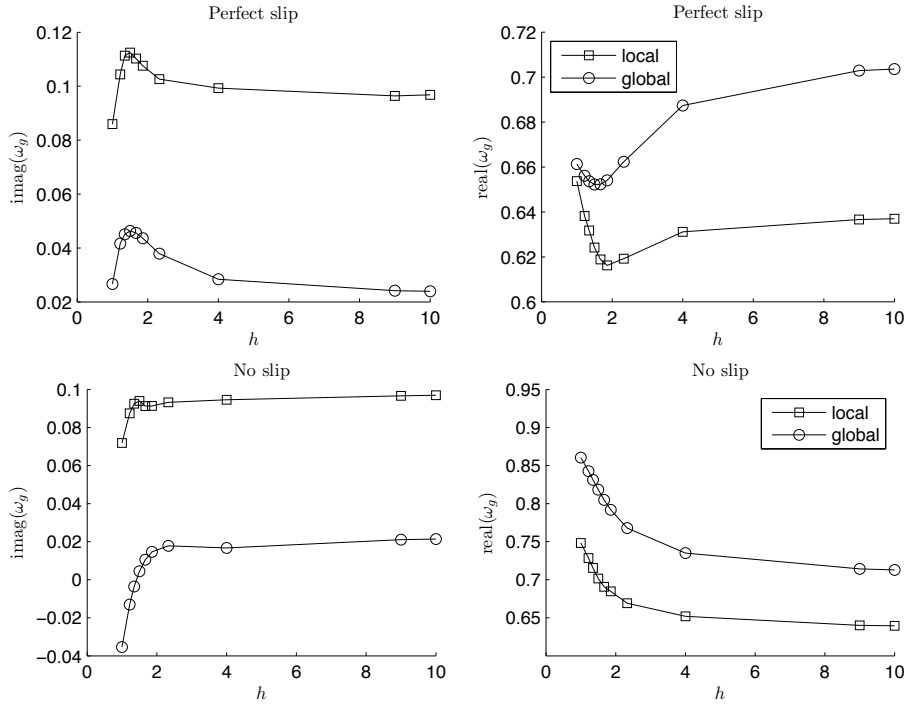


FIGURE 11. Growth rate, ω_{gi} (left) and frequency, ω_{gr} (right) of the linear global mode calculated with the local analysis (squares) and the global analysis (circles) for free slip boundaries (top) and no slip boundaries (bottom)

rate, ω_{0i} and the k_i^+ and k_i^- branches are shown in Fig 12(b) and 13(b).

When the confining walls are far away ($h \gg 1$), the recirculation zone of the case with free slip is almost the same size as that for the case with no slip and, as would be expected, the flows are equally unstable. As the flows become more confined, the recirculation zone of the case with free slip lengthens, while that of the case with no slip shortens. This is the first reason why the cases with free slip are more globally unstable than those with no slip. It is identical to the first reason in §6. If this first effect acted alone, confinement would destabilize flows with free slip but stabilize flows with no slip.

Perfect slip		
h	$\omega_g(\text{loc})$	$\omega_g(\text{glob})$
1.000	0.6538 + 0.085942i	0.6613 + 0.026651i
1.220	0.6383 + 0.104380i	0.6562 + 0.041594i
1.350	0.6318 + 0.111333i	0.6537 + 0.045078i
1.500	0.6242 + 0.112461i	0.6523 + 0.046319i
1.670	0.6189 + 0.110243i	0.6523 + 0.045606i
1.860	0.6163 + 0.107583i	0.6541 + 0.043574i
2.330	0.6192 + 0.102644i	0.6624 + 0.037869i
4.000	0.6311 + 0.099269i	0.6874 + 0.028373i
9.000	0.6367 + 0.096425i	0.7030 + 0.024166i
10.000	0.6370 + 0.096776i	0.7036 + 0.023956i
No slip		
h	$\omega_g(\text{loc})$	$\omega_g(\text{glob})$
1.000	0.7482 + 0.071893i	0.8606 - 0.035369i
1.220	0.7286 + 0.087469i	0.8426 - 0.013077i
1.350	0.7155 + 0.092530i	0.8311 - 0.003578i
1.500	0.7017 + 0.093950i	0.8183 + 0.004457i
1.670	0.6907 + 0.091285i	0.8049 + 0.010542i
1.860	0.6847 + 0.091329i	0.7918 + 0.014624i
2.330	0.6692 + 0.093271i	0.7678 + 0.017788i
4.000	0.6520 + 0.094551i	0.7350 + 0.016713i
9.000	0.6400 + 0.096620i	0.7143 + 0.021059i
10.000	0.6395 + 0.096926i	0.7129 + 0.021374i

TABLE 2. Data in Fig. 11

When the confining walls become closer (h decreasing), the absolutely unstable region extends further downstream of the recirculation zone in the case with free slip but not in the case with no slip. This shows that the boundary layer velocity profile makes the shear layer less locally unstable, as seen in §6. If this second effect acted alone, confinement would slightly destabilize flows with free slip but stabilize flows with no slip.

When the confining walls are close ($h < 2$), the absolutely unstable region upstream of the recirculation zone extends far into the co-flow region. This is the effect of confinement described by Rees & Juniper (2010). (In that paper, h is defined differently, such that h in this paper equals $(1 + h)/(1 - h)$ in that paper.) The global instability reaches a maximum (Fig.11) around $h = 1.5$, which matches exactly the value of

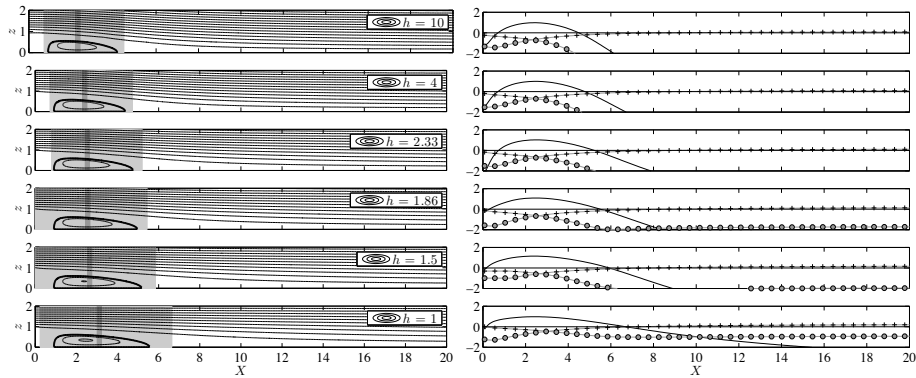


FIGURE 12. Streamlines (right) and ω_{0i} ($-$), k^+ ($+$) and k^- (\circ) (left) for the free slip case at $\Lambda^{-1} = -1.2$ as h varies. The absolutely unstable region is shaded in grey and the position of the wavemaker region is shown in dark grey.

$h = 0.2$ at which Rees and Juniper (Fig.8d) predict that the absolute instability is maximal. If this third effect acted alone, confinement would destabilize flows with free slip (until $h \approx 1.5$) and also destabilize flows with no slip, probably to a similar value of h .

Through the local analysis, we can now explain the effect of confinement on the stability of viscous wake flows and explain the results in Fig. 11, which is the main aim of this paper. In the case with free slip, the three effects described above work together: confinement increases the size of the recirculation zone, extends the absolutely unstable region downstream of the recirculation zone and also extends it upstream of the recirculation zone, until $h \approx 1.5$. In the case with no slip, the first two effects work against the third: confinement decreases the size of the recirculation zone, slightly reduces the absolutely unstable region downstream of the recirculation zone but also extends it upstream of the recirculation zone, probably also until $h \approx 1.5$. At the Reynolds number studied here, these effects almost exactly cancel out until $h \approx 1.5$, at which point all effects become stabilizing. In the local analysis of the no slip case, there is a slight peak around $h = 1.5$ but this is not seen in the global analysis.

The eigenfunctions from the local analysis are compared with those from the global analysis in figure 14 (free slip) and 15 (no slip). The

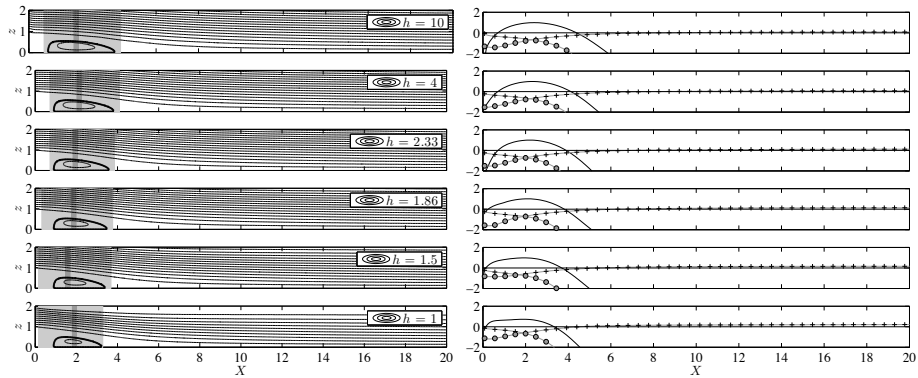


FIGURE 13. As for Fig. 12 but for the no slip case.

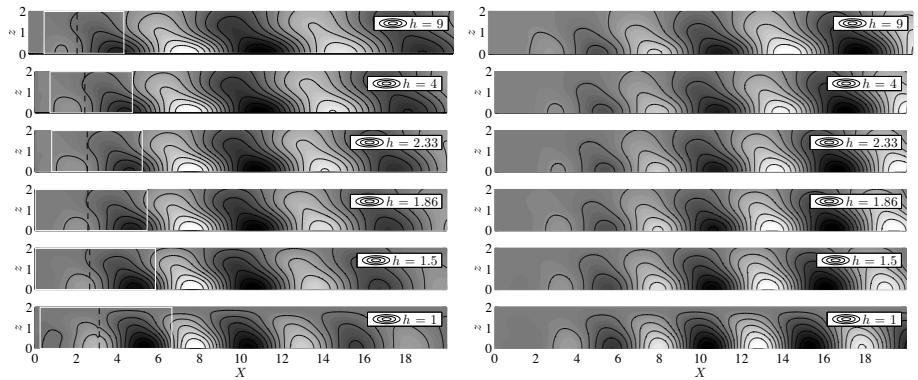


FIGURE 14. $\tilde{v}(x, y)$ eigenfunctions for the free slip cases calculated with a local analysis (left) and a global analysis (right).

behaviour is the same as that seen in figures 9 and 10 and the difference arises because the flow is locally non-parallel. This is most noticeable in the no slip cases at smaller values of h because the flow is more non-parallel for these flows than it is at larger values of h .

8. Conclusions

Confined wake flows are frequently found in industry and in model problems. Our previous work at high Reynolds numbers shows that confinement is destabilizing. Our previous work at medium to low Reynolds numbers, however, seems to give contradictory results. The aim of this

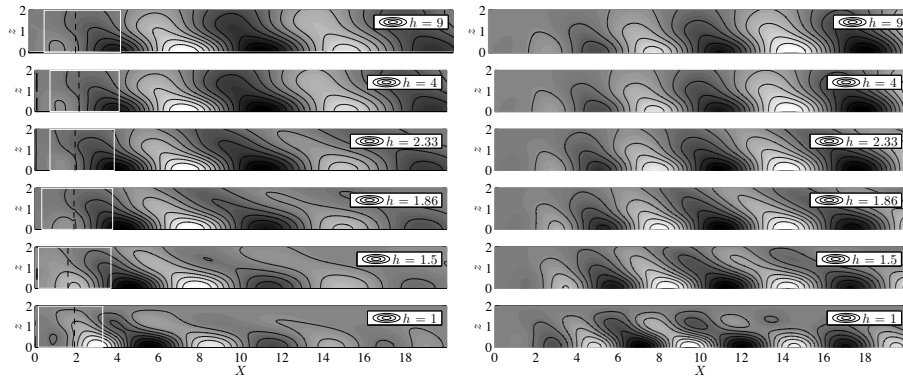


FIGURE 15. As for Fig. 14 but for the no slip cases.

paper is to resolve the apparent contradiction.

We consider, at $Re = 100$, two types of confined wake flows: one with free slip at the walls and one with no slip. We perform two types of analysis: a local stability analysis and a global stability analysis. These show that the global instability is caused by an absolutely unstable region centred on the recirculation zone. The local analysis always slightly over-predicts the global growth rate, as expected from previous work, but provides useful qualitative information about the effect of confinement on the flow.

We find that confinement acts in three ways: (i) it modifies the length of the recirculation zone, (ii) it brings the boundary layers closer to the shear layers, which changes their stability and (iii) it makes the flow more locally absolutely unstable when the confinement ratio, h , is around 1.5. Depending on the flow parameters, these effects can work with or against each other to destabilize or stabilize the flow.

In a flow with free slip, in which effect (ii) does not play a role, confinement lengthens the recirculation zone and makes the flow more absolutely unstable around $h = 1.5$, both of which are destabilizing effects. Effects (i) and (iii) therefore work with each other to make the flow most globally unstable around $h = 1.5$, as seen in Fig. 11 (top left).

In a flow with no slip, confinement shortens the recirculation zone and brings the boundary layers closer to the shear layers, both of which are stabilizing. For $h > 1.5$, effects (i) and (ii) work against effect (iii) and confinement has little overall effect on the stability. For $h < 1.5$, effects (i) and (ii) work with effect (iii) and confinement has a strongly stabilizing effect. This can be seen in Fig 11 (bottom left).

Rees & Juniper (2010) used a local analysis analysis to consider the third effect in isolation, while Tammisola *et. al* (2011) used a global analysis to consider all three effects together. These studies had contradictory results. By combining local and global analyses, we have been able to isolate the three effects described above and therefore resolve the apparent contradiction in our previous work. This shows the value of a combined local and global approach to shear flow instabilities, in which a global analysis gives accurate results, while a local analysis gives physical insight.

References

- BEARMAN, P. W. & ZDRAVKOVICH, M. 1978 Flow around a circular cylinder near a plane boundary *J. Fluid Mech.* **89**, 33–47.
- BIANCOFIORE, L., GALLAIRE, F. & PASQUETTI, R. 2011 Influence of confinement on a two-dimensional wake *Submitted to J. Fluid Mech.*
- CHOMAZ, J-M., HUERRE, P. & REDEKOPP, L. 1991 A frequency selection criterion in spatially-developing flows *Stud. Appl. Math.* **84**, 119144.
- COOPER, A. J. & CRIGHTON, D. G. 2000 Global modes and superdirective acoustic radiation in low-speed axisymmetric jets *Eur. J. Mech. B* **19**, 559574.
- DAVIS, R. W., MOORE, E. F & PURTELL, L. P. 1983 A numerical-experimental study of confined flow around rectangular cylinders *Phys. Fluids* **27**(1), 46–59.
- FISCHER, P. F. 1997 An overlapping schwarz method for spectral element solution of the incompressible Navier–Stokes equations *J. Comp. Phys.* **133** 84–101
- GIANNETTI, F. & LUCHINI, P. 2007 Structural sensitivity of the first instability of the cylinder wake *J. Fluid Mech.* **581**, 167–197.
- HEALEY, J. J. 2007 Enhancing the absolute instability of a boundary layer by adding a far-away plate *J. Fluid Mech.* **579**, 29–61.
- HUERRE, P. & MONKEWITZ, P. A. 1990 Local and global instabilities in spatially developing flows *Ann. Rev. Fluid Mech.* **22**, 473–537.
- HUERRE, P. & MONKEWITZ, P. A. 2000 Open shear flow instabilities. In *Perspectives in fluid dynamics : a collective introduction to current research* (eds. G. K. Batchelor, H. K. Moffat & M. G. Worster) C.U.P.
- HWANG, R. R. & YAO, C-C. 1997 A numerical study of vortex shedding from a square cylinder with ground effect *J. Fluids Eng.* **119**, 512–518.
- JUNIPER, M. P & CANDEL, S. M. 2003 The stability of ducted compound flows and consequences for the geometry of coaxial injectors *J. Fluid Mech.* **482**, 257–269.
- JUNIPER, M. P. 2006 The effect of confinement on the stability of planar shear flows *J. Fluid Mech.* **565**, 171–195.
- JUNIPER, M. P. 2007 The full impulse response of two-dimensional shear flows and implications for confinement *J. Fluid Mech.* **590**, 163–185.
- KIM, D-H., YANG, K-S. & SENDA, M. 2004 Large eddy simulation of turbulent flow past a square cylinder confined in a channel *Computers & Fluids* **33**, 81–96.

- LUNDELL, F., SÖDERBERG, L. D. & ALFREDSSON, P. H. 2011 Fluid Mechanics of Papermaking *Annu. Rev. Fluid Mech.* **43**, 195–217,
- MONKEWITZ, P. A., HUERRE, P., & CHOMAZ, J-M. 1993 Global linear stability analysis of weakly non-parallel shear flows *J. Fluid Mech.* **251**, 1–20.
- PIER, B. 2002 On the frequency selection of finite-amplitude vortex shedding in the cylinder wake *J. Fluid Mech.* **458**, 407–417.
- REES, S. J. & JUNIPER, M. P. 2010 The effect of confinement on the stability of viscous planar jets and wakes *J. Fluid Mech.* **656**, 309–336.
- RICHTER, A. & NAUDASCHER, E. 1976 Fluctuating forces on a rigid circular cylinder in confined flow *J. Fluid Mech.* **78**, 561–576.
- SCHMID, P. J. 2007 Nonmodal stability theory *Ann. Rev. Fluid Mech.* **39**, 129–162.
- TAMMISOLA, O., LUNDELL, F., SCHLATTER, P., WEHRFRITZ, A. & SÖDERBERG, L. D. 2011 Global linear and nonlinear stability of viscous confined plane wakes with co-flow *J. Fluid Mech.* (accepted)

Paper 5

Oscillatory sensitivity patterns for global modes in wakes

By O. Tammisola¹

¹Linné FLOW Centre, KTH Mechanics, Royal Institute of Technology, SE-100 44 Stockholm, Sweden

Submitted.

In this work, marginally unstable co-flow wakes at intermediate Reynolds numbers are studied with a structural sensitivity approach. Wakes at two different confinement values are investigated, termed as *unconfined* ($h = 9$) and *confined* ($h = 1$) for simplicity. As a first quantification, the overlap between the absolute value of direct and adjoint global modes is considered. Confined wakes, as well as unconfined wakes at $Re = 100$, are found to have a single region of strong structural sensitivity region close to the inlet, in agreement with previous findings for cylinder wakes close to the critical Reynolds number. For unconfined wakes at $Re = 400$, a second longer region of high structural sensitivity is found downstream of the first one. Secondly, the sensitivity to base flow modifications is considered, following the linear theory, valid for small modifications. A spatially oscillating sensitivity pattern is found inside the second, downstream, region. In particular, it is found that the same change in the base flow can either destabilize or stabilize the flow, depending on the position where it is applied. It is shown that the sensitivity pattern remains unchanged for different choices of streamwise boundary conditions and numerical resolution. It is confirmed that the eigenvalues from the linear problem move according to this sensitivity pattern, when a small base flow modification is introduced in the direct problem, thus eliminating any uncertainties related to the adjoint computations. Finally, we look at the implications of a small control cylinder on the flow, partly by modelling it as a volume force and partly by recomputing the base flow and stability in the direct problem. The findings have direct implications on the numerical resolution needed for wakes at higher Reynolds numbers. Furthermore, they provide one more possible explanation to why confined wakes have a more narrow frequency spectrum than unconfined wakes.

1. Introduction

Above a critical Reynolds number (Re), wake flows are susceptible to self-sustained oscillations at a distinct frequency. A well-known example is the von Kármán vortex street for a flow past a solid cylinder, which beats at the nondimensional frequency (Strouhal number) 0.2, and appears for $Re > 47$, based on the cylinder diameter and inflow velocity. The critical Reynolds number coincides with the value of Re for which a global eigenmode for the linearized Navier-Stokes equations first becomes unstable, and the frequency of oscillation at the onset is close to the frequency of the linear mode. On the other hand, as long as the growth rates for all linear eigenmodes are negative, no self-sustained oscillations occur.

Due to the success of global linear stability theory for the cylinder flow, new theories have emerged to determine the sensitivity to forcing of this flow, based on the global linear eigenmodes and the eigenmodes for the adjoint linearized Navier-Stokes equations. In particular, the sensitivity of the growth rate and frequency of the global mode to structural changes in the momentum equations was examined by Giannetti & Luchini (2007). One goal was to determine regions where a small control cylinder should be placed in order to have a maximal effect on the stability, and hopefully stabilize the global mode. This would then theoretically explain the stabilizing effect observed in experiments of Strykowski & Sreenivasan (1990). The theoretical approach was taken further by Marquet, Sipp & Jacquin (2008) by introducing the sensitivity to (arbitrary) base flow modifications, and sensitivity to a static volume forcing. Further, they modelled a small control cylinder as a volume force, taking into account the effect of this force on the base flow, and compared their results favorably to the experimental regions where vortex shedding was suppressed (Strykowski & Sreenivasan 1990). In Pralits, Brandt & Giannetti (2010), both the effects on the base flow and the disturbance were modelled for a rotating cylinder. When presenting this chronological flow of discoveries, it should also be denoted that an expression specifically for the sensitivity for a control cylinder was presented earlier in the sometimes overlooked work of Hill (1992).

Furthermore, cylinders confined to a channel have been studied in DNS by *e.g.* Richter & Naudascher (1976), who found that confinement increased the level of lift fluctuations and made the frequency spectrum more concentrated around the dominant frequency, especially at higher

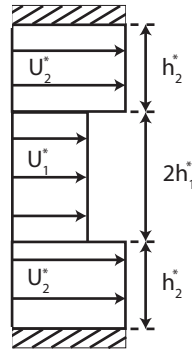


FIGURE 1. The inlet profile with dimensional parameters.

Reynolds numbers ($Re > 750$). More well-defined frequency peaks for half-confined cylinder wakes have also been reported by Bearman & Zdravkovich (1978) at $Re = 350$.

The present work deals with a slightly different wake flow, the co-flow wake. Here, one inner flow stream with low velocity meets and mixes with two outer flow streams with high velocity (see the inlet profile in figure 1). The strength of the wake is determined by the shear ratio between inner and outer flows at the inlet. Viscous spatially developing co-flow wakes have been analysed by linear global modes in Tammisola, Lundell, Schlatter, Wehrfritz & Söderberg (2011), and by a local WKBJ analysis of the same base flows in Juniper, Tammisola & Lundell (2011). In particular, both works addressed the effect of confinement on the global stability of co-flow wakes at intermediate wake Reynolds numbers ($Re = 100-400$). It was found that confinement was globally stabilizing, partly due to a decreasing wake length and partly since the boundary layers at the walls made the wake less locally unstable. At $Re = 400$, the shear ratios at the onset of global instability for unconfined and confined wakes were practically equal, and this was attributed to a similar base flow development in the upstream region ($x < 50$). On the other hand, previous local analyses have shown that confinement can have a destabilizing effect through saddle point interaction (Juniper (2006), Rees & Juniper (2010)), especially at high Reynolds numbers. This effect was also visible in the local analysis of the spatially developing wakes at moderate Re , but shadowed by other effects (Juniper *et al.* 2011).

The present work was initiated to see whether the equal stability limits at $Re \approx 400$ are due to similar base flows in the upstream region. This would imply that the *wavemaker regions* for both flows are identical, and located close to the inlet. The findings will show that although the hypothesis is not completely untrue, dynamics of the unconfined wakes in Tammisola *et al.* (2011) are fundamentally different from the confined ones, and show surprising features.

The manuscript is organized as follows: the relevant background is given in § 1, the mathematical description of the sensitivities in § 2, the wavemakers and sensitivities to generic base flow modifications are shown in § 3, and their further verification in § 4 (with numerical details left to Appendix § 6). The sensitivity to a volume force and its application on a small control cylinder are presented in § 5. The results are summarized and discussed in § 6. Further, results for a co-flow wake with a slightly different geometry are shown in Appendix § 6, and an expression for the volume force generated by the small cylinder derived in Appendix § 6.

2. Definitions of parameters and sensitivity measures

The problem is nondimensionalized based on the inlet profile, and the dimensional quantities denoted by $\tilde{\cdot}$. The parameter definitions are as follows (see figure 1):

- Confinement parameter h :

$$h = \frac{\tilde{h}_2}{\tilde{h}_1}, \quad (1)$$

- Reynolds number Re :

$$Re = \frac{\tilde{U}_2 \tilde{h}_1}{\tilde{\nu}}, \quad (2)$$

where $\tilde{\nu}$ is the kinematic viscosity of the fluids,

- *Shear ratio* describing the strength of the shear between the fluids at the inlet compared to their momentum

$$\Lambda = \frac{(\tilde{U}_1 - \tilde{U}_2)}{(\tilde{U}_1 + \tilde{U}_2)}. \quad (3)$$

The inverse of the shear ratio, Λ^{-1} , is more often used here. A high absolute value of this quantity means a strong co-flow (base bleed), for example: $\Lambda^{-1} = -1.5$ means $\tilde{U}_1/\tilde{U}_2 = 0.2$, $\Lambda^{-1} = -1$ means $\tilde{U}_1/\tilde{U}_2 = 0$ (no co-flow).

The base flow (U, V, P) is obtained by solving the steady Navier-Stokes (N-S) equations. Other governing equations that are solved are:

(a) The linear global system:

$$\begin{aligned}
 -\frac{\partial u}{\partial t} - U\frac{\partial u}{\partial x} - V\frac{\partial u}{\partial y} - u\frac{\partial U}{\partial x} - v\frac{\partial U}{\partial y} \\
 -\frac{\partial p}{\partial x} + \frac{1}{Re}\left(\frac{\partial^2 u}{\partial x^2} + \frac{\partial^2 u}{\partial y^2}\right) = 0
 \end{aligned} \tag{4}$$

$$\begin{aligned}
 -\frac{\partial v}{\partial t} - U\frac{\partial v}{\partial x} - V\frac{\partial v}{\partial y} - u\frac{\partial V}{\partial x} - v\frac{\partial V}{\partial y} \\
 -\frac{\partial p}{\partial y} + \frac{1}{Re}\left(\frac{\partial^2 v}{\partial x^2} + \frac{\partial^2 v}{\partial y^2}\right) = 0
 \end{aligned} \tag{5}$$

$$\frac{\partial u}{\partial x} + \frac{\partial v}{\partial y} = 0 \tag{6}$$

where (u, v, p) is the disturbance. The global mode ansatz is made in these equations, and they are solved with respect to the complex eigenvalue ω :

$$[u, v, p] = [\hat{u}(x, y), \hat{v}(x, y), \hat{p}(x, y)]e^{-i\omega t}. \tag{7}$$

(b) The adjoint linear global system:

$$\begin{aligned}
 -\frac{\partial u^+}{\partial t} - U\frac{\partial u^+}{\partial x} - V\frac{\partial u^+}{\partial y} + u^+\frac{\partial U}{\partial x} + v^+\frac{\partial U}{\partial y} \\
 +\frac{\partial p^+}{\partial x} - \frac{1}{Re}\left(\frac{\partial^2 u^+}{\partial x^2} + \frac{\partial^2 u^+}{\partial y^2}\right) = 0
 \end{aligned} \tag{8}$$

$$\begin{aligned}
 -\frac{\partial v^+}{\partial t} - U\frac{\partial v^+}{\partial x} - V\frac{\partial v^+}{\partial y} + u^+\frac{\partial U}{\partial y} + v^+\frac{\partial V}{\partial y} \\
 \frac{\partial p^+}{\partial y} - \frac{1}{Re}\left(\frac{\partial^2 v^+}{\partial x^2} + \frac{\partial^2 v^+}{\partial y^2}\right) = 0
 \end{aligned} \tag{9}$$

$$\frac{\partial u^+}{\partial x} + \frac{\partial v^+}{\partial y} = 0, \tag{10}$$

where where (u^+, v^+, p^+) is the adjoint disturbance.

The global mode ansatz is made also in these equations, and they are solved with respect to the complex eigenvalue ω^+ :

$$[u^+, v^+, p^+] = [\hat{u}^+(x, y), \hat{v}^+(x, y), \hat{p}^+(x, y)]e^{-i\omega^+ t}. \tag{11}$$

In the continuous formulation (with correct boundary conditions for the adjoint problem), it can be shown that $\omega^+ = \omega^*$, where the star denotes complex conjugate. Hence, the comparison of adjoint and direct eigenvalues serves as a nice resolution check for both direct and adjoint problems.

The adjoint needs to fulfill the following normalization condition, for the sensitivity expressions presented here to be valid:

$$\int u^{+*}u = 1. \quad (12)$$

The numerical solution and boundary conditions are briefly described in Appendix §6).

The sensitivity of the eigenvalue to modifications of a quantity ϕ is defined as:

$$\delta\omega = \int \gamma(x, y)\delta\phi(x, y)dxdy, \quad (13)$$

where γ is a sensitivity distribution. In other words, by integrating the product of the modification (*e.g.* the base flow changes) and the corresponding sensitivity function (*e.g.* sensitivity to base flow modifications), one obtains the change in the eigenvalue. Observe that the expression above is complex, and that the changes in growth rate and frequency can be treated separately.

The wavemakers presented in this report are described by the following equations:

(1) The general structural sensitivity (Giannetti & Luchini 2007). The upper bound of the sensitivity to perturbations in the u -momentum equation (eq. 4) is obtained from:

$$S(x, y) = |\hat{u}(x, y)||\hat{u}^+(x, y)|. \quad (14)$$

This means that $|\delta\omega| \leq S(x, y)A$, where A is the perturbation amplitude.

(2) The sensitivity to generic base flow modifications (Marquet *et al.* 2008), where the modified base flow is not necessarily a solution to N-S. (a) for the streamwise component:

$$S_U(x, y) = \left(\int (\hat{u}^{+*}\hat{u} + \hat{v}^{+*}\hat{v})dxdy \right)^{-1} \left[-\frac{\partial\hat{u}^*}{\partial x}\hat{u}^+ - \frac{\partial\hat{v}^*}{\partial x}\hat{v}^+ + \frac{\partial\hat{u}^+}{\partial x}\hat{u}^* + \frac{\partial\hat{u}^+}{\partial y}\hat{v}^* \right], \quad (15)$$

where the stars denote complex conjugates, and (b) for the vertical component:

$$S_V(x, y) = \left(\int (\hat{u}^* u^+ + \hat{v}^* v^+) dx dy \right)^{-1} \left[-\frac{\partial \hat{u}^*}{\partial y} \hat{u}^+ - \frac{\partial \hat{v}^*}{\partial y} \hat{v}^+ + \frac{\partial \hat{v}^+}{\partial x} \hat{u}^* + \frac{\partial \hat{u}^+}{\partial y} \hat{v}^* \right]. \quad (16)$$

Note that both (2a) and (2b) are complex quantities, where the sensitivity of the growth rate is obtained from the real part and the sensitivity of the frequency by the imaginary part (where the latter differs from Marquet *et al.* (2008) due to a different definition of the eigenvalue).

The expressions (a) and (b) can be further divided as the sensitivity of energy production (first two terms) and sensitivity of base flow advection (second two terms). In this report, we define the following expressions for the growth rate sensitivity:

$$S_{prod} = \sqrt{S_{U,prod}^2 + S_{V,prod}^2} \quad (17)$$

and

$$S_{adv} = \sqrt{S_{U,adv}^2 + S_{V,adv}^2}, \quad (18)$$

where

$$\begin{aligned} S_{U,prod} &= real \left(\int (\hat{u}^{++} \hat{u} + \hat{v}^{++} \hat{v}) dx dy \right)^{-1} \left[-\frac{\partial \hat{u}^*}{\partial x} \hat{u}^+ - \frac{\partial \hat{v}^*}{\partial x} \hat{v}^+ \right], \\ S_{U,adv} &= real \left(\int (\hat{u}^{++} \hat{u} + \hat{v}^{++} \hat{v}) dx dy \right)^{-1} \left[\frac{\partial \hat{u}^+}{\partial x} \hat{u}^* + \frac{\partial \hat{u}^+}{\partial y} \hat{v}^* \right], \\ S_{V,prod} &= real \left(\int (\hat{u}^{++} \hat{u} + \hat{v}^{++} \hat{v}) dx dy \right)^{-1} \left[-\frac{\partial \hat{u}^*}{\partial y} \hat{u}^+ - \frac{\partial \hat{v}^*}{\partial y} \hat{v}^+ \right], \\ S_{V,adv} &= real \left(\int (\hat{u}^{++} \hat{u} + \hat{v}^{++} \hat{v}) dx dy \right)^{-1} \left[\frac{\partial \hat{v}^+}{\partial x} \hat{u}^* + \frac{\partial \hat{v}^+}{\partial y} \hat{v}^* \right]. \end{aligned}$$

(3) The sensitivity to a steady and unsteady volume force (Pralits *et al.* 2010).

The sensitivity to a steady volume force is given by:

$$S_F = U^+, \quad (19)$$

where U^+ is the solution to the adjoint base flow equations:

$$-U_j \frac{\partial U_i^+}{\partial x_j} + U_j^+ \frac{\partial U_j}{\partial x_i} - \frac{\partial P^+}{\partial x_i} - \frac{1}{Re} \left(\frac{\partial U_i^+}{\partial x_j \partial x_j} \right) = -\frac{\partial \hat{u}_j^*}{\partial x_i} \hat{u}_j^+ + \frac{\partial \hat{u}_i^+}{\partial x_j} \hat{u}_j. \quad (20)$$

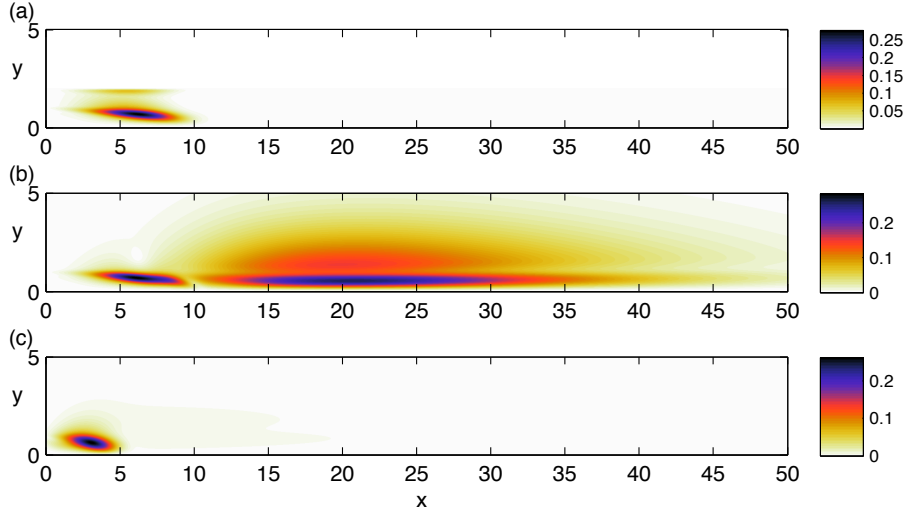


FIGURE 2. The structural sensitivity S for wakes: (a) $Re = 398$ and $h = 1$, (b) $Re = 398$ and $h = 9$, (c) $Re = 100$ and $h = 9$. The region $y > 0$ is shown — the sensitivity at $y < 0$ is the mirror image.

Further, to model a small control cylinder we assume a force proportional to the velocity: A steady force $F_i = \delta(x - x_0)(y - y_0)M_{ij}u_j$, and an unsteady force $f = \delta(x - x_0)(y - y_0)m_{ij}u_j$. The matrices $M = M(x, y)$ and $m = m(x, y)$ are related to the specific drag model for the small cylinder, and are given in Appendix §6 for the model used in the present work.

The sensitivity to the small control cylinder is then given by (Pralits *et al.* 2010):

$$\delta\omega = U_i^+ M_{ij} U_j + u_i^+ M_{ij} u_j. \quad (21)$$

3. General structural sensitivities of co-flow wakes

Here, we present the sensitivity distributions for the most unstable mode of three wakes: high Reynolds number confined ($Re = 398$, $h = 1$), high Reynolds number unconfined ($Re = 398$, $h = 9$), and low Reynolds number unconfined ($Re = 100$, $h = 9$). Only the upper halves of the sensitivity distributions are shown, since the symmetry of the base flow implies that they are symmetric around the centerline. The magnitude of the sensitivity for structural perturbations S (equation 14) for each of the wakes is shown in figure 2. We begin with the confined wake.

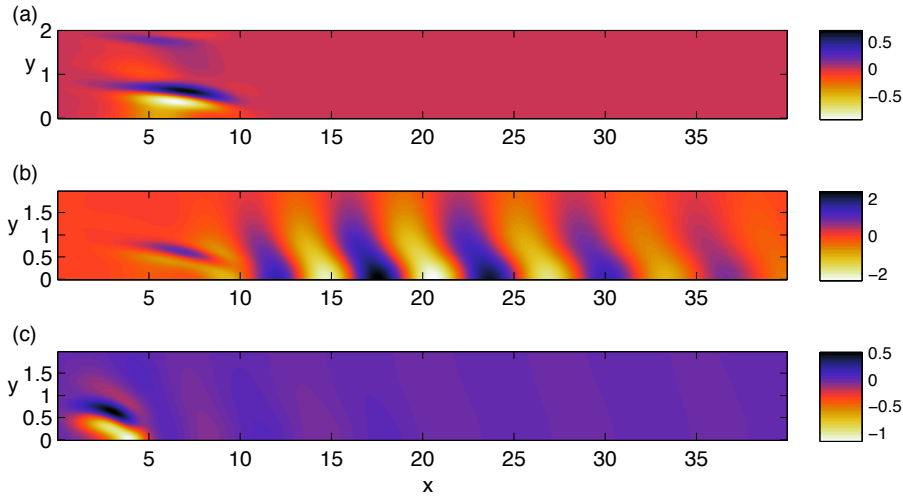


FIGURE 3. The sensitivity of the growth rate to generic modifications in streamwise base flow velocity ($real[S_U]$): (a) $Re = 398$ and $h = 1$, (b) $Re = 398$ and $h = 9$, (c) $Re = 100$ and $h = 9$. Note that the axis limits differ from the ones in figure 2. The region $y > 0$ is shown — the sensitivity at $y < 0$ is the mirror image.

For the confined wake (figure 2 a), high amplitude of the structural sensitivity S is found in the region $0 < x < 10$. The maximum of the sensitivity lies around the shear layer, but the sensitivity also has a visible amplitude close to the wall, showing an effect of confinement. Apart from the confinement effect, this is similar to the wavemakers for cylinder wakes at slightly supercritical Reynolds numbers shown in the previous works (Giannetti & Luchini (2007), Pralits *et al.* (2010)).

The structural sensitivity of the unconfined wake for the same parameters is shown in figure 2 b. There is a similar high sensitivity region close to the inlet, and the overall maximum of the sensitivity is at $x \approx 6.2$. However, a second region of high sensitivity appears downstream, and is extremely elongated with a maximum at $x \approx 20$. The second region also extends higher up in the outer flow, at $y = 4$ the amplitude is still 0.03, *i.e.*, 10% of the total maximum amplitude of S . There are no additional sensitivity regions, and the sensitivity has no visible amplitude outside the figure frame shown (neither downstream nor upwards). The same quantity for the unconfined wake at a lower Reynolds number (figure 2 c) again shows only one sensitivity region.

As one would expect, the sensitivity region is located closer to the inlet and down to the low speed region close to the symmetry line (where a separation bubble might occur depending on parameters), again in full agreement with cylinder wakes at slightly supercritical Reynolds numbers.

Now, we leave the arbitrary structural perturbations, and look specifically at how small perturbations of the base flow field affect the stability. First, the sensitivity of the global mode growth rate to generic modifications in the streamwise base flow velocity is considered. We begin again with the confined wake (figure 3 a). The growth rate is increased if the streamwise velocity is decreased in the lower part of the shear layer, and increased in the upper part. The effect is very intuitive, since both changes make the wake stronger, inside the region where the wavemaker is strong (figure 2 a). In addition, the growth rate increases if the velocity is increased close to the wall, *i.e.*, if the boundary layer near the wall is removed, in agreement with Juniper *et al.* (2011).

For the unconfined wake (figure 3 b), the base flow modification acts in a more curious way. There are similar structures upstream as in the confined case, but the sensitivity is clearly stronger inside the downstream located wavemaker region of figure 2 b. Furthermore, inside this region, the sensitivity oscillates between positive and negative values, with a similar wavelength as the one for the direct eigenmode! This means that if we introduce a small base flow modification for example at the centerline ($y = 0$), at $x = 17$ or $x = 23$ we get an increased growth rate, but when doing the same at $x = 21$ or $x = 27$, the growth rate decreases. At the low Reynolds number but unconfined wake (figure 3 c), the sensitivity is again concentrated close to the inlet, although some traces of a wave-like sensitivity at a low amplitude are seen downstream. More extensive parameter variations have shown that the change between the two states is continuous, as the Reynolds number increases. The sensitivity to base flow modifications for unconfined wakes is surprising and counterintuitive, as opposed to the confined wakes. The rest of this manuscript exclusively investigates this phenomenon.

Next, we divide the sensitivity to base flow modifications into changes in production, and changes in advection. The former is shown for all wakes in figure 4. From figure 4 b it is seen that the production part of the unconfined wake is still more localized in the upstream wavemaker region, and does not substantially differ from the same of the confined wake at the same Reynolds number in figure 4 a. Figure 5 b reveals

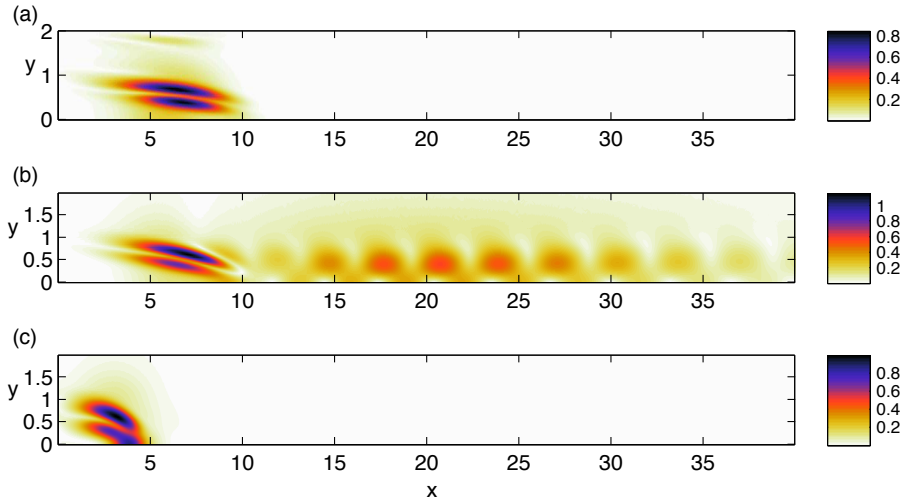


FIGURE 4. The magnitude of the sensitivity of the growth rate to generic base flow modifications, production part S_{prod} : (a) $Re = 398$ and $h = 1$, (b) $Re = 398$ and $h = 9$, (c) $Re = 100$ and $h = 9$. The region $y > 0$ is shown — the sensitivity at $y < 0$ is the mirror image.

that the oscillating sensitivity is mostly due to changes in advection (note that the colormaps in figures 4 b and 5 b are different). This shows that the main source of the instability still comes from the upstream wavemaker, while the downstream wavemaker acts to either heal the symptoms or to increase the sickness, by letting the disturbance be convected downstream in different amounts. Being the dominant contributor to the sensitivity to base flow modifications, the downstream wavemaker should in any case not be overlooked.

4. Verification of the oscillating sensitivity pattern of the unconfined wake at $Re = 398$

As the Reynolds number increases, the co-flow wake becomes increasingly parallel and therefore the global modes are more non-normal (Chomaz 2005). It is thus essential to verify that the oscillating sensitivity is not a product of an insufficient resolution, boundary conditions or even a particular numerical discretisation method. Both the wavemaker and the sensitivity to base flow modifications of the unconfined wake have been verified by changing the methods for computing the base flow and stability, the resolution, and by changing the location of the boundaries of the

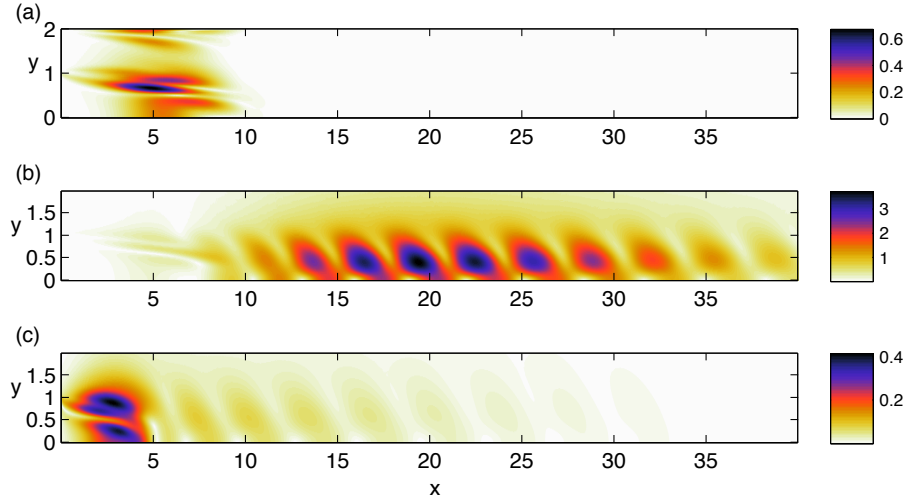


FIGURE 5. The magnitude of the sensitivity of the growth rate to generic base flow modifications, advection part S_{adv} : (a) $Re = 398$ and $h = 1$, (b) $Re = 398$ and $h = 9$, (c) $Re = 100$ and $h = 9$. The region $y > 0$ is shown — the sensitivity at $y < 0$ is the mirror image.

computational domain. The whole pattern remained unchanged, and in particular, the phase and location of maximal sensitivity for the same wake did not change. Modelling the region before the wake inlet more carefully has also been tested, including a rounded-edge splitter plate with a finite thickness, where boundary layers are allowed to develop. This naturally changes the base flow, and therefore the sensitivities, but the oscillating pattern remains, and in fact has an even higher amplitude in this case. The results of the numerical tests are summarized in table 1 in Appendix § 6, and the results for a round-edged plate with boundary layers in Appendix § 6.

It is easy to test whether the adjoint-based sensitivity distributions are the true ones for a certain linear global mode problem, with prescribed boundary conditions. This can be done by applying a series of localized base flow modifications to the problem, and recalculating the direct eigenvalues. Here, the V -component of the base flow is altered by superposing a gaussian centered around the line $y = 0.5$:

$$V_{mod} = V + Ae^{[-100(x-x_{mod})^2-100(y-0.5)^2]}$$

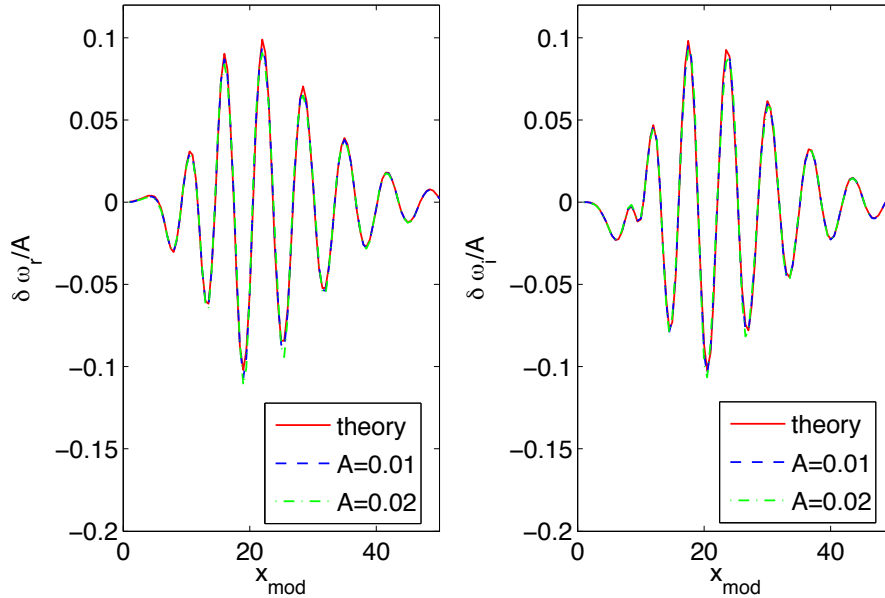


FIGURE 6. (a) The frequency and (b) the growth rate of the most unstable eigenvalue with modifications of different amplitude along the line $y = 0.5$ (varying x_{mod}), normalized with the amplitude: the theoretical curve obtained directly from the sensitivity distributions (solid), global modes recomputed with $A = 0.01$ (---), global modes recomputed with $A = 0.02$ (-.)

The derivatives of V are altered accordingly. The amplitude A of the base flow modification needs to be small enough for the linear theory to be valid, and the appropriate level is found by trial and error.

The theoretical movement of the eigenvalue, when such a modification is applied, is obtained from the sensitivity distributions by integrating the product of $(V_{mod} - V)$ and the sensitivity distribution over the computational domain.

These theoretical curves with $A = 1$ as a function of x_{mod} are shown with solid lines in figure 6 a (growth rate part) and 6 b (frequency part). The other line styles represent movements of eigenvalue that is obtained by applying the base flow modification in the direct problem and recomputing the eigenvalues. Different maximum amplitudes of the

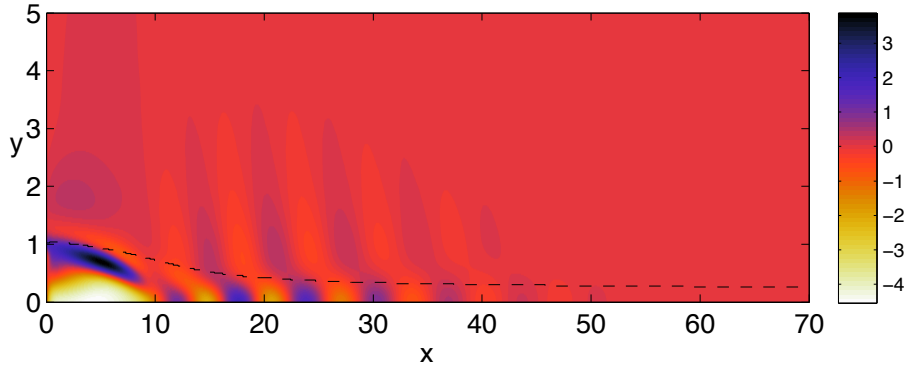


FIGURE 7. Sensitivity to a steady volume force in the streamwise direction (positive forcing direction aligned with $\bar{e}_x = (1, 0)$). The streamline starting between the two flow streams at the inlet is shown with a dashed line. The region $y > 0$ is shown — the sensitivity at $y < 0$ is the mirror image.

gaussian are chosen: $A = 0.02$ (10 % of the maximum amplitude for V , and $\approx 2\%$ of the maximum amplitude for U) and $A = 0.01$, and the result is normalized with A . The curves with both amplitudes have a rather nice collapse with the theoretical curve.

These results show that the sensitivity is inherent to the physical problem, and is not related to errors in the numerical or analytical solution of the problem.

5. Sensitivity to a volume force and implications for passive control

Response to local base flow modifications was examined previously. This provides insight on where local changes of the base flow profile are most efficient. However, when a real passive control is applied locally, it can have a global effect through transport and production by the base flow. In other words, the modified base flow field will still satisfy Navier-Stokes equations.

Next, passive control is modeled as a steady volume force (19), so that the modified base flow satisfies the steady Navier-Stokes equations. The resulting growth rate sensitivity distribution for a volume force applied in the streamwise direction is seen in figure 7. By following the streamline starting between the outer and inner flow at the inlet (dashed line), it is obvious that shear below this line controls the flow.

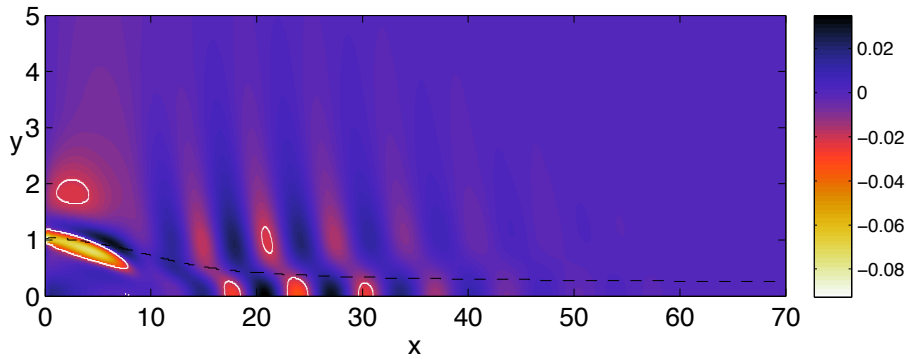


FIGURE 8. Sensitivity to a control cylinder of radius 0.02. Light regions imply a reduced growth rate of the global mode, and dark regions an increased growth rate. The white contours surround the regions where the model predicts stabilization. The streamline starting between the two flow streams at the inlet is shown with a dashed line. The region $y > 0$ is shown — the sensitivity at $y < 0$ is the mirror image.

The growth rate of the global mode increases, if the flow is accelerated in the upper part of this "inner flow", and decelerated in the lower part. Further downstream, the oscillating pattern is visible, but has a lower amplitude. Observe that this does not contradict the previous results, since the present analysis can take into account non-local changes, such as a modification of the wake length due to local changes in the upstream flow.

5.1. Sensitivity to a small control cylinder

Next, a small control cylinder is modeled as a steady and unsteady volume force, following Pralits *et al.* (2010) (and equivalent to Hill (1992)). Here, Re_c is the Reynolds number of the small cylinder. Pralits *et al.* (2010) modelled the force using the Lamb-Oseen drag coefficient for a cylinder valid for $Re_c \ll 1$, and Hill (1992) adjusted constants in a low Reynolds number drag coefficient model. Here, we use the model of Imai (1951) that is shown to give good agreement with experiments for $5 < Re_c < 100$ in Zdravkovich (1997):

$$C_D = \left(0.707 + \frac{3.42}{\sqrt{Re_c}} \right)^2. \tag{22}$$

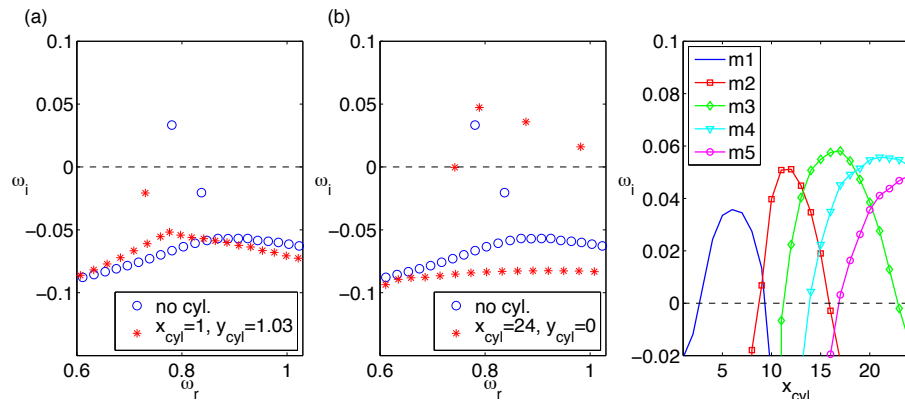


FIGURE 9. A cylinder with $r = 0.02$ included in the base flow and global mode computations: (a) spectra with a cylinder in $x_{cyl} = 1, y_{cyl} = 1.03$ compared to the spectra without control cylinder, (b) the same with $x_{cyl} = 24, y_{cyl} = 0$, (c) the growth rate of the most unstable mode as a function of x_{cyl} , when $y_{cyl} = 1.03$.

The lift on the control cylinder due to local shear is assumed to be negligible. Estimates based on the low Reynolds numbers lift model of Filon (1926) and maximal circulation indicated that the lift on the control cylinder was two orders of magnitude less than the drag.

The predicted change in the growth rate of the global mode, when a cylinder with radius 0.02 is inserted in different positions of the flow domain, is shown in figure 8. The colorscale gives the magnitude and direction of the change (positive or negative), as a function of the position of the control cylinder. First, we denote that this change has mostly the opposite sign compared to the sensitivity to a steady volume forcing in figure 7. This is due to the fact that there is no reverse flow. Hence, the cylinder decelerates the flow everywhere, corresponding to a negative volume force. The next observation is that the forcing with a control cylinder is more efficient in regions with a high base flow velocity, since it results in larger velocity difference and therefore a larger drag. The significance of the outer flow is somewhat increased in figure 8 compared to figure 7, and the dominant white region close to the centerline in figure (7) is neither stabilizing nor destabilizing for the control cylinder in figure 8.

5.2. Global stability with insertion of the control cylinder

Finally, we turn to the physical implications on the global stability as a whole. The boundaries of the regions where the control cylinder is supposed to stabilize this particular global mode (so that $\omega_i \leq 0$) are indicated by the white contours. We now investigate the actual global mode problem, where the base flow and stability are recomputed with the small cylinder included. In Tammisola *et al.* (2011) it was shown that the stability for converged linear global modes matches exactly the stability limits seen in direct numerical simulations for co-flow wakes.

In the following, the control cylinder is inserted in the position $x = x_{cyl}$, $y = y_{cyl}$ in the global mode computation. We start by investigating the strongest sensitivity region close to the inlet, and follow the line $y_{cyl} = 1.03$, at $0 < x_{cyl} < 5$. The computations show that with this position of the control cylinder, all global modes are stabilized. An example spectrum for $x_{cyl} = 1, y_{cyl} = 1.03$ is shown in figure 9 a, compared to the original spectrum. Thus, the flow can be controlled inside the stabilizing region found close to the inlet.

Now, we try to insert the cylinder inside one of the smaller regions downstream, where the cylinder is also predicted to stabilize the flow (*i.e.* $\omega_i < 0$): at $x_{cyl} = 24$, $y_{cyl} = 0$. The spectrum (figure 9 b) has changed completely, and now contains four unstable modes instead of one. It is even difficult to guess where the original global mode would be, to decide whether it has stabilized as theory predicts. Following the global mode with different x_{cyl} the line $y_{cyl} = 1.03$ (figure 9 c) reveals that a second mode becomes unstable when $x_{cyl} \approx 9$, and soon after this, the original mode stabilizes. A third mode becomes unstable at $x \approx 12$, while the second mode stabilizes at $x \approx 16$. This development continues with several modes. Each individual mode also increases in frequency with increasing x_{cyl} , and thus forms an arch in the spectrum with increasing x_{cyl} .

The instability has completely changed its character due to insertion of the tiny cylinder. So, even if control could not be established in the downstream region, it is by no means less dynamically important than the upstream region. In fact, changes downstream have a strikingly big influence on the linear dynamics of the flow, in the light of the results presented in both this and previous sections.

6. Summary and discussion

In this study it is seen that the linear structural sensitivity for weakly confined (here termed unconfined) co-flow wakes at $Re \approx 400$ shows two distinct regions of high sensitivity. The first region is in the near-field of the wake ($x < 10$), as is usual for wake flows. Such a region appears both for confined and unconfined wakes, and for wakes at lower Re , as well as cylinder wakes in previous works (*e.g.* Giannetti & Luchini (2007)). The second region however has not been observed in other flow cases. This second region is elongated and extends until $x \approx 50$ in the streamwise direction, and also higher up in the free stream in the vertical direction (up to $y \approx 5$).

The sensitivity to generic base flow modifications shows a spatially oscillating pattern inside the downstream sensitivity region mentioned above. If the base flow is modified in a certain spatial position, then the global mode is stabilized or destabilized depending on the streamwise coordinate of the modification. Specifically, the change in both growth rate and frequency oscillates between positive and negative values as a function of the chosen streamwise coordinate for the modification.

The sensitivity downstream can have both physical and numerical consequences, and we address first the computational ones. The impact on the numerical solution of the problem is the high resolution needed inside the whole region of high sensitivity. This concerns the resolution of both the computed base flow, and the "apparent base flow" in the stability problem, *i.e.*, the resolution of the global mode computation. While the wakes at lower Reynolds numbers only require high resolution close to the inlet, the wakes at $Re \approx 400$ must be well resolved inside a long region downstream. The need of increasing streamwise resolution is counterintuitive, since the flow becomes more parallel for higher Re , but nevertheless was clearly observed during the previous study of Tammissola *et al.* (2011). Here, it should be stressed that all flows and their sensitivities in the present work have gone through careful studies of resolution and boundary condition independence, described in Appendix § 6.

When the flow is modified (or controlled) in a real physical or numerical experiment, one has to take account the global effect of even a localized feedback. For example, smoothing of the shear layer in one upstream position can alter the length and strength of the whole wake downstream. To take the global effects on the base flow into account, the sensitivity to a steady volume force (of a small amplitude) incorporated in the Navier-Stokes equations was studied. The sensitivity to

a volume force was strongest upstream, but also appeared downstream with the familiar oscillatory pattern. For a second wake introduced in Appendix §6 for comparison, the downstream sensitivity was stronger than the upstream one.

Finally, the effect of a small control cylinder ($r = 0.02$) on the stability of the flow was studied, both indirectly from the prediction based on a sensitivity distribution, and directly by including a cylinder in the global mode problem. There are several regions in space, where a control cylinder could be placed to stabilize the global mode, according to the sensitivity distribution.

The first region is in the upper part of the shear layer close to the inlet. The direct global mode study confirms that the flow is indeed stabilized by a control cylinder inside this region. The other regions are partly in the outer flow close to the inlet, and partly inside the oscillatory pattern downstream. Since the latter is the focus of this study, the cylinder was placed in the downstream region. Here, the result was again a destabilization of several global modes. In fact, the spectra are similar to the spectra with a large generic base flow modification (Appendix §6). The theory and sensitivity distributions presented here are only valid for small forcing and small base flow modifications, and the limit of "small enough" depends on the flow in question.

It is legitimate to ask why a small cylinder far downstream had such a big impact on the flow, and also why the flow is sensitive to base flow modifications downstream. This flow is known to be convectively unstable at $x > 10$, so why would any effect be convected downstream, and change the frequency in the absolutely unstable region?

The proposed explanation to the cylinder effect is similar to edge tones in a free shear layer (Hussain & Zaman 1978). It is known that a hot wire can create additional frequencies in shear layer experiments, and that these "tones" depend on the placement of the hot-wire probe. The oscillations creating the tones occur in the region between the inlet and the hot-wire probe, and lead to frequency jumps in the response when the hot wire is traversed in the streamwise direction. Further, the amplitude of each fundamental tone grows initially, then decays, and gives place to another fundamental tone (Hussain & Zaman 1978). This is very similar to the spectra as a function of cylinder position in the present work (figure 9). An unconfined co-flow wake at $Re = 400$ has a strong advection, and the wake in the present work is also slightly accelerated by the slow development towards a parabolic profile. It is

thus possible that the wake acts as a shear layer with an appropriate forcing. It should be noted that both edge tones, and global modes in cavities exploiting the same mechanism (*e.g.* Rowley, Colonius & Basu (2002)), are usually discussed in the context of compressible flows. However, the same feedback mechanism has been observed for global modes in a smooth incompressible cavity (Åkervik, Høpfner, Ehrenstein & Henningson 2007). Downstream traveling waves reflected back from the downstream edge of the cavity were evident in the pressure trace of the optimal initial condition, and the global spectrum was also seen to be dependent on the cavity length (Åkervik 2011).

Both phenomena — the oscillating sensitivity distributions for small forcing, and the cascade of modes dependent on the position of the control cylinder — seem to be connected to the strong advection. The sensitivity distributions show that the flow is very sensitive to changes in advection downstream. Let us assume that for small changes in advection (local deceleration or acceleration), a tiny amount of the global mode is reflected upstream by *e.g.* pressure feedback. This reflected part can be either in phase or out of phase with the "true mode" in the position of the "true wavemaker", at the time of the instantaneous reflection. Thus, it can have either destructive or constructive interference with the wavemaker.

If the reflection is strong enough (corresponding to a large base flow modification), possibly there is also a reflection from the inlet. There is always a solid boundary present at the inlet, either through a splitter plate between the flow streams (physical effect) or through a zero disturbance condition at the wake inlet (numerical effect), the latter case if no extensional regions as in the present work (described in 6) are applied. This feedback mechanism similar to cavity flows would then dominate the absolute instability, leading to the observed generation of new modes.

Although the observations in the present work are interesting from a fundamental point of view, a definite next step is to see if and to which extent they carry over to a nonlinear setup. Although the linear spectrum is very sensitive to downstream forcing, there always seems to be at least one linear mode available to start the initial growth process, and the shape and frequency of the final nonlinear oscillation need not be as sensitive. Only a further study by nonlinear simulations and/or experiments can answer this question. There is no conclusive evidence of edge tones for wake experiments, although suggested to be seen by

e.g. Kovaszny (1949). Periodic minima and maxima of the vortex formation length, a quantity inversely proportional to maximum of u_{rms} (Williamson 1996), are reported also for a cylinder wake at $Re \approx 750$ in Unal & Rockwell (1987), when a splitter plate is traversed in the streamwise direction in a cylinder wake. At low Reynolds numbers ($Re \approx 140$), no such effects were seen. Co-flow wakes could turn out to be a suitable flow case for such studies.

In previous work with cylinder flows at high Re , confined wakes had more narrow spectral distributions than unconfined wakes (*e.g.* Richter & Naudascher (1976)). Randomness in the downstream sensitivity for unconfined wakes seen here, that was completely absent for the confined wake, could contribute to the appearance of a broader spectrum.

Following people are especially acknowledged for sharing their thoughts around the sensitivities: Fredrik Lundell, Philipp Schlatter, Luca Brandt, Jan Pralits, Milos Ilak, and Matthew Juniper. The support from the European Union FP6 Project Ecotarget and the Swedish Research Council, Linné FLOW Centre is gratefully acknowledged.

Appendix A: Numerical treatment

The first numerical setup (figure 10 a) utilizes a damping region concept, also used in Tammisola *et al.* (2011). In this setup, the base flow is computed in the region $x > 0$, and the inlet profile shown in figure 1 is set at $x = 0$. In the stability problem however, the numerical domain is continued to the region $x < 0$, where we set a no slip condition between the two fluid streams, resembling an "infinitely thin plate". The base flow is kept equal to the inlet profile in this region. The purpose of this "damping region" of length d is only to let the global mode decay more smoothly, and avoid spurious reflections from the inlet, without altering the base flow. Then, the length d can be varied to test the dependence of the inlet boundary condition of the global mode, and L the dependence for the outlet boundary condition.

The sensitivities are also seen to be essentially invariant with respect to both the numerical discretisation used, resolution and the boundary conditions of the stability problem. The outlet boundary condition used were the following. At the inlet, a homogeneous Dirichlet condition is set (zero disturbance):

$$\hat{u}(-d, y) = \hat{v}(-d, y) = 0. \quad (23)$$

Base flow	Stability	L	d	md_1	md_2	$\max(S_{adv})$	pos. of $\max(S_{adv})$
Comsol	Comsol	250	10	0.07	0.18	3.7437	(19.41,0.4000)
Nek5000	Comsol	250	20	0.07	0.2	4.1940	(19.50,0.4000)
Comsol	Comsol	160	10	0.07	0.18	3.7392	(19.41,0.4000)
Comsol	Comsol	160	110	0.07	0.18	3.8430	(19.42,0.4000)
Comsol	Comsol	95	10	0.04	0.14	3.7995	(19.35,0.4000)

TABLE 1. The maximal value of S_{adv} and its location in space for different numerical configurations.

At the walls we have a no slip condition:

$$\hat{u} = \hat{v} = 0. \quad (24)$$

At the centerline antisymmetry is imposed (since all the unstable modes were known to be antisymmetric):

$$\hat{u}(x, 0) = \frac{\partial \hat{v}}{\partial y}(x, 0) = \hat{p}(x, 0) = 0. \quad (25)$$

At the outlet, a stress-free condition was chosen, although the tests showed that the choice was not important here:

$$-\hat{p} + \frac{1}{Re} \frac{\partial \hat{u}}{\partial x} = \frac{\partial \hat{v}}{\partial x} = 0. \quad (26)$$

In table 1, the numerical accuracy is quantified by the maximum value of the magnitude of the advective part of the sensitivity to base flow modifications (S_{adv}). This is the part that contains most of the oscillating behaviour. Two different codes are used for calculating the base flow: the Nek5000 spectral element code and the Comsol Multiphysics finite element code. In the Nek5000 simulation, the inlet profile needs to be slightly smoothed, but even this is seen to have a very minor effect on the results. For the stability, we use mainly Comsol Multiphysics, that has been verified against our own spectral software FLUPACK in Tammisola *et al.* (2011). FLUPACK has problems to resolve the sensitivities very accurately at high Reynolds numbers, due to the point distribution (Gauss-Lobatto points). Therefore, we perform a verification between FLUPACK and Comsol at $Re = 158$, and with a probably too short domain ($L = 50$), to meet the resolution requirements. Despite the short domain, the oscillatory pattern is still strikingly similar to the one obtained from Comsol with a long domain (S_V for both shown in figure 11).

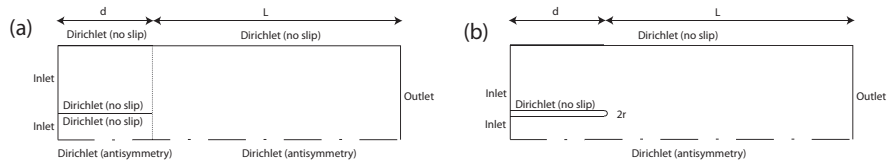


FIGURE 10. Illustration of the two computational domains used in this study: (a) inlet profile at $x = 0$ combined with a damping region at $-d < x < 0$ (all results except appendix 6) (b) inlet profile at $x = -d = -1$ combined with a splitter plate at $-d < x < 0$ (appendix 6).

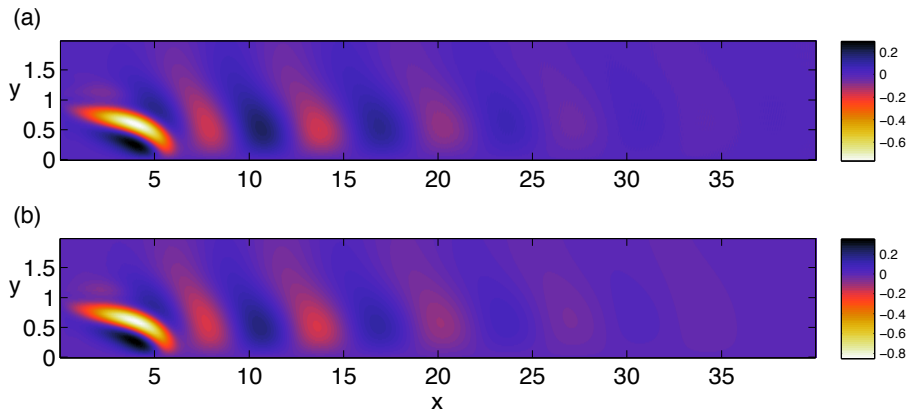


FIGURE 11. S_V for the same base flow, with stability computed in (a) FLUPACK (b) Comsol.

Appendix B: Results for a round-edged plate with a boundary layer before the inlet

Here, the sensitivity is computed with a more realistic inflow model. The fluid streams are separated prior the wake (at $-d < x < 0$) by a round-edged plate of finite thickness (figure 10 b). The base flow profile is allowed to develop prior to the wake and develop thin boundary layers at $x < 0$. Since boundary layers have a damping effect on the stability, the development region has to be kept rather short at these Reynolds numbers. In this section, results are presented for $d = 1$.

In the following, the round-edged plate setup will be called setup B, and the setup used in the main body of the paper and § 6 (described in § 6) will be called setup A.

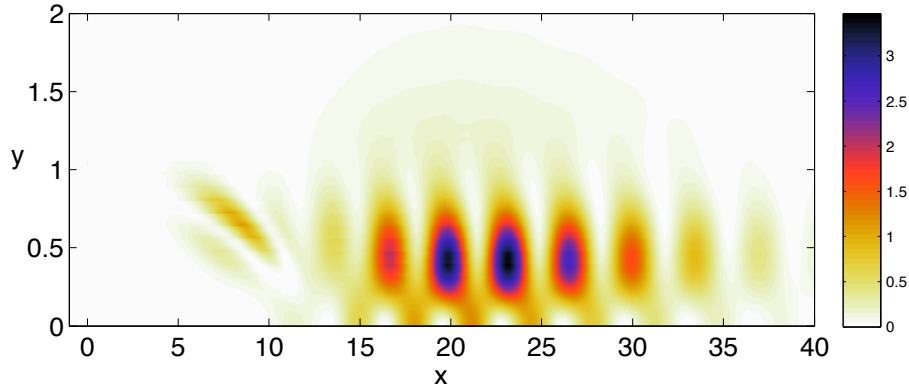


FIGURE 12. The change to generic changes in base flow advection, S_{adv} , for the round-edged plate.

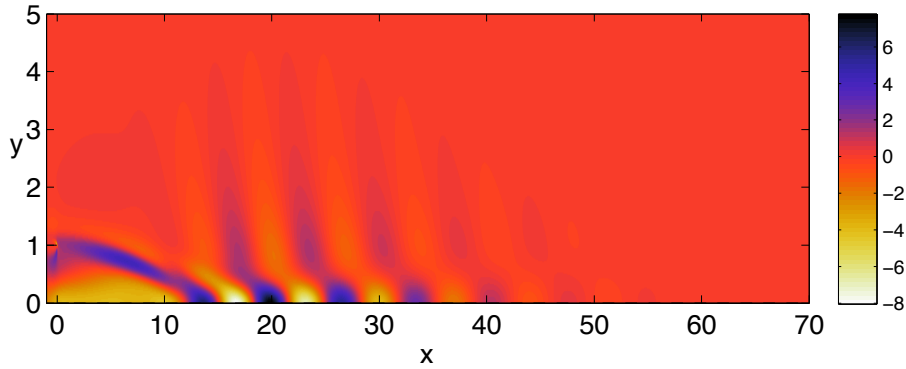


FIGURE 13. Sensitivity to a steady volume force in the stream-wise direction (positive forcing direction aligned with $\bar{e}_x = (1, 0)$), for the round-edged plate case. The streamline starting between the two flow streams at the inlet is shown with a dashed line. The region $y > 0$ is shown — the sensitivity at $y < 0$ is the mirror image.

The advective part of the sensitivity to base flow modifications for setup B is shown in figure 12, and shows an even stronger oscillatory pattern than for setup A shown previously (figure 5). The same is true for the sensitivity to a steady volume force shown for setup B in figure 13 (compared to the one for setup A shown in figure 7), and the sensitivity to a control cylinder for setup B in figure 14 (compared to figure 8 for setup A). Since the oscillatory patterns appear for both setups, we

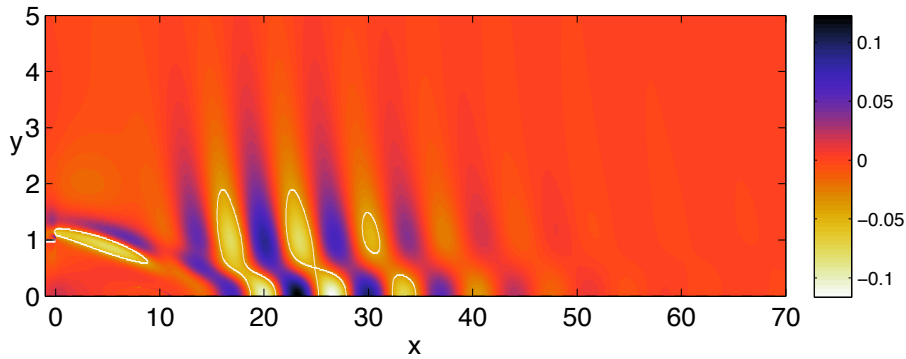


FIGURE 14. Sensitivity to a control cylinder of radius 0.02 for a round-edged plate. Region where stabilization is predicted is marked by the white contours.

have now verified that the inlet modeling used for setup A does not cause the oscillations. Together with the tests of different discretisations, streamwise boundary conditions and resolutions presented in 6, it can be concluded that the oscillations most probably have a physical origin.

The verification of the sensitivity to base flow modification is again performed by modifying the actual base flow by the distribution 4 in different positions x_{mod} , and recomputing the direct global modes in all cases. The result is compared to the prediction from adjoint-based sensitivity distributions, for different amplitudes of the base flow modification; for setup B, both small and larger amplitudes were tested. The movement of the most unstable mode with a base flow modification of a small amplitude is shown in figures 15 (a) (growth rate) and 15 (b) (frequency). These small amplitude modifications agree well with the theory. However, when the modification amplitude increases to $A = 0.02$ (figures 15 c-d), which is 10% of the maximal vertical velocity, the solution starts to deviate from the theoretical curve. For $A = 0.05$ and $A = 0.1$ the original mode soon gives place to new modes. Every "jump" in the frequency curve in figure 15 (d) indicates that a new mode has taken over as the most unstable mode.

Appendix C: Linearized drag model for the control cylinder

The dimensional drag force per unit spanwise length for the control cylinder is expressed in tensor form as:

$$D_{F,i}^* = \frac{1}{2} C_{D,tot} \rho^* |U_{tot}^*| D^* U_{tot,i}^* \quad , \quad (27)$$

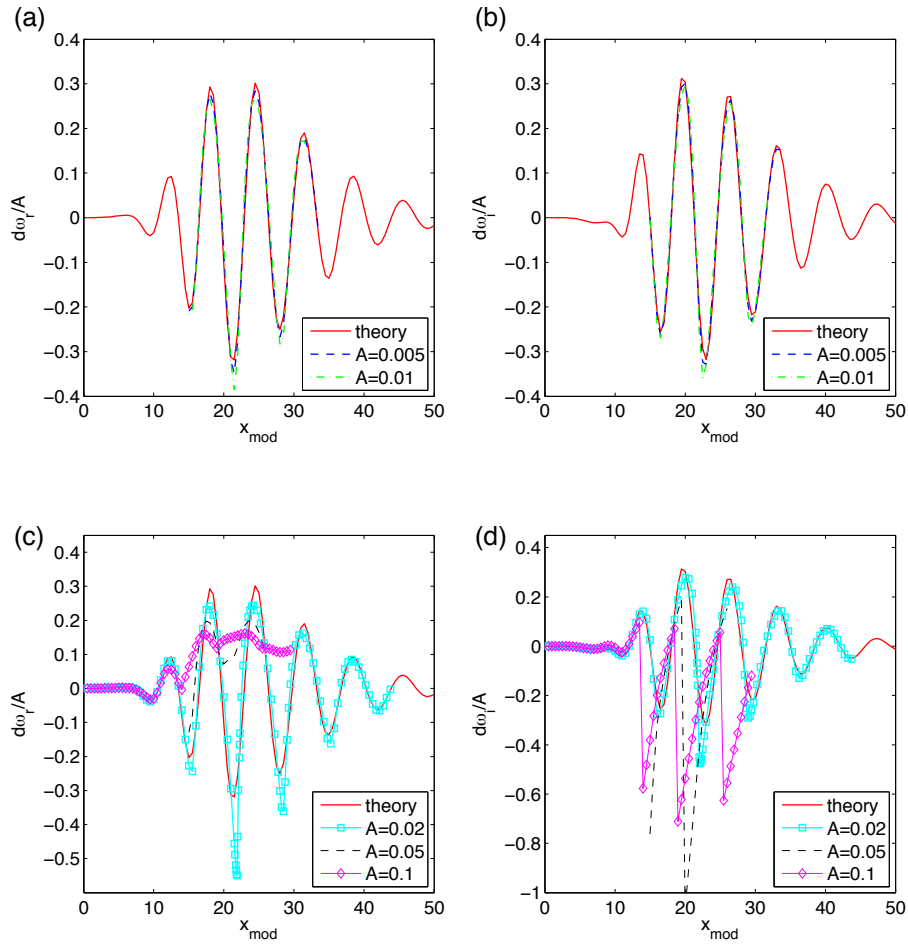


FIGURE 15. The change in the frequency and the growth rate of the most unstable eigenvalue with modifications of different amplitude along the line $y = 0.5$ (varying x_{mod}): (a) frequency, small amplitude modifications, (b) growth rate, small amplitude modifications, (c) frequency, large amplitude modifications, (d) growth rate, large amplitude modifications.

where ρ^* is the density, D the diameter of the control cylinder, $C_{D,tot}$ the drag coefficient of the control cylinder, and U_{tot}^* the total velocity field, and in nondimensional form:

$$D_{F,i} = \frac{D_{F,i}^*}{\frac{1}{2}\rho^*U_2^{*2}h_1^*} = C_{D,tot}|\bar{U}_{tot}|DU_{tot,i} \quad .$$

Let us now divide the total quantities (with subscript "tot") into a steady and unsteady linear part (uppercase vs. lowercase letters): $C_{D,tot} = C_D + c_D$, $U_{tot,i} = U_i + u_i$. Then we get:

$$D_{F,i} = D (C_D |\bar{U}_{tot}| U_i + C_D |\bar{U}_{tot}| u_i + c_D |\bar{U}_{tot}| U_i + c_D |\bar{U}_{tot}| u_i). \quad (28)$$

The last term is neglected in the linear approximation. Further, we need to linearize $|U_{tot}|$:

$$\begin{aligned} |\bar{U}_{tot}| &= \sqrt{(U + u)^2 + (V + v)^2} \\ &\approx \sqrt{U^2 + V^2} + \frac{1}{2} [U^2 + V^2]^{(-1/2)} (2Uu + 2Vv) \\ &= |\bar{U}| + \frac{(Uu + Vv)}{|\bar{U}|}, \end{aligned}$$

which leads to:

$$\begin{aligned} D_{F,i} &\approx D \left(C_D |U_{tot}| U_i + C_D |U_{tot}| u_i + c_D |U_{tot}| U_i \right) \\ &\approx D \left(C_D |\bar{U}| U_i + C_D \frac{(Uu + Vv)}{|\bar{U}|} U_i + C_D |\bar{U}| u_i + \right. \\ &\quad \left. + C_D \frac{(Uu + Vv)}{|\bar{U}|} u_i + c_D |\bar{U}| U_i + c_D \frac{(Uu + Vv)}{|\bar{U}|} U_i \right) \\ &\approx D \left(C_D |\bar{U}| U_i + C_D \frac{(Uu + Vv)}{|\bar{U}|} U_i + C_D |\bar{U}| u_i + c_D |\bar{U}| U_i \right) \quad (29) \end{aligned}$$

Now it remains to find C_D and c_D , by linearizing an appropriate expression for $C_{D,tot}$. An empirical expression for a cylinder in a uniform stream in good agreement with experiments for $5 < Re < \infty$ is according to Zdrakovich found from Imai 1957:

$$C_{D,tot} = \left(0.707 + \frac{3.42}{\sqrt{Re_c}} \right)^2, \quad (30)$$

where Re_c is the cylinder Reynolds number. For the flow case in the present work this is rewritten according to:

$$C_{D,tot} = \left(0.707 + \frac{3.42}{\sqrt{Re |\bar{U}_{tot}| D}} \right)^2. \quad (31)$$

By inserting (29) into this and developing, we get:

$$\begin{aligned}
C_{D,tot} &= \left(0.707 + \frac{3.42}{\sqrt{Re|\bar{U}_{tot}|D}} \right)^2 \\
&\approx \left(0.707 + \frac{3.42}{\sqrt{Re|\bar{U}|D}} \right)^2 \\
&\quad + 2 \left(0.707 + \frac{3.42}{\sqrt{Re|\bar{U}|D}} \right) \frac{3.42}{\sqrt{ReD}} \left[-\frac{1}{2} |\bar{U}|^{-3/2} \frac{(Uu + Vv)}{|\bar{U}|} \right] \\
&= \left(0.707 + \frac{3.42}{\sqrt{Re|\bar{U}|D}} \right)^2 \\
&\quad - \frac{3.42}{\sqrt{Re|\bar{U}|D}} \left(0.707 + \frac{3.42}{\sqrt{Re|\bar{U}|D}} \right) \left[\frac{(Uu + Vv)}{|\bar{U}|^2} \right].
\end{aligned}$$

This can be written in a simple form by introducing functions varying with the local velocity, $\alpha = 3.42/\sqrt{Re|\bar{U}|D}$ and $\beta = (0.707 + \alpha)$:

$$C_D = \beta^2$$

and

$$c_D = -\alpha\beta \frac{(Uu + Vv)}{|\bar{U}|^2}$$

Now we can identify components and divide the drag into steady and unsteady parts as:

$$D_{F(steady),i} = D\beta^2|\bar{U}|U_i \quad (32)$$

$$\begin{aligned}
D_{F(unsteady)} &= D \left[\beta^2 U_i \frac{(Uu + Vv)}{|\bar{U}|^2} + \beta^2 |\bar{U}| u_i - \alpha\beta |\bar{U}| U_i \frac{(Uu + Vv)}{|\bar{U}|^2} \right] \\
&= D (\beta^2 - \alpha\beta|\bar{U}|) U_i \frac{(Uu + Vv)}{|\bar{U}|^2} + D\beta^2 |\bar{U}| u_i. \quad (33)
\end{aligned}$$

Now when the components of the linearized force have been obtained, they should be considered as point forces in the steady equations and linearized momentum equations, respectively (to obtain the correct total force on the flow). The sensitivities can now be obtained *e.g.* from the expressions of Pralits *et al.* (2010), repeated again for convenience.

For an unsteady force of the form $f = \delta(x - x_0)(y - y_0)m_{ij}u_j$, the sensitivity is given by:

$$\delta\omega = u_i^+ m_{ij} u_j,$$

and for a steady force of the form: $F = \delta(x - x_0)(y - y_0)M_{ij}u_j$:

$$\delta\omega = U_i^+ M_{ij} U_j.$$

The normalization can be skipped, since our adjoints are already appropriately normalized, according to (12).

The above expressions give:

$$\begin{aligned} M_{UU} &= D\beta^2|\bar{U}|, & M_{VV} &= D\beta^2|\bar{U}|, & M_{UV} &= M_{VU} = 0, \\ m_{uu} &= D(\beta^2 - \alpha\beta|\bar{U}|)U^2/|\bar{U}|^2 + D\beta^2|\bar{U}|, \\ m_{uv} &= D(\beta^2 - \alpha\beta|\bar{U}|)UV/|\bar{U}|^2, \\ m_{vu} &= D(\beta^2 - \alpha\beta|\bar{U}|)UV/|\bar{U}|^2, \\ m_{vv} &= D(\beta^2 - \alpha\beta|\bar{U}|)V^2/|\bar{U}|^2 + D\beta^2|\bar{U}|. \end{aligned}$$

References

- ÅKERVIK, E. 2011 personal communication.
- ÅKERVIK, E., HEPFFNER, J., EHRENSTEIN, U. & HENNINGSON, D. S. 2007 Optimal growth, model reduction and control in a separated boundary-layer flow using global eigenmodes. *Journal of Fluid Mechanics* **579**, 305–314.
- BEARMAN, P. W. & ZDRAVKOVICH, M. M. 1978 Flow around a circular cylinder near a plane boundary. *Journal of Fluid Mechanics* **89**, 33–47.
- CHOMAZ, J.-M. 2005 Global Instabilities in Spatially Developing Flows: Non-Normality and Nonlinearity. *Annual Review of Fluid Mechanics* **37**, 357–392.
- FILON, L. N. G. 1926 The forces on a cylinder in a stream of viscous fluid. *Proceedings of the Royal Society A* **113**, 7–27.
- GIANNETTI, F. & LUCHINI, P. 2007 Structural sensitivity of the first instability of the cylinder wake. *Journal of Fluid Mechanics* **581**, 167–197.
- HILL, D. 1992 A theoretical approach for analyzing the restabilization of wakes. *AIAA Paper* pp. 92–0067.
- HUSSAIN, A. K. M. F. & ZAMAN, Q. 1978 The free shear layer tone phenomenon and probe interference. *Journal of Fluid Mechanics* **87** (02), 349–383.
- IMAI, I. 1951 On the asymptotic behaviour of viscous fluid flow at a great distance from a cylindrical body, with special reference to filon’s paradox. *Proceedings of the Royal Society A* **208**, 487–516.
- JUNIPER, M., TAMMISOLA, O. & LUNDELL, F. 2011 Comparison of local and global stability properties of confined wake flows. *Submitted to Journal of Fluid Mechanics* .
- JUNIPER, M. P. 2006 The effect of confinement on the stability of two-dimensional shear flows. *Journal of Fluid Mechanics* **565**, 171–195.
- KOVASZNAY, L. 1949 Hot-Wire Investigation of the Wake behind Cylinders at Low reynolds Numbers. *Proceedings of the Royal Society of London. Series A. Mathematical and Physical Sciences* **198** (1053), 174–190.
- MARQUET, O., SIPP, D. & JACQUIN, L. 2008 Sensitivity analysis and passive control of cylinder flow. *Journal of Fluid Mechanics* **615**, 221–252.
- PRALITS, J., BRANDT, L. & GIANNETTI, F. 2010 Instability and sensitivity of the flow around a rotating circular cylinder. *Journal of Fluid Mechanics* **650**, 513–536.

- REES, S. J. & JUNIPER, M. P. 2010 The effect of confinement on the stability of viscous planar jets and wakes. *Journal of Fluid Mechanics* **656**, 309–336.
- RICHTER, A. & NAUDASCHER, E. 1976 Fluctuating forces on a rigid circular cylinder in confined flow. *Journal of Fluid Mechanics* **78**, 561–576.
- ROWLEY, C. W., COLONIUS, T. & BASU, A. J. 2002 On self-sustained oscillations in two-dimensional compressible flow over rectangular cavities. *Journal of Fluid Mechanics* **455**, 315–346.
- STRYKOWSKI, P. J. & SREENIVASAN, K. R. 1990 On the formation and suppression of vortex 'shedding' at low reynolds numbers. *Journal of Fluid Mechanics* **218**, 71–107.
- TAMMISOLA, O., LUNDELL, F., SCHLATTER, P., WEHRFRITZ, A. & SÖDERBERG, L. D. 2011 Global linear and nonlinear stability of viscous confined plane wakes with co-flow. *Journal of Fluid Mechanics* **675**, 397–434.
- UNAL, M. F. & ROCKWELL, D. 1987 On vortex formation from a cylinder. part 2. control by splitter-plate interference. *Journal of Fluid Mechanics* **190**, 513–529.
- WILLIAMSON, C. H. K. 1996 Vortex dynamics in the cylinder wake. *Annual Review of Fluid Mechanics* **28**, 477–539.
- ZDRAVKOVICH, M. M. 1997 *Flow around circular cylinders*, , vol. 1. Oxford University Press.

Paper 6

6

Surface tension induced global destabilisation of plane jets and wakes

By **OUTI TAMMISOLA**¹,
FREDRIK LUNDELL^{1,2}, and
L. DANIEL SÖDERBERG^{2,3}

¹ Linné FLOW Centre, KTH Mechanics, Royal Institute of Technology, SE-100 44 Stockholm, Sweden

²Wallenberg Wood Science Center, KTH Mechanics, SE-100 44 Stockholm, Sweden

³Innventia AB, BOX 5604, SE-114 86, Stockholm, Sweden

To be submitted.

The effect of surface tension on global stability of confined co-flow jets and wakes at a moderate Reynolds number is studied. The flow cases under study are globally stable without surface tension. It is found that surface tension can cause the flow to be unstable if the inlet shear is strong enough. For even stronger surface tension, the flow is re-stabilized. As long as there is no change of the most unstable mode, increasing surface tension seems to decrease the oscillation frequency and increase the wavelength of the mode. The critical shear (minimum shear at which an instability is found) is found to occur for anti-symmetric disturbances for the wakes and symmetric disturbances for the jets. However, at stronger shear, the opposite symmetry might be the most unstable one, in particular for wakes at high surface tension. The results show strong effects of surface tension that should be possible to reproduce experimentally as well as numerically.

1. Introduction

There are many examples where surface tension between immiscible fluids has an important roll in fluid dynamic processes. Some examples illustrating the width of the applications are atomization in *e.g.* irrigation and combustion applications, the stability of the headbox jet in papermaking or breaking waves and the related gas transport to the ocean.

This work concentrates on the effect of surface tension on global stability of a family of jet and wake flows. The term global stability

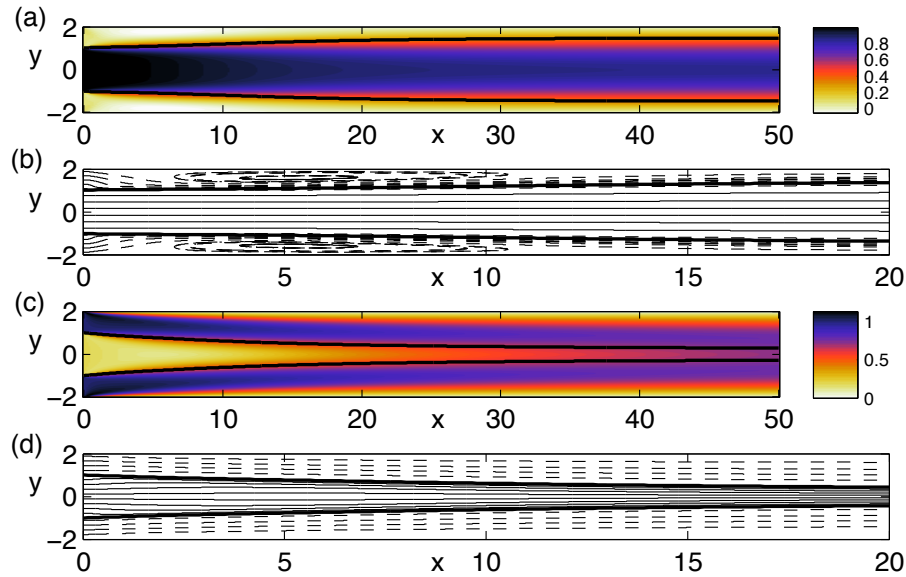


FIGURE 1. Example of jet ($\Lambda^{-1} = 1.2$, a, b) and wake ($\Lambda^{-1} = -1.4$, c,d) base flows under study. The streamline separating the inner and outer flow (at which surface tension is applied) is bold, the inner streamlines are solid and the outer streamlines are dashed.

means that self-sustained instabilities are sought for. When such instabilities exist, the flow acts as an oscillator at a certain frequency (a famous example is the von Kármán vortex street behind a cylinder). This is different from studies of convective instabilities, which investigate the ability of a flow to spatially amplify a disturbance convected by the flow. Surface tension enters the problem through the boundary condition on the interface between two fluids. In a previous work, it has been shown (Tammisola *et al.* 2011b) that surface tension increased the growth rate of global modes for a wake flow, and that the most unstable mode changed from antisymmetric to symmetric for strong surface tension. Here, the effect of surface tension on wake and jet flows is studied in a wider parameter space.

The flow cases under study are illustrated in figure 1. The flow is plane and two-dimensional and consists of one inner stream surrounded by two outer streams. The inner stream can be either slower (wake) or faster (jet) than the outer streams, which both have the same velocity.

The height of the inner flow is $2h_1^*$ (the superscripts denote dimensional parameters) and the height of each outer stream is h_2^* (the total channel height is $2h_1^* + 2h_2^*$). The coordinates are x, y for the streamwise and vertical directions, respectively, and the origin is at the centre of the channel at the inlet. The inlet velocity of respective stream is constant over the cross section and equals U_1^* in the inner stream and U_2^* in the outer streams. The velocity scale is defined as U_{ref}^* and is chosen as the largest of the two velocities, *i.e.* U_1^* for jets and U_2^* for wakes. Lengths are scaled with the height of the inner stream h_1^* . Neglecting surface tension and assuming that the two streams have the same kinematic viscosity ν^* , these flows can now be characterized by three nondimensional parameters:

$$Re = \frac{U_{ref}^* h_1^*}{\nu^*}, \quad h = \frac{h_2^*}{h_1^*}, \quad \Lambda = \frac{U_1^* - U_2^*}{U_1^* + U_2^*}, \quad (1)$$

which define the Reynolds number, confinement parameter and shear ratio, respectively. In the present study, $Re = 316$ and $h = 1$ have been chosen. Introducing the surface tension γ^* , one additional parameter appears, namely the Weber number:

$$We = \frac{\rho^* U_{ref}^* h_1^*}{\gamma^*} \quad (2)$$

where ρ^* is the density of the fluids (the two streams are assumed to have the same density).

The division to two fluids occurs along the streamlines originating from the inlet and drawn with thick lines in figure 1. In (b,d), additional streamlines are shown: solid indicating the inner flow and dashed indicating the outer flows.

The study of these flow cases was inspired by earlier work on absolute instability of weakly-nonparallel jet and wakes flows (*e.g.* Huerre & Monkewitz (1990) and Juniper (2006)) without surface tension. The reason for choosing this particular flow problem as a model problem is that the global stability of single phase wake flows ($\Lambda^{-1} < 0$) has been studied and understood with different methods (global stability, local absolute instability and direct numerical simulations) by Tammissola *et al.* (2011*a*); Juniper *et al.* (2011). In those two studies, the different methods were compared and the effects of Re , Λ and h were outlined. Furthermore, it was found that the global method as used in this work successfully predicted the onset and growth of instabilities in the direct numerical simulations and that the combination of the three methods

allowed the physical origins to be investigated. For complete parametric dependencies, the works cited above should be consulted.

When it comes to single phase uniform density co-flow jets ($\Lambda^{-1} > 0$) at the Re of the present study, they are globally stable for oscillatory modes, and these authors are not aware of any related results in the literature. At higher Re and the case of $U_2^* = 0$ (no outer flow), results for confined axisymmetric jets have been reported by *e.g.* Villiermaux & Hopfinger (1994). The recirculation bubble formed due to confinement caused self-sustained low-frequency oscillations.

The influence of surface tension on two example wakes at fixed shear was investigated in Tammisola *et al.* (2011*b*). These wakes had one unstable mode without surface tension, the well-known antisymmetric von Kármán mode. Intermediate surface tension ($We^{-1} \approx 0.1$) considerably increased the growth rate of the most unstable mode, while strong surface tension ($We^{-1} \approx 0.5$) stabilized the wakes. The frequency of the most unstable mode decreased with surface tension. The first example wake at $Re = 100$ had at maximum one unstable mode, while the behaviour of the second wake at $Re = 316$ was more interesting: for intermediate surface tension, several unstable modes appeared, and for a certain range of We , the most unstable mode was symmetric. It was conjectured that surface tension could move the stability boundaries for uniform density wakes, and due to the appearance of symmetric modes, the mechanism might be present for jets as well. In studies based on the locally parallel assumption (*e.g.* Rees & Juniper (2009)), absolute instability has been found also for jets with surface tension, which supports the hypothesis. Furthermore, a relaxational plane water jet in air can possess absolute instability (Söderberg 2003). For water sheets with uniform velocity profiles, a curious neutral absolute instability with zero frequency and infinite wavelength has been reported (Li & Tankin 1991).

In the present work, we investigate the global destabilization due to surface tension of confined ($h = 1$) wakes and jets with constant density and viscosity at $Re = 316$. Governing equations and numerical methods are presented in section 2. Results for wakes and jets with a varying degree of surface tension and varying inlet shear are presented and discussed in section 3, and the main conclusions summarized in section 4. An appendix, in which the linearized boundary conditions on the free surface are given explicitly, is also provided.

2. Methods

2.1. Base flows

The base flows are similar to those used in Tammisola *et al.* (2011a) and were calculated using the Nek5000 spectral element (SEM) code, developed by Paul Fischer, Argonne Laboratory, Argonne, USA (Fischer 1997). Below, some issues specific to the present study are presented and discussed.

The restrictions of the present work (constant density and viscosity) were made in order to be able to use high-accuracy base flows from single phase calculations. This approximation was used also in a previous work (Tammisola *et al.* 2011b) and is motivated by the following observations:

1. The steady interface position between any two fluids (also with density/viscosity gradients) must follow a streamline of the steady base flow. This is the only possibility, since the velocity component normal to the interface has to vanish.
2. The curvature of the steady base flow without surface tension is small, except for the immediate vicinity of the inlet ($x < 0.1$). On the other hand, accurately determining the curvature at the inlet would require contact line modeling, which is out of the scope of this work, and is a research topic in itself.

The capillary pressure gradients that would exist due to interface curvature are at least an order of magnitude smaller than other pressure gradients in the flow even at very high surface tension ($We^{-1} = 2$).

Without surface tension, the only oscillations occurring in the flow are antisymmetric and thus, steady base flows can be obtained by imposing a symmetry condition along the centreline.

2.2. Global stability analysis

The stability analysis is made by assuming small disturbances, so that the Navier-Stokes equations can be linearized around the steady state. The flow field is decomposed into a steady and fluctuating part so that $U^{(tot)} = U + u$, $V^{(tot)} = V + v$, $P^{(tot)} = P + p$ and $H^{(tot)} = H + \eta$ where $U^{(tot)}$ and $V^{(tot)}$ are the velocity components in x and y , respectively, $P^{(tot)}$ is the pressure and $H^{(tot)}$ is the position of the interface between the fluids. An overbar will be used to denote a vector of the two velocity components. Furthermore, we make the global mode Ansatz independent of the z -coordinate:

$$u_k(x, y, t) = \hat{u}_k(x, y)e^{-i\omega t}, \quad (3)$$

$$v_k(x, y, t) = \hat{v}_k(x, y)e^{-i\omega t}, \quad (4)$$

$$p_k(x, y, t) = \hat{p}_k(x, y)e^{-i\omega t}, \quad (5)$$

$$\eta(x, t) = \hat{\eta}(x)e^{-i\omega t}, \quad (6)$$

where ω is the complex angular frequency and the subscript k refers to flow domain 1 and 2. In the following, this subscript is often skipped and in these cases \hat{u} , \hat{v} and \hat{p} refer to the disturbance distributions in the full domain. The division into two domains and introduction of η is necessary in order to include the effect of surface tension on the interface via the conditions coupling the two domains, as described in the next subsection.

Inserting the ansatz (3-6) into the *linearized Navier-Stokes equations* (LNSE) gives:

$$-U \frac{\partial \hat{u}}{\partial x} - V \frac{\partial \hat{u}}{\partial y} - \hat{u} \frac{\partial U}{\partial x} - v \frac{\partial U}{\partial y} \quad (7)$$

$$- \frac{\partial \hat{p}}{\partial x} + \frac{1}{Re} \left(\frac{\partial^2 \hat{u}}{\partial x^2} + \frac{\partial^2 \hat{u}}{\partial y^2} \right) = -i\omega \hat{u} \quad (8)$$

$$-U \frac{\partial \hat{v}}{\partial x} - V \frac{\partial \hat{v}}{\partial y} - \hat{u} \frac{\partial V}{\partial x} - \hat{v} \frac{\partial V}{\partial y} \quad (9)$$

$$- \frac{\partial \hat{p}}{\partial y} + \frac{1}{Re} \left(\frac{\partial^2 \hat{v}}{\partial x^2} + \frac{\partial^2 \hat{v}}{\partial y^2} \right) = -i\omega \hat{v} \quad (10)$$

$$\frac{\partial \hat{u}}{\partial x} + \frac{\partial \hat{v}}{\partial y} = 0. \quad (11)$$

This system has to be equipped with boundary conditions both at the interface between domains 1 and 2, and at the boundaries of the computational domain.

The conditions at the vertical boundaries are straightforward. The condition at the wall is:

$$\hat{u}_2(x, h+1) = \hat{v}_2(x, h+1) = 0, \quad (12)$$

(note that h is the confinement parameter and not the disturbance of the surface; this notation has been chosen in order to be consistent with previous work) and at the centerline, for antisymmetric modes:

$$\hat{u}_1(x, 0) = \frac{\partial \hat{v}_1}{\partial y}(x, 0) = \hat{p}_1(x, 0) = 0, \quad (13)$$

and symmetric modes:

$$\frac{\partial \hat{u}_1}{\partial y}(x, 0) = \hat{v}_1(x, 0) = 0. \quad (14)$$

At the streamwise boundaries we set Dirichlet conditions, and combine this with a fringe region at the outlet. In this region, the disturbance is gradually forced towards zero by a volume force (inspired by the SIMSON code, see Chevalier *et al.* (2007)). Especially for jets, this turned out to be a better choice than the conventional Neumann condition at the outlet providing faster convergence of the eigenvalues as the length of the domain was increased.

The flow has to satisfy physical constraints at the interface $y = H + \eta$, where the capillary force is imposed as a stress discontinuity. The interface conditions are presented in tensor form, where $\hat{u}_{k,i}$ now represents the streamwise disturbance velocity for $i = 1$ and the vertical disturbance velocity for $i = 2$. The nonlinear conditions are given here in order to explain the origin of the interface conditions. They must be linearized to yield at the steady position of the interface ($y = H$), which becomes more cumbersome; the linearization procedure and resulting conditions are presented in Appendix A. The physical conditions at the interface are:

1. Continuity of the velocities at the interface

$$U_{1,i}^{(tot)} = U_{2,i}^{(tot)} \quad . \quad (15)$$

2. Continuity of the tangential force at the interface

$$\tilde{t}_i S_{1,ij}^{(tot)} \tilde{n}_j = \tilde{t}_i S_{2,ij}^{(tot)} \tilde{n}_j \quad , \quad (16)$$

where \tilde{t} is the tangent vector of the interface (that depends on both H and η), \tilde{n} the normal vector, and

$$S_{ij}^{(tot)} = -P^{(tot)} \delta_{ij} + \frac{1}{Re} \left(\frac{\partial U_i^{(tot)}}{\partial x_j} + \frac{\partial U_j^{(tot)}}{\partial x_i} \right)$$

is the stress tensor with pressure included.

3. Jump in the normal stress due to surface tension, dependent on the local surface curvature:

$$\tilde{n}_i S_{1,ij}^{(tot)} \tilde{n}_j = \tilde{n}_i S_{2,ij}^{(tot)} \tilde{n}_j - \frac{1}{We} \left(\frac{\partial \tilde{n}_x}{\partial x} \right) \quad . \quad (17)$$

4. The interface displacement follows the vertical displacement of a particle at the interface:

$$\frac{\partial H^{(tot)}}{\partial t} + U^{(tot)} \frac{\partial H^{(tot)}}{\partial x} = V^{(tot)} \quad . \quad (18)$$

The stability analysis is performed by discretizing equations (8–11) using Chebyshev-polynomials in both the streamwise and vertical directions:

$$\hat{u}(x, y) \approx \sum_{i=1}^{N_x} \sum_{j=1}^{N_y} c_{ij} \phi^i(x) \phi^j(y) \quad (19)$$

where ϕ^k is the k^{th} Chebyshev polynomial. The values of the unknown coefficients c_{ij} are obtained by requiring the discretised equations to be satisfied exactly at the $N_x \times N_y$ collocation points, which are selected as the Gauss-Lobatto points to assure an exponential convergence rate (Weideman & Reddy 2000). The domain $[-1, 1] \times [-1, 1]$ is stretched linearly in the vertical and horizontal directions to $[0, L_x] \times [0, H(x)]$ for the inner and $[0, L_x] \times [H(x), h + 1]$ for the outer flow. The two domains are connected with the interface conditions (see appendix A).

The matrix resulting from the discretized equations and boundary conditions becomes too large for the problem to be solved serially. Therefore, the matrix is built and the eigenvalue problem solved in parallel, using our code FLUPACK based on parallelised Arnoldi algorithm obtained from the PARPACK mathematical library (Maschhoff & Sorensen 1996), and parallel linear algebra operations from ScaLAPACK (Blackford *et al.* 1997). Further details of the code can be found in Chapter 5 of this thesis. The matrix eigenvalue problem is solved directly, as opposed to the time-stepping approach (Tuckerman & Barkley 2000), which would have been necessary for three-dimensional problems.

It can be shown that for linear problems, any disturbance can be expressed as a sum of symmetric and antisymmetric components, and also that for symmetric base flows these two components can be computed separately. Thus, we use the upper half of the flow domain only.

3. Results and Discussion

Stability results for a confinement $h = 1$ and a Reynolds number $Re = 316$ will be shown for different Weber numbers and shear ratios. This choice has been made in order to illustrate how surface tension on the interface can affect the stability of the flow. With a four-dimensional parameter space at hand (h, Re, We, Λ) , a complete parameter study is

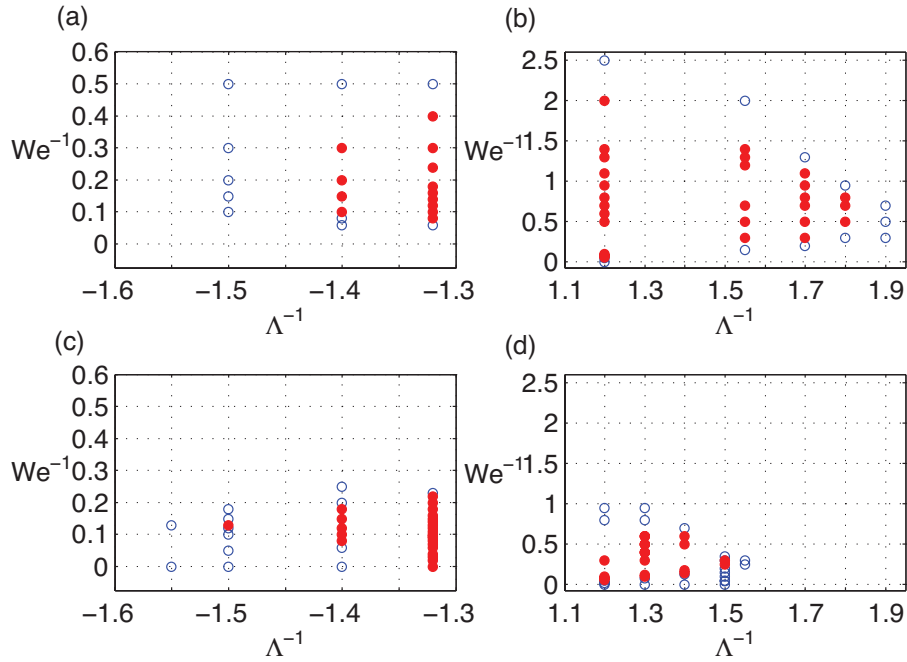


FIGURE 2. Global stability as a function of $1/We$ and $1/\Lambda$ for wakes (a,c) and jets (b,d). Results for symmetric (a,b) and antisymmetric (c,d) disturbances are shown. Filled symbols (red) show unstable and open (blue) show stable cases.

not feasible. First, the stability as such, *i.e.* sign of ω_i , will be studied, of course with an emphasis on the bifurcation to instability. This study will be followed by a presentation of spectra and eigenmodes for one selected jet and wake with varying surface tension. The latter presentation is made in order to illustrate how the capillary forces on the interface can affect the eigenvalues and amplitude distributions.

3.1. Stability as a function of $1/We$ and $1/\Lambda$

Figure 2 shows the stability for a large number of combinations of $1/We$ and $1/\Lambda$. The unstable cases are shown with filled (red) markers and the stable with open (blue) markers. Wakes ($1/\Lambda < 0$) are shown in (a,c) and jets ($1/\Lambda > 0$) in (b,d). Note that the vertical axis is different for jets and wakes, respectively. The first row, (a,b), shows the stability of symmetric disturbances and the second row, (c,d), shows antisymmetric disturbances. All four cases show a region of global instability.

All data in figure 2 show a similar overall behaviour. For all values of $1/\Lambda$ shown except $1/\Lambda = -1.32$, the flows are stable at $1/We = 0$ (no surface tension). As $1/We$ is increased (upwards in each figure), the flows eventually become unstable and as $1/We$ is increased even further, the flows get stable again.

Focus now on the range of destabilization for different shear ratios ($1/\Lambda$). Since an increasing absolute amplitude of $1/\Lambda$ means decreasing shear, these results show that surface tension can induce global instability if the shear is large enough. Thus, one can define a critical shear and surface tension as the maximum absolute value of $1/\Lambda$ for which the flow can be unstable, and the corresponding value of We is the critical Weber number. An indication of the critical shear can be obtained by studying the leftmost filled symbol in (a,c) and the rightmost filled symbol in (b,d), although the focus on the present study is to illustrate the overall behaviour of the flows, rather than pin-pointing the exact critical value(s) of some parameter(s).

Analyzing figure 2 in more detail, we will start by looking at the differences between the jets and the wakes. For the jets (left column), the critical value of $1/\Lambda$ is distinctively higher than for the wakes (left column), as well as the critical $1/We$. This means that jets are destabilized at weaker shear than wakes (and thus are more unstable than wakes in this sense), but also that a stronger surface tension is needed for jets at the critical point. Note also that the symmetry for which the critical shear is weakest is different for jets and wakes. The anti-symmetric disturbances on wakes in (c) demonstrate a weaker critical shear than the symmetric ones in (a). For the jets, the situation is the opposite: the critical shear for symmetric disturbances in (b) is weaker than for the antisymmetric disturbances in (d).

One can also make conclusions by comparing the two rows in figure 2 showing results for different symmetries. The symmetric disturbances (a,b) are unstable for higher values of $1/We$ than the antisymmetric ones (c,d). For the wakes, this means that there are considerable parameter regions where there are unstable symmetric disturbances even though the antisymmetric disturbances (which are the ones unstable for the weakest shear as discussed above) are stable. This behaviour was observed also in the detailed study of selected wake flows by Tammisola *et al.* (2011b).

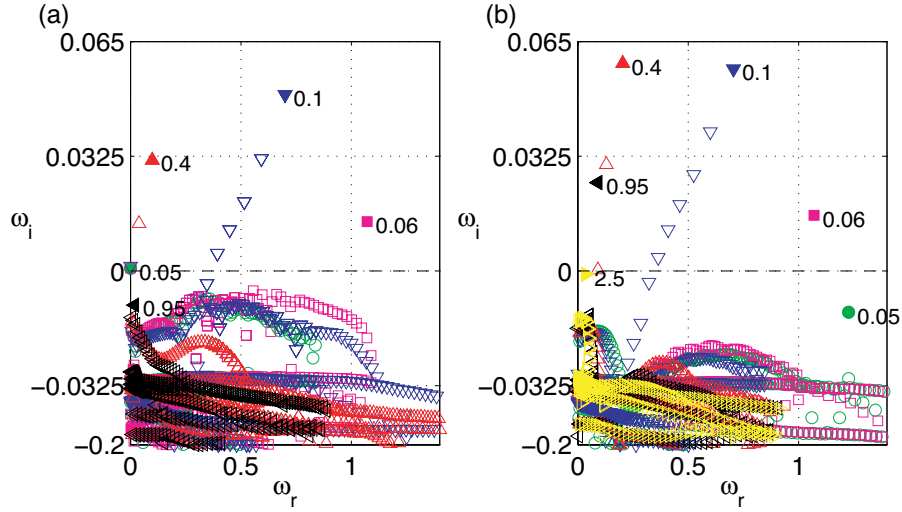


FIGURE 3. Spectra for $1/\Lambda = 1.2$ (a jet flow), antisymmetric disturbances in (a) and symmetric in (b). Spectra for different $1/We$ are shown with different combinations of marker and colors. For each $1/We$, the most unstable eigenvalue is shown with a filled marker and the value of $1/We$ is given next to it. Note that the vertical axis below -0.0325 has been compressed by a factor of 10.

3.2. Spectra and modes for a jet, $1/\Lambda = 1.2$

The spectra and modes reveal more details of the instabilities. Results for a jet with $1/\Lambda = 1.2$ (*c.f.* figure 1 a) are shown in figure 3 (spectra) and 4 (modes). Starting with the spectra in figure 3, the global oscillatory modes are found as eigenvalues that are separated both from the stable continuous spectra with lower values of ω_i and the steady modes with $\omega_r = 0$. For both antisymmetric and symmetric disturbances, there is a bifurcation from stable to unstable eigenvalues between $1/We = 0.05$ and 0.06 . The growth rate (ω_i) then grows as $1/We$ is increased and the frequency (ω_r) decreases. At $1/We = 0.1$ and 0.4 , there are several unstable modes.

Figure 4 shows the eigenmodes for the most unstable eigenvalues in figure 3, for some values of $1/We$. In figure 4, antisymmetric (a, c, e) and symmetric (b, d, f) modes of the \hat{u} disturbance are shown for increasing values of $1/We$. The oscillation of the interface is indicated by a solid line; note that the amplitude of this oscillation is arbitrary and has been

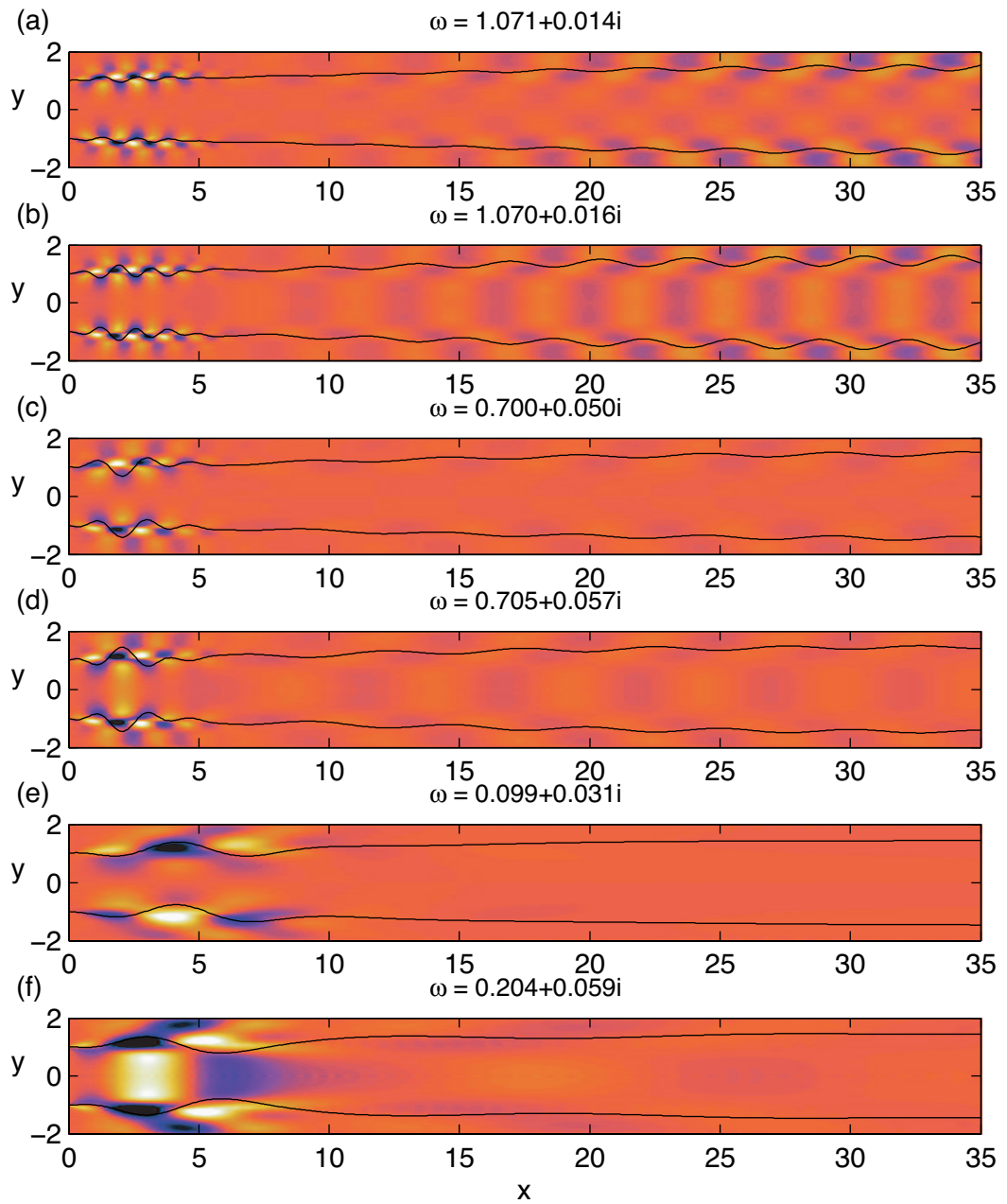


FIGURE 4. Real part of \hat{u} for $1/\Lambda = 1.2$ for antisymmetric (a,c,e) and symmetric (b,d,f) disturbances for $1/We = 0.06$ in (a,b), 0.1 in (c,d) and 0.4 in (e,f). The oscillation of the free surface is illustrated with solid curves.

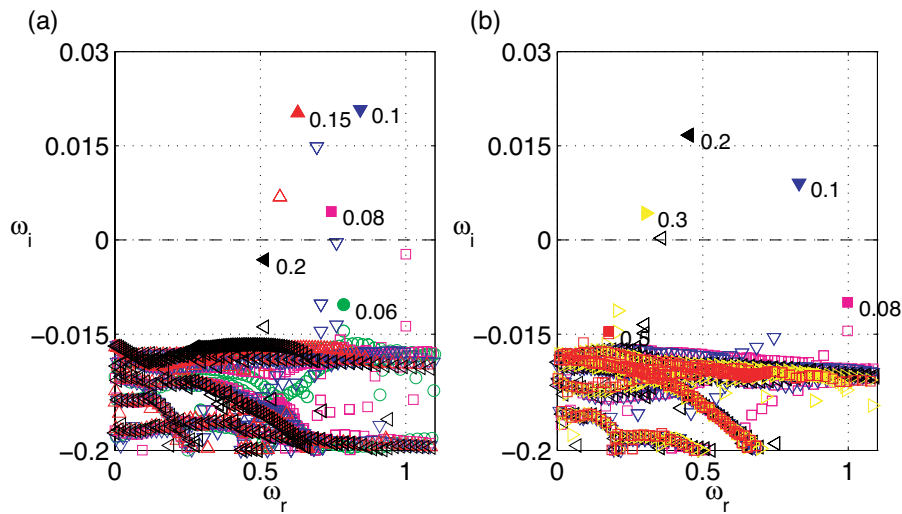


FIGURE 5. Spectra for $1/\Lambda = -1.4$ (a wake), antisymmetric disturbances in (a) and symmetric in (b). Spectra for different $1/We$ are shown with different combinations of marker and colors. For each $1/We$, the most unstable eigenvalue is shown with a filled marker and the value of $1/We$ is given next to it. Note that the vertical axis below -0.015 has been compressed a factor of 10.

chosen for its graphical appearance. It should also be emphasized that the computational domain is considerably longer than the region shown and that the eigenvalues are converged with respect to the box length for all results shown.

The modes in figure 4 show a consistent development as $1/We$ is increased. As the surface tension gets stronger and stronger, the most unstable mode exhibits an increase in its wavelength. A possible explanation might be that smaller waves are damped by the strong surface tension. When it comes to the origin of the surface tension induced global instability as such, it is probably relying on an interplay between wave motions in the flow and on the surface (which is turned into an active part of the oscillatory system when surface tension is present). The purpose of this work is not to scrutinize the details of this interplay but to demonstrate and somewhat systematize the overall effects of surface tension.

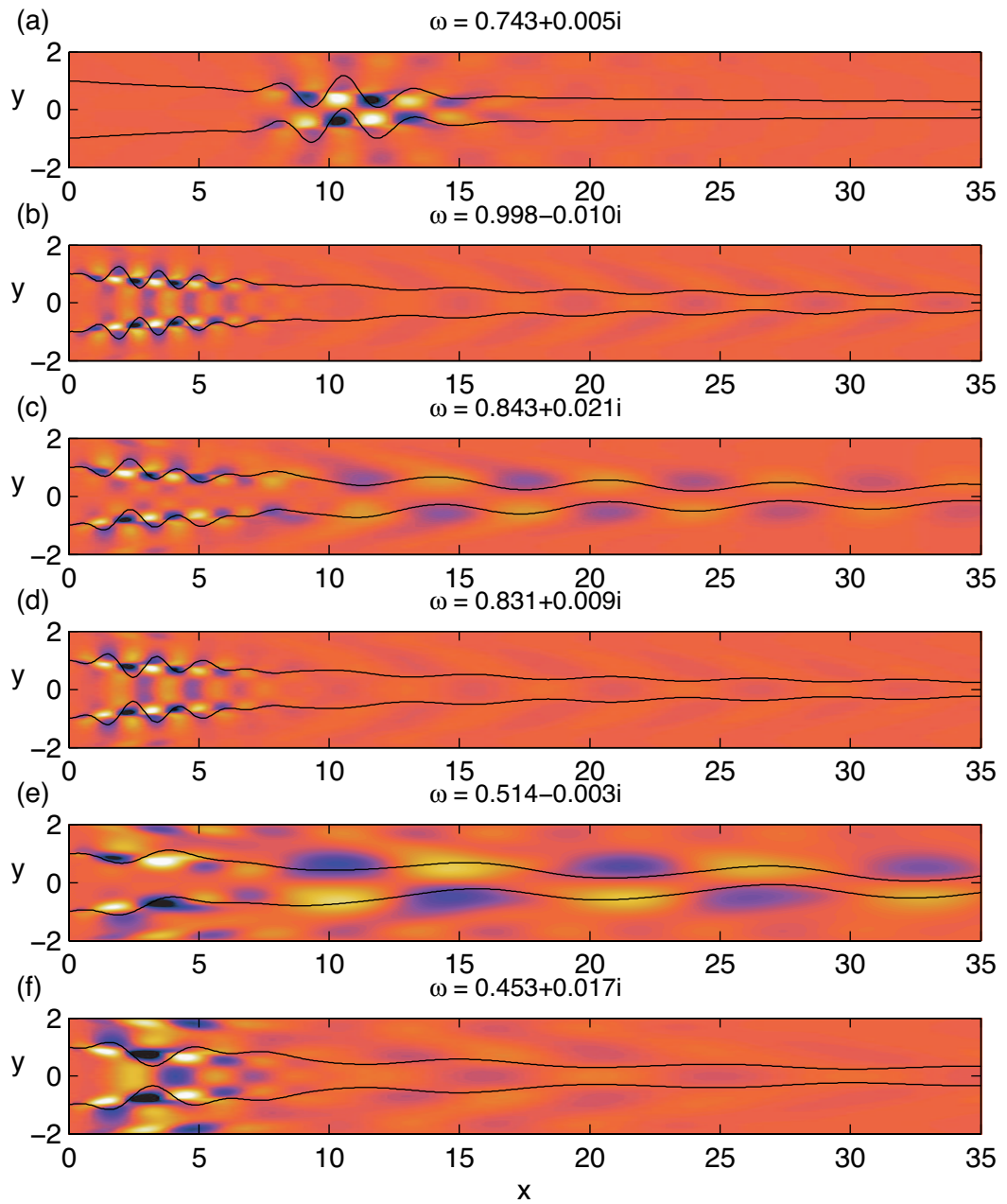


FIGURE 6. Real part of \hat{u} for $1/\Lambda = -1.4$ for antisymmetric (a,c,e) and symmetric (b,d,f) disturbances for $1/We = 0.08$ in (a,b), 0.1 in (c,d) and 0.2 in (e,f). The oscillation of the free surface is illustrated with solid curves.

3.3. Spectra and modes for a wake, $1/\Lambda = -1.4$

Overall, the behaviour of the spectra and modes for the wake shown in figures 5 and 6 are similar to those of the jet discussed above. For low $1/We$, the flow is stable. If $1/We$ is increased, single unstable modes appear and as $1/We$ is increased further, the growth factor reaches a maximum before it becomes negative and the flow is stable again. In general, it is also so that the frequency decreases as $1/We$ is increased, and the corresponding wavelength of the mode in figure 6 increases.

However, these wake modes illustrate an additional feature compared to the jet modes, namely a mode-switching. Looking at the details of figure 5 (a), it is seen that the frequency of the most unstable mode *increases* from $1/We = 0.08$ to 0.1. Furthermore, the corresponding modes in figure 6 (a) and (c) show that the structure of the mode changes completely, from a mode situated relatively far from the inlet around $x \approx 10$, whereas the other modes in figure 6 all have their maximum amplitude at $x < 5$. Thus, the most unstable modes switches from $1/We = 0.08$ to 0.1, explaining the odd behaviour of the frequency. In fact, the mode in figure 5 (a) that is most unstable at $1/We = 0.1$ is seen also at $1/We = 0.08$ as a stable mode, with a frequency higher than that of the $1/We = 0.1$ mode.

4. Conclusions

The main conclusions from this work is summarized as follows:

- Global stability of plane jet and wake flows has been studied.
- As surface tension is increased from zero, many wakes and jets are first destabilized and then stabilized again.
- There is a critical value of weakest shear (largest Λ^{-1}) at which each flow can be made unstable by surface tension.
- At this critical point, the most unstable mode is symmetric for the jets and antisymmetric for the wakes.
- The global mode shapes are considerably different when surface tension is applied, compared to *e.g.* vortex streets: the wavelength decreases and the amplitude maximum moves closer to the inlet.

The results clearly point out parameter regions that should be interesting for numerical and experimental investigations of the flow case. Such studies should be performed for two reasons, the first of which is of course a validation of the present results. A previous study in single-phase flows (Tammissola *et al.* 2011a) has shown that the global stability predicts the initial growth (and thereby the stability limit) in DNS well,

and thus it should be possible to extract the initial growth of the global mode from a careful DNS or possibly a measurement.

The second interesting feature that needs to be studied is the connection between the global linear frequencies and mode shapes and the saturated nonlinear state at which the flow arrives after exponential disturbance growth. Also in Tammisola *et al.* (2011a), the linear global modes were sometimes different from the saturated nonlinear state. In the two-phase case, this issue gets even more interesting since there can be drop pinch-off and other processes which further complicate the nonlinear state. An unstable linear global mode near the nozzle could thus lead to everything from small-amplitude waves to a complete breakup to small droplets. Thus, future studies can demonstrate to what extent the global frequency and mode shapes give an indication of the final drop sizes, breakup, and other two-phase features.

Appendix A: Linearised boundary conditions at the interface

Linearisation and transformation to $y = H$

Here the boundary conditions are linearised and transformed to the unperturbed surface location $y = H$.

In order to do this, the velocity at the perturbed surface location is expressed as a series expansion w.r.t. η and only the linear terms w.r.t. disturbance quantities are kept. The terms concerning base flow only disappear (since the base flow satisfies the boundary condition at $y = H$), and the expressions can readily be Fourier/Laplace transformed. The condition (15) transforms to:

$$\hat{u}^1 + \hat{\eta} \frac{\partial U^1}{\partial y} = \hat{u}^2 + \hat{\eta} \frac{\partial U^2}{\partial y}, \quad (20)$$

$$\hat{v}^1 + \hat{\eta} \frac{\partial V^1}{\partial y} = \hat{v}^2 + \hat{\eta} \frac{\partial V^2}{\partial y}, \quad (21)$$

The expression for the stress condition is somewhat more complicated. Let us divide the stress tensor further to:

$$S_{ij}^{(tot)} = -P^{(tot)} \delta_{ij} + \frac{2}{Re} E_{ij}^{(tot)},$$

where

$$E_{ij}^{(tot)} = \frac{1}{2} \left(\frac{\partial U_i^{(tot)}}{\partial x_j} + \frac{\partial U_j^{(tot)}}{\partial x_i} \right).$$

is the rate of deformation tensor.

The rate of deformation tensors $E_{k,ij}$ (with $k = 1$ or 2 for the two domains) consist of partial derivatives of the velocities only, *i.e.* they can be divided into two separate parts — one tensor for the base flow ($E_{k,ij}$) and one for the disturbance ($e_{k,ij}$):

$$E_{tot,ij}^k = E_{ij}^k + e_{ij}^k. \tag{22}$$

Now by doing the same linearisation as above for u , v and p , we get the value of e_{ij} at $y = H$:

$$E_{ij}(H + \eta) \approx E_{ij}(H) + e_{ij}(H) + \eta \frac{\partial E_{ij}}{\partial y}.$$

Let us assume that the surface normal can be written as:

$$\tilde{n}_i = \tilde{N}_i + \tilde{n}'_i, \tag{23}$$

where \tilde{N}_i only consists of base flow terms and \tilde{n}'_i is a linear function of the disturbance quantities. Then the linearised condition (equations 16 and 17) at $y = H$ with base flow terms subtracted becomes:

$$\begin{aligned} & (-P^1 + P^2)\delta_{ij}\tilde{n}'_j + \frac{2}{Re}(E_{ij}^1 - E_{ij}^2)\tilde{n}'_j + \\ & (-p^1 + p^2)\delta_{ij}\tilde{N}_j + \frac{2}{Re}(e_{ij}^1 - e_{ij}^2)\tilde{N}_j + \\ & + \eta\tilde{N}_j \frac{\partial}{\partial y}(-P^1 + P^2)\delta_{ij} + \frac{2}{Re}\eta\tilde{N}_j \frac{\partial}{\partial y}(E_{ij}^1 - E_{ij}^2) = \\ & -\frac{1}{We}(\tilde{N}_i \frac{\partial \tilde{n}'_j}{\partial x_j} + \tilde{n}'_i \frac{\partial \tilde{N}_j}{\partial x_j}). \end{aligned} \tag{24}$$

Components of the surface normal

Now it remains to find the base flow and disturbance parts of the interface normal, \tilde{N}_i and \tilde{n}_i , respectively. The surface normal can be written in terms of $H^{(tot)}$ as:

$$\tilde{n} = \frac{\left(-\frac{\partial H^{(tot)}}{\partial x}, 1\right)}{\sqrt{1 + \left(\frac{\partial H^{(tot)}}{\partial x}\right)^2}} \tag{25}$$

This equation will be nonlinear in $\frac{\partial\eta}{\partial x}$ due to its presence in the denominator. Thus we introduce:

$$\varphi = \frac{1}{\sqrt{\left(\frac{\partial H}{\partial x} + \frac{\partial\eta}{\partial x}\right)^2 + 1}} \quad (26)$$

The desired form (equation 23) can be achieved by expanding the surface normal in $\frac{\partial\eta}{\partial x}$:

$$\tilde{n}_j \approx \tilde{n}_j|_{\frac{\partial\eta}{\partial x}=0} + \left(\frac{\partial\tilde{n}_j}{\partial\left(\frac{\partial\eta}{\partial x}\right)} \Big|_{\frac{\partial\eta}{\partial x}=0} \right) \frac{\partial\eta}{\partial x}, \quad (27)$$

where \tilde{N}_j is identified as the first and \tilde{n}'_j as the second term.

After straightforward calculations we get the following equations for the surface normal components:

$$\bar{N} = \left(-\frac{\partial H}{\partial x} f, f \right), \quad (28)$$

$$\bar{n}' = \left(\left(-f - \frac{\partial H}{\partial x} g \right) \frac{\partial\eta}{\partial x}, g \frac{\partial\eta}{\partial x} \right), \quad (29)$$

where

$$f = \varphi|_{\frac{\partial\eta}{\partial x}=0} = \left[1 + \left(\frac{\partial H}{\partial x} \right)^2 \right]^{-1/2}$$

and

$$g = \frac{\partial\varphi}{\partial\left(\frac{\partial\eta}{\partial x}\right)} \Big|_{\frac{\partial\eta}{\partial x}=0} = -\frac{\partial H}{\partial x} \left[1 + \left(\frac{\partial H}{\partial x} \right)^2 \right]^{-3/2}$$

Equation for the interface motion

The equation of motion for the free surface at $y = H + \eta$ is:

$$\frac{\partial(y - H^{(tot)})}{\partial t} + \bar{u}^{(tot)} \cdot \nabla(y - H^{(tot)}) = 0. \quad (30)$$

After writing out the terms we get:

$$-\frac{\partial\eta}{\partial t} - U^{(tot)} \frac{\partial(H + \eta)}{\partial x} + V^{(tot)} = 0.$$

After linearisation, and when the base flow terms are removed, this equation at $y = H$ reads:

$$\frac{\partial \eta}{\partial t} + \frac{\partial H}{\partial x} u + U \frac{\partial \eta}{\partial x} + \frac{\partial H}{\partial x} \frac{\partial U}{\partial y} \eta - v - \frac{\partial V}{\partial y} \eta = 0. \quad (31)$$

0.1. *Boundary conditions for the global eigenvalue problem*

In order to get boundary conditions for the eigenvalue problem, we again substitute the global mode ansatz (3–6) in the linearised boundary conditions presented the previous subsections. This replaces all disturbance terms a with their Fourier transformed counterparts \hat{a} , except the t -derivatives, which transform to $\frac{\partial a}{\partial t} = -i\omega \hat{a}$.

We arrive at the following conditions at the interface:

$$\hat{u}^1 + \hat{\eta} \frac{\partial U^1}{\partial y} = \hat{u}^2 + \hat{\eta} \frac{\partial U^2}{\partial y} \quad (32)$$

$$\hat{v}^1 + \hat{\eta} \frac{\partial V^1}{\partial y} = \hat{v}^2 + \hat{\eta} \frac{\partial V^2}{\partial y} \quad (33)$$

$$\begin{aligned} &(-P^1 + P^2) \delta_{ij} \hat{n}'_j + \frac{2}{Re} (E_{ij}^1 - E_{ij}^2) \hat{n}'_j + \\ &(-\hat{p}^1 + \hat{p}^2) \delta_{ij} N_j + \frac{2}{Re} (\hat{e}_{ij}^1 - \hat{e}_{ij}^2) N_j + \\ &+\hat{\eta} N_j \frac{\partial}{\partial y} (-P^1 + P^2) \delta_{ij} + \frac{2}{Re} \hat{\eta} N_j \frac{\partial}{\partial y} (E_{ij}^1 - E_{ij}^2) = \\ &\quad -\frac{1}{We} \left(N_i \frac{\partial \hat{n}'_j}{\partial x_j} + \hat{n}'_i \frac{\partial N_j}{\partial x_j} \right) \end{aligned} \quad (34)$$

$$-i\omega \hat{\eta} + \frac{\partial H}{\partial x} \hat{u} + U \frac{\partial \hat{\eta}}{\partial x} + \frac{\partial H}{\partial x} \frac{\partial U}{\partial y} \hat{\eta} - \hat{v} - \frac{\partial V}{\partial y} \hat{\eta} = 0, \quad (35)$$

where $\hat{n}' = \left[\left(-f - \frac{\partial H}{\partial x} g \right) \frac{\partial \hat{\eta}}{\partial x}, g \frac{\partial \hat{\eta}}{\partial x} \right]$ and $\hat{e}_{ij} = \frac{1}{2} \left(\frac{\partial \hat{u}_i}{\partial x_j} + \frac{\partial \hat{u}_j}{\partial x_i} \right)$.

References

- BLACKFORD, L. S., CHOI, J., CLEARY, A., D'AZEVEDO, E., DEMMEL, J., DHILLON, I., DONGARRA, J., HAMMARLING, S., HENRY, G., PETITET, A., STANLEY, K., WALKER, D. & WHALEY, R. C. 1997 *ScaLAPACK Users' Guide*. Philadelphia, PA: Society for Industrial and Applied Mathematics.
- CHEVALIER, M., SCHLATTER, P., LUNDBLADH, A. & HENNINGSON, D. S. 2007 SIMSON: a pseudo spectral solver for incompressible boundary layer flows. *Tech. Rep. TRITA-MEK 2007:07*. KTH Mechanics, Royal Institute of Technology, Stockholm, Sweden.
- FISCHER, P. F. 1997 An Overlapping Schwarz Method for Spectral Element Solution of the Incompressible Navier-Stokes Equations. *Journal of Computational Physics* **133**, 84–101.
- HUERRE, P. & MONKEWITZ, P. A. 1990 Local and global instabilities in spatially developing flows. *Annual Review of Fluid Mechanics* **22**, 473–537.
- JUNIPER, M., TAMMISOLA, O. & LUNDELL, F. 2011 Comparison of local and global stability properties of confined wake flows. *To be submitted to Journal of Fluid Mechanics* .
- JUNIPER, M. P. 2006 The effect of confinement on the stability of two-dimensional shear flows. *Journal of Fluid Mechanics* **565**, 171–195.
- LI, X. & TANKIN, R. S. 1991 On the temporal instability of a two-dimensional viscous liquid sheet. *Journal of Fluid Mechanics* **226**, 425–443.
- MASCHHOFF, K. J. & SORENSEN, D. 1996 P_ARPACK: An Efficient Portable Large Scale Eigenvalue Package for Distributed Memory Parallel Architectures. In *Applied Parallel Computing: Industrial Computation and Optimization* (ed. J. Wasniewski), pp. 478–486. Berlin /Heidelberg: Springer.
- REES, S. J. & JUNIPER, M. P. 2009 The effect of surface tension on the stability of unconfined and confined planar jets and wakes. *Journal of Fluid Mechanics* **633**, 71–97.
- SÖDERBERG, L. D. 2003 Absolute and convective instability of a relaxational plane liquid jet. *Journal of Fluid Mechanics* **493**, 89–119.
- TAMMISOLA, O., LUNDELL, F., SCHLATTER, P., WEHRFRITZ, A. & SÖDERBERG, L. D. 2011a Global linear and nonlinear stability of viscous confined plane wakes with co-flow. *Journal of Fluid Mechanics* .

- TAMMISOLA, O., LUNDELL, F. & SÖDERBERG, L. D. 2011*b* Effect of surface tension on global modes of confined wake flows. *Physics of Fluids* **23**, 014108.
- TUCKERMAN, L. & BARKLEY, D. 2000 Bifurcation analysis for timesteppers. In *NUMERICAL METHODS FOR BIFURCATION PROBLEMS AND LARGE-SCALE DYNAMICAL SYSTEMS* (ed. Doedel, E and Tuckerman, LS), *IMA VOLUMES IN MATHEMATICS AND ITS APPLICATIONS*, vol. 119, pp. 453–466. 233 SPRING STREET, NEW YORK, NY 10013, UNITED STATES: SPRINGER, Workshop on Numerical Methods for Large-Scale Dynamical Systems, MINNEAPOLIS, MN, SEP 29-OCT 03, 1997.
- VILLERMAUX, E. & HOPFINGER, E. J. 1994 Self-sustained oscillations of a confined jet: a case study for the non-linear delayed saturation model. *Physica D* **72**, 230–243.
- WEIDEMAN, J. A. C. & REDDY, S. C. 2000 A MATLAB Differentiation Matrix Suite. *Transactions on Mathematical Software* **26** (4), 465–519.